

Ultra Low Temperature Susceptometer and Magnetometer - Study of the Spin Glass Series $\text{LiHo}_x\text{Er}_{1-x}\text{F}_4$

THÈSE N° 5510 (2012)

PRÉSENTÉE LE 5 OCTOBRE 2012
À LA FACULTÉ DES SCIENCES DE BASE
LABORATOIRE DE MAGNÉTISME QUANTIQUE
PROGRAMME DOCTORAL EN PHYSIQUE

ÉCOLE POLYTECHNIQUE FÉDÉRALE DE LAUSANNE

POUR L'OBTENTION DU GRADE DE DOCTEUR ÈS SCIENCES

PAR

Julian PIATEK

acceptée sur proposition du jury:

Prof. V. Savona, président du jury
Prof. H. Rønnow, directeur de thèse
Prof. J.-Ph. Ansermet, rapporteur
Dr N. Laflorencie, rapporteur
Dr D. Silevitch, rapporteur



ÉCOLE POLYTECHNIQUE
FÉDÉRALE DE LAUSANNE

Suisse
2012

The yeoman's work in any science,
and especially physics,
is done by the experimentalist,
who must keep the theoreticians honest.

— Michio Kaku

To my family and mi Vida...

Acknowledgements

My thesis supervisor, Hernik Rønnow, deserves thanks for the major role he has played in shaping my work. Even though he had very little time, he would always be willing to discuss problems, whether they be technical, or related to data interpretation and theoretical concepts. Henrik's special gift – his infinite supply of unique ideas, which he generates non-stop – has been an invaluable tool. I would like to thank Ivica Živković for the role he played as co-director of my Master's theses, and the patience he showed in passing on much of his knowledge on AC susceptibility. The collaboration with Ivica allowed the dilution SQUID project to be realised – the concept along with many of the design elements, result from a large number of conversations we had.

Without the help from the workshops at ICMP, it is doubtful that I would have been able to implement the measurement techniques I have used. I am thankful to C. Amendola, G. Beney, F. Bertrand, G. Camarda, D. Clément, P. Cuanillon, D. Godat, G. Grandjean, P. Guex, B. Guisolan, O. Haldimann and M. Longchamp for all their technical help. I am grateful to K. Krämer for supplying the majority of the samples which I have measured. I would also like to acknowledge the help received from the local contacts at these neutron scattering experiments: N. B. Christensen, K. Prokes and M. Laver.

All of the current and previous group members have had a positive effect on me during my time at LQM. The first member I met was G. Nilsen, who graciously shared his passion and positive attitude towards science with me. J. Larrea kept me company in “the Halle” during the early days and was always up for a coffee break. K. Prsa and I. Kovacevic would actually listen when I would talk for hours on end about the operation of dilution fridge, and thankfully haven't posted the 10 hours of video on Youtube. My understanding of many theoretical aspects has greatly benefited from the knowledge of B. Dalla Piazza. The coffee breaks where we discussed some crazy interpretation of data, or plans for some obscure calculation have played an invaluable role in this thesis. The neutron scattering experiments would not have gone so smoothly if not for the help of N. Nikseresht and N. Tsyulin, the neutron scattering oriented members of the lab. Lunch just wouldn't have been the same without the *Cerberations*, who could always find the same nationalistic discussions interesting. The summer students I have had, K. Sen, S. Joglekar, S. Debler and J. Yu, taught me patience when explaining concepts and forced me to truly understand what I was doing.

I would not have come to be here if it were not for my parents, who have always encouraged me to satisfy my curiosity. They kindly volunteered to proofread my thesis for me, even when I

Acknowledgements

gave them about 5 minutes notice. I thank my brothers, Anton and Stefan for wasting their time having pointless discussions about all those things I find interesting, but probably aren't to anyone else. Last but not least I thank Mercè, for supporting me throughout the entire thesis and making life more enjoyable. Gracias mi Vida!

Lausanne, 20 July 2012

J.O.P.

Abstract

The first part of this thesis discusses technical details relating to measurements of magnetic properties at ultra low temperatures. The implementation of AC susceptibility at temperatures down to 30 mK is introduced and used as a platform to showcase selected quantum magnets measured during the thesis. Each presented system illustrates a particular strength of AC susceptibility. This is followed by in-depth analysis of the design and implementation of a new solution for a SQUID magnetometer capable of running below 100 mK. The system employs a piezomotor to move the sample inside a dilution fridge, rather than the existing designs, which involve moving the entire dilution fridge. Furthermore, the system is completely modular, allowing for rapid removal from the fridge, and opening the possibility to use it on virtually any commercial dilution refrigerator.

The latter part of the thesis presents a comprehensive study of a new family of model magnets, $\text{LiHo}_x\text{Er}_{1-x}\text{F}_4$, which combines the Ising spins of ferromagnetic LiHoF_4 with the XY ones of antiferromagnetic LiErF_4 . The temperature-doping ($T - x$) phase diagram has been studied using AC susceptibility, and three key regions investigated in detail using additional neutron scattering experiments and mean-field calculations. The first region, $x \gtrsim 0.6$, corresponds to an Ising ferromagnet, where $T_c(x)$ decreases linearly and faster than what mean-field predicts. At $T < T_c$ a so-called embedded spin-glass state is observed. The second region, $0.6 \gtrsim x \gtrsim 0.3$, undergoes a spin-glass transition, where needle-like spin clusters form along the Ising axis below $T_g(x) \sim 0.4 - 0.5$ K. Applying a field along the Ising axis at $T < 200$ mK produces a thermal runaway in the $x = 0.50$ sample, when the field reaches a value of $H = 0.029 \pm 0.002$ T. The final region, $x \lesssim 0.3$, corresponds to an antiferromagnetically coupled spin-glass, which shows archetypal spin-glass behaviour.

Keywords: Dilution SQUID magnetometer, AC susceptibility, spin-glass, elastic neutron scattering, thermal runaway

Résumé

La première partie de cette thèse porte sur les technicalités qu'impliquent les mesures de propriétés magnétiques à très basses températures. La réalisation de mesures de susceptibilité magnétique alternée à des températures de l'ordre de 30 mK est introduite et utilisée pour donner un premier aperçu de certains des différents matériaux étudiés dans cette thèse. Chaque cas particulier illustre l'une des qualités des mesures de susceptibilité magnétique alternée. Suit ensuite une analyse poussée de la conception nouvelle d'un magnétomètre à interférences quantiques (SQUID) capable de fonctionner à des températures inférieures à 100 mK. Le nouveau concept implique l'utilisation d'un moteur piézoélectrique faisant se mouvoir l'échantillon mesuré à l'intérieur du cryostat à dilution en lieu et place de faire se mouvoir le cryostat dans son entièreté comme cela avait été réalisé jusqu'à présent. De plus, ce nouveau concept, de par sa modularité, ouvre la possibilité d'adaptations sur virtuellement n'importe quel cryostat à dilution disponible commercialement.

La seconde partie de la thèse présente une étude poussée d'une nouvelle famille de matériaux magnétiques prototypiques, $\text{LiHo}_x\text{Er}_{1-x}\text{F}_4$, combinant les spins Ising du ferro-aimant LiHoF_4 avec ceux, XY, de l'anti-ferro-aimant LiErF_4 . Le diagramme de phase température-dopage ($T - x$) a été étudié au moyen de la mesure de susceptibilité alternée, et trois régions clés de ce diagramme ont été étudiées plus à fond au moyen d'expériences de diffraction de neutrons et de calculs de champs moyens. La première région, $x \gtrsim 0.6$, correspond à un régime ferro-magnétique de type Ising pour lequel $T_c(x)$ décroît linéairement, mais plus rapidement que la prédiction de champs moyen. Lorsque $T < T_c$, le système entre dans un état appelé verre de spin "embedded". Dans la seconde région, $0.6 \gtrsim x \gtrsim 0.3$, le système entre dans une phase de verre de spin composé de domaines magnétiques en forme d'aiguille orientées le long de l'axe Ising à des températures de l'ordre de $T_g(x) \sim 0.4 - 0.5$ K. L'application d'un champ magnétique le long de l'axe Ising à des températures $T < 200$ mK résulte en une "fuite en avant thermique" pour l'échantillon avec $x = 0.50$ et un champ $H = 0.029 \pm 0.002$ T. La dernière région, pour $x \lesssim 0.3$, correspond à un verre de spin anti-ferro-magnétiquement couplé, présentant les propriétés conventionnelles d'un tel système.

Mots-clés: Magnétomètre à interférence quantiques à températures de dilution, susceptibilité magnétique alternée, verre de spin, diffraction de neutron, fuite en avant thermique

Contents

Acknowledgements	v
Abstract	vii
Résumé	ix
Table of Contents	xiii
List of figures	xviii
1 Introduction	1
1.1 Ultra Low Temperature Physics	2
1.1.1 Dilution Refrigerator	2
1.1.2 Thermometry	5
1.2 Spin-Glasses	5
1.2.1 What Makes a Spin-Glass	6
1.2.2 Phenomenology	8
1.2.3 Experimentalist's Picture of a Spin-Glass	15
1.2.4 Related Phenomena	16
1.3 Outline of this Work	16
2 AC Susceptibility	19
2.1 Principle of AC susceptibility	20
2.2 Implementation	22
2.2.1 Measuring the Susceptibility	22
2.2.2 Mounting in the Dilution Fridge	24
2.3 Disordered TaS ₂ – A Superconducting Dichalcogenide	25

Contents

2.4	Low Dimensional & Frustrated Quantum Magnets	28
2.4.1	Spangolite	28
2.4.2	$\text{KTi}(\text{SO}_4)_2 \cdot \text{H}_2\text{O}$	30
2.4.3	Ba_2YMoO_6	32
2.4.4	LiErF_4	33
2.5	Overview and Future Perspectives	34
2.5.1	Strengths	35
2.5.2	Weaknesses	35
2.5.3	Future Perspectives	36
3	SQUID Magnetometry	37
3.1	Theory	37
3.2	Principle of Operation	39
3.3	First Prototype	42
3.3.1	Design Considerations	42
3.3.2	Challenges and Solutions	45
3.3.3	Intermediate Results	52
3.4	Final Configuration	54
3.4.1	Support Structure	55
3.4.2	1K Pot	56
3.4.3	Mixing Chamber and Sample	57
3.5	Outlook	59
3.5.1	AC Susceptibility	59
3.5.2	Magnetoelectric Effect	60
4	$\text{LiHo}_x\text{Er}_{1-x}\text{F}_4$	61
4.1	The LiReF_4 Model Magnets	61
4.1.1	$\text{LiHo}_x\text{Y}_{1-x}\text{F}_4$	64
4.1.2	LiErF_4	65
4.1.3	$\text{LiHo}_x\text{Er}_{1-x}\text{F}_4$	65
4.2	AC Susceptibility Overview	65
4.3	Tools for Detailed Investigation	70

4.3.1 Neutron Scattering	70
4.3.2 Mean-Field Calculations	77
4.4 Embedded Spin-Glass	80
4.4.1 Ferromagnetic State	80
4.4.2 Spin-Glass State	85
4.4.3 T_c vs. x	90
4.5 Ferromagnetic Spin-Glass	95
4.5.1 Neutron Scattering	95
4.5.2 Zero Field AC Susceptibility	104
4.5.3 Susceptibility in a Longitudinal Field	106
4.5.4 Field Induced Thermal Runaway	112
4.6 Antiferromagnetic Spin-Glass	121
5 Conclusion	127
5.1 $\text{LiHo}_x\text{Er}_{1-x}\text{F}_4$	127
5.2 Dilution SQUID	130
6 Outlook	131
6.1 $\text{LiHo}_x\text{Er}_{1-x}\text{F}_4$	131
6.2 Dilution SQUID	131
A $\text{LiHo}_x\text{Er}_{1-x}\text{F}_4$ Preparation and Quality Control	133
B Determination of T_g in Spin-Glasses	137
C Crystal Field Point Charge Calculation	139
D Initial Interpretation of the Thermal Runaway in $\text{LiHo}_{0.50}\text{Er}_{0.50}\text{F}_4$	141
Bibliography	147
Curriculum Vitae	157

List of Figures

1.1	Schematic drawing and photo of a dilution fridge	3
1.2	Diagram of a frustrated triangular antiferromagnet	6
1.3	Field cooled and zero-field cooled magnetisation for $\text{Cu}_{1-x}\text{Mn}_x$	8
1.4	Typical AC susceptibility of spin-glasses	10
1.5	AC susceptibility spectroscopy on $\text{LiHo}_{0.045}\text{Y}_{0.955}\text{F}_4$	11
1.6	Temperature dependence of $-\chi_3$ above T_g in $\text{Ag}_{1-x}\text{Mn}_x$	12
2.1	Typical configuration of an inductive susceptometer	20
2.2	Schematic drawing of the AC susceptibility set-up.	22
2.3	Diagrams of the longitudinal and transverse susceptometers	23
2.4	Photo of the AC susceptibility setup	24
2.5	Photo of the d - TaS_2 sample stick	26
2.6	Schematic showing probable magnetic field lines for different stackings of TaS_2	26
2.7	In-plane electrical resistivity and c -axis AC susceptibility of d - TaS_2	27
2.8	Magnetic susceptibility of spangolite	29
2.9	High temperature magnetic susceptibility of $\text{KTi}(\text{SO}_4)_2 \cdot \text{H}_2\text{O}$	31
2.10	Low temperature real susceptibility, $\chi'(H)$ and $\chi'(T)$, of $\text{KTi}(\text{SO}_4)_2 \cdot \text{H}_2\text{O}$	31
2.11	Low temperature AC susceptibility of Ba_2YMoO_6	33
2.12	Phase diagram and critical scaling of AC susceptibility in LiErF_4	34
3.1	Schematic diagram and flux-to-voltage transfer function of a DC-SQUID	39
3.2	Operating principle of a second order gradiometer	41
3.3	Energy sensitivity ϵ of the DC SQUID vs. $\Gamma (\propto T)$	44
3.4	Principle of motion of the piezomotor translation stage	45

List of Figures

3.5	Capacitor mounted on the SQUID package	47
3.6	Schematic representation of the envisaged flux transformer	49
3.7	Photo of the components of the flux transformer	50
3.8	Heat generated by moving the piezomotor	52
3.9	Photo of the piezomotor mounted in the first prototype of the Dilution SQUID	53
3.10	Magnetisation of a paramagnetic salt measured in the SQUID prototype.	54
3.11	Photo of the final piezomotor and pick-up coil support structure	55
3.12	Photo of the 1K pot showing various elements of the Dilution SQUID	56
3.13	Photo of the mixing chamber with the magnetometer module attached	57
3.14	Photo of the sample cold plate and thermal decoupler of the magnetometer . .	58
4.1	Diagram showing the crystal structure of the LiReF_4 system.	62
4.2	Effect of ramp rate on typical features of $\chi(T)$ in $\text{LiHo}_x\text{Er}_{1-x}\text{F}_4$	66
4.3	Overview of the AC susceptibility data	68
4.4	Experimental phase diagram of $\text{LiHo}_x\text{Er}_{1-x}\text{F}_4$	69
4.5	Schematic of the E4 diffractometer	75
4.6	Schematic of the RITA-II triple axis spectrometer	75
4.7	Photos of the neutron experiment sample holders	77
4.8	ω -scans across the (2,2,0) and (1,1,2) Bragg peaks in $\text{LiHo}_{0.79}\text{Er}_{0.21}\text{F}_4$	81
4.9	H_a dependence of the (2,2,0) Bragg peak in $\text{LiHo}_{0.79}\text{Er}_{0.21}\text{F}_4$	82
4.10	H_a field dependent detector efficiency correction for (2,2,0) Bragg peak in $\text{LiHo}_{0.79}\text{Er}_{0.21}\text{F}_4$ at e4	83
4.11	H_a dependence of the (1,1,2) and (2,2,0) Bragg peaks in $\text{LiHo}_{0.79}\text{Er}_{0.21}\text{F}_4$	83
4.12	Temperature dependence of the (1,1,2) and (2,2,0) Bragg peaks in $\text{LiHo}_{0.79}\text{Er}_{0.21}\text{F}_4$	84
4.13	Q_l scans centred around (1,1,0) in $\text{LiHo}_{0.79}\text{Er}_{0.21}\text{F}_4$	86
4.14	Temperature scans taken on $\text{LiHo}_{0.675}\text{Er}_{0.325}\text{F}_4$ at 7.7, 77 and 770 Hz	87
4.15	Frequency dependence of T_f in $\text{LiHo}_{0.675}\text{Er}_{0.325}\text{F}_4$	88
4.16	Comparison of the mean-field and experimental $T_C - x$ phase diagrams	91
4.17	Effect of a single impurity on nearest neighbour Ho spins	92
4.18	Dipole field created by Ho and Er	93
4.19	Scattered intensity pseudo-colour map around (2,0,0) in $\text{LiHo}_{0.50}\text{Er}_{0.50}\text{F}_4$	96

List of Figures

4.20 Q_h and Q_l scans centred around $Q = (2, 0, 0)$ in $\text{LiHo}_{0.50}\text{Er}_{0.50}\text{F}_4$	97
4.21 H_a and T dependence of ferromagnetic correlations in $\text{LiHo}_{0.50}\text{Er}_{0.50}\text{F}_4$	98
4.22 Fits of the ferromagnetic correlations in $\text{LiHo}_{0.50}\text{Er}_{0.50}\text{F}_4$	99
4.23 Scattered intensity pseudo-colour map around $(0, 0, 2.5)$ in $\text{LiHo}_{0.50}\text{Er}_{0.50}\text{F}_4$. . .	101
4.24 Search for antiferromagnetic correlations in $\text{LiHo}_{0.50}\text{Er}_{0.50}\text{F}_4$	102
4.25 H_a and T dependence of the possible antiferromagnetic correlations in $\text{LiHo}_{0.50}\text{Er}_{0.50}\text{F}_4$	103
4.26 Fit of the antiferromagnetic correlations in $\text{LiHo}_{0.50}\text{Er}_{0.50}\text{F}_4$	104
4.27 Temperature scans on $\text{LiHo}_{0.50}\text{Er}_{0.50}\text{F}_4$ comparing χ_{zz} and χ_{xx}	105
4.28 Frequency dependence of T_f in $\text{LiHo}_{0.50}\text{Er}_{0.50}\text{F}_4$	106
4.29 H_a and H_c scans on $\text{LiHo}_{0.50}\text{Er}_{0.50}\text{F}_4$ at $T = 0.05$ K	108
4.30 Hysteresis in χ_{zz} observed in H_c scans on $\text{LiHo}_{0.50}\text{Er}_{0.50}\text{F}_4$	108
4.31 H_c scans of χ_{zz} taken at different temperatures in $\text{LiHo}_{0.50}\text{Er}_{0.50}\text{F}_4$	109
4.32 T and H_c dependence of χ_{zz} as seen by temperature scans in $\text{LiHo}_{0.50}\text{Er}_{0.50}\text{F}_4$.	110
4.33 Comparison between χ_{xx} and χ_{zz} in H_c scans in $\text{LiHo}_{0.50}\text{Er}_{0.50}\text{F}_4$	111
4.34 T and H_c dependence of χ_{xx} in $\text{LiHo}_{0.50}\text{Er}_{0.50}\text{F}_4$	111
4.35 Photo of the sample used to measure simultaneous AC susceptibility, magnetisa- tion and magnetocaloric effect in $\text{LiHo}_{0.50}\text{Er}_{0.50}\text{F}_4$	112
4.36 Temperature dependent ZFC and FC χ' , χ'' and M in $\text{LiHo}_{0.50}\text{Er}_{0.50}\text{F}_4$	113
4.37 Hysteresis scan from ZFC in $\text{LiHo}_{0.50}\text{Er}_{0.50}\text{F}_4$ showing χ' , χ'' , T_{sample} and M . . .	115
4.38 H_z ramp rate dependence of χ' , χ'' , T_{sample} and M in $\text{LiHo}_{0.50}\text{Er}_{0.50}\text{F}_4$	116
4.39 H_z scans followed by time scans in $\text{LiHo}_{0.50}\text{Er}_{0.50}\text{F}_4$, measuring χ' , χ'' , T_{sample} and M , and showing a thermal runaway	118
4.40 Local heating of $\text{LiHo}_{0.50}\text{Er}_{0.50}\text{F}_4$ in zero field at 50 mK followed by time scans showing the relaxation of χ' , χ'' and T_{sample}	119
4.41 H_z scan followed by sample heating pulse and subsequent relaxation measuring χ' , χ'' , T_{sample} and M in $\text{LiHo}_{0.50}\text{Er}_{0.50}\text{F}_4$	120
4.42 Frequency dependence of T_f in $\text{LiHo}_{0.25}\text{Er}_{0.75}\text{F}_4$	122
4.43 Neutron scattering data on $\text{LiHo}_{0.25}\text{Er}_{0.75}\text{F}_4$	124
4.44 T and H_c dependence of the spin-glass state in $\text{LiHo}_{0.25}\text{Er}_{0.75}\text{F}_4$	125
4.45 Search for ferromagnetic correlations in $\text{LiHo}_{0.25}\text{Er}_{0.75}\text{F}_4$	126
5.1 Experimental phase diagram of $\text{LiHo}_x\text{Er}_{1-x}\text{F}_4$	128

List of Figures

A.1	EDX spectrum of $\text{LiHo}_x\text{Er}_{1-x}\text{F}_4$ used to determine the Ho:Er ratio	134
A.2	SEM image of $\text{LiHo}_{0.90}\text{Er}_{0.10}\text{F}_4$ showing LiF inclusions	134
B.1	Determination of T_g in $\text{LiHo}_{0.50}\text{Er}_{0.50}\text{F}_4$	138
D.1	Frequency dependence of χ_{zz} in H_c scans on $\text{LiHo}_{0.50}\text{Er}_{0.50}\text{F}_4$ at $T = 0.05$ K . . .	142
D.2	Rate dependence of χ_{zz} in H_c scans on $\text{LiHo}_{0.50}\text{Er}_{0.50}\text{F}_4$ at $T = 0.04$ K	143
D.3	Rate and frequency dependence of χ_{zz} peak in H_c field scans	143
D.4	H_c scans followed by time scans measuring χ_{zz} on $\text{LiHo}_{0.50}\text{Er}_{0.50}\text{F}_4$	144
D.5	Rate dependence of χ_{zz} in H_c scans on $\text{LiHo}_{0.50}\text{Er}_{0.50}\text{F}_4$ at $T = 0.04$ K	145

1 Introduction

In the natural sciences, simplistic models are made and used to capture and explain complex phenomena observed in the world around us. A good model is one which, while remaining relatively simple, is capable of explaining certain aspects of a physical problem. A good example of such a model is that of the ideal gas, where atoms and molecules in a gas are treated as hard spheres, much like tiny snooker balls. Although the model is not capable of explaining the vast majority of physics of gases due to its simplicity, it can explain the behaviour of helium gas remarkably well. In order to better reveal the behaviour of a gas, this model has been built upon, adding complexity and improving both understanding and predictive power.

In the field of condensed matter physics, models are used in exactly the same way. A theory which can explain a particular group of phenomena is devised and experimentally tested (or experimental data is taken and then a theory devised). A particular challenge which exists in understanding real systems is that many interesting effects observed (e.g. superconductivity, Bose-Einstein condensation...) are a result of the dynamics of a very large number of interacting objects. The problems are sufficiently complex that analytical solutions are rarely possible and one must turn to the power of computers in order to gain understanding. Unfortunately quantum mechanical problems do not scale well when it comes to the memory requirements to calculate the properties of many interacting particles. Today we are capable of calculating what happens when around 40 objects interact, which is a far cry from the 10^{23} or so objects in any macroscopic solid. Faced with such a daunting task, one very productive way to proceed in the field of quantum magnetism is to identify and study model magnets – magnets which happen to be a very good realisation of a relatively simple theoretical model. The bulk of this thesis is focused on an experimental investigation of one such model magnet, the dipolar coupled $\text{LiHo}_x\text{Er}_{1-x}\text{F}_4$.

The second core aspect of this thesis is the development of experimental techniques used to measure magnetic systems at ultra low temperatures. In experimental physics, a very large amount of time is spent in making sure that experiments will give results of acceptable quality. In my opinion, the development, strengths and weaknesses of experimental tools and

methods which are discovered during a Ph.D. thesis are often overlooked and should receive more attention. A Ph.D. thesis is more than a collection of original research aiming to solve a problem in the scientific world, it is also the starting point for new students – a framework to pass on knowledge gained over several years of research. Thus in this text my aim is to pass on valuable information, not only on the physics observed in the various systems measured, but equally on the practical aspects relating to probing and extracting the information.

1.1 Ultra Low Temperature Physics

In order to study $\text{LiHo}_x\text{Er}_{1-x}\text{F}_4$, one pre-requisite is ultra low temperatures, temperatures well below 1 K and typically down to 30 mK. Getting down to such a low temperature represents a great challenge for a variety of reasons. If we think about cooling things in every day life, we typically evaporate some refrigerant from a liquid to a gas and in doing so remove heat. The first challenge to cooling down to ultra low temperatures is that all liquids which one could use for cooling become solids below ~ 20 K, with the single exception of Helium. At atmospheric pressures, liquid helium evaporates at 4.2 K, and thus by liquefying helium, temperatures down to 4.2 K are now fairly routine. By pumping on this liquid helium and reducing the vapour pressure, it is possible to lower the temperature further still, to around 1 K. To get to lower temperatures still, it is possible to use isotopic ^3He instead of the much more common (and significantly cheaper) ^4He . Pumping on a volume of liquid ^3He decreases the temperature to ~ 250 mK, as is done in a so-called ^3He fridge. If temperatures colder than this are needed, the most typical solution is to use a piece of equipment called a dilution refrigerator. This machine is capable of cooling to temperatures of only several mK in the most powerful variants. This section discusses the key elements of a dilution refrigerator before moving on to other challenges at *dilution temperatures* (tens of mK), such as thermometry and considerations for experimental probes.

1.1.1 Dilution Refrigerator

The general idea of a dilution refrigerator (or fridge) was first proposed by H. London in 1951 [52], with the first prototype of a device being built some ten years later. Since then, dilution fridges have become key instruments in low-temperature laboratories. There exists a large amount of literature explaining the principles of operation and design considerations, such as in books by Pobell [73] or White and Meeson [92]. The introduction presented will therefore skip past the detailed explanation of *how and why* a dilution fridge cools to such low temperatures and focus on the key elements of a dilution fridge, and how these relate to performance.

The operating principle of a dilution fridge is to evaporate liquid ^3He into liquid ^4He across a phase boundary which occurs below temperatures around several hundred mK. Due to the unique properties of mixtures of ^3He and ^4He this evaporation is capable of removing heat down to absolute zero (although technical constraints make this unviable). Fig. 1.1 shows

1.1 Ultra Low Temperature Physics

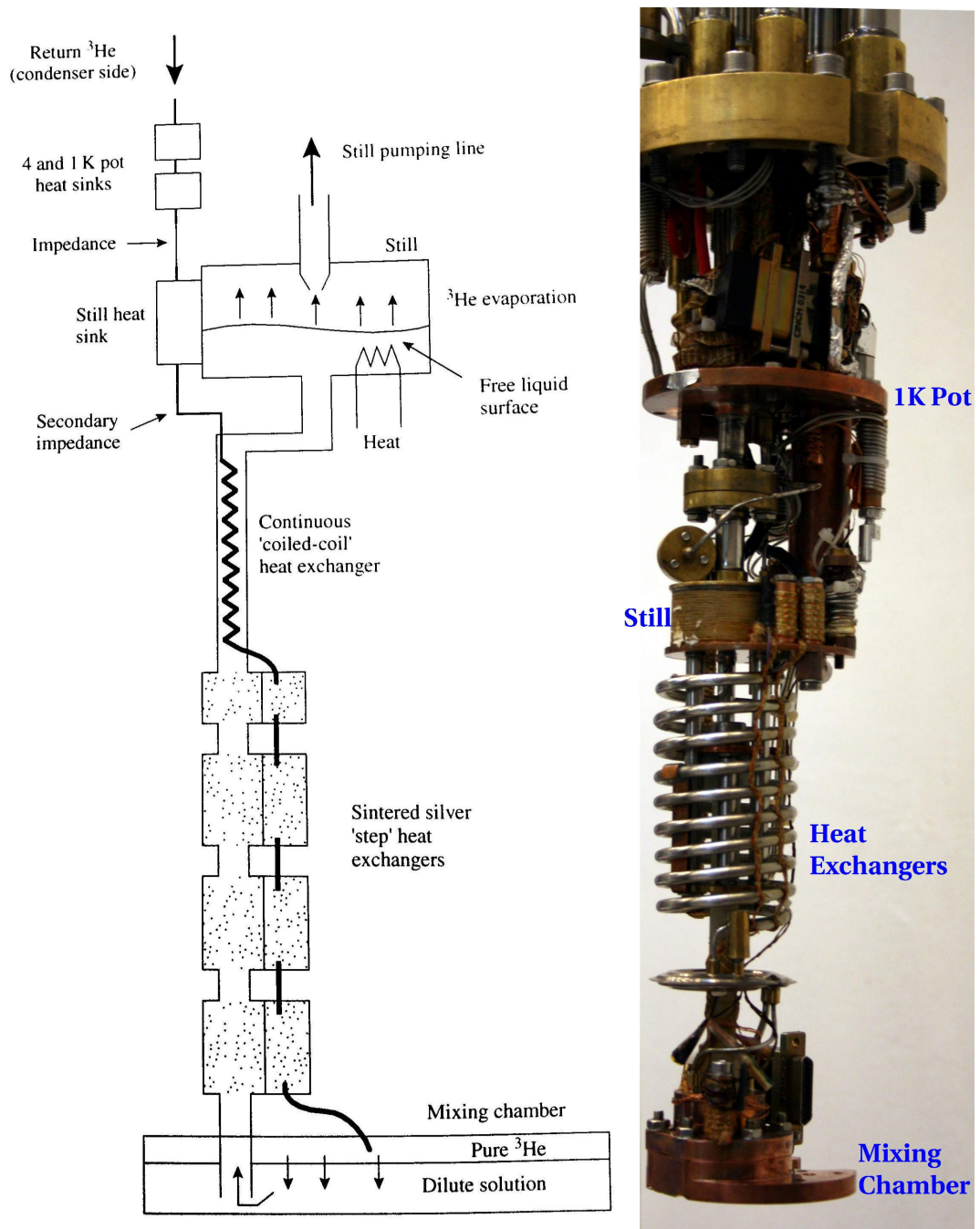


Figure 1.1: [Left] Schematic drawing of a dilution fridge (taken from White and Meeson [92]). [Right] Photo of the Oxford Instruments Kelvinox dilution fridge used for measurements in this work. The ^3He flows into the 1K pot where it is condensed and flows through several heat exchangers into the mixing chamber. A phase separation occurs inside the mixing chamber and the ^3He evaporates from the rich phase into the dilute phase, where it passes back up through the heat exchangers and is pumped from the still and returned to the 1K pot.

a schematic diagram of a dilution fridge on the left and a photo of the Oxford Instruments Kelvinox dilution fridge used in this work on the right. It is difficult to explain the operation of a dilution fridge in several sentences, partially due to the complexity of it and partially due to the procedure required before it is actually running as a dilution fridge. In this context, “running” means that there is a phase separation between a ^3He rich phase, which can be thought of as pure ^3He , and a dilute phase, which consists of 6 – 7% of ^3He inside liquid ^4He . To understand the operation of the fridge once this phase separation has been established, we follow the route taken by the ^3He through the fridge while referring to the various elements shown in Fig. 1.1.

The ^3He flows from room temperature through several heat exchanges inside the cryostat where it is cooled down to 4.2 K by the liquid ^4He and then passes into the so-called *1K pot*. The 1K pot gets its name from the fact that a small reservoir of liquid ^4He is pumped there, which lowers the temperature, typically to ~ 1.5 K. The ^3He passes through the 1K pot where the temperature is low enough that it condenses into a liquid, the ^3He rich phase. From here the liquid flows through a large series of heat exchangers, which exchange heat with the outgoing dilute phase, before reaching the *mixing chamber*. Inside the mixing chamber, the ^3He evaporates into the liquid ^4He (the dilute phase) and the resulting gas of ^3He makes its way back up through the heat exchangers to the *still*. A powerful vacuum pump is attached to the still which is used to pump off and recirculate the ^3He , making the fridge a continuous cycle device. The still is typically equipped with a heater to maintain the temperature at some optimal value (typically 600 – 800 mK, depending on the system) to maximise the flow of ^3He .

The cooling power at the phase separation is related to the amount of ^3He that can be transferred across the phase separation line as follows [73]:

$$\dot{Q}(T) = 84\dot{n}T^2, \quad (1.1)$$

where $\dot{Q}(T)$ is the temperature-dependent heat transfer and \dot{n} is the number of moles of ^3He passing from the rich to the dilute phase in one second. Therefore the first thing one must do in order to have a good fridge is to have a large flow of ^3He through the system. This is done with the help of powerful vacuum pumps, which pump the ^3He from the still. The second challenge in creating a well balanced and powerful dilution fridge requires great knowledge on the thermal properties of various materials at low temperatures and ingenuity. The cooling power is always going to be very small as $T \rightarrow 0$, and the only way to achieve the lowest temperatures is by reducing heat leaks into the system. The main heat load is of course the “hot” ^3He coming down from the 1K pot, so this liquid must be cooled sufficiently before it gets to the mixing chamber. This explains the large number of (rather complex) heat exchangers on a dilution fridge. Dilution fridges are typically rated and compared by their cooling power at a temperature of 100 mK, which is typically in the region of 20-40 μW for a small system and ~ 400 μW for a powerful model. The Oxford Instruments Kelvinox fridge used in this work typically has a cooling power of ~ 30 μW at 100 mK.

1.1.2 Thermometry

Thermometry at such low temperatures requires new thermometer materials, as thermometers which are sensitive at higher temperatures typically lose their sensitivity at low temperatures. One must therefore find a system which has a clear and reproducible signal in the temperature range from several mK up to several K. The thermometer also needs to be easy to measure and well thermalised to the dilution fridge. The most typical solution is to use thick film RuO₂ resistors with a room temperature resistance in the region of several kΩ. The advantage of these resistors is that they are cheap, small (thus easy to thermalise) and offer a reproducible temperature dependence. Before such resistors can be used for reproducible measurements, they must first be thermally cycled to 77 K roughly 100 times [35]. This thermal cycling decreases the 4.2 K variability in resistance from several percent to around one part per thousand. At low temperatures, the resistance increases exponentially and can be best fit by a 5th order polynomial of the following form:

$$\log\left(\frac{1}{T}\right) = \sum_{n=0}^5 a_n \log(R - R_{300K})^n, \quad (1.2)$$

where the resistance is measured in kΩ.

Calibration of the thermometer used in this work has been carried out using a 202 series SRD1000 fixed point and CMN1000 measurement system from Hightech Development Leiden [15]. The system uses 13 superconducting references (SRD1000) between 14 mK and 7.2 K, each one with an uncertainty in the transition temperature of < 1% and typically < 0.2%. The second part of the thermometer (CMN1000) measures the susceptibility of the paramagnetic salt Ce₂Mg₃(NO₃)₁₂ · 24H₂O (commonly referred to as CMN), which remains paramagnetic down to ~ 2 mK. The susceptibility is very well described by a Curie-Weiss law:

$$\chi \propto \frac{1}{T - \theta_{CW}}, \quad (1.3)$$

with $\theta_{CW} = -0.004$ mK

The CMN1000 thermometer measures the paramagnetic susceptibility from CMN, taking the discrete temperatures from the fixed point thermometer to fit the Curie-Weiss law above. By using this in conjunction with the reference temperatures from the superconducting fixed point device, continuous thermometry is possible between 10 mK and 8 K.

1.2 Spin-Glasses

Simply put, a spin-glass is a magnetic state where spins are *frozen* and therefore do not fluctuate as in a paramagnet or diamagnet, but at the same time there is no true long range

order. In many ways it is simply the magnetic analogue to a structural glass, where the atoms are frozen but amorphous. Spin-glasses show interesting dynamics which are typically visible across the entire range of frequencies we are capable of measuring, from mHz up to THz. They are easier to study than conventional glasses both because of the simple quantum behaviour of spins and the ability to easily measure their response, making spin-glass physics a very lively field of research. Furthermore, the statistical theories developed for spin-glasses have successfully been applied to many problems including error-correcting codes, image restoration and neural networks [69]. In this section the elements required to make a spin-glass are introduced, followed by a discussion of their characteristic signatures and some related phenomena.

1.2.1 What Makes a Spin-Glass

Before discussing the experimental hallmarks of a spin-glass, it is intuitive to get a feeling for what kind of material will form a spin-glass. In magnetism, it is uncommon for a particular system to remain disordered at zero temperature. The order can either be characterised as long range order, where the spins are correlated over very large lengths or short range order, where highly frustrated spins form a quantum state such as a singlet state. In many ways a spin-glass is something in between these two extremes, where frustration stops long range order forming and a microscopic disorder in the system prevents short range order. It is this combination of both frustration and disorder which make a system form a spin-glass.

1.2.1.1 Frustration

Frustration is the name given to the phenomena where a spin is incapable of simultaneously satisfying all the interactions with neighbouring spins. The simplest example of this is the antiferromagnet on a triangular lattice shown in Fig. 1.2. The magnet consists of three spins, each coupled to the other two antiferromagnetically, at the apexes of an equilateral triangle. If the bottom left spin is set as spin up, then the bottom right spin must be spin down, and this

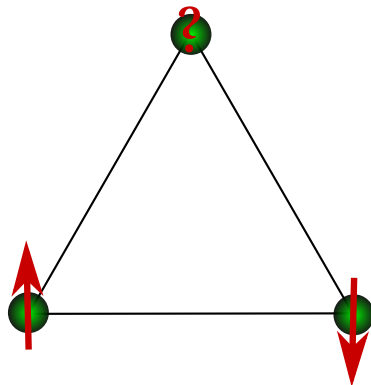


Figure 1.2: Diagram of a frustrated triangular antiferromagnet.

leads to the top spin wanting to be simultaneously spin up and spin down; it is not possible to satisfy the anti-ferromagnetic coupling with both neighbours simultaneously.

This kind of geometric frustration is perhaps the most interesting and widely studied form of frustration, but it is not the only kind which can exist. Frustration can also be due to competing interactions, as is the case in the $J_1 - J_2$ frustrated 1D chains, where the nearest neighbour interaction (J_1) and next nearest neighbour interaction (J_2) have similar amplitudes but cannot be simultaneously satisfied. An example of this would be if both J_1 and J_2 had negative signs, implying antiferromagnetic correlations. The interaction itself can also be inherently frustrated, as is the case for the dipolar interaction, where the unique shape of the field generated by a single dipole frustrates neighbouring spins.

1.2.1.2 Disorder

Disorder, or randomness, implies that the interactions between spins cannot be represented in a periodic (ordered) manner. In nature, spin-glasses do exist as binary alloys of a non-magnetic metal, containing a small percentage of magnetic impurities. In these alloys one finds spins which are placed on a periodic lattice at random resulting in a spin-glass. One can also make disorder by taking a non-magnetic chemical compound and replacing a small portion of one of the non-magnetic ion species with a magnetic one; the magnetic ions will pick a site purely at random (of course while keeping within the chemical constraints of the compound). Another logical way in which this can be done is to take an amorphous material containing spins; the spins in such an amorphous material will have different inter-atomic spacings. These are all examples of *site-randomness*, where the position of the spin is random, however it is even possible to have disorder on a perfect lattice. Such randomness comes about from a random type of bond between spins and is known as *bond-randomness*. Taking a perfect lattice and making the interaction between neighbouring spins randomly either ferromagnetic or antiferromagnetic is an example of this kind of disorder.

1.2.1.3 Spin-Glass Materials

Given the various ways in which both frustration and disorder can be realised, it is normal to assume that spin-glass phases are present in a very large number of materials. Indeed, even if they were not really identified as a separate class of magnetic materials until the 1970s, spin-glasses have been studied since the 1930s without realising what they were [66]. The first materials to be identified as spin-glasses are the *canonical spin-glasses* which consist of binary alloys such as $\text{Au}_{1-x}\text{Fe}_x$, $\text{Ag}_{1-x}\text{Mn}_x$ and $\text{Cu}_{1-x}\text{Mn}_x$ [see for example 17, 67], where the frustration is due to the random site disorder coupled with the RKKY interaction. Several years later, the first insulating spin-glasses were identified, of which $\text{Eu}_x\text{Sr}_{1-x}\text{S}$ was the first discovered non-metallic spin-glass [56, 57]. In general, insulating spin-glasses are found in crystalline chemical compounds where the material is doped with a non-magnetic ion and frustration can be either geometric, or due to frustrated interactions.

1.2.2 Phenomenology

As with most complex systems, it is very difficult to give a clear and concise description of how a spin-glass behaves; indeed this is the topic of several books, such as those by Mydosh [66] or Fischer and Hertz [29]. Given the existence of such books, only a brief introduction to some of the most common experimental probes which are well suited to studying spin-glasses is given. The experimental features observed in AC susceptibility, which is possibly the most used and powerful probe for measuring spin-glasses, are presented before discussing the dynamics of the system. The figures presented here show typical behaviour of spin-glass, and are thus taken from the existing literature, and appropriately referenced.

1.2.2.1 Spin-Glass Probes

As the temperature is lowered from the high temperature paramagnetic state to below the frequency dependent freezing temperature T_f , several experimental techniques are capable of detecting signatures of the spin-glass state. Here, the experimental signatures observed in DC magnetisation, μ SR and neutron scattering are discussed. The first technique to be considered is magnetisation measurements in a small DC field (which typically requires a SQUID magnetometer to achieve the required sensitivity).

In a magnetisation measurement, there are two ways one can cool the sample for performing a measurement. The first consists of cooling the sample from high temperature in a DC field and measuring the magnetisation in this field; this is known as a *field cooled* (FC) measurement. The second measurement is a *zero-field cooled* (ZFC) measurement; the sample is cooled to base temperature in zero external field, the field is then turned on (to the same value as in the FC case) and magnetisation is measured as a function of temperature. If one compares ZFC and FC measurements for a spin-glass, as is done in Fig. 1.3 (taken from Nagata et al. [67]) one finds that the two scans overlap perfectly at $T > T_f$, but below this temperature they begin to diverge.

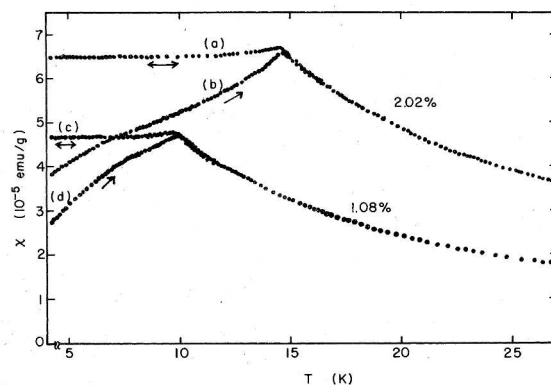


Figure 1.3: Field cooled (a,c) and zero-field cooled (b,d) magnetisation for $\text{Cu}_{1-x}\text{Mn}_x$ (1 and 2 at. %) as a function of temperature measured in 6 gauss. Taken from Nagata et al. [67].

This behaviour is similar to that of a ferromagnet, however there are certain features which can be effectively used to distinguish between ferromagnetic and glassy behaviour. Typically in a ferromagnet at low temperatures even the smallest external fields allow for domains aligned along the field to become dominant. This has two effects: firstly in the FC scan, the magnetisation typically grows as the temperature is reduced and the second is that the ZFC scan has a shallow slope and is often flat across a large range of temperatures $< T_C$. In a spin-glass on the other hand, reducing the temperature freezes more and more spins into the glassy state, implying that the FC scan is typically flat below T_f and the ZFC scan has a steeper slope than a ferromagnet and keeps reducing to the lowest temperatures.

A second method which is rather common in the study of spin-glasses is muon spin relaxation (μ SR). In a μ SR experiment, a beam of positive muons is implanted into the sample, where it will precess around any *local* magnetic fields in the sample. After $2.2 \mu\text{s}$ the muon decays into a positron and the asymmetry in the emission direction of the positrons is measured. This asymmetry can, in principle, give information about both the strength of the local fields and the rate at which they fluctuate. In the case of low-field experiments, the difference between forward and backward emission of positrons is related to the spin-relaxation function $G_z(t)$, which can be used to determine the characteristic relaxation time τ of the system. The power of μ SR is that it allows measurements of a very large range of high frequencies, from roughly $10^5 - 10^{10}$ Hz, measuring a large range of spin-glass dynamics.

The typical signature of a spin-glass is that the system does not have a single exponential correlation time, but a distribution which is stretched out and corresponds to the sum of the dynamics of individual clusters. We can determine some kind of characteristic frequency by assuming there is a Lorentzian distribution of random internal fields, which fluctuate as a markovian process $e^{-\nu t}$, where ν is the characteristic frequency. Furthermore, plotting the characteristic correlation time on a log scale as a function of temperature should give a straight line for a spin-glass. An example of μ SR measurements on the canonical spin-glasses can be found in Uemura et al. [91], and a general introduction to μ SR techniques and applications can be found in Blundell [12].

Another technique which is capable of measuring rapid dynamics in spin-glasses is neutron scattering, which is capable of measuring frequencies in the range of $10^8 - 10^{13}$ Hz. The higher frequencies can be accessed by measuring the quasi-elastic scattering using a standard spectrometer. In order to measure the lower frequencies, special instruments which have very high energy resolution, such as spin echo spectrometers, are required. Looking at the inelastic scattering in units of time, one once again finds a response which is stretched out compared with a single exponential and a similar dependence of the correlation time.

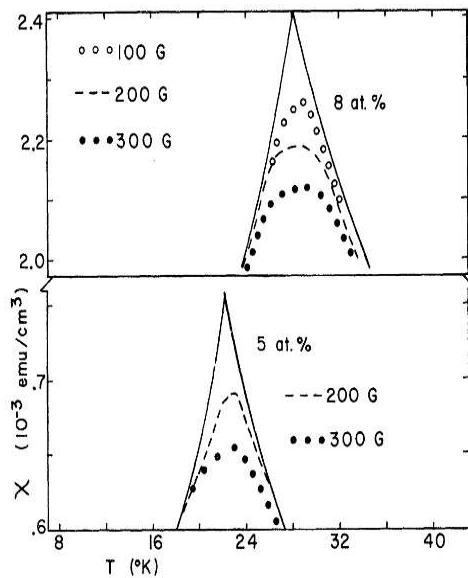
In elastic neutron scattering, a typical feature of a spin-glass is short-ranged correlations, which begin to appear at $T > T_f$. The correlations give rise to a broad Lorentzian distribution of diffuse scattering centred around the position where a Bragg peak would appear in the case of long-range ordering of the spins. The intensity of this scattering increases monotonically as

the temperature is lowered and the spin-spin correlation length grows.

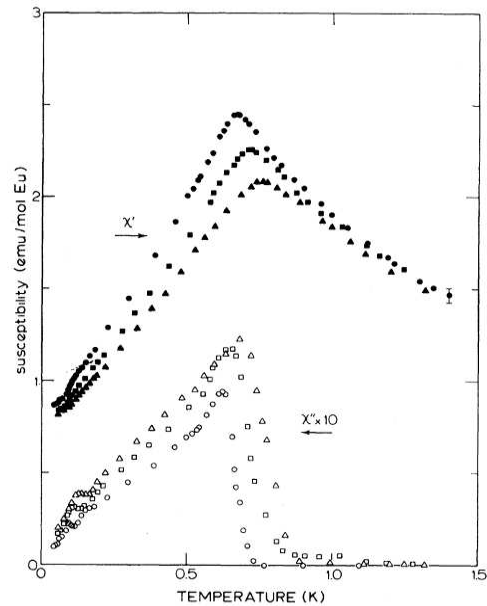
1.2.2.2 Signatures in AC Susceptibility

One of the most available and powerful techniques for the study of spin-glasses is AC susceptibility. This technique measures the magnetic susceptibility by applying an extremely small oscillating field (typically < 0.1 Oe) and measuring the response from the system. The spin-glass freezing is seen as a divergent frequency dependent peak in χ' . Fig. 1.4 shows the typical temperature dependence for spin-glasses, with Fig. 1.4a showing measurements on the canonical spin-glass $\text{Au}_{1-x}\text{Fe}_x$ (taken from Cannella and Mydosh [17]) and Fig. 1.4b the insulating spin-glass $\text{Eu}_{0.2}\text{Sr}_{0.8}\text{S}$ (taken from Hüser et al. [40]). The scans on $\text{Au}_{1-x}\text{Fe}_x$ show the reason why spin-glasses had eluded researchers for such a long time; the application of even a small DC field smears out and rounds the sharp transition seen in zero field (continuous line). The large field effect is rather surprising, as a $T_f \approx 25$ K implies that $k_B T_f \gg \mu_{eff} H$, even for fields above 1000 gauss, which are able to completely smear out the spin-glass transition.

Close examination of the T_f peak at different frequencies reveals that as the frequency is decreased the peak shifts to lower temperatures, as can be seen in Fig. 1.4b. A large range of frequencies can be measured using AC susceptibility, typically in the range of several mHz up to



(a) AC susceptibility of $\text{Au}_{1-x}\text{Fe}_x$ with $x = 5$ and 8 at. %, showing the zero field curves and broadening due to an applied field. Taken from Cannella and Mydosh [17].



(b) Temperature dependence of the real χ' (solid symbols) and imaginary χ'' (hollow symbols) for $\text{Eu}_{0.2}\text{Sr}_{0.8}\text{S}$. circles – 10.9 Hz, squares – 261 Hz, triangles – 1969 Hz. Taken from Hüser et al. [40].

Figure 1.4: Typical AC susceptibility of spin-glasses.

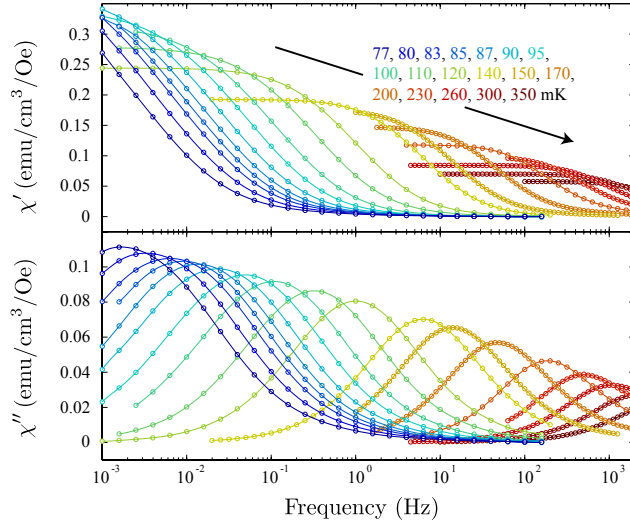


Figure 1.5: AC susceptibility spectroscopy on $\text{LiHo}_{0.045}\text{Y}_{0.955}\text{F}_4$. The top panel shows χ' and the bottom panel χ'' in the temperature range of 77 to 350 mK. Taken from Quilliam et al. [74].

several kHz. Measuring at higher frequencies is generally not possible as the copper coils of the inductive susceptometers do not remain transparent to the high frequency electromagnetic field produced and effectively shield the sample. Lower frequencies are out of bounds simply because the measurement times become too long to be practical.

The relationship between the real part χ' , the dispersion, and the imaginary part χ'' , the absorption, of the complex susceptibility in spin-glasses has a unique form (although only easily observed in insulating materials). Both χ' and χ'' show frequency dependent peaks, with an inflection point in χ'' at the peak position in χ' . This is distinct from the case of a ferromagnet, which can also show a large imaginary component due to domain wall motion, where χ'' suddenly becomes non-zero at the position of the peak in χ' .

Measuring the susceptibility as a function of frequency at fixed temperatures, turns the technique into a spectroscopic probe. An example of this is shown in Fig. 1.5 which shows measurements on $\text{LiHo}_{0.045}\text{Y}_{0.955}\text{F}_4$ in the frequency range of $10^{-3} - 10^3$ Hz. The typical feature of a spin-glass is a broad temperature-dependent peak in $\chi''(\omega)$ and a suppression in $\chi'(\omega)$ as the frequency is increased. It can be shown that when looking at the susceptibility as a function of frequency, $\chi'(\omega)$ and $\chi''(\omega)$ are related by the following equation [66]:

$$\chi''(\omega) \approx -\frac{\pi}{2} \frac{\partial \chi'(\omega)}{\partial \ln(\omega)}, \quad (1.4)$$

Finally, it has been shown both experimentally by Lévy [50], as shown in Fig. 1.6, and theoretically by Ogielski [70], that the non-linear AC susceptibility χ_{nl} diverges at T_g .

Perhaps the simplest way to define the non-linear susceptibility is as follows:

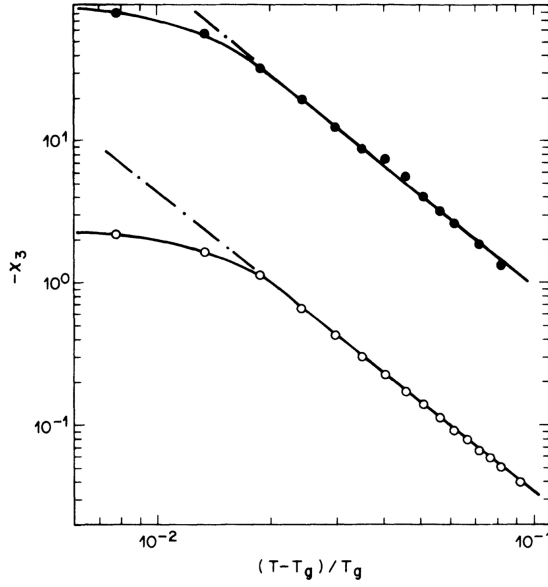


Figure 1.6: Temperature dependence of $-\chi_3$ above T_g in $\text{Ag}_{1-x}\text{Mn}_x$ measured at 10^{-2} Hz in static fields of 0 (open circles) and 90 G (solid circles) as a function of reduced temperature t . The line corresponds to a slope of $\gamma = 2.3$. Taken from Lévy [50].

$$\chi_{nl} = 1 - \frac{M}{\chi_0 H}, \quad (1.5)$$

where $\chi_0 = M/H$ in the limit $H \rightarrow 0$. Taking this approach allows for the magnetisation to be expressed in odd powers of the field, yielding:

$$\chi_{nl} = a_3 (\chi_0 H)^2 - a_5 (\chi_0 H)^4 + \dots \quad (1.6)$$

If the AC susceptibility is measured in an external DC field H_0 , the total field will be given by $H_0 + h \cos \omega t$, where h is the AC field oscillating at a frequency of ω . The signal observed in the susceptometer is therefore proportional to:

$$\chi_1 + 2H_0^2 \chi_3 + \dots, \quad (1.7)$$

giving $\chi_{nl} \propto \chi_3$. If H_0 is sufficiently large, then χ_3 will dominate the total expression for the susceptibility and therefore give the behaviour of the non-linear susceptibility. The difficulty in accurately measuring a spin-glass using this method is that χ_3 is much smaller than χ_1 , so the DC field must be reasonably large. This serves to round off the spin-glass transition, making the interpretation of the data difficult.

An alternative, and arguably more sensitive method, is to measure the 3rd harmonic of the AC susceptibility directly in an applied AC field and zero DC field, as the non-linear susceptibility

is proportional to χ_3 (while including some higher order terms which are several orders of magnitude smaller than χ_3 [50]). The advantage of this technique is that there is no need to apply a large DC field to reveal the non-linear susceptibility, so the system will be less perturbed. It is important to note that the AC fields applied are still appreciable, so care must be taken in interpreting results.

1.2.2.3 Dynamics

One way in which it is possible to begin to *classify* spin-glasses is by characterising the frequency dependence of T_f . If one plots $1/T_f$ as a function of $\log_{10}(f)$ one typically finds a straight line over a large range of frequencies, which can be used to determine the spin-glass frequency sensitivity (which is sometimes referred to as the Mydosh parameter) [55, 66, 85]:

$$\mathcal{K} = \frac{\Delta T_f}{T_f \Delta \log_{10}(f)}, \quad (1.8)$$

In this equation ΔT_f is the amount by which T_f has changed by changing the frequency of the measurement by $\Delta \log_{10}(f)$. Table 1.1 shows typical values of \mathcal{K} for the canonical spin-glasses, insulating spin-glasses and, as a comparison, superparamagnets.

Spin-glass type	\mathcal{K}
Canonical (metallic)	0.002 – 0.01
Insulating	0.01 – 0.1
Superparamagnets	> 0.1

Table 1.1: Spin-glass frequency sensitivity \mathcal{K} for different classes of spin-glass

It should be noted that \mathcal{K} is not very well defined and can only be used as a rough guideline. The issue with this way of characterising spin-glasses stems from the difficulty in deciding *which* T_f to use. As T_f depends on frequency, and in a large number of cases does not appear to converge (to either a high frequency or a low frequency limit), there is no physical reason to prefer a particular AC field frequency for the choice of T_f . This ambiguity in the value of T_f used to determine \mathcal{K} can change the value by a factor of 2 for the results presented in this document.

In order to better understand the dynamics of a spin-glass, the frequency dependence of T_f can be represented in terms of a dynamical scaling relation. An intuitive starting point for this is the thermal activation (Arrhenius law) of a superparamagnet:

$$\tau = \tau_0 \exp\left(\frac{E_a}{k_B T}\right), \quad (1.9)$$

where $\tau = 1/\omega$, τ_0 is a microscopic limiting relaxation time and E_a is the energy barrier separating the spin up and spin down states of the magnetic clusters. In a superparamagnet, below a blocking temperature T_B , which is on the order of $E_a/25k_B$, the fluctuations come on to time scales which are detectable by AC susceptibility. For a spin-glass, applying this exponential dependence of frequency on freezing temperature results in a relatively good fit for most data, although the fit parameters take completely unphysical values. For a canonical spin-glass one finds $E_A \approx 4500$ K and $\tau_0 \approx 10^{-200}$ s [66], which are clearly not related to the actual processes in the system. Even though this approach fails to give insights into the spin-glass state, it can successfully be used to distinguish between superparamagnetism and glassiness.

The second approach borrows concepts from the studies of structural glasses, and attempts to model dynamics using the Vogel-Fulchner law [66]:

$$\omega = \omega_0 \exp\left(-\frac{E_a}{k_B(T_f - T_0)}\right), \quad (1.10)$$

where T_0 is a parameter, which in the case of structural glasses is called the *ideal glass temperature*. The extra parameter allows for better fits and brings E_a and ω_0 to more physical values. The problem with this approach is that there is no clear definition of what exactly T_0 represents and what an acceptable/physical value would be.

The final approach comes from the standard theory for dynamical scaling near a phase transition at T_c [10, 29]. The result from dynamic scaling relates the correlation length ξ to a critical relaxation time $\tau \sim \xi^z$. Combining this with the fact that the correlation length diverges with temperature, one can write the power law divergence:

$$\tau = \tau_0 \left(\frac{T}{T - T_c}\right)^{zv}, \quad (1.11)$$

where zv is the dynamical exponent. This can be written in the language of a spin-glass as [66]:

$$\tau = \tau_0 \left(\frac{T_g - T_f}{T_f}\right)^{-zv}, \quad (1.12)$$

where T_g is the spin-glass transition temperature and T_f is the frequency dependent freezing temperature determined by the peak in χ' . The problem with this approach is that the value of zv varies between around 4 and 12 for various spin-glass systems, which is much larger than $zv \sim 2$ for conventional phase transitions [70, 71].

A final issue with all three approaches is that different experimental systems and setups can lead to different determinations of T_f at the same frequency. There are several related features occurring at slightly different temperatures, observable in AC susceptibility, which are

commonly used to determine T_f . The historical approach, and possibly still the most common, is taking the peak in χ' of a temperature scan at fixed frequency as T_f . A second approach still uses temperature scans, but uses the peak in χ'' as this can be shaper and more easy to extract, particularly in systems showing some kind of re-entrant behaviour. A final approach uses the peak in χ'' observed in frequency scans at fixed temperature to determine T_f . Although all three methods show similar dynamic scaling, it is very likely that if comparisons were made between all features there would be a slight difference between the parameters generated in fitting the scaling.

1.2.3 Experimentalist's Picture of a Spin-Glass

The experimental techniques presented indicate that there are two key features in a spin-glass. The first is the presence of correlations, both temporal and spatial at $T > T_f$, which we can think of as small clusters. The second feature is that there is no single correlation time, but a very broad distribution of correlation times. These two features are rather naturally linked; there exist many different clusters of different sizes and the relaxation rate of a single cluster depends on its size – larger clusters relax more slowly.

To build up the spin-glass, we start with building blocks consisting of dynamic magnetic clusters which form from the paramagnetic collection of spins. There is a competition between the thermal fluctuations in the system $k_B T$ and the short range interactions between the spins $J(r_{ij})$, where r_{ij} is the separation between two spins. As the temperature is lowered, clusters, which have both a correlation length ξ_{SG} and some net moment, begin to form when $J(r_{ij}) > k_B T$. As the temperature decreases further, ξ_{SG} increases, and the clusters grow in size. Accompanying this spatial correlation is the temporal relaxation rate of the clusters $1/\tau$. μ SR and inelastic neutron scattering measurements show that there is clearly not a single relaxation time and effectively different clusters must have different relaxation times. Furthermore all the forms of spectroscopy presented show that the relaxation times of clusters grow as T is reduced to T_g .

As $T \rightarrow T_f$ the random anisotropy in the system causes correlated spin clusters to freeze out in random directions. At T_f there is some sort of percolation and an infinite spin cluster consisting of rigidly frozen spins is generated. This infinite cluster is composed of many smaller clusters that are frozen in random orientations. The spins in this infinite cluster are correlated, but their local direction is determined by the smaller clusters which froze out at higher temperatures. Thus the small clusters, which exist inside the infinite cluster, still maintain their identity but as they are fixed by the infinite cluster, they are unable to respond to an external field.

In general for a percolation transition, the order parameter is given by the fraction of spins inside the percolated state. This implies that some small clusters of spins will not be included inside the infinite cluster and will therefore remain superparamagnetic. Therefore, even below T_f , there will be a broad distribution of relaxation rates coming from the superparamagnetic

clusters.

Finally we note that in this model of a spin-glass, the freezing temperature is a function of the frequency of measurement. As the infinite spin cluster is itself a dynamic entity with both weak and strong links and many excitations, it will also show frequency dependent behaviour. At high frequencies, the slow dynamics of the infinite cluster will not be seen, so T_f will appear to be higher than if a lower frequency probe were to be used. As the frequency of measurement decreases, the observed freezing temperature should begin to converge to the zero frequency glass transition temperature T_g . The challenge experimentally is how to determine and measure the properties of the equilibrium phase transition given the very large time scales involved.

1.2.4 Related Phenomena

Re-entrant Spin-Glass: In a large number of spin-glasses, when the concentration of magnetic ions is increased, the correlations between spins will increase and a ferromagnetic ground state will emerge. In many cases, the spin-glass state is capable of crossing over into the ferromagnetic phase. As the temperature is decreased, the sample will first go from paramagnetic into a long-range ordered ferromagnetic state. At lower temperatures the more disordered spin-glass state appears from the ordered ferromagnetic state. This state is referred to as a re-entrant spin-glass, as the system re-enters the frozen state out of another ordered state, rather than a paramagnetic one.

Superparamagnetism: Imagine a collection of *clusters* of spins. The clusters consists of strongly correlated spins, but there are no interactions between individual clusters. At high temperature, the clusters will fluctuate in a paramagnetic way, and as they have a large effective spin (a super spin) are known as superparamagnets. As the temperature is lowered, anisotropy effects become important and the system can be modelled in terms of an energy-barrier model. In the simplest case, there are two easy orientations of magnetisation separated by an energy barrier related to the anisotropy. The relaxation between the two magnetisation states of a cluster follows thermal activation (Arrhenius law). For this reason, spin-glasses and superparamagnets share many similar experimental signatures, even though their microscopic configuration is different.

1.3 Outline of this Work

The balance of this thesis is divided into five chapters:

- **Chapter 2** discusses AC susceptibility as an experimental technique and its implementation at LQM. An overview of some of the strengths and weaknesses of this technique is explored in several compounds which I have measured as part of collaborations with other researchers and groups.

1.3 Outline of this Work

- **Chapter 3** discusses the theoretical aspects and design requirements of the SQUID magnetometer capable of running at $T < 100$ mK. The initial design is presented, leading naturally into a discussion on challenges, and resulting solutions, in developing the magnetometer. The chapter concludes with a detailed explanation of the final prototype and some preliminary results.
- **Chapter 4** introduces $\text{LiHo}_x\text{Er}_{1-x}\text{F}_4$, which is the compound I spent the majority of my time investigating. I start by introducing the experimental phase diagram and a general overview of the powder AC susceptibility data taken on 11 samples. I then expand on this, investigating three regions of the phase diagram, the re-entrant spin-glass phase, the ferromagnetic spin-glass phase and the antiferromagnetic spin-glass phase. I describe the detailed study on each phase in order to understand the ground state properties using a combination of AC susceptibility, elastic neutron scattering and mean-field calculations.
- **Chapters 5 and 6** conclude the work and discuss future research.

2 AC Susceptibility

The magnetic susceptibility χ is a measure of a system's ability to respond to an external DC field H . It is defined as:

$$\chi = \frac{M}{H}, \quad (2.1)$$

where M is the magnetisation of the sample. There are effectively two fundamentally different ways in which the susceptibility can be measured. The first consists of measuring the magnetisation of the sample in a relatively large external field, typically on the order of 100 Oe, and then determine the susceptibility. The second method involves using a much smaller oscillating field H_{AC} , which can be much less than 1 Oe, and measuring the AC susceptibility, which is defined as follows:

$$\chi_{AC} = \frac{dM}{dH}. \quad (2.2)$$

Thus the susceptibility is the low field gradient of the magnetisation vs. field curve which would typically be measured with a magnetometer. There are several benefits of AC susceptibility when compared to the DC technique. The first of these, which has already been mentioned, it is possible to measure the AC susceptibility in much smaller excitation fields. AC susceptibility also allows for spectroscopic measurements; it is possible to measure as a function of frequency in the range of $\sim 1\text{mHz} - 10\text{kHz}$ depending on the characteristics of the system used. The large range of dynamic responses can be used to probe, for example, the behaviour of the relaxation in glassy materials or the domain wall dynamics in ferromagnets.

In this chapter the principle of AC susceptibility measurements, along with the implementation at the Laboratory for Quantum Magnetism are explored in detail. Several systems which I measured using this set-up are then briefly discussed as a means of demonstrating some of the strengths and weaknesses of this technique as a probe of quantum magnets at low temperatures.

2.1 Principle of AC susceptibility

There are several different techniques one can use to measure the AC susceptibility, such as inductive, torque, SQUID, etc. I will focus only on the inductive technique here, as it is perhaps the simplest and also the type I have used. The *susceptometer* in this technique has a general form shown in Fig. 2.1.

In this configuration, a uniform external AC magnetic field is generated around the sample by supplying a current in the *primary* inductive coil. A voltage is produced via induction in the *compensated secondary coil* and is a measure of the response of the sample in the oscillating field. The term compensated implies the secondary coil is mounted in such a way that the voltage induced from the primary oscillating field in the secondary coil is (ideally) zero, and only the response from the sample is measured. Naturally, perfect compensation is not possible, so there is always a background signal due to the imbalance in the compensation of the secondary coils.

In general, when measuring AC susceptibility, the sample is in an external field B_{ext} consisting of a DC field B_0 (typically from a superconducting magnet) and an AC field $B_{AC} = B_a \cos(\omega t)$ generated using a small inductor coil. The total external field can be written as:

$$B_{ext} = B_0 + B_a \cos(\omega t). \quad (2.3)$$

To understand exactly what is being measured in AC susceptibility, the space average magnetic field *inside* the sample can be defined:

$$\bar{B}(t) = \frac{\phi_m(t)}{S}, \quad (2.4)$$

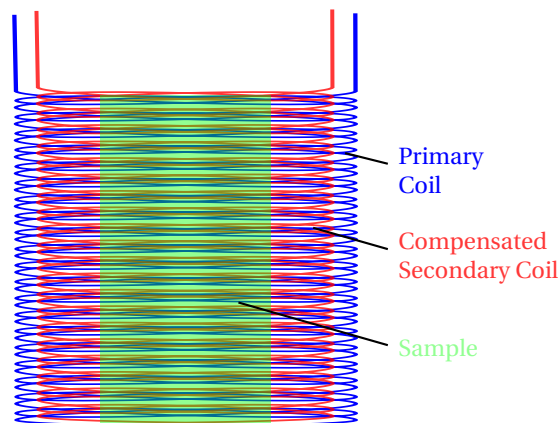


Figure 2.1: Typical configuration of an inductive susceptometer. The AC field is produced by the *primary coil* and the response from the sample is measured by a *compensated secondary coil*.

2.1 Principle of AC susceptibility

where S is the cross-sectional area of the sample. The magnetisation of the sample therefore follows naturally:

$$M(t) = \bar{B}(t) - B_{ext}(t) = \frac{\phi_m(t)}{S} - B_{ext}(t). \quad (2.5)$$

The complex AC susceptibility components are now introduced and are defined as [59]:

$$\chi' = \frac{1}{\pi B_a} \int_0^{2\pi} M(\omega t) \cos(\omega t) d(\omega t), \quad (2.6)$$

$$\chi'' = \frac{1}{\pi B_a} \int_0^{2\pi} M(\omega t) \sin(\omega t) d(\omega t). \quad (2.7)$$

The physical interpretation of the complex susceptibility is as follows. The real part of the susceptibility, χ' , is related to the time average of the magnetic energy stored in the volume occupied by the sample [34]:

$$W_m = \chi' \frac{B_a^2}{2\mu_0} \quad (2.8)$$

The imaginary part of the susceptibility, χ'' , is related to the energy which is converted into heat during one cycle of the AC field [22]:

$$W_q = -2\pi\chi'' \frac{B_a^2}{2\mu_0} \quad (2.9)$$

The real part of the susceptibility is related to how easy it is for magnetic flux to penetrate into the sample. In the case of a paramagnet at low temperatures, the spins will be easily polarised by a magnetic field and thus the magnetic flux will be able to pass through without much difficulty, and χ' is positive and large. On the other hand, if we consider a superconductor, the Meissner effect shields the volume of the sample from the magnetic field and χ' is negative and large. In both these examples χ'' would be zero (assuming the paramagnet is an insulator). Examples of classes of materials with considerable χ'' are metals, where eddy currents absorb energy, ferromagnets, where domain wall motion occurs and “glassy” materials where clusters of spins relax at appropriate time-scales.

Turning towards the measurement of susceptibility, the voltage produced in the secondary coil is proportional to $\chi' + i\chi''$ and can be written as [96]:

$$v_{rms} = [1/\alpha V_s f H_{rms} (\chi' + i\chi'')], \quad (2.10)$$

where v_{rms} is the measure *rms* voltage, α is the system calibration coefficient, which determines the conversion of flux to voltage inside the pick-up coil, V_s is the sample volume, f is the frequency of the AC field and H_{rms} is the *rms* AC field. This shows a very important limitation of an inductive AC susceptometer – the amplitude of the signal is proportional to the frequency, making low frequencies very difficult to measure.

2.2 Implementation

The implementation an ultra low temperature AC susceptibility measurement system requires two points to be addressed: 1) The design of a susceptometer and how the signal is measured. 2) How the susceptometer and sample are attached on the dilution fridge.

2.2.1 Measuring the Susceptibility

In order to measure the complex susceptibility, we need to run a current through the primary coils and very accurately measure a voltage and phase shift relative to H_{AC} in the secondary coils. An illustration of how this is done is shown in Fig. 2.2. The current which generates the field in the primary coils is produced by a Keithley 6221 AC/DC current source. A TTL signal passes the frequency and phase information to a Signal Recovery 7265 lock-in amplifier. The voltage induced in the secondary coils passes through 20 kHz low pass filters before being measured by a lock-in amplifier. The lock-in amplification technique is indispensable as it allows for a voltage at a specific frequency to be recovered from noise which can be several

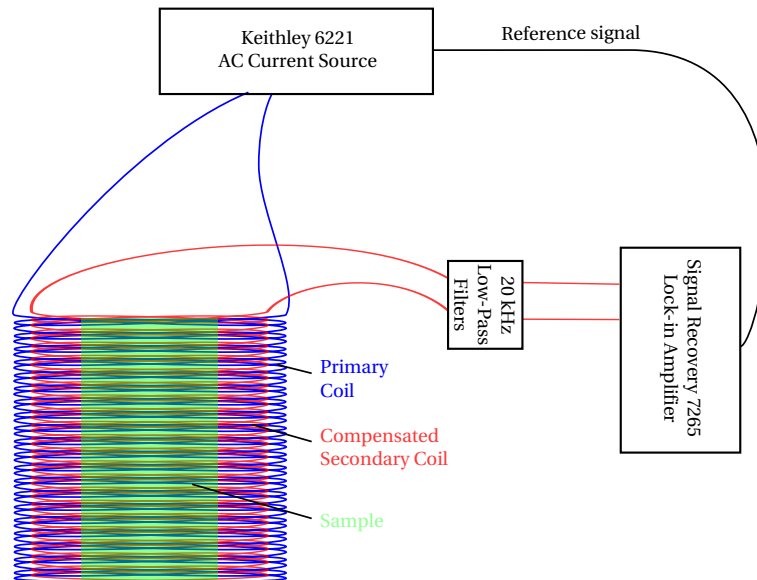


Figure 2.2: Schematic drawing of the AC susceptibility set-up. The primary coils are driven by a Keithley 6221 AC current source and the response of the sample measured in a Signal Recovery 7265 lock-in amplifier.

2.2 Implementation

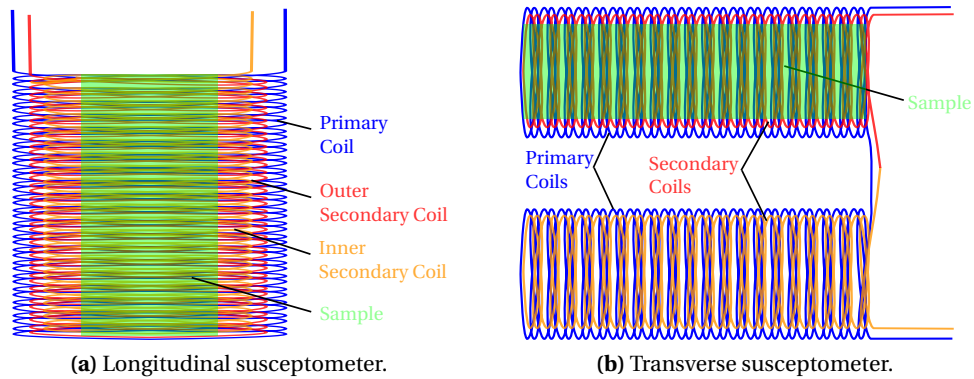


Figure 2.3: Diagrams of the longitudinal (a) and transverse (b) susceptometers used.

orders of magnitude larger than the signal of interest.

Two different types of susceptometers are used with this electronics setup. The first is a commercially available *longitudinal susceptometer* made by CMR-direct, where the susceptibility is measured along the same direction as a DC field. The configuration of the coils in this system is shown in Fig. 2.3a. The second susceptometer is a home made *transverse susceptometer*, which is shown schematically in Fig. 2.3b. This susceptometer is built such that the susceptibility is measured perpendicular to an applied DC field.

The longitudinal susceptometer consists of three concentric coils, each 10 mm long, wound one on top of the other. The outermost coil is the primary coil, which consists of ~ 4000 turns of $25\ \mu\text{m}$ copper wire. The innermost (~ 5000 turns of $25\ \mu\text{m}$ copper wire) and middle (~ 3000 turns of $25\ \mu\text{m}$ copper wire) coils (the secondary coils) are wrapped with opposite polarity, so the voltage from a given flux will be positive in one of the coils and negative in the other and their amplitudes are matched to be as close as possible. The net result is that if there is no sample present the resulting signal from the field produced by the primary coil is very small. When a sample is placed inside the susceptometer, it fills a larger fraction of the inner coil than the outer coil and the signal measured is proportional to the ratio of the filling factors times the susceptibility of the sample. The current used to drive the coils is typically $10\ \mu\text{A}$, which corresponds to a field of $\sim 40\ \text{mOe}$.

The transverse susceptometer is slightly more complex, consisting of two primary and two secondary coils. The primary coils, which are connected in series and wound with the same polarity, are each $20\ \mu\text{m}$ long and contain 1275 turns of $200\ \mu\text{m}$ copper wire. The secondary coils, which sit centred inside the primary coils, connected in series with opposite polarity, are 10 mm long and contain 1096 turns of $50\ \mu\text{m}$ copper wire. In order to properly balance the coils, one of the primary coils has an additional 9 turns around the centre, which were carefully added in order to cancel out the voltage induced by the driving field. The current used to drive the coils is adjusted to get the same AC field as with the longitudinal coils.

2.2.2 Mounting in the Dilution Fridge

As dilution fridges take a considerable amount of time to be prepared and cooled down to low temperatures, and some measurements consist of just a single scan, a decision was made to mount up to three samples simultaneously. This is achieved by placing three susceptometers, two longitudinal and the transversal one, in Delrin plastic holders suspended from a carbon fibre tube, which is attached to the bottom half of a weak-link connection to the mixing chamber as is shown in Fig. 2.4. These materials were chosen due to their mechanical strength and the fact that they are not susceptible to eddy current heating in a ramping magnetic field. The Delrin plastic also has a relatively small magnetic susceptibility, so should not produce a significant background during measurements. A spacer is attached beneath the pick-up coils to ensure that there are no touches with the IVC can. The spacer consists of a Delrin ring with fibre glass spikes pointing outwards and is attached to the main rod using $\sim 50 \mu\text{m}$ multifilament Kevlar threads, which ensure a very good thermal decoupling between 4K IVC can and the samples at $\sim 50 \text{ mK}$. The temperature is controlled on the mixing chamber and measured both on the mixing chamber and on the weak link block, which is in direct thermal contact with the sample.

The samples are small enough to fit inside the 2 mm bore of the susceptometers. The weak-link thermometer and the samples are thermalised using $4 \times 200 \mu\text{m}$ diameter copper wires (for each sample), which are wrapped around the thermometer, and then coated in a thin

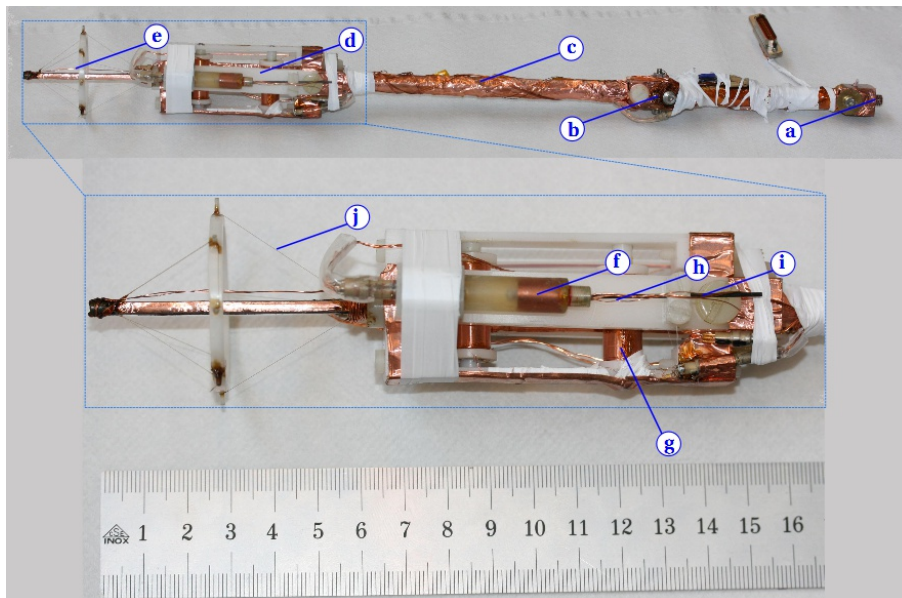


Figure 2.4: Photo of the AC susceptibility setup. (a) Connection to mixing chamber. (b) Bottom of weak-link, where thermometer is mounted. (c) Carbon fibre tube with a strip of copper foil to thermalise. (d) Delrin holder for three susceptometers. (e) Spacer. (f) Longitudinal coil. (g) Transverse coil. (h) Copper wires to thermalise sample. (i) Carbon fibre rod for mechanical attachment of sample. (j) $\sim 50 \mu\text{m}$ Kevlar thread.

2.3 Disordered TaS₂ – A Superconducting Dichalcogenide

layer of GE varnish. A short segment of the wire is also mechanically pressed under a copper washer onto the surface of the weak link block to ensure the best possible thermal contact. The other end of the wires are attached to the samples by encapsulating both the sample and the wires in Stycast W19, ensuring a good thermal contact between the two. A small carbon fibre rod is also inserted into the Stycast which can be used to clamp the sample down onto the coil holders, avoiding the sample moving during cooling and applying DC fields.

2.3 Disordered TaS₂ – A Superconducting Dichalcogenide

In this section I discuss AC susceptibility measurements on disordered TaS₂ (*d*-TaS₂) which turns out to be a granular superconductor. I detail some of the key strengths of AC susceptibility which make it a suitable tool to understand the physics of this sample and study (particularly identify) superconductors in general.

The 2D transition metal dichalcogenides are interesting as they show strong competition between various charge density wave (CDW), Mott insulating, and superconducting states [43]. Pure 1T-TaS₂ exhibits a unique sequence of such CDW and Mott phases, primarily due to the strong electron-phonon and coulomb interactions [94]. It has been shown by Sipos et al. [86] that applying pressure suppresses the Mott transition and promotes a superconducting phase, which appears above 2.5 GPa. It is known that adding disorder to 1T-TaS₂ suppresses the metal-insulator transition [26, 65, 98], and by adding tiny amounts (< 0.1%) of copper, we were able to bring about a superconducting state at low temperatures [95].

As the dichalcogenides form thin *flakes* (<100 μm thick), measuring the superconducting transition using a magnetisation measurement becomes rather tricky. The apparent magnetisation due to the Meissner effect is proportional to the volume, and the very small volume of sample will give a small magnetisation. Measuring the resistance of the sample can give an indication of superconductivity, although unless $R \rightarrow 0$ this does not give immediate proof of bulk superconductivity as there are many processes which are capable of generating a drop in resistivity. AC susceptibility is a probe perfectly suited to measuring such a superconductor, as it works with very small fields (typically < 1 Oe), removing the risk of the external field being larger than the critical field, and a Meissner expulsion is a very strong signal. As with magnetisation measurements, the small sample thickness provides a particular challenge for AC susceptibility.

In order to make the signal large enough to be measurable, five 1.6 mm² flakes were stacked 1.5 mm apart, fixed into shelves cut into a carbon fibre rod using GE varnish. The sample was thermalised using four 200 μm diameter copper wires which were also glued down with GE varnish. Finally Teflon tape was wrapped around the carbon fibre rod to ensure neither the sample of the copper wires could become unglued while cooling down. Fig. 2.5 shows a photo of the prepared sample stick, indicating the different elements. This configuration gives a much larger expelled field volume due to the Meissner effect, greatly increasing the signal relative to simply stacking the pieces directly on top of each other, as can be seen in Fig. 2.6.

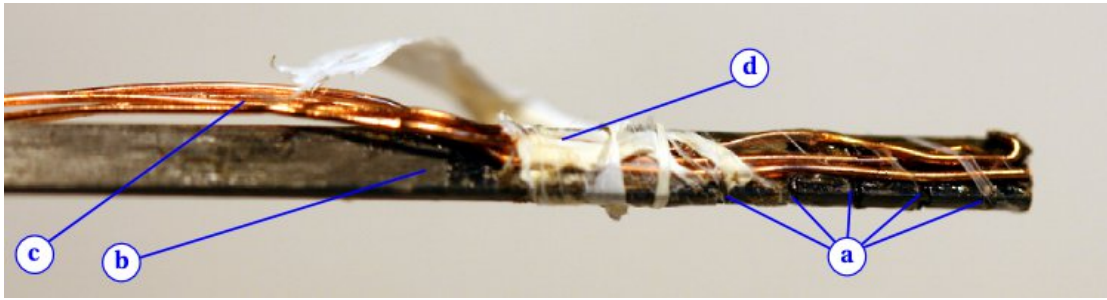


Figure 2.5: Photo of the d -TaS₂ sample stick. (a) the five 1.6 mm² plates glued into (b) the carbon fibre rod, (c) copper wires to thermalise the sample and (d) Teflon tape (shown unwrapped) to hold everything in place.

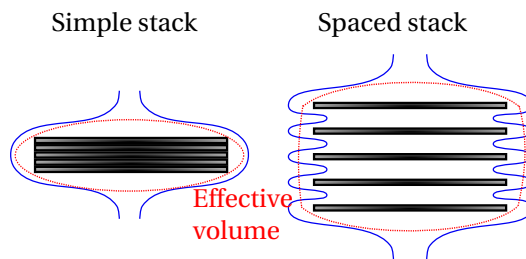


Figure 2.6: Schematic showing probable magnetic field lines for different stackings of TaS₂. Stacking the wafers while leaving a gap between them produces a larger effective superconducting volume.

The in-plane electrical resistivity of pristine TaS₂ and d -TaS₂ were both measured and are compared in Fig. 2.7 (a). At high temperatures the two compounds show identical behaviour, indicating a minimally perturbed sample, while at lower temperatures the large jump at the metal-insulator transition, T_{MI} , and the associated hysteresis in pristine TaS₂ is completely suppressed in d -TaS₂. At temperatures below ~ 15 K, the resistivity begins to decrease again and below 2.1 K suddenly drops (Fig. 2.7 (b)) suggesting the onset of a superconducting state. The large residual resistivity at 350 mK indicates that superconductivity is not bulk and only exists in spatially separated regions, which do not percolate through the material.

The AC susceptibility was measured along the c -axis with a field of 0.29 Oe oscillating at a frequency of 546 Hz. Fig. 2.7 (c) shows the classical hallmarks of a granular superconducting transition at the same temperature as the resistivity drops. χ' becomes negative due to the Meissner effect while χ'' displays a broad peak. We speculate that the dissipative signal seen here is due to junctions between small superconducting clusters which are likely nucleated by the CDW structure. Both χ' and χ'' begin to change at 2.9 K with the peak in χ'' coinciding with the drop in resistivity at 2.1 K. This behaviour is interpreted as superconductivity occurring below 2.9 K on the individual superconducting regions with phase coherence between them achieved at 2.1 K, but not leading to percolation. The field-dependent susceptibility shown in Fig. 2.7 (d) supports this reasoning. At a relatively low field of 0.1 T, most of the Meissner effect has already been suppressed, but a small portion, corresponding to the 2.1–2.9 K signal,

2.3 Disordered TaS₂ – A Superconducting Dichalcogenide

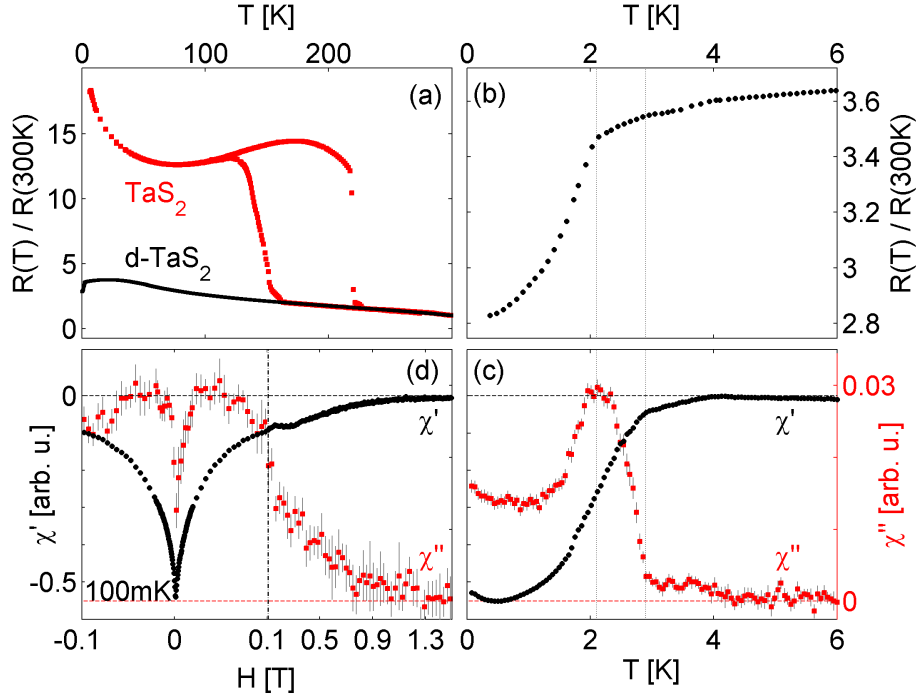


Figure 2.7: In-plane electrical resistivity and c -axis AC susceptibility of d -TaS₂. (a) The resistivity of both compounds is indistinguishable above the MI transition at 180-220 K, which is present in pure TaS₂ but completely absent in d -TaS₂. (b) At low temperatures the resistivity suddenly drops at 2.1 K, suggesting superconductivity. (c) Zero-field temperature-dependent complex AC susceptibility confirms the superconducting state. (d) Field dependence of χ at 100 mK. Taken from Xu et al. [95].

persists right up to fields of 1 T.

Due to the non-standard set-up employed here to measure the very weak Meissner expulsion it is not possible to determine the reduced superconducting volume fraction $\nu = (V_{sc}/V)$ directly. Using a simple 2D model based on an effective medium approximation, which neglects the small conductivity along the c -axis, allows ν to be approximated. This model links the critical superconducting volume fraction required for percolation ν_c to the relative change in resistance by:

$$\frac{\nu}{\nu_c} = \left(\frac{\Delta R}{R} \right), \quad (2.11)$$

where $\nu_c = 0.676$. From the resistivity data measured, we find $\nu = 0.15$ which is well below the percolation limit and is consistent with the weak Meissner expulsion observed.

2.4 Low Dimensional & Frustrated Quantum Magnets

Two classes of magnetic materials which are of particular interest in condensed matter physics are low dimensional magnets and frustrated magnets. These are quite typically treated together as both can in principle give rise to exotic quantum ground-states. Moreover, it is not simply that the physics in both kinds of systems is similar, it is quite typical that the most interesting frustrated magnets also have low dimensionalities. In this section, several magnets which have been studied with the help of AC susceptibility are briefly discussed to illustrate its power in such systems.

2.4.1 Spangolite

Spangolite, $\text{Cu}_6\text{Al}(\text{SO}_4)(\text{OH})_{12}\text{Cl}\cdot 3\text{H}_2\text{O}$, is a hydroxyhydrated copper aluminium sulfate mineral which has well separated depleted triangular layers of copper ions, and is an approximation of the maple leaf lattice [30, 38]. This system is the only currently known experimental realisation of the spin $s = 1/2$ on a maple leaf lattice, which is expected to have a six sub-lattice ordered ground state [83]. Details of the crystallographic structure relating to the position of the magnetic Cu^{2+} ions and their interactions can be found in [28].

A very brief summary of configuration of magnetic ions in spangolite is that there are two unique Cu^{2+} sites, each giving rise to two sets of pure trimers. There are two more types of trimers which are due to the linking of these pure trimers. There are thus four types of trimers containing either three, two, one or zero copper ions from each site. There are thus five different possible interactions, and the overall exchange will be weakly anti-ferromagnetic.

Magnetic susceptibility in the range of 0.1 – 300 K has been used to understand the magnetic structure of this compound. The susceptibility was measured using a Quantum Design MPMS SQUID magnetometer in the temperature range of 2 – 300 K and the AC susceptibility setup described previously for temperatures between 0.1 and 3 K. The AC measurements were taken using an excitation frequency of 990 Hz and an AC field amplitude of 42 mOe.

The general features of the susceptibility are shown in Fig. 2.8 (a), which contains a broad maximum at $T \sim 40$ K and an upturn at low temperatures. This behaviour is typical of a spin-dimer system containing a low temperature paramagnetic tail. The low temperature susceptibility is scaled to overlap with the SQUID data between 2 and 3 K by first subtracting the background from the AC coils and then scaling by a constant. This low temperature data is fitted with a Curie-Weiss law:

$$\chi = \frac{C}{(T - \theta_{CW})}, \quad (2.12)$$

where C is the Curie constant and θ_{CW} is the Curie-Weiss temperature. The fit, shown in Fig. 2.8 (b), yields a Curie-Weiss temperature of $\theta_{CW} = -1.434 \pm 0.003$ K and Curie constant

2.4 Low Dimensional & Frustrated Quantum Magnets

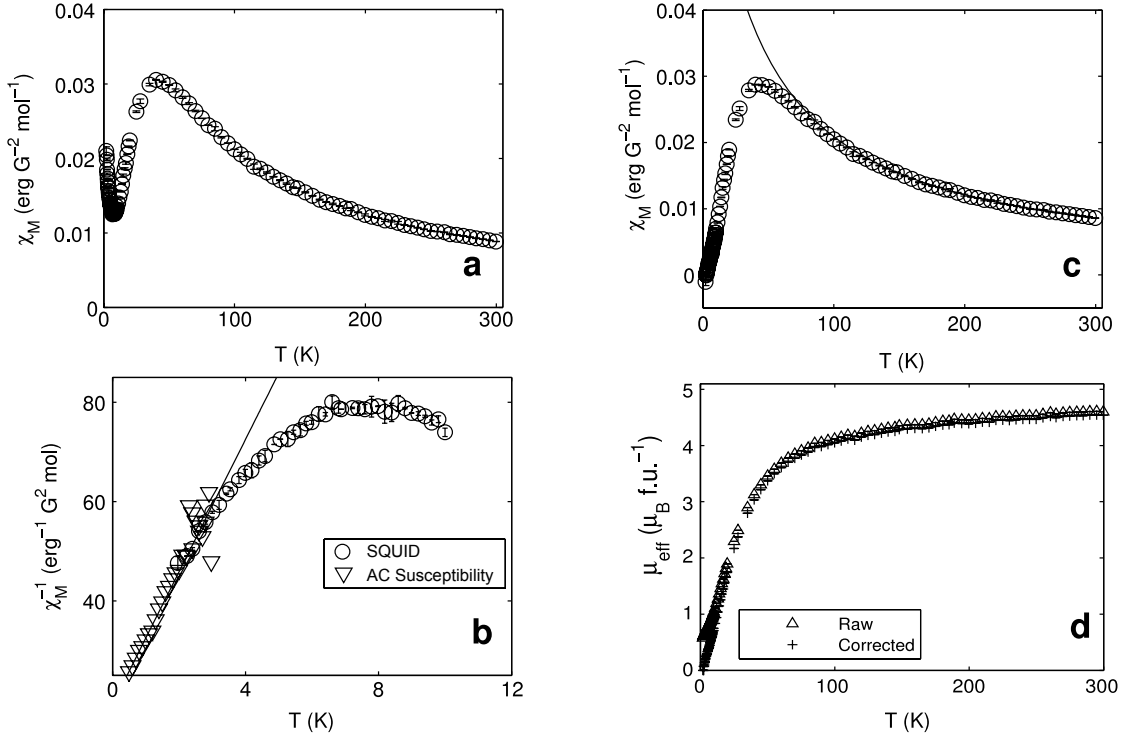


Figure 2.8: Magnetic susceptibility of spangolite. (a) The susceptibility shows a broad peak at $T \sim 40$ K and a minimum at 8 K, below which an upturn attributed to a Curie tail is observed. (b) The inverse low temperature AC susceptibility is scaled and offset to overlap with the Curie tail in the SQUID data. The line shows a Curie-Weiss law fitted to both data sets. (c) The susceptibility with the low temperature paramagnetic tail subtracted. The line is a Curie Weiss law fitted to the data above 100 K. The effective moment found from the susceptibility without the Curie tail subtracted (Raw) and with this correction (Corrected). Adapted from Fennell et al. [28].

of $C = 0.0749 \pm 0.0001 \text{ erg G}^{-2} \text{ mol}^{-1} \text{ K}$. From this Curie constant the effective moment is determined as:

$$\mu_{\text{eff}} = \frac{(3k_B C / N_A)^{1/2}}{\mu_B}, \quad (2.13)$$

where μ_B is the Bohr magneton and N_A is the Avogadro constant. This gives an effective moment of $\mu_{\text{eff}} = 0.772 \pm 0.001 \mu_B / \text{f.u.}$ (with f.u. being a formula unit). Comparing this to the spin-only magnetic moment:

$$\mu = g(s(s+1))^{1/2}, \quad (2.14)$$

with $s = 1/2$ and $g = 2$ implies that $\sim 7.5\%$ of the spins make up this paramagnetic tail (as there are 6 spins per formula unit).

The paramagnetic tail is assumed to be parasitic in nature, coming from magnetic impurities in the spangolite samples. This seemingly large level of impurities is quite plausible as the samples are produced naturally by geological processes, so high levels of impurities are practically

guaranteed. It is possible to subtract this extracted tail from the data to reveal the intrinsic susceptibility of spangolite, as is done in Fig. 2.8 (c). At high temperatures this susceptibility follows Curie-Weiss behaviour, with $\theta_{CW} = -38 \pm 1$ K and $C = 0.0749 \pm 0.0001$ erg G⁻² mol⁻¹ K, which gives an effective moment of $\mu_{\text{eff}} = 4.79 \pm 0.01$ μ_B /f.u.. This is significantly less than what one would expect for the six spins per unit cell, which give 10.39 μ_B /f.u.. Fig. 2.8 (d) shows the effective moment obtained from the susceptibility using the expression $\mu_{\text{eff}} = \sqrt{8\chi T}$, both with and without the correction of removing the low temperature paramagnetic signal. The moment tends to a value of 4.55 μ_B /f.u., but does not saturate in the temperature range studied.

The form of susceptibility here is typical of a system with a singlet ground state. The simplest possible realisation of such a system would be the formation of non-interacting dimers, and in this case the high temperature moment would correspond to six $s = 1/2$. The susceptibility indicates that the moment is severely reduced, so cannot be explained by such a simple model. One possible explanation for this reduced moment is that the copper ions could be substituted with a diamagnetic one. This is, however, somewhat unlikely, as roughly half of the ions would have to be replaced, leading to very drastic dilution. With such large dilution it is doubtful that singlets would be able to form at low temperatures. Another possible explanation is that the trimers interact to form strongly bound clusters. This would require a significantly smaller moment of $\mu_{\text{eff}} = 3.46$ μ_B /f.u. compared to the $\mu_{\text{eff}} = 4.79 \pm 0.01$ μ_B /f.u. observed. In order to fully understand the magnetic properties of spangolite, larger high purity samples would be needed so that additional experiments can be carried out.

2.4.2 $\text{KTi}(\text{SO}_4)_2 \cdot \text{H}_2\text{O}$

$\text{KTi}(\text{SO}_4)_2 \cdot \text{H}_2\text{O}$ is a realisation of the $s = 1/2$ frustrated chain antiferromagnet. Unlike all other realisations of this model which have been discovered and experimentally probed, the spin originates from Ti^{3+} ions. Without going in to details, the advantage of these ions over the typical Cu^{2+} ions is that the exchange couplings are normally smaller. Experimentally, one key result of this weak exchange is that the fields required to fully saturate the magnetic moment are easily achievable with standard superconducting magnets. Initial SQUID magnetometry and specific heat showed behaviour consistent with short-range ordering along the magnetic chains [68]. The data does not fit the simple Bonner-Fisher curve [13], indicating it is not a simple $s = 1/2$ Heisenberg chain. The simplest additional term in the Hamiltonian is a frustrated next nearest neighbour, which if true would make the magnet a $J_1 - J_2$ frustrated chain. In this model J_1 corresponds to the nearest neighbour exchange and J_2 to the next nearest neighbour exchange.

The frustrated chain model shows a range of exotic quantum ground states, which depend on the signs of J_2 and J_1 along with the value of the frustration parameter $\alpha = J_2/J_1$. Exact diagonalisation of this Hamiltonian with fits to the data finds two possible solutions shown in Fig 2.9, which is taken from [47]. The fits have rather different values of $\alpha = 0.29$, $g = 1.80$ and

2.4 Low Dimensional & Frustrated Quantum Magnets

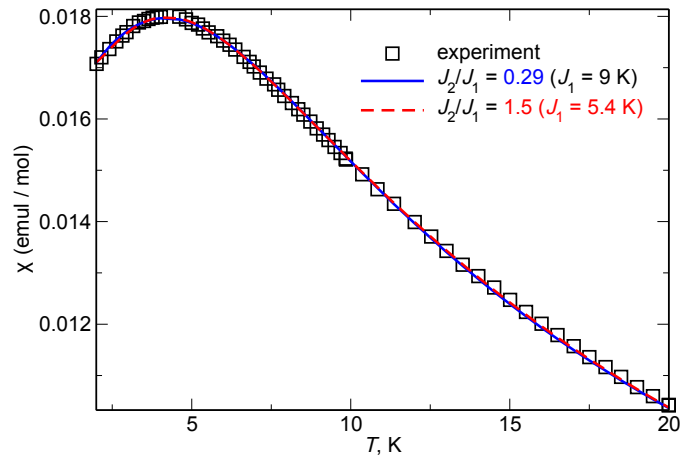


Figure 2.9: High temperature magnetic susceptibility of $\text{KTi}(\text{SO}_4)_2 \cdot \text{H}_2\text{O}$ indicating the two possible fits found by direct diagonalisation of the $J_1 - J_2$ Hamiltonian. Taken from [47].

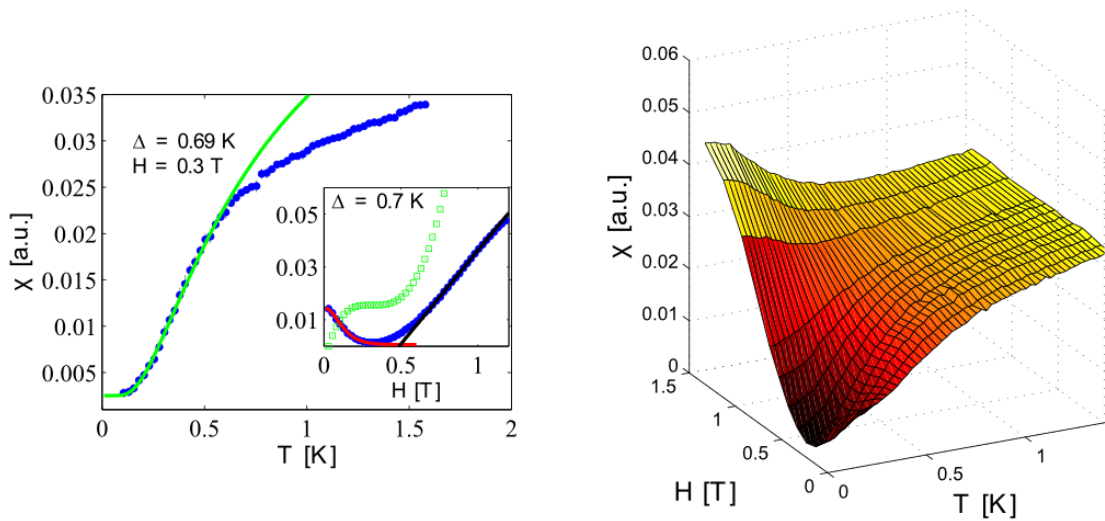


Figure 2.10: Low temperature field and temperature-dependent real susceptibility χ' of $\text{KTi}(\text{SO}_4)_2 \cdot \text{H}_2\text{O}$. [Left] temperature dependence in 0.3 T with an exponential fit of the gap opening. [inset] Field dependent susceptibility (solid points) at 80 mK with a Brillouin fit to defect spin contribution. The open symbols show the magnetisation obtained by integrating the susceptibility. [right] Temperature scans taken at 0.1, 0.2, 0.3, 0.4, 0.5, 0.6, 0.7, 0.8, 1.1, 1.3 and 1.5 T.

$J_1 = 9.5$ K in one case and $\alpha' = 1.5$, $g' = 1.74$ and $J_1' = 5.4$ K in the other case, but both imply that the system is in the dimer spin liquid phase. The gap to the lowest triplet depends on both J_1 and α and is predicted to be $\Delta' \approx 0.12J_1' \approx 0.65$ K for the second set of fit parameters, and vanishingly small for the first set of fit parameters [92].

AC susceptibility measurements taken down to 80 mK were used to determine the value of a possible gap. The left panel of Fig. 2.10 shows the temperature-dependent susceptibility at 0.3 T and in the inset the field-dependent susceptibility taken at 80 mK. Below around 0.65 K, the susceptibility suddenly drops and falls off exponentially as $T \rightarrow 0$. This is consistent with a gap opening, and fitting the data (green line on the graph), yields a value of $\Delta = 0.69$ K. When the field is applied at base temperature, the susceptibility initially drops, which can be due to a paramagnetic $s = 1/2$ defect contribution and can be fit using a Brillouin function. As the field is increased further, the susceptibility increases at around 0.5 T which is consistent with the gap closing.

Mapping out the field-temperature susceptibility, as is done on the right panel of Fig. 2.10, shows that interestingly the temperature of the downturn in χ' remains constant in field until it eventually disappears. This behaviour could be an indication of a spin-Peierls transition [37].

The measurements on both spangolite and $\text{KTi}(\text{SO}_4)_2 \cdot \text{H}_2\text{O}$ demonstrate that temperature and field dependent susceptibility at very low temperatures can be used to determine and remove paramagnetic impurity contributions.

2.4.3 Ba_2YMoO_6

Ba_2YMoO_6 is an $s = 1/2$ cubic B-site ordered double perovskite, which does not show conventional order down to the lowest temperatures. A comprehensive study has been performed by de Vries et al. [24] consisting of DC and AC susceptibility, specific heat and μSR in the temperature range of 2 K to 300 K. They find that the inverse susceptibility has a kink at around 50 K which corresponds to a frequency dependent peak in the imaginary component of the complex susceptibility. Interestingly this peak increases with amplitude at higher frequencies, unlike in a conventional spin-glass state. The specific heat shows a peak which coincides with the kink in inverse susceptibility and has been attributed to a gap opening, which is consistent with the system entering into a valence bond glass (VBG) [90]. The μSR data shows that the spins gradually slow down as the temperature is lowered to 2 K, but does not appear to follow a muon relaxation consistent with that of a spin-glass [91, 93].

Further studies have been carried out in order to better determine whether this VBG is the true ground state. AC susceptibility measurements at temperatures down to 50 mK indicate some kind of freezing of the spins at a temperature around 600 mK, which shows up as a frequency dependent peak in χ' , as shown in Fig. 2.11. The low temperature Curie tail is fitted and finds an effective moment of 8 % of that at high temperature, implying that the spin-glass consists

2.4 Low Dimensional & Frustrated Quantum Magnets

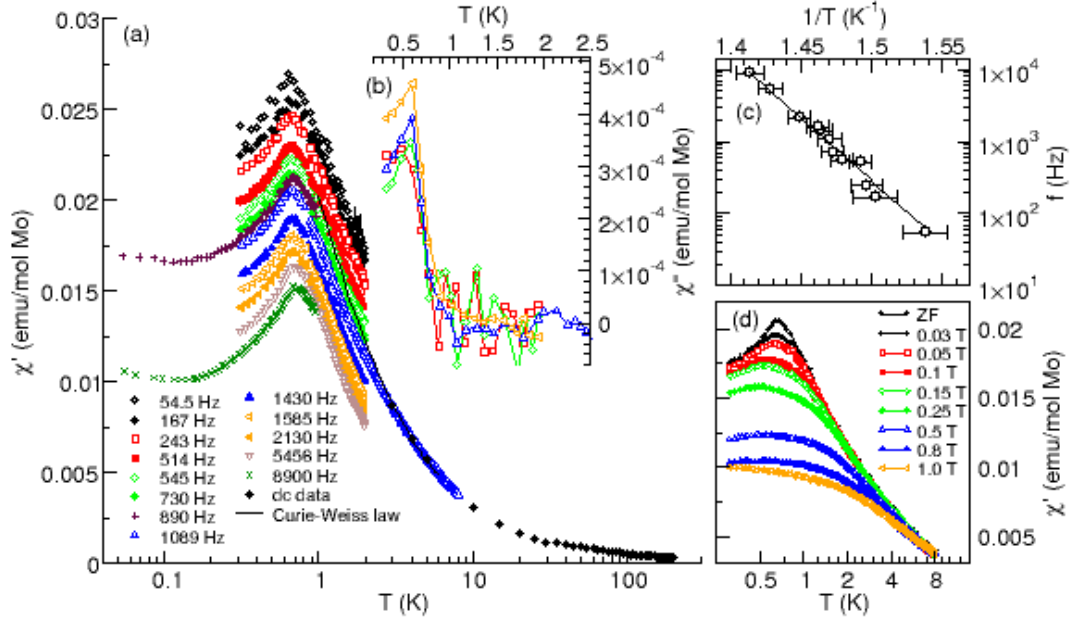


Figure 2.11: Temperature, frequency and field-dependent AC susceptibility of Ba_2YMoO_6 . (a) χ' and (b) χ'' as a function of temperature for frequencies in the range of 54 to 8900 Hz with χ' scaled on to high temperature SQUID data. (c) Arrhenius fit to the frequency dependence of the peak in χ' . (d) Field dependence of χ' , showing an immediate rounding and smearing of the peak, typical in spin-glasses. [Taken from de Vries et al. [25]]

of 8 % of spins which do not take part in the valence bond glass. Measuring in a DC field also shows behaviour which is typical of a low temperature spin-glass, with a DC field very quickly smearing out the peak.

The idea that the spin-glass consists of only a small fraction of the spins and the rest are locked up in the valence bond glass state is confirmed by μSR in this temperature range [25]. The data shows behaviour which can not be fit using a Lorentzian distribution of exponential relaxation times as one would expect for a spin-glass. The μSR data does however indicate that there is a very strong slowing down of the spins and that below around 200 mK the dynamics no longer change, as one would expect for a spin-glass well below T_f .

2.4.4 LiErF_4

The LiReF_4 family of magnets are a set of model dipolar coupled magnets which typically order at low temperatures with the type of order determined by the local crystal field anisotropy. The magnetic moment of LiErF_4 has XY anisotropy and as a result orders antiferromagnetically below $T_N = 0.370$ K [8, 9]. AC susceptibility complements specific heat and neutron scattering measurements as part of a complete investigation of the low temperature behaviour of this compound. The conclusions of this work are that the classical phase transition shows non-mean-field critical scaling, consistent with the 2D $XY/h4$ universality class. A quantum phase

transition observed $H = 4$ kOe when the field is applied along the crystallographic c -axis, and exhibits three-dimensional classical behaviour in accordance with the one dimension lower classical transition.

The AC susceptibility measurements have been used to map out the field-temperature phase diagram in high detail, as can be seen in the left panel of Fig. 2.12. The phase diagram has been mapped out by measuring the temperature dependence of χ' at fixed field. Each scan has then been normalised to the maximum susceptibility, giving a very clear phase boundary. The value of the peak in χ' gives T_N and is represented on the graph as a white cross.

The second thing which AC susceptibility was used for was to investigate any quantum critical scaling. This was done by taking temperature scans at H_C and values immediately above and below it. At H_C , quantum critical scaling is observed with an exponent of 0.70 ± 0.03 which crosses over to regular Curie-Weiss behaviour above 250 mK.

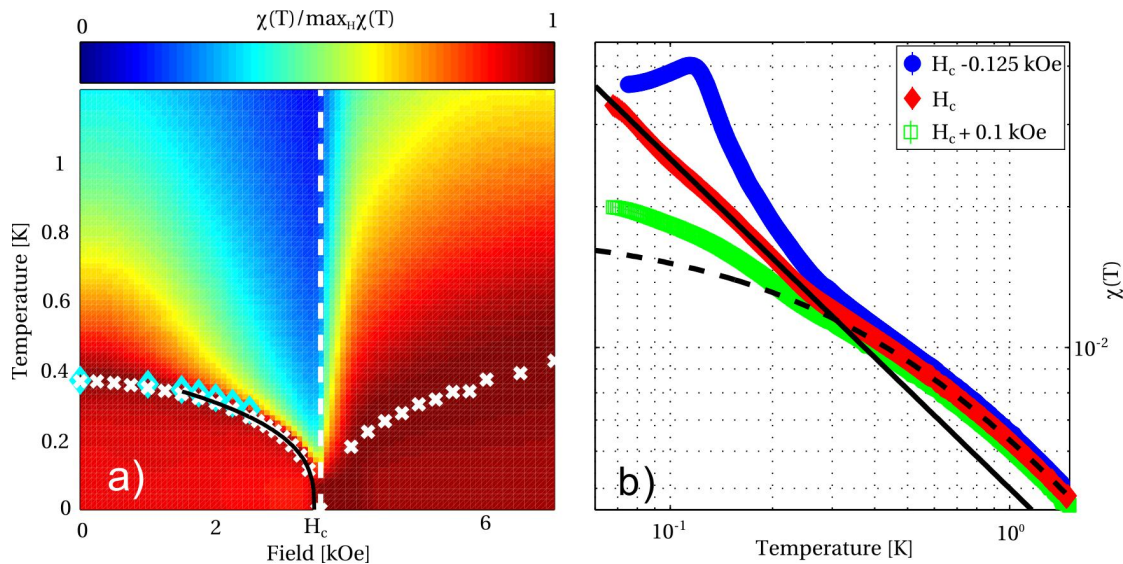


Figure 2.12: Normalised AC susceptibility measurements giving the phase diagram [left] and critical scaling [right] of AC susceptibility in LiErF_4 . At H_C the susceptibility shows quantum critical scaling with exponent 0.70 ± 0.03 (Solid line) up to a crossover to regular Curie-Weiss behaviour at around 250 mK.

2.5 Overview and Future Perspectives

These experimental results show that AC susceptibility is a powerful probe for very different physical phenomena on a large range of samples. It is of course not without its weaknesses, which can be either intrinsic to the method or due to the implementation on this system. Here I will briefly summarise its strengths and weaknesses, and offer some ideas for how to improve the existing setup.

2.5.1 Strengths

The main strength of AC susceptibility as an experimental technique at dilution temperatures is that it is relatively quick and easy to implement. The equipment required to measure AC susceptibility is not particularly expensive and once it has been set-up, mounting a sample and measuring it is straightforward. Indeed, once an appropriate setup has been made, the primary challenge in measuring the majority of samples is getting the dilution fridge operating in a satisfactory manner.

AC susceptibility is ideally suited to determining whether there are changes in the properties of a system at low temperatures. In the case of superconductors, it is arguably the ultimate technique for determining a superconducting transition, as the Meissner effect is unambiguous and the measurements are for all practical purposes zero-field. One can also gain information on the type of superconductivity (i.e. I or II, bulk or granular, etc.) by carefully studying χ'' .

When studying purely magnetic systems, AC susceptibility can be used as a quick check to see whether something interesting happens, before moving on to more expensive and time consuming experiments. With AC susceptibility it is possible to determine whether the system orders or not, and gives an idea on the type of order present. It can also be used to infer information about the ground-state of short-range ordered systems where, for example, spins form singlet states at low temperatures. The ability to change the frequency across a large range allows for the relatively slow dynamics of spin-glasses, superparamagnets, and domain wall dynamics in ferromagnets, to be measured.

2.5.2 Weaknesses

The biggest issue with AC susceptibility is that in magnetic systems the susceptibility is often not what one would really like to know; the magnetisation is much more interesting. Knowing the magnetisation allows us to say something meaningful about the state being measured, whereas with only AC susceptibility this is very difficult in the best cases. Related to this is the fact that it is very difficult to determine the absolute units of susceptibility from an AC susceptometer. Whereas in a SQUID, simply measuring a sample with a known mass gives the units of magnetisation, in AC susceptibility this is not enough. To determine absolute units, one must know the sample size and geometry very precisely, and even with this information the transformation from a measured voltage to units of susceptibility is far from trivial.

The other weaknesses are related to the implementation of setup. Currently, the sensitivity is not perfect. The bulk of the measurements have been done on $\text{LiHo}_x\text{Er}_{1-x}\text{F}_4$, which has a huge effective moment of over $10 \mu_B$ per ion. For these measurements the sensitivity is more than ample, but when measuring systems containing $s = 1/2$ it becomes difficult to extract the signal from the noise. The problem really shows when measuring systems like doped $s = 1/2$ spin ladders, where for example, only 5 % of the magnetic ions are unpaired, while all others form singlets. In these compounds it is often impossible to measure a meaningful signal, even

where the signal is maximal.

Related to the problem with sensitivity is the difficulty of measuring at low frequencies. As this implementation of AC susceptibility uses an inductive coil to measure the response from the sample, the voltage measured is proportional to the frequency. It becomes very challenging to measure signals at frequencies < 10 Hz, as the sensitivity just isn't good enough.

2.5.3 Future Perspectives

The sensitivity of the AC susceptibility system is something that can in principle be improved. By designing and constructing better coils, it should be possible to increase the sensitivity by at least an order of magnitude. In order to do this there are two steps which would greatly improve sensitivity. The first is to change the primary coil into one made from superconducting wire. The superconducting wire will only generate heating due to inductive power dissipation, thus larger currents (and therefore larger fields) can be supplied when measuring samples with very small signals. The second step one could take is to change the secondary coils from being wound on top of each other to next to each other. This will mean that when the compensation is done, the second coil will not be measuring any response from the sample, giving a larger signal. Moreover, it is possible to reduce to background relative to the current coils by adding or removing extra turns on one of the secondary coils until the imbalance is minimised.

There is a question as to whether there is any merit to taking these steps, as an even more sensitive, and frequency independent measurement system can be made using a SQUID sensor. Furthermore using a SQUID it is possible to measure not only AC susceptibility, but also magnetisation. The following chapter deals with the design, constructing and testing of such a DC magnetometer. With a SQUID magnetometer already existing, building a detection system which can be plugged into the SQUID and is optimised for doing AC measurements would arguably be less work than making a more sensitive inductive susceptometer.

3 SQUID Magnetometry

A Superconducting **QU**antum **I**nterference **D**evice (SQUID) combines two quantum phenomena, Josephson Tunnelling and flux quantisation to produce one of the most sensitive measuring devices possible. A very good book which details both theoretical and practical aspects of all kinds of SQUID devices is the SQUID Handbook by Clarke and Braginski [21].

The SQUID magnetometer discussed in this chapter has been designed to measure samples down to temperatures below 100 mK. One very important design criteria for the system is flexibility: the dilution fridge is used for many different types of measurements and the magnetometer does not change this. Therefore, the magnetometer has been designed in such a way that it can be easily swapped out for alternative measurement probes in a reproducible manner.

The chapter starts by introducing the theory behind SQUID devices and principle of operation of a magnetometer using a SQUID sensor. The design considerations for the magnetometer system are then given, followed by the technical challenges encountered during the prototyping phase, along with their solutions. The results of the first prototype are presented before moving on to the description of the final prototype of the magnetometer. The final sections deal with results of the system and an outlook on what it will be routinely used for and how it can be further developed and improved.

3.1 Theory

A SQUID exploits some of the unique quantum properties found in closed superconducting circuits. In order to fully understand the operation principle of a SQUID we first demonstrate that the flux in a superconducting ring must be quantised, as was first predicted by London in 1950 [51]. The superconducting state can be characterised by the complex order parameter:

$$\psi = \left| \psi(\vec{r}) e^{i\varphi(\vec{r})} \right|, \quad (3.1)$$

where $|\psi(\vec{r})|^2$ is the density of Cooper pairs and $\varphi(\vec{r}) = \vec{p} \cdot \vec{r} / \hbar$ is the phase. In the presence of a magnetic field $\vec{B} = \vec{\nabla} \times \vec{A}$, the generalized momentum is $\vec{p} = 2m\vec{v} - 2e\vec{A}$, as the Cooper pairs have charge $2e$ and mass $2m$.

Considering the current flowing inside a superconducting ring, the current density can be determined by inserting Eq. 3.1 into the standard quantum mechanical expression:

$$\vec{j} = -i\hbar \frac{e}{m} (\psi^* \vec{\nabla} \psi - \psi \vec{\nabla} \psi^*) - \frac{4e^2}{m} \psi^* \psi \vec{A}, \quad (3.2)$$

$$\vec{j} = \left(\frac{2e\hbar}{m} \vec{\nabla} \varphi - \frac{4e^2}{m} \vec{A} \right) |\psi|^2. \quad (3.3)$$

Inside the bulk of the superconductor, the current density $\vec{j} = 0$, so the current can only flow within a surface layer whose thickness is comparable to the London penetration depth. This implies that the integral $\oint \vec{j} \cdot d\vec{l}$ along a closed path deep inside the bulk must be zero, i.e.:

$$\oint \left(\frac{2e\hbar}{m} \vec{\nabla} \varphi - \frac{4e^2}{m} \vec{A} \right) \cdot d\vec{l} = 0. \quad (3.4)$$

By applying Stokes' theorem, $\oint \vec{A} \cdot d\vec{l} = \iint \vec{\nabla} \times \vec{A} \cdot d\vec{S} = \iint \vec{B} \cdot d\vec{S} = \Phi$, the magnetic flux within the ring can be calculated. Furthermore, the total phase accumulated along a closed path is:

$$\oint \vec{\nabla} \varphi \cdot d\vec{l} = 2\pi n. \quad (3.5)$$

Combining Eq. 3.3 with Eq. 3.4 yields the flux quantisation inside the superconducting ring:

$$\Phi = n \frac{h}{2e} = n\Phi_0, \quad (3.6)$$

where $\Phi_0 = h/2e = 2.07 \times 10^{-15}$ Wb is the *flux quantum*. If this ring is placed inside a field, which is a classical variable and can therefore be changed smoothly, a screening current I_s may be required to flow through the ring to ensure the quantisation of flux:

$$\Phi = \Phi_{\text{ext}} + LI_s = n\Phi_0, \quad (3.7)$$

where L is the self inductance of the ring.

In order to go from the superconducting ring to a SQUID device, the superconducting ring is interrupted by either one (RF-SQUID) or two (DC-SQUID) Josephson junctions. A Josephson junction is a very thin insulating layer sandwiched between two superconductors which

3.2 Principle of Operation

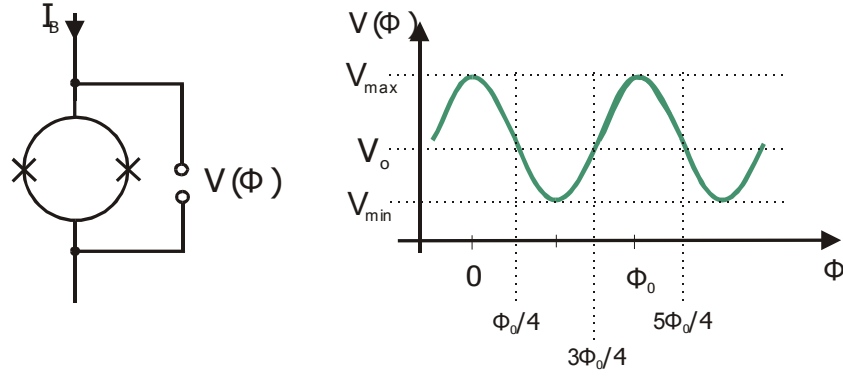


Figure 3.1: [left] Schematic diagram of a DC-SQUID. Applying a biasing current $I_B > I_c$ causes flux passing through the ring to generate a potential difference. [right] The potential difference oscillates ones for every flux quanta which passes through the SQUID. Taken from Mück [63].

suppresses the superconductivity locally but still allows the Cooper pairs to pass via quantum tunnelling. Adding such insulating layers means that the condition $\vec{j} = 0$ everywhere inside the composite ring can now no longer be satisfied as $\vec{j} \neq 0$ inside the Josephson junction. The net result of this on the screening current is:

$$I_s = I_c \sin\left(\frac{2\pi\Phi}{\Phi_0}\right) = I_c \sin\left[2\pi\left(n - \Phi/\Phi_0\right)\right] = I_c \sin\varphi', \quad (3.8)$$

where I_c is the Josephson critical current, the maximum current which can pass through the link without dissipation, and φ' is an extra contribution to the phase term from the insulating segment. When the current in the ring is larger than I_c , dissipation occurs inside the Josephson junction and is equivalent to adding a resistor in parallel to it. In the case of a DC-SQUID, where there are two Josephson junctions it can be shown that when a bias current $I_{bias} > I_c$ is applied across the entire ring and flux passing through the ring generates a potential difference which takes the general form of:

$$V(\Phi) \propto \frac{I_c}{2} \left[\sin\varphi' - \sin\left(\varphi' - 2\pi\frac{\Phi_{ext} + LI_s}{\Phi_0}\right) \right], \quad (3.9)$$

implying that for each flux quanta which passes through the system a full oscillation of voltage is observed. Fig. 3.1 shows a schematic representation of a DC-SQUID and the resulting flux-to-voltage transfer function.

3.2 Principle of Operation

The most important question when designing a magnetometer based on a SQUID is how to get from a device where there are voltage oscillations as flux passes through it into a system which

measures magnetisation. There are two things which must be considered in such a system: first, the signal coming from the sample needs to be detected by the SQUID and secondly the change in voltage across the SQUID needs to be measured appropriately.

One simple way to measure the amount of flux passing through the SQUID would be to count the number of oscillations in the voltage, i.e. the number of flux quanta which pass through the SQUID. Taking such an approach, while fairly straightforward, only uses a small fraction of the available sensitivity of the SQUID. A much more sophisticated approach, which allows for a sensitivity of $\sim 10^{-6} \Phi_0$ in a bandwidth of 1 Hz is to measure the flux passing through the SQUID using a *flux-locked loop* (FLL). This makes the SQUID operate in a feedback circuit as a null detector for magnetic flux by applying a small current in a feedback coil placed close to the SQUID. The feedback coil is connected in series with the feedback resistor, which can be set to values between 5 k Ω and 185 k Ω . As magnetic flux through the SQUID changes, the electronics apply a voltage to the feedback coil, generating a current, determined by the feedback resistor. The resulting field generated perfectly cancels out the flux passing through the SQUID. Measuring the voltage applied to the feedback coil therefore gives information about how much flux is passing through the SQUID sensor.

A SQUID is very sensitive to any kind of magnetic field and this implies that special care must be taken when mounting it in a measurement system. Commercial SQUID chips are designed to operate in zero field and as a result if they are in a field which is on the order of one Oersted or larger, they will cease to work. For this reason almost all SQUID systems are placed inside a superconducting enclosure, ensuring that the field always remains sufficiently small.

To get the flux from a sample to the SQUID inside the shielded environment, a superconducting circuit terminating in pick-up coils is required. The circuit is attached to the SQUID sensor with the aid of two superconducting pads which are on the SQUID package and coupled to the SQUID via the *SQUID input coil*. It is important to have a good superconducting contact between the pickup coil wires and these superconducting pads, and for this reason, special care is taken in preparing the surface of the wires. The superconducting wires most typically used are single filament NbTi wires which are embedded in either a copper or a bronze matrix. First, the electrical insulation must be removed from the ends of the wires which are then etched with nitric acid. The acid dissolves the non-superconducting matrix, leaving bare NbTi wires. These are then pressed down on to the superconducting pads using a niobium washer, which breaks the oxide layer which builds up on the NbTi wires, ensuring a good contact.

As SQUIDs are such sensitive devices, the pick-up coils must be built in such a way that it is only the signal from the sample, and not external fields, which couple to the SQUID. The most common way to do this is to use a gradiometer, which in the simplest case consists of two coils, separated by distance d , wound in opposite directions. This 1st order gradiometer will cancel out any stray flux produced by a uniform field and it is only the gradient of a field which will be detected.

A 2nd order gradiometer consists of 2N windings of a coil sitting between 2 coils each with N

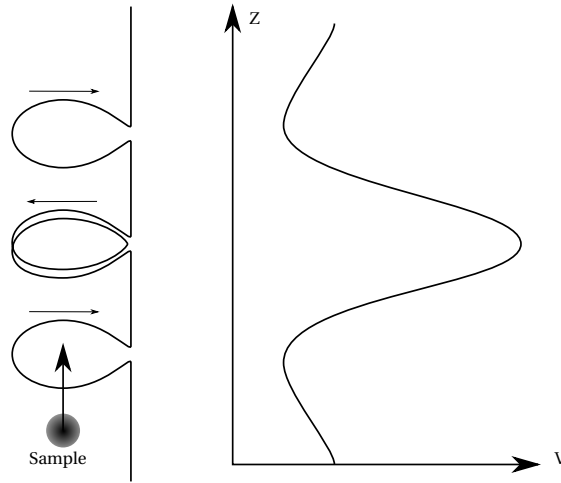


Figure 3.2: Operating principle of a second order gradiometer. As the sample is pulled through the pick-up coils, a voltage is generated by the feedback electronics cancelling out the flux which is passing through the pick-up coils.

windings in the opposite direction. Furthermore, the reciprocity principle [58] relates the flux Φ through a coil produced by a magnetic moment $\vec{\mu}$ at position \vec{r} to the field \vec{B} produced by the same coil at \vec{r} when carrying a current I :

$$\vec{B} \cdot \vec{\mu} = \Phi I. \quad (3.10)$$

It can be shown that a single-loop coil produces a dipole field, a 1st order gradiometer produces a quadrupole field and a 2nd order gradiometer produces an octupole field. These coils therefore produce a field which varies as r^{-3} , r^{-4} , r^{-5} respectively. This implies that of the three types of gradiometer, the 2nd order gradiometer will be least affected by external fields.

The magnetic moment is measured by pulling the sample through the pick-up coils as is shown in Fig. 3.2. The result of the moment moving through the coils is to produce a feedback voltage curve which has the form represented on the right side of the figure. To determine the moment of the sample, first the induced flux from a point-like dipole with moment $\vec{\mu} \parallel \vec{z}$ at a position z along the axis in a loop with radius a placed at $z = z_0$ is calculated:

$$\Phi_{loop}(z) = \frac{\mu_0}{2} f(z - z_0) \mu,$$

$$f(z - z_0) = \frac{a^2}{[a^2 + (z - z_0)^2]^{3/2}} = \frac{1}{a} \left[1 + \frac{z_0^2}{a^2} \left(\frac{z}{z_0} - 1 \right)^2 \right]^{-3/2}.$$

If the outer coils in the gradiometer are now placed at $z = d$ and $z = -d$, the total flux in the pick-up coil becomes:

$$\Phi_{pu}(z) = N \frac{\mu_0 \mu}{2} [f(z-d) - 2f(z) + f(z+d) \mu]. \quad (3.11)$$

The Helmholtz geometry, $a = 2d$, is most typically adopted for 2^{nd} order gradiometer pick-up coils.

The flux at the SQUID sensor can be related to the flux from the pick-up coil via the following expression:

$$\Phi_{SQUID} = \mathcal{M} I_s = f_{tr} \Phi_{pu}, \quad (3.12)$$

where \mathcal{M} is the mutual inductance between the SQUID and the SQUID input coil and f_{tr} is the flux transfer ratio [20], defined by:

$$f_{tr} = \frac{\mathcal{M}}{L_{pu} + L_{leads} + L_{in}}, \quad (3.13)$$

where the inductances are those of L_{pu} the pick-up coil, L_{leads} the leads, and L_{in} the SQUID input coil. In order to determine the moment originating from the sample, the SQUID is calibrated using a standard magnetic reference. In this way there is a direct conversion between a voltage and the moment inside the pick-up coils.

3.3 First Prototype

The challenge of getting a fully functioning SQUID magnetometer at dilution temperatures is in moving the sample through the magnetometer pick-up coils. The only existing system in the literature has a modified mixing chamber of the dilution fridge, which is made of Kapton, and the sample sits *inside* the mixing chamber. The entire dilution fridge is then moved inside the superconducting magnet where the pick-up coils are mounted [62]. Although this solution does prove to create an effective and versatile magnetometer, the modifications required to the dilution fridge and superconducting magnet system are too great to make it viable unless the idea is to use the dilution fridge only for measuring magnetisation. The implementation presented here is designed to make the entire system highly modular, allowing for the dilution fridge to remain capable of measuring any of the other experimental probes at LQM without requiring more than several minutes to change probes.

3.3.1 Design Considerations

The principal design considerations boil down to three points:

- Where and how to attach the SQUID sensor to the fridge.

- How the pick-up coils should be mounted inside the system.
- How to move the sample while maintaining a sufficiently low temperature.

These three points will be tackled separately in the following paragraphs.

The SQUID sensor has two basic requirements to be able to operate; it must be colder than the T_c of the superconductor in the Josephson junction and it must be in a sufficiently small magnetic field. Not only does the SQUID have to be in a small field, but due to its extremely high sensitivity, it must be shielded from all sources of EM noise. For these reasons SQUID systems will typically have the sensor itself enclosed in a niobium shield. Niobium has an $H_c(0)$ of 0.82 T [27], which sets a limit of where relative to the magnet it can be placed to be able to use the system for measurements in fields up to 9T. The stray field coming from the magnet drops below this value at a distance roughly corresponding to the height of the 1K pot. The SQUID can therefore either be placed on the 1K pot itself or on the roof of the inner vacuum chamber (IVC) can, which is the vacuum can inside which all the low temperature (< 1 K) parts of the fridge reside.

The temperature requirements also allow for the SQUID to be placed either on the 1K pot or on the roof of the IVC can, as the superconducting material in the SQUID is niobium ($T_c = 9.2$ K). In practice there are several advantages and disadvantages of each location. Placing the SQUID on the IVC can has the advantage that there is no extra heat load into the dilution fridge, as no wires would reach the low-temperature parts of the fridge. The disadvantage is that the system would only be able to operate when the IVC can is fully submerged in helium, which corresponds to keeping the cryostat over 60% full and thus filling with helium every day while measuring. On the other hand, the 1K pot would bring more challenges in operating the dilution fridge, due to the added heat load to the 1K pot, but would in principle allow for operation with any helium level in the system. Attaching the SQUID to the 1K pot also brings the advantage of increased sensitivity due to the lower temperature of the SQUID as shown in Fig. 3.3. For these reasons the decision was taken to mount the SQUID on the 1K pot.

The pick-up coils have to be mounted at the centre of the superconducting magnet, and need to be done in such a way that they do not vibrate relative to it. The reason behind this is rather simple: if the coils are not perfectly wound then as the field changes flux will pass through them. As the coils vibrate in the non-uniform magnetic field the varying flux passing through the pick-up coils produces noise. In the worst cases the noise can be large enough that the SQUID will be saturated, making measurements impossible.

Apart from this mechanical constraint, the pick-up coils must also remain in a superconducting state, which means staying below roughly 9 K, as they are made from NbTi superconducting wire. The decision was taken to mount the pick-up coils on a carbon fibre rod which is mechanically anchored to the wall of the IVC can using two copper beryllium springs. In order to make sure that the magnet does not move relative to the dilution fridge, three copper beryllium springs were attached to the top plate of the superconducting magnet, which the dilution

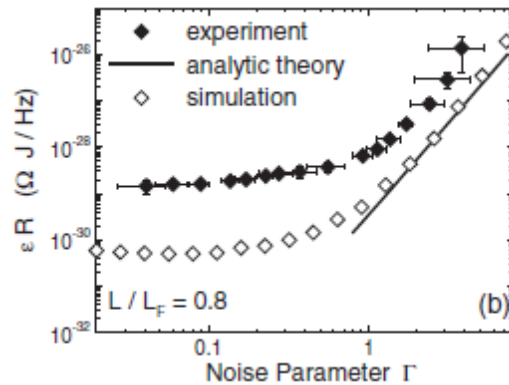


Figure 3.3: Energy sensitivity ϵ of the DC SQUID vs. $\Gamma (\propto T)$, with a smaller ϵ implying higher sensitivity.[taken from 21, p. 63].

fridge rests on when lowered.

The largest challenge in such a system is getting the sample to move while keeping the temperature constant. One possible solution to moving the sample is to move the entire dilution fridge, which is how the other existing dilution temperature magnetometer was built [62]. The problem with this approach is that it does require a heavily modified dilution fridge so that large amounts of (magnetic) materials are not pulled through the pick-up coil system. The idea was to take a much smaller scale approach by using a piezoelectric actuator driven translation stage (which will be referred to as the piezomotor from now on) to move the sample through a distance of at most 20 mm.

The piezomotor chosen is a translation stage from Attocube, which works on a stick-slip principle, as shown in Fig. 3.4. A rod is attached to a piezoelectric stack and the translation stage is clamped on to this rod, with a very finely turned frictional force. The force is such that if the piezoelectric stack is expanded or contracted slowly then the translation stage stays attached to the rod and moves several microns. If on the other hand the piezoelectric stack is accelerated very quickly (typically in a few microseconds), the movement is so fast that the inertia of the translation stage overcomes friction. The translation stage slips on the rod and stays in almost the same position. By applying a saw-tooth voltage profile, this stick-slip motion causes to the translation stage to move across the length of the rod.

The downside of this kind of motion is that with each step, when the translation stage slips on the rod, a small amount of heat is generated. The amount of heat generated is unknown and difficult to calculate, although it has been reported that such stick-slip motion does not significantly increase the temperature of a dilution fridge [5]. For this reason the initial design was to mount the piezomotor directly onto the mixing chamber with the sample thermalised via the piezomotor itself along with a thermal link of copper wires.

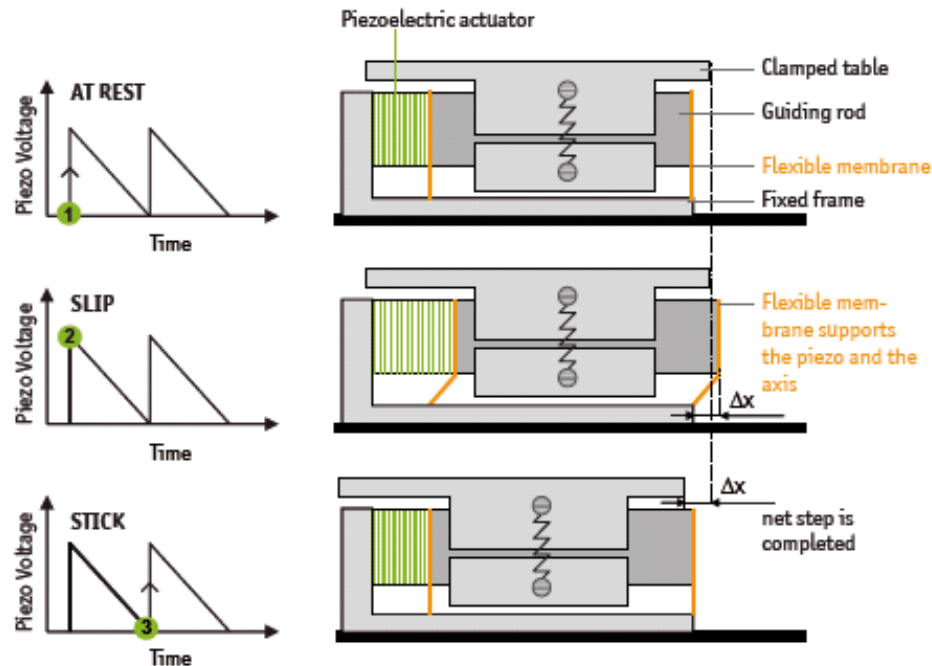


Figure 3.4: Principle of motion of the piezomotor translation stage. A very rapid change in voltage causes the guiding rod to move so fast that it overcomes the inertia of the clamped table, which therefore doesn't move. If a the voltage changes more slowly, the clamped table moves with the guiding rod. By repeating this process many times, the clamped table moves over macroscopic distances. [Taken from 6]

3.3.2 Challenges and Solutions

In implementing the magnetometer measurement system there were many technical challenges which had to be overcome. This section is designed to serve as some kind of a reference guide to anyone interested in designing and building a SQUID system operating at dilution temperatures; hopefully transferring some useful knowledge. For this reason I specify not only problems which were encountered in this implementation, but also problems which are typical but were not observed due to good design and planning.

3.3.2.1 SQUID Environment

One of the most common problems one can experience with a SQUID is the environment in which it is being used. SQUIDS are incredibly sensitive devices and can be very easily rendered inoperable due to excessive RF noise. A particular problem with a SQUID in a very noisy environment is that there is essentially no way of knowing why the SQUID is not working. If the noise is sufficiently large, upon cooling down the SQUID will simply have no response whatsoever. There are several things one can do in order to minimise the possible headaches, which I will list below.

- **Use very well shielded cables.** The cables which connect the SQUID to the feedback electronics are possibly the biggest problem when dealing with RF noise. Depending on the electronics being used, either twisted pair or coaxial cables can be used to carry the signals. Special care should be made when choosing the shield for the cables, as the typical mesh shield is normally not sufficient to get the best signal from a SQUID. The ideal shield to use is a thin walled tube, such as a brass tube for twisted pair wiring, or a semi rigid coaxial cable.
- **Ensure that the SQUID is in a good Faraday cage.** In the case of operation in the dilution fridge this is not an issue, as the fridge is closed using an indium seal. Due to the long times involved in preparing and cooling a dilution fridge, it is preferable to be able to test the SQUID in a simpler environment, such as in a transport Dewar. During such tests, it was found that having even a tiny gap due to a rubber O-ring on a KF joint was enough to completely suppress the SQUID voltage oscillations. For this reason commercial magnetometers actually have a conductive O-ring seal.
- **Avoid introducing antenna effects.** The other source of RF getting into the SQUID are (other) wires which are used in the system. Essentially any wire going into the cryostat can behave as an antenna and very quickly cause the signal to deteriorate. To reduce the effect π -filters (which cut off frequencies above several MHz) should always be present on all wires going into the cryostat. Ideally, if there is no need for high frequencies a filter with an even lower cut-off frequency should be used.
- **Filter RF noise on the pick-up circuit.** In order to minimise the impact of RF noise on the pick-up side of the SQUID system, one can attach a capacitor in parallel to the pick-up/input coils. It has been found that WIMA brand foil capacitors still function normally at liquid helium temperatures and for the typical inductances of SQUID input coils, a value of around 100 nF works well. In the case of this particular SQUID, it was possible to attach the capacitor directly to the SQUID package by soldering¹ it on to the pick-up coils contact pads as shown in Fig. 3.5. The resulting advantage of this configuration is twofold. First, the capacitor and additional wiring is inside the superconducting SQUID shield and thus shielded from RF noise. Second, there is almost no chance of the wires breaking or pulling on and damaging the SQUID as the capacitor is permanently fixed.

There are two possible ways in which one can wire up the SQUID to the feedback electronics, either by using a well shielded twisted pair of wires, or two well shielded coax cables. As coax cables have a low inductance, it is possible to modulate the SQUID FLL using a square-wave. This increases the sensitivity of the measurement by a factor of $\sqrt{2}$ compared to a twisted pair wires which can only use a sine-wave modulation. As the electronics being used are designed for low resistance cables (< several Ohms), two semi-rigid copper coax cables were run from the top of the fridge down to the 1K pot. The construction of the cable is an inner

¹One should take special care if soldering something electrically attached to a SQUID as they are easily burned by discharges. It is recommended to solder with a *disconnected* soldering iron.

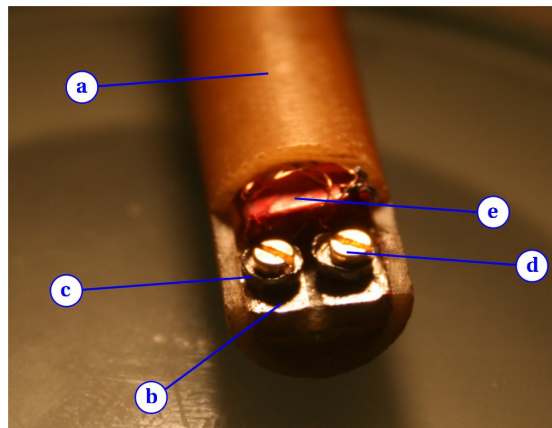


Figure 3.5: Picture showing the capacitor mounted in parallel with the pick-up coil and directly attached to the SQUID package. (a) SQUID package. (b) Pick-up coils superconducting contact pad. (c) Niobium washer. (d) Screw. (e) 100 nF foil capacitor. The advantage of this configuration is that the capacitor and additional wiring are shielded from RF noise.

core consisting of a steel mesh with a copper matrix, a Teflon insulating layer and then an outer shield which is a thin-walled copper tube. The large amount of copper implies that there will be a large heat load down to the 1K pot, which coupled with the thick insulating layer between core and shield makes it hard to cool down the coaxial cable. As the SQUID sits in a vacuum inside the IVC, it is essentially only the cables which thermalise it down to 1.5 K. It turns out that one particular challenge was to get the SQUID superconducting without adding in too much extra wire, which would negate the advantage of using coax-cables, and more importantly keeping these wires well shielded against RF noise. The solution was well thermalise the coax cables on to the roof of the IVC can by soldering them on to a copper heat sink. This was complemented by around 10 cm of twisted pair constantan wire (with a resistance of around 1 Ohm) which is thermalised on the 1K pot. In order to reduce any RF noise, the thermal anchoring was done inside the same closed copper can which holds the SQUID.

3.3.2.2 Pick-up Coils

The pick-up coils, which can have various configurations depending on the order of gradiometer desired, essentially serve to carry the flux from the sample to the SQUID. In order to transport the flux, the pick-up coils must be attached to the SQUID input coil in a purely superconducting circuit. There are several potential problems which can arise due to the pick-up coils, such as:

- Picking up too much magnetic noise.
- Non-superconducting link to the SQUID.
- Coils vibrating relative to the DC field.

The pick-up coils form a superconducting circuit spanning a considerable distance (remember that the SQUID has to be far enough from the DC field that the shield remains superconducting), and this implies that the circuit behaves like an *antenna* for magnetic fields. The effects of this are reduced slightly by making the circuit out of twisted pair wires, although it is still incredibly sensitive to any kind of magnetic signal. To make sure that the signal remains noise free, the wires must be shielded with a superconductor. This was achieved by taking single flux core lead/tin solder and removing the flux by heating to 80°C and melting the flux. After the flux has melted it flows out of the solder and leaves a hollow superconducting tube. All that has to be done now is to remove the final residues of flux by flushing the tube with ethanol several times and the pick-up coil wire can be inserted into the shield. Alternatively it would be possible to use niobium capillaries, although these are very expensive compared to the home made solution.

If any part of the circuit is in a non-superconducting state, the flux will no longer be carried to the SQUID and it will appear as if there were no pick-up coils attached. An intermediate situation, which is unfortunately very common, is that when the pick-up coils are attached to the SQUID, an oxide layer is present on the wires. This oxide layer results in a tunnel barrier and simultaneously reduces the SQUID signal and increases noise. The way in which this problem is solved in almost all SQUID applications is to fix the wire onto a superconducting pad mechanically, pressing it with a niobium washer. The force generated by the washer is large enough that the oxide layer on the niobium titanium wire cracks and there is a good superconducting contact. The downside of this method is that 1) there is no way of knowing whether the connection is good without cooling down and 2) the wires are very likely to break each time they are attached or detached.

Finally, if the pick-up coil is not directly attached to the magnet then vibrations will cause a large amount of noise. Even in the case of a perfectly wound second order gradiometer, this will be a major problem as the field is effectively changing very quickly and therefore the second differential of the field is not negligible. The situation is worsened by the fact that the pick-up coils are wound by hand, so there will be some imbalance. For this reason the pick-up coils were mechanically anchored to the magnet using a series of stiff copper beryllium springs. There are three springs attached to the magnet base plate, which press against the outside wall of the IVC can once the fridge is inserted into the cryostat. Two more springs are attached to the pick-up coil tube, which serve to both centre the coils and mechanically couple the pick-up coil to the IVC can. Taken together, these two sets of springs imply that the pick-up coils will vibrate with the superconducting magnet.

3.3.2.3 SQUID Sensitivity

As has been mentioned several times, SQUIDs are extremely sensitive devices. In order to increase the useful range of the device, the feedback electronics contain a resistor in series with the feedback of the coil. Changing the resistance of the feedback coil allows the +/- 12 V to produce a different range of magnetic fields to cancel out the flux entering the SQUID. The

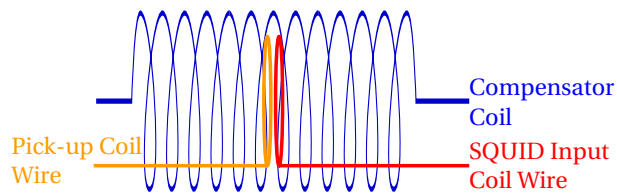


Figure 3.6: Schematic representation of the envisaged flux transformer. Two superconducting circuits, one attached to the pick-up coil and the other to the SQUID input coil, are coupled via two superconducting loops. The loops coupling the two circuits are inside a larger coil which can be used to actively reduce the flux entering the SQUID, thus increasing the dynamic range.

feedback resistor can be set at 5 k Ω , 10 k Ω , 20 k Ω , 30 k Ω , 50 k Ω , 85 k Ω , 125 k Ω , and 185 k Ω . As the compensating field scales roughly inversely to the feedback resistance, this corresponds to two orders of magnitude of range of flux which can be measured. In order to further increase the range, one must introduce a so called *flux transformer*. This device serves to decrease the flux transmitted to the SQUID input coil from the pick-up coils. There are two ways one can make such a transformer, either passively where coil geometries give a fixed transformation ratio, or actively, where an external field is generated to reduce the flux in the pick-up circuit. An active flux transformer, or flux compensator, is much more versatile as it can give a much wider range of sensitivity, but comes with the disadvantage that the signal will get somewhat more noisy. Due to the very low temperatures at which samples are measured in this system and the large magnetic fields available, it was decided that a versatile active flux transformer was the best option.

The most basic design of an active flux transformer is to introduce an additional coil in the superconducting wire coming from the pick-up coils and to wrap an inductive coil, the *flux compensator coil*, around it. By applying a current to the flux compensator a field is generated which can be used to reduce the flux inside the pick-up coil wire. Once again, it is a good idea to place the entire flux transformer inside a superconducting shield to reduce noise. The idea being to run the entire SQUID in a null voltage mode, where the flux being generated by the pick-up coil is being cancelled out by a field generated by the flux compensator.

The flux transformer used is of a slightly more complex design and removes the need to make *any* superconducting joints each time the SQUID magnetometer set-up is mounted or removed. The basic idea is that the SQUID itself remains attached to the 1K pot permanently along with one half of the flux transformer – the flux compensator side. The SQUID input coil would be connected to a single superconducting loop, or *flux transfer coil*, which sits in the middle of the flux compensator. The pick-up coils would now no longer be attached directly to the SQUID, but would also be a closed circuit with the pick-up coils on one end and a flux transfer coil on the other end. Now to attach the pick-up coils to the SQUID via a purely superconducting circuit, all that is needed is to place the two flux transfer coils next to each other inside the flux transformer. A schematic representation of this flux transformer, which can be considered a 1:1 transformer with an external compensation coil, is shown in Fig. 3.6

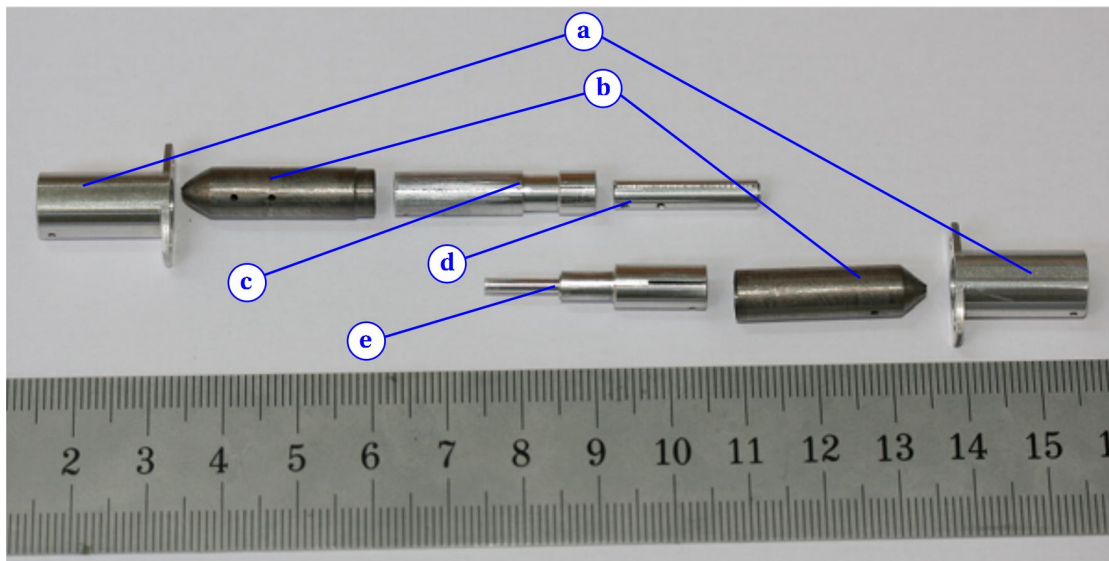


Figure 3.7: Components of the flux transformer. The top four pieces make up the SQUID side of the flux transformer and are permanently mounted on the 1K pot. The bottom three pieces make up the pick-up coil side of the flux transformer and are permanently attached to the pick-up coil. a) Flux transformer holder/1K pot mount. b) Niobium zirconium shield. c) Mount for compensation coil. d) Mount for SQUID superconducting loop. e) Mount for pick-up coil superconducting loop.

The pieces required to make the resulting flux transformer are shown in Fig. 3.7. The top part of the picture shows the pieces which are permanently mounted on the 1K pot (the SQUID side of the flux transformer), and the bottom part shows the pieces which are disconnected each time the magnetometer is to be removed. The flux transformer is held in place by two aluminium holders (a). The upper holder is glued onto the copper SQUID enclosure using Stycast 2850 FT, and the lower part is screwed into the upper one using two m2.5 screws. The flux transformer sits inside a niobium zirconium shield (b), which serves to keep the environment free from all external magnetic fields. The compensation coil, which consists of 15 turns of niobium titanium wire in a copper matrix, is wrapped around an aluminium support (c). The flux transfer coil for the SQUID side is wound around the rightmost end of the aluminium support (d), where there is a 0.2 mm wide rim to hold the coil. Likewise in the aluminium support (e) there is also such a rim, which is located at the left end of the intermediate diameter cylinder. Piece (d) sits inside piece (c) and the 10 mm long end of piece (e) slides into a matched diameter hole in (d) so that the two coils are in contact. These three pieces have been machined to have very high precision (with deviations of <0.01 mm) from the specified dimensions, so that when the system is unmounted and remounted all the coils sit in the exact same location. Furthermore, the two screws which attach the top part to the bottom ensure that there is no change in rotation, which could introduce offsets.

3.3.2.4 Sample Movement

The final challenge, and by far the largest in this SQUID magnetometer is the sample movement. The preferable solution is that the piezomotor generates a sufficiently small amount of heat that it can be run at dilution temperatures, as was advertised by Attocube. In order to properly characterise the performance of the piezomotor at low temperatures, it was run in the dilution fridge without anything attached to the translation stage. The position of the translation stage on the piezomotor is measured using a resistive encoder².

Measurements of the distance per step, velocity and heat generated were made for several frequencies and voltages of the saw-tooth profile. The results of these measurements are summarised in Fig. 3.8. The top left panel shows the distance per step as a function of voltage and the top right shows the velocity as a function of frequency. The bottom two panels show the heat generated in μW for a velocity of $1 \mu m s^{-1}$ as a function of the applied voltage and frequency.

The important results from this test are that the distance per step depends linearly on the voltage and is independent of the frequency, and increasing the frequency simply increases the velocity while maintaining the same step size. Increasing the step size by increasing the voltage increases the heat generation faster than the gain in velocity. On the other hand increasing the frequency does not increase the heat generated per step. This implies that the optimal way to run the system in terms of minimising heat generation is to use relatively high frequencies and low voltages.

Unfortunately, the amount of heat generated is still too much to allow for feasible operation at low temperatures. A single dipole curve scan in the SQUID should not take longer than several minutes in order to be useful for measuring a sample. Taking for example 5 minutes per dipole curve (which is already a bit longer than one would like) implies a velocity of $66 \mu m s^{-1}$ which corresponds to over 1 mW of power dissipation into the dilution fridge. This is clearly far too large for a fridge with a mere $25 \mu W$ cooling power at 100 mK.

The solution to this limitation was to mechanically fix the piezomotor to the 1K pot while thermally coupling it to the IVC can. The first iteration of this is shown in Fig. 3.9. The piezomotor (d) sits underneath the mixing chamber (a), supported by three fibre-glass rods (b) which are attached to the 1K pot. These fibre-glass rods effectively thermally decouple the piezomotor from the 1K pot, allowing for it to be anchored to the IVC can using some copper springs (e). The sample is mounted on a long thin walled 3 mm OD carbon fibre tube (f), hopefully thermally decoupling it from the relatively high temperature of the piezomotor. Carbon fibre was chosen as it is a very good trade-off between high mechanical rigidity and low thermal conductivity [80]. The sample is thermally coupled to the mixing chamber using a slightly coiled bunch of ten $50 \mu m$ diameter copper wires (c). The wires are coiled slightly so

²Unfortunately it seems that the resistive encoder is made out of RuO_2 given that the resistance increases exponentially below 4 K. Measurements were still possible when measuring the potential difference drop using a lock-in amplifier.

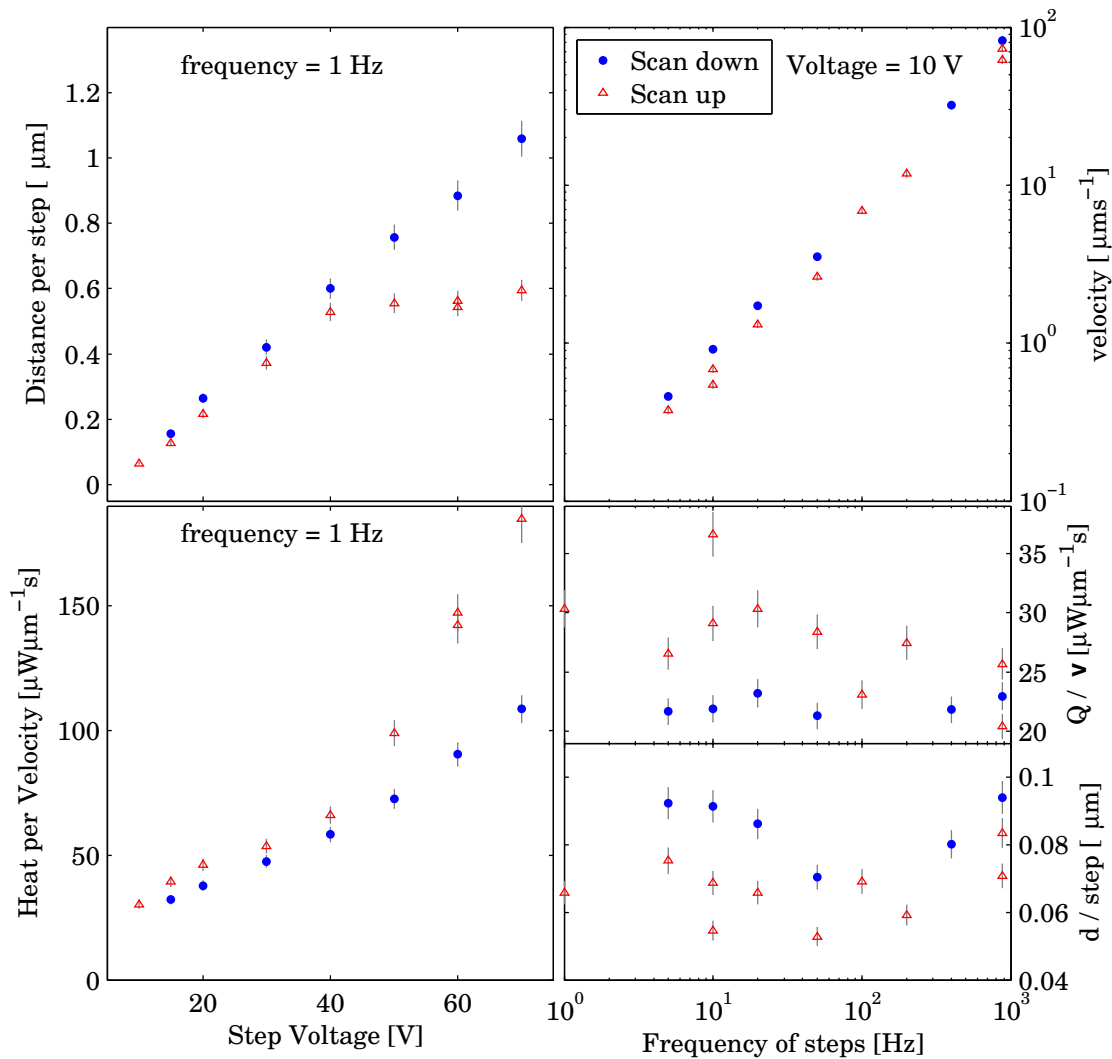


Figure 3.8: Heat generated by moving the piezomotor as a function of voltage and frequency. The heat is expressed as power dissipated (in μW) to achieve a velocity of $1 \mu\text{ms}^{-1}$.

that when the piezomotor moves, they can easily uncoil and not inhibit the movement of the sample.

3.3.3 Intermediate Results

The magnetometer system was attached to the dilution fridge, with the SQUID and flux transformer mounted on the 1K pot. The piezomotor was mounted as described above and the pick-up coils were wound around a carbon fibre tube which hangs from the piezomotor support. All of the superconducting wires were shielded using hollowed out lead solder and the pick-up coil was mechanically anchored to the magnet with copper beryllium spring as described in section 3.3.2.2. In this configuration, the mixing chamber was able to cool down to 100 mK. The temperature dependence of a paramagnetic salt was measured in the remnant

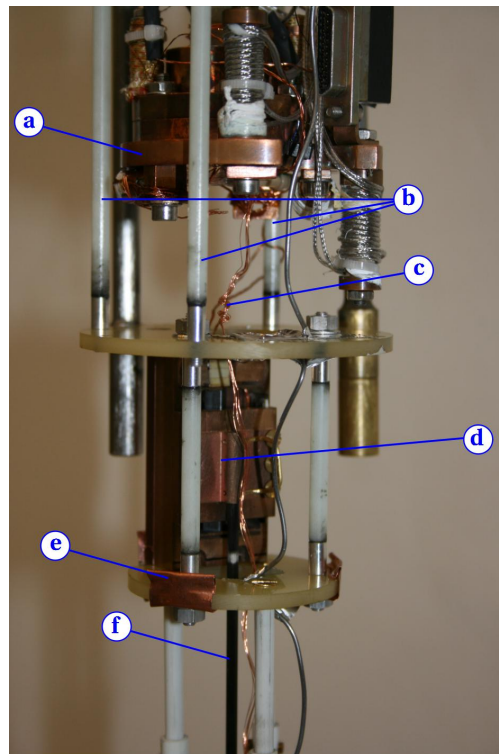


Figure 3.9: Photo of the position and mounting of the piezomotor in the first prototype of the Dilution SQUID. (a) Mixing chamber. (b) Fibre glass support rods which attach the piezomotor to the 1K pot. (c) Ten $50\ \mu\text{m}$ copper wires to thermalise the sample to the mixing chamber. (d) Piezomotor. (e) Copper springs to thermalise the piezomotor to the IVC can. (f) Carbon fibre sample support tube.

field of the magnet (several Oe.) in order to try to determine the temperature of the sample relative to the fridge. The sample was positioned in the centre of the gradiometer and then the temperature was ramped while recording the voltage being applied to the feedback coil. The results are shown in Fig. 3.10a. The sample follows Curie-Weiss behaviour down to a temperature of around 500 mK, where it begins to deviate as a temperature gradient begins to build up between the sample and the mixing chamber. Using the paramagnetic behaviour as a thermometer determines the temperature of the sample to be 385 ± 5 mK when the dilution fridge reaches 100 mK.

At the same time, it was necessary to determine if the piezomotor was powerful enough to bend the copper wires and thus move the sample at such low temperatures. As the sample temperature and the mixing chamber temperature begin to deviate at ~ 500 mK, the tests were carried out at this temperature. This test was the proof of concept for the piezomotor driven dilution SQUID – it demonstrated that such a motor can be used to move the sample without generating excessive noise in the SQUID signal. It was noticed during these measurements, that the high voltages used to cause the piezoelectric effect can interfere with the SQUID electronics. If a sufficiently large voltage is used then the SQUID feedback electronics unlocked

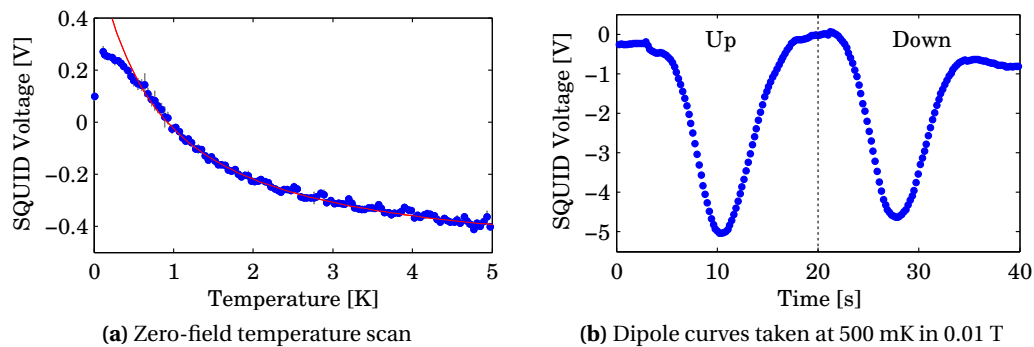


Figure 3.10: Magnetisation measurements of a paramagnetic salt from the first SQUID prototype, showing (a) zero field temperature scan and (b) dipole curves at 500 mK in 0.01 T. The temperature scan was made by positioning the sample in the middle of the gradiometer and recording the feedback voltage while ramping the temperature. The dipole curves consist of moving the sample at a continuous velocity in one direction for 20 s then the opposite direction for the following 20 s.

and the measured voltage jumps by several volts, typically overloading. For this reason, the measurements were carried out using the minimum voltage (15 V) required for sample movement. The dipole curve created by moving the piezomotor across the full 20 mm range is shown in Fig. 3.10b. The voltage is plotted as a function of time, with the direction of travel inverted after 20 s. There is a small change in the intensity of the dipole curve between scans in one direction and the other, which is likely due to the heat generated by piezomotor being conducted through the carbon fibre tube.

There are several factors which could be resulting in the somewhat high temperatures both on the mixing chamber and sample. For the mixing chamber, the most likely source of heat is a contact between the fibre glass rods and the copper base plate. In essence the three fibre-glass rods do not provide a sufficiently rigid support structure, resulting in one of them touching the mixing chamber. The large temperature gradient between the sample and the mixing chamber indicates that the thermal link between the piezomotor and the sample is too great. There are two ways this situation can be improved: either by reducing the thermal conductivity of the sample mount, or by increasing the thermal conductivity between the sample and the mixing chamber.

3.4 Final Configuration

The final configuration of the SQUID magnetometer system, which aims to overcome the shortcomings of the first prototype, is presented in this section. This section is divided into discussions on the support structure, the 1K pot, the mixing chamber and the sample area.

3.4.1 Support Structure

The role of the support structure is to hold the piezomotor and pick-up coils in place. A photo of the support structure is shown in Fig. 3.11. The support structure consists of fibre glass tubes which have had a segment removed, so that the mixing chamber and sample can still be accessed. Starting from the top of the support structure (left in the picture) a large fibre glass tube (a) connects the 1K pot and the piezomotor (c). The support is screwed onto a titanium ring which is permanently mounted on the 1K pot. The piezomotor attaches on to a titanium ring which sits at the bottom of this large tube. An aluminium rod (d) is used to thermalise the piezomotor to the 1K pot temperature, which should decrease the thermal load from the piezomotor down to the sample considerably.

A second fibre glass tube is attached to the bottom of the piezomotor, once again by attaching both pieces to a titanium ring. This fibre glass tube ends in a conical piece made out of Delrin plastic, which serves two purposes. The first is to hold the carbon fibre tube onto which the pick-up coils are wound (f). The second purpose of this piece is the conical shape which allows the entire structure to be easily inserted into the IVC can. At the bottom of the carbon fibre tube containing the pick-up coils, are the two copper beryllium springs which remove issues related to the magnet or pick-up coils vibrating. The twisted pair superconducting pick-up coil wires are in a superconductor shield (c) and terminate inside the lower half of the flux transformer (b). The ends of the wires have been etched with nitric acid to remove the copper matrix and pressed together inside a small piece of hollowed out solder to ensure a good superconducting connection.

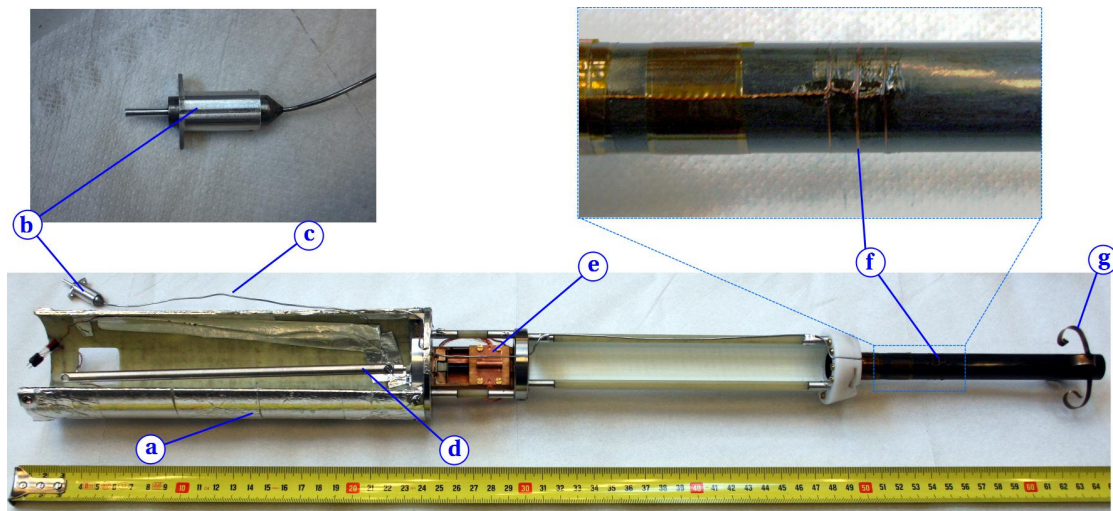


Figure 3.11: Photo of the final piezomotor and pick-up coil support structure. (a) Fibre glass tube to attach piezomotor to 1K pot. (b) Pick-up coil side of the flux transformer (lower side). (c) Superconducting shielded twisted pair superconducting pick-up coil wires. (d) Aluminium thermal anchoring rod between piezomotor and 1K pot. (e) Piezomotor with no sample attached. (f) Second order gradiometer pick-up coils. (g) Copper beryllium springs.

3.4.2 1K Pot

The 1K pot holds several key components for the operation of the SQUID magnetometer, with a fair portion of them permanently mounted – even as the fridge is being used for other measurements. A photo of the 1K pot with the entire magnetometer system attached is shown in Fig. 3.12. Starting from the top of the dilution fridge, the copper coax cables (a) can be seen soldered on to copper heat sinks screwed on to the roof of the IVC can. The SQUID sits inside a superconducting niobium titanium shield which is placed inside a copper can (c) which is mounted permanently on the 1K pot plate (b). Apart from the mechanical attachment the copper can serves to both thermalise the superconducting shield and shield the SQUID sensor from RF noise. The SQUID side of the flux transformer (d) is glued on to the top part of the copper SQUID enclosure using Stycast 2850 FT. This side of the flux transformer is attached to the SQUID using twisted pair superconducting wires in a super conducting shield. A small heater (i) wrapped around these wires allows the SQUID to be decoupled from the pick-up coils when ramping DC fields. The final piece which is permanently attached to the 1K pot is a titanium support ring (e), on to which the support structure for the pick-up coils and piezomotor is attached.

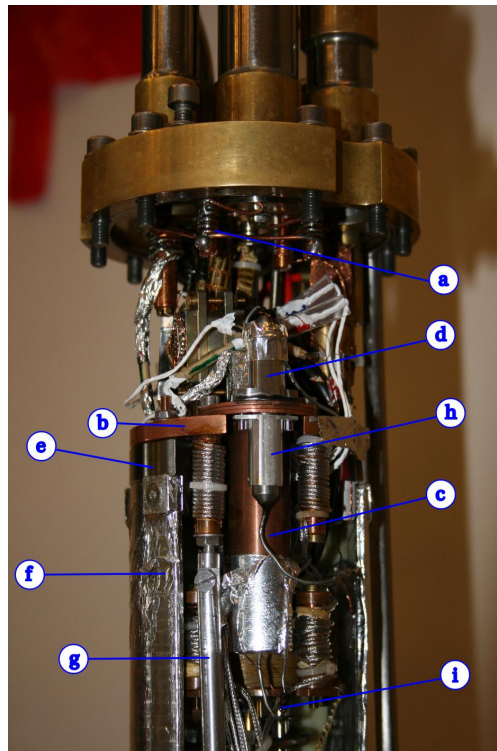


Figure 3.12: Photo of the 1K pot showing various elements of the Dilution SQUID. (a) Thermal anchoring of coaxial cables. (b) 1K pot heat sink plate. (c) Copper SQUID enclosure. (d) SQUID side of flux transformer. (e) Titanium ring attachment for support structure. (f) Pick-up coil & piezomotor support structure. (g) Piezomotor thermal anchoring rod. (h) Pick-up coil side of flux transformer. (i) Heater to decouple SQUID from pick-up coils.

3.4 Final Configuration

All of the key components of the fridge sit inside the support structure (f) for the pick-up coils and piezomotor. In order to reduce any possible negative effects due to radiation heating from the fibre glass rod, it has been covered in aluminium foil, bringing its temperature down to that of the 1K pot. The piezomotor thermalising rod (g) attaches on to one of the pre-existing wire heat sinks on the 1K pot. Apart from attaching these two components, the pick-up coil side of the flux transformer (h) must also be attached using two screws. The beauty of this particular design structure is that to go from the “bare fridge” to the SQUID magnetometer probe only involves changing a few electrical connections and doing up a few screws, an operation which takes less than 10 minutes.

3.4.3 Mixing Chamber and Sample

Once the support structure is mounted, the mixing chamber sits inside of it, as shown in Fig. 3.13. The large fibre glass tube of the support structure (a) goes around the mixing chamber (b) leaving a space of roughly 3 mm around all sides. The thermal link down to the sample makes use of a 6 mm diameter solid copper cold finger which is held in place by a gold plated copper clamp (d) screwed onto the mixing chamber. The cold finger is roughly 1 cm off the central axis, allowing it to pass parallel to the sample stick. The aluminium thermalising rod for the piezomotor (c) passes through the *line of sight port* of the mixing chamber where it is anchored onto an aluminium block which is screwed on to the back of the piezomotor using aluminium screws.

The piezomotor is attached to a copper block, ensuring that it can be cooled easily. Some preliminary tests using the piezomotor in this set-up indicated that the translation stage table

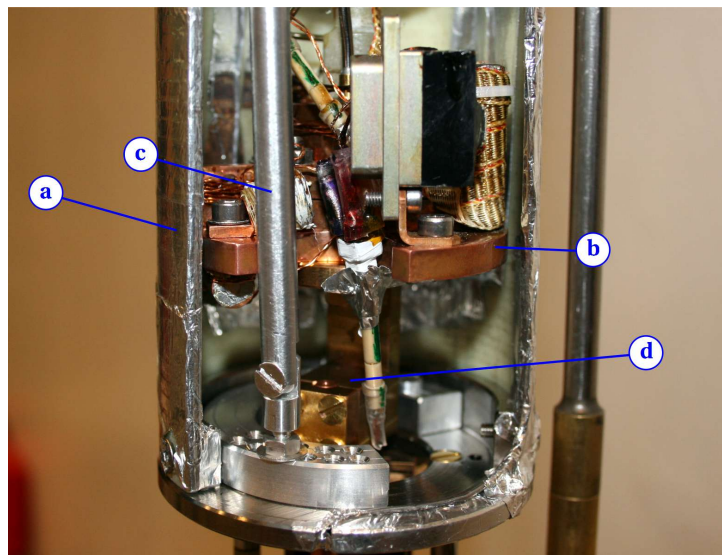


Figure 3.13: Photo of the mixing chamber with the magnetometer module attached. (a) Support structure. (b) Mixing chamber plate. (c) Aluminium piezomotor thermal anchoring rod. (d) Cold finger for thermalising sample.

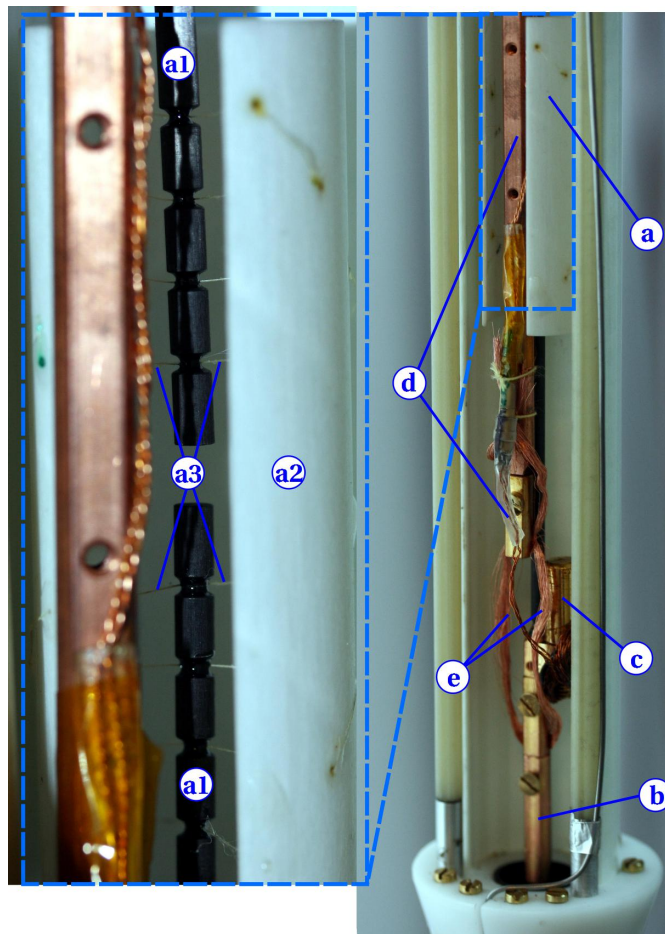


Figure 3.14: Photo of the sample cold plate and thermal decoupler of the SQUID magnetometer. (a) Thermal decoupler consisting of two carbon fibre rods (a1) suspended from a fibre glass tube (a2) using 50 μm diameter Kevlar threads (a3). (b) Sample cold plate with thermometer (c) is thermalised to the cold finger (d) via a bundle of 50 μm diameter copper wires (e).

is thermally decoupled from the rest of the piezomotor. This makes perfect sense, as the table is only attached to the guiding rod using a weak frictional force, which implies that thermal contact will necessarily be poor. In order to improve the situation, a bundle of roughly twenty filaments of 50 μm wire were clamped onto the copper mounting block on one end and between the carbon fibre rod holder and translation stage table on the other.

The sample must be mechanically attached to the piezomotor while remaining thermally coupled to the mixing chamber. A photo of the region where the various thermal decouplings and couplings take place is shown in Fig. 3.14. The sample is connected to the piezomotor via the thermal decoupler (a). This component consists of two 2.5 mm diameter carbon fibre rods (a1) which are suspended from a fibre glass tube (a2) using 50 μm diameter multifilament Kevlar threads (a3). This decreases the thermal conductivity of the resulting piece by over a factor of 10 as compared to a thin walled carbon fibre tube while maintaining good mechanical

rigidity. A gold-plated copper piece (b) is attached to the end of the carbon fibre rod which serves as the cold-plate to which the sample is thermalised. The sample holder (not shown) consists of a carbon fibre rod with a strip of 100 μm thick copper foil glued on to one side which is clamped into the cold-plate. In order to have an accurate reading of the sample temperature, a thermometer (c) is attached directly to the cold plate.

The sample is thermalised to a copper cold finger which is attached to the mixing chamber. In order to allow the sample to be moved by the piezomotor while remaining cold, the thermalisation is carried out using a bundle of roughly 50 copper wires of 50 μm each.

3.5 Outlook

The SQUID presented here has been a very challenging project and has thus far produced promising results. The system is capable of moving a sample through the pick-up coils in an acceptable time while keeping the sample at a relatively low temperature, allowing for both temperature and field-dependent magnetisation to be measured between 0.1 K and 6 K up to 9 T. The base temperature of the sample is limited by the fact that the piezomotor generates large amounts of heat relative to the cooling power of the dilution fridge, and without a major redesign this cannot be changed.

One possible way to improve this aspect would be to use a piezomotor which does not use stick-slip motion to generate the movement. A good candidate for this is an *inchworm* device, where the movement is still carried out using the piezoelectric effect but does not work against friction [97]. Unfortunately an appropriate compact inchworm piezomotor is not commercially available and building one would be a large project in itself.

An alternative solution would be to use something like the Piezo LEGS motor produced by MICROMO, which would require the manufacturer developing a version intended for low temperature use (the materials must have matched thermal expansions coefficients).

Along with the ability to measure DC magnetisation, this unique modular design allows for the SQUID sensor to be used for other types of measurements with relative ease. Two such probes are currently planned: AC susceptibility and magnetoelectric effect measurements.

3.5.1 AC Susceptibility

Measuring AC susceptibility using a SQUID offers some advantages compared to the existing inductive set-up presented earlier. Using a SQUID will allow for samples with very small moments to be measured due to its very high sensitivity. The sensitivity of the SQUID measurement system also does not depend on the frequency being measured, unlike in an inductive susceptometer. This implies that frequencies below 1 Hz should be both possible and relatively easy to measure.

In order to measure AC susceptibility with a SQUID, an oscillating field needs to be generated and the response from the sample recorded in pick-up coils. An effective way to do this would be to wind an excitation coil (with something on the order of 1000 windings) directly on top of the SQUID pick-up coils, which should be either a 1st or 3rd order gradiometer. The former will have a larger sensitivity to the sample, while the latter will be less affected by external fields. Such odd order gradiometers are particularly effective, as one end of the gradiometer will measure a positive signal and the other a negative signal of the same size, assuming the coils are perfectly balanced and are in a uniform field. If a sample was placed in only one end of the gradiometer then the resulting signal would be the response of the sample. As it is not possible to perfectly balance such coils, a *trim coil* may be used to remove any background signal noise from imbalance. This coil is wrapped on top of the driving coil over the end of the gradiometer, which remains empty and is tuned in such a way that the resulting signal without sample is zero.

Given the modular design of the DC SQUID magnetometer, the best way to build an AC system is to build not just new pick-up coils but a new support structure. The structure can be a little bit simpler than for the magnetometer, as there is no need to attach the piezomotor. A new lower half of the flux transformer, dedicated for this support structure, would also be needed. This gives the flexibility to either measure DC magnetisation or AC susceptibility.

3.5.2 Magnetoelectric Effect

Multiferroic and magnetoelectric materials are at the centre of a very active and intense field of research. The magnetoelectric effect can be expressed as the application of an electric field inducing a finite magnetisation or vice-versa. Typically, measurements are done by applying a magnetic field and measuring the electric polarisation in the material. Another way of measuring this magnetoelectric effect would be to apply electric fields to the sample and measure the change in SQUID voltage. The changes are typically very small, however, and in a DC measurement, would require potentially damaging voltages to see a signal. An alternative way to measure the effect is by using an AC electric field combined with a lock-in amplifier to measure the changes in the SQUID signal. This should allow for voltages below 15 V to produce a measurable signal, which is easily achieved in the current setup.

4 $\text{LiHo}_x\text{Er}_{1-x}\text{F}_4$

The LiReF_4 family of magnets have been studied for over 30 years [36], revealing a plethora of intriguing phenomena ranging from quantum criticality [11, 78], glassiness [4, 76, 77] and the controversial [45, 74, 75] possibility of an exotic *anti-glass* phase [31, 32]. The interesting physics observed experimentally in these compounds is complemented by the relatively simple and remarkably well characterised Hamiltonian. This combination makes the LiReF_4 magnets an ideal playground, allowing relatively straightforward theoretical predictions to be made and tested on a clean model system.

The discussion begins in Section 4.1 with an introduction to the Hamiltonian followed by a very brief overview of $\text{LiHo}_x\text{Y}_{1-x}\text{F}_4$ and LiErF_4 , the most studied members of the family, and details the choice of $\text{LiHo}_x\text{Er}_{1-x}\text{F}_4$ as a model system to be studied. Section 4.2 gives an overview of powder AC susceptibility measurements taken on 11 samples across the entire range of x and presents the experimental phase diagram of $\text{LiHo}_x\text{Er}_{1-x}\text{F}_4$. This is followed by a description of the algorithms used to carry out mean-field calculations and an introduction to neutron scattering in Section 4.3. Both of these tools, along with additional AC susceptibility measurements have been used to characterise three different regions of the phase diagram: the embedded spin-glass, the ferromagnetic spin-glass and the antiferromagnetic spin-glass. These phases correspond to $x \sim 0.8$, $x = 0.5$, $x = 0.25$ and are treated in Sections 4.4, 4.5 and 4.6 respectively.

4.1 The LiReF_4 Model Magnets

The LiReF_4 magnets crystallise in a tetragonal structure with space group $I4_1/a$. Each of the four *Re* ions occupies a position with S_4 symmetry and is surrounded by 8 fluorine ions, which generate the local crystal field environment that determines the anisotropy of the spin-environment. The LiReF_4 unit cell is shown in Fig. 4.1, and the unit cell parameters of LiHoF_4 , LiErF_4 and LiYF_4 are given in Table. 4.1

One of the key strengths of the LiReF_4 family as model magnets is their relatively simple and

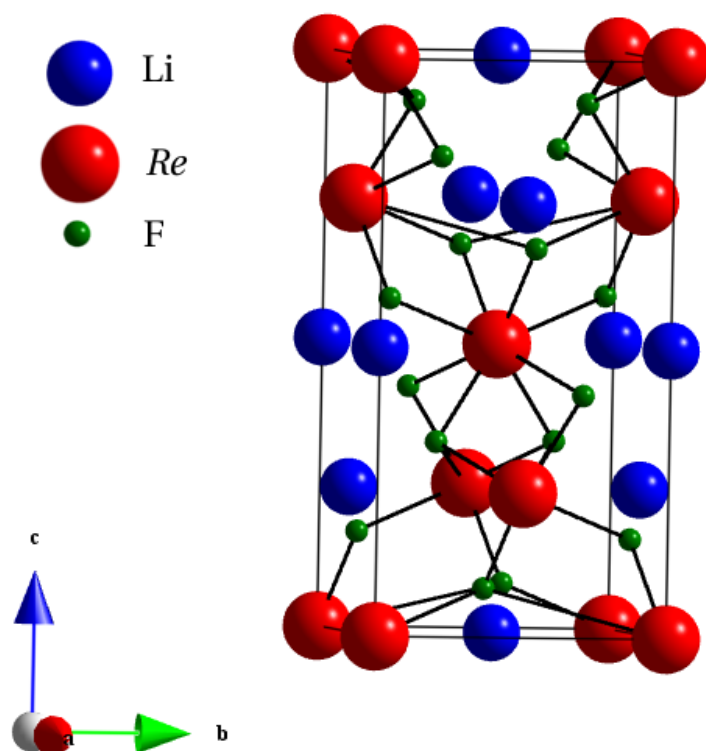


Figure 4.1: Diagram showing the tetragonal crystal structure of the LiReF_4 system. Red spheres are rare-earth ions, blue are lithium and green are fluorine. The black bonds indicate the fluorine ions which contribute to the crystal field around the rare-earth ions.

Compound	c [Å]	a [Å]	c / a	Unit Cell Volume [Å ³]
LiHoF_4	10.75	5.175	2.077	287.9
LiErF_4	10.70	5.162	2.073	285.1
LiYF_4	10.74	5.175	2.075	287.6

Table 4.1: Unit Cell Parameters for LiHoF_4 , LiErF_4 and LiYF_4 (taken from Misra and Felsteiner [61]).

well characterised Hamiltonian:

$$\mathcal{H} = \sum_i [H_{CF}(\mathbf{J}_i) + \mathcal{A}\mathbf{J}_i \cdot \mathbf{I}_i - g\mu_B \mathbf{J}_i \cdot \mathbf{H}] - \frac{1}{2} \sum_{ij} \sum_{\alpha\beta} \mathcal{J}_D D_{\alpha\beta}(ij) \mathbf{J}_{i\alpha} \mathbf{J}_{j\beta} - \frac{1}{2} \sum_{ij}^{n,n} \mathcal{J}_{12} \mathbf{J}_i \cdot \mathbf{J}_j, \quad (4.1)$$

where H_{CF} is the crystal field, \mathcal{A} is the hyperfine coupling, \mathbf{J}_i and \mathbf{I}_i are respectively the electronic angular momentum and the nuclear spin of the i^{th} ion, \mathcal{J}_D is the dipole coupling, $D_{\alpha\beta}(ij)$ is the classical dipole tensor and \mathcal{J}_{12} is the exchange coupling. There are 5 terms in this Hamiltonian, which, moving from left to right in the equation, correspond to (1) the crystal field, (2) the hyperfine interaction, (3) the Zeeman splitting, (4) the dipole interaction and (5) a nearest neighbour interaction term. It was understood relatively early on that the two dominating terms in the Hamiltonian are the local crystal field environment and the long-range dipole-dipole interaction [36].

The crystal field H_{CF} is given by:

$$H_{CF} = \sum_{l=2,4,6} B_l^0 \mathbf{O}_l^0 + \sum_{l=4,6} B_l^4(c) \mathbf{O}_l^4(c) + B_6^4(s) \mathbf{O}_6^4(s), \quad (4.2)$$

with B_m^n the crystal field parameters, and \mathbf{O}_m^n Stevens operators, which are given following the convention described by Hutchings [41]. In order to compress the formulae slightly we use the typical abbreviation $X \equiv J(J+1)$, leading to:

$$\begin{aligned} \mathbf{O}_2^0 &= 3\mathbf{J}_z^2 - X, \\ \mathbf{O}_4^0 &= 35\mathbf{J}_z^4 - (30X - 25)\mathbf{J}_z^2 + 3X^2 - 6X, \\ \mathbf{O}_4^4 &= \frac{1}{2}(\mathbf{J}_+^4 - \mathbf{J}_-^4), \\ \mathbf{O}_6^0 &= 231\mathbf{J}_z^6 - (315X - 735)\mathbf{J}_z^4 + (105X^2 - 525X + 294)\mathbf{J}_z^2 - 5X^3 + 40X^2 - 60X, \\ \mathbf{O}_6^4(c) &= \frac{1}{4}[(11\mathbf{J}_z^2 - X - 38)(\mathbf{J}_+^4 + \mathbf{J}_-^4) + (\mathbf{J}_+^4 + \mathbf{J}_-^4)(11\mathbf{J}_z^2 - X - 38)], \\ \mathbf{O}_6^4(s) &= \frac{1}{4i}[(11\mathbf{J}_z^2 - X - 38)(\mathbf{J}_+^4 - \mathbf{J}_-^4) + (\mathbf{J}_+^4 - \mathbf{J}_-^4)(11\mathbf{J}_z^2 - X - 38)]. \end{aligned} \quad (4.3)$$

The x-axis can be chosen arbitrarily, and in this case has been done by rotating the coordinate system around the crystal symmetry z-axis, such that the parameter $B_4^4(s) = 0$, removing an additional $\mathbf{O}_6^4(s)$ term which would otherwise be present. Although it is technically possible to calculate the crystal field parameters, the accuracy of these calculations is rarely acceptable and the experimentally determined values are more commonly used. The crystal field parameters have been measured for both LiHoF₄ [79] and LiErF₄ [49] using inelastic neutron scattering and are given in Table 4.2.

Compound	B_2^0	$10^3 B_4^0$	$10^3 B_4^4$	$10^5 B_6^0$	$10^5 B_6^4(c)$	$10^5 B_6^4(s)$
LiErF ₄	.060	-0.12	-4.33	-0.19	-8.50	-2.27
LiHoF ₄	-0.06	0.35	3.6	0.04	7.0	± 0.98

Table 4.2: Crystal field parameters for LiHoF₄ [taken from 79] and LiErF₄ [Taken from 49].

The other term in the Hamiltonian which dominates the low temperature physics is the dipole-dipole interaction:

$$-\frac{1}{2} \sum_{ij} \sum_{\alpha\beta} \mathcal{J}_D D_{\alpha\beta}(ij) \mathbf{J}_{i\alpha} \mathbf{J}_{j\beta}. \quad (4.4)$$

The dipole coupling strength is given by $\mathcal{J}_D = (g\mu_B)^2$ and the classical dipole tensor, $D_{\alpha\beta}(ij)$, takes the standard form:

$$D_{\alpha\beta}(ij) = \frac{3(r_{i\alpha} - r_{j\alpha})(r_{i\beta} - r_{j\beta}) - |\mathbf{r}_i - \mathbf{r}_j|^2 \delta_{\alpha\beta}}{|\mathbf{r}_i - \mathbf{r}_j|^5}. \quad (4.5)$$

4.1.1 $\text{LiHo}_x\text{Y}_{1-x}\text{F}_4$

LiHoF₄ is a dipolar coupled Ising ferromagnet below $T_C = 1.53$ K, which is considered a good realisation of the *transverse field Ising model*, with a quantum phase transition at $H_C \approx 50$ kOe when the field is applied perpendicular to the c -axis. Doping with non-magnetic Y turns the system into a realisation of the *random field Ising ferromagnet model* [81]. A good summary of the theoretical and experimental understanding of this dilution series can be found in the review article by Gingras and Henelius [33].

Early studies using AC susceptibility and specific heat determined the nature of the classical phase transition. With the aid of spectroscopic techniques, the crystal field parameters were determined and the Hamiltonian was written down [2, 7, 8, 9, 36, 60, 61]. It was only after 20 years had passed that attention shifted to the quantum phase transition, which was observed by Bitko and Rosenbaum [11]. Since that observation, theoretical and experimental studies have focused on a quantitative and complete explanation of the ground state and quantum phase transition [11, 18, 78, 82, 89].

The bulk of the research in recent times has focused on $\text{LiHo}_x\text{Y}_{1-x}\text{F}_4$. For dopings between $x = 1$ and $x \sim 0.5$ the system remains ferromagnetic, but as the holmium content decreases further, re-entrant behaviour. At lower x , the ferromagnetic order is suppressed and gives way to a conventional spin glass transition [4], although this point is debated [45]. As x approaches zero, there is an ongoing discussion about the existence of an exotic *anti-glass* state [31, 32, 75, 76, 77], which shows very unusual dynamics in AC susceptibility measurements.

4.1.2 LiErF₄

LiErF₄ is an *XY* antiferromagnet which orders at $T_N = 0.370$ K and has a quantum phase transition, when a field is applied along the crystallographic *c*-axis, at $H = 4$ kOe. Until very recently, only a relatively small amount of work had been carried out on LiErF₄, related to the classical phase transition and crystal field parameters [8, 9]. Recent work carried out by Kraemer et al. [49] focuses on the critical behaviour of both the classical and quantum phase transition using neutron scattering, AC susceptibility and specific heat. The conclusions of this work are that the classical phase transition shows non-mean-field critical scaling, consistent with the 2D *XY*/h4 universality class. The quantum phase transition exhibits three-dimensional classical behaviour in accordance with the one dimension lower classical transition. It is proposed that the intrinsically frustrated nature of the dipole interaction effectively strengthens the role of fluctuations and results in the dimensional reduction.

4.1.3 LiHo_{*x*}Er_{1-*x*}F₄

The interest in studying LiHo_{*x*}Er_{1-*x*}F₄ stems from the physics present in LiHo_{*x*}Y_{1-*x*}F₄, which are a result of both the frustration from the dipole-dipole interaction and the disorder due to the random position of the Ho³⁺ ions. As the spins in LiErF₄ have *XY* anisotropy perpendicular to the Ising axis of LiHoF₄, they could act as a tuning parameter for off-diagonal terms in the Hamiltonian, effectively allowing the frustration to be tuned. This can both be applied to the long-range ordered states, where the addition of Er should reduce both T_C and H_C and also to the spin-glass regions. In the case of the glassy regions, the increased frustration is likely to have the effect of increasing the temperature scale slightly due to the higher density of magnetic ions.

4.2 AC Susceptibility Overview

Before inspecting the results of AC susceptibility measurements, it is important to take a step back and evaluate how to conduct the experiments. In these compounds, spin-glass behaviour is very likely which requires particular care in the measurement method. The first thing to do is to ensure that any applied fields are as small as possible, as the features of spin-glasses are smeared out even by low amplitude fields. This is not a problem here as the typical driving field is 42 mOe, which should not perturb the system too much. A more difficult consideration is the best way to carry out measurements when ramping the sample temperature.

In spin-glass systems, time and path dependent effects, such as ageing, memory and rejuvenation [19, 54, 44, 46], make direction and rate of temperature ramps while measuring a sample an important consideration. This is compounded with difficulties relating to the thermal properties of the LiReF₄ family of magnets at low temperatures. Being electrical insulators means that the samples will necessarily have a low thermal conductivity [73], so reaching thermal equilibrium will take some time. Additionally, both LiErF₄ and LiHoF₄ have a large

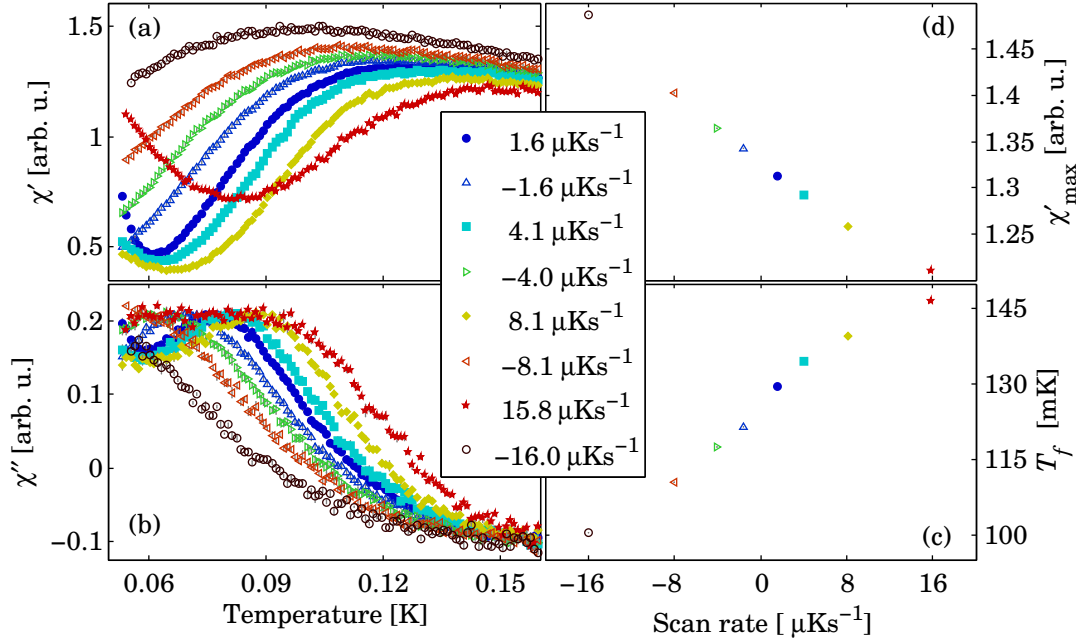


Figure 4.2: (a) Real and (b) imaginary susceptibility of $\text{LiHo}_{0.79}\text{Er}_{0.21}\text{F}_4$ taken at scan rates of $1.6 \mu\text{K/s}$ – $16 \mu\text{K/s}$ across the spin-glass freezing at 11.3 Hz. Solid points show scans from low to high temperature and the empty points scans from high to low temperature. (c) Temperature and (d) amplitude of the peak in χ' as a function of scan rate.

specific heat [60], meaning that a large amount of heat must be put in to, or taken out of, the sample to result in a temperature change. Taken together, these three effects imply that if the temperature is ramped too rapidly then the system can be very far away from equilibrium. An example of this is shown in Fig. 4.2, which consists of temperature scans on $\text{LiHo}_{0.79}\text{Er}_{0.21}\text{F}_4$, taken while ramping the temperature both up (solid points) and down (empty points) at rates of $1.6, 4, 8$ and $16 \mu\text{Ks}^{-1}$.

The scans were taken at 11.3 Hz, as this pushes the peak in susceptibility to lower temperatures where thermalisation times are longer. Panels (a) and (b) show the real and imaginary susceptibility respectively. Panels (c) and (d) show the Temperature of the peak in χ' (determined by the temperature of the maximum) and its amplitude respectively, as a function of scan rate. The hysteresis observed is likely a combination of thermalisation effects and spin-glass relaxation effects. It is very difficult to separate these two effects as the spin-glass relaxation effects are an intrinsic magnetic property and it is difficult to modify the thermal properties of the sample. It should however be noted that due to the choice of relatively low frequencies coupled with one of the lowest transition temperatures observed, this situation is a worst case scenario. As a result of these findings, all data as a function of temperature was taken while ramping from low to high temperatures, and the scans were divided up into different ramp rates depending on the temperature region as shown in Table 4.3.

AC susceptibility measurements were carried out on powder samples, ground from small

4.2 AC Susceptibility Overview

Temperature (K)	<0.1	0.1–0.2	0.2–0.4	0.4–0.75	0.75–1.25	1.25–2.5	2.5–6.5
Rate (μKs^{-1})	4	8	16	40	80	160	400

Table 4.3: Typical ramp rates for temperature scans on $\text{LiHo}_x\text{Er}_{1-x}\text{F}_4$ across the temperature range accessible in the dilution fridge.

crystals of $\text{LiHo}_x\text{Er}_{1-x}\text{F}_4$ which were made by Karl Krämer from the University of Bern. Information related to the sample preparation process and quality controls can be found in Appendix A. Measurements were also carried out on pieces cut from large single crystals, which were bought from a company which makes lasing materials (LiYF doped with $\sim 1\%$ Re is used in commercial lasers). In total, the temperature dependent AC susceptibility of 13 different compositions (in addition to LiHoF_4 and LiErF_4) has been measured down to ~ 30 mK. The compounds which have been measured are $x = 0.86, 0.79, 0.765, 0.70, 0.675, 0.57, 0.54, 0.50, 0.47, 0.25, 0.2, 0.1$ and 0.06

A general overview of the AC susceptibility data as a function of temperature for $x = 0.86, 0.765, 0.675, 0.57, 0.47, 0.2, 0.1$ and 0.06 is shown in Fig 4.3. The left column shows χ' and the right column shows χ'' at several frequencies, for each of the aforementioned compounds. The high temperature paramagnetic signal in χ' has been fit with a Curie-Weiss law to determine the background of the susceptometer coils (which changes slightly on each cool down) and subsequently subtracted from the data. The real susceptibility has then been normalised such that the maximum signal observed corresponds to 1 and the high temperature limit paramagnetic signal corresponds to zero. The imaginary signal has been adjusted so that in the paramagnetic region $\chi'' = 0$, and is on the same absolute scale as χ' .

The evolution of the samples is studied starting from large x , where the typical signatures of ferromagnetic order are observed. These consist of a frequency independent divergent peak in χ' corresponding to T_C and a sudden onset of χ'' at this temperature, peaking at a slightly lower temperature. The sudden onset of χ'' corresponds to the formation of domain walls in the ferromagnet and frequency dependent peak at lower temperatures corresponds to the motion of these domain walls. When $T < T_C$ there is frequency dependence in χ' , which, like that in χ'' , can also be attributed to domain wall motion in the sample. With the exception of $x = 0.9$, at low temperatures, a second frequency dependent peak in χ'' is observed at the lowest temperatures and corresponds to a plateau in χ' . As will be discussed later, this is likely due to the formation of a spin-glass inside the ferromagnetic super-structure. As x is decreased in this *embedded spin-glass phase*, T_C moves linearly with x to lower temperatures and the low temperature peak in χ'' broadens and moves to higher temperatures. The term embedded spin-glass is used instead of the more common re-entrant spin-glass, as it seems that in these compounds the spin-glass exists embedded inside the long range ferromagnetic order.

As x drops below ~ 0.6 , the long range ferromagnetism is suppressed and the peak position begins to depend on frequency – the system appears to be a spin-glass. It seems logical to

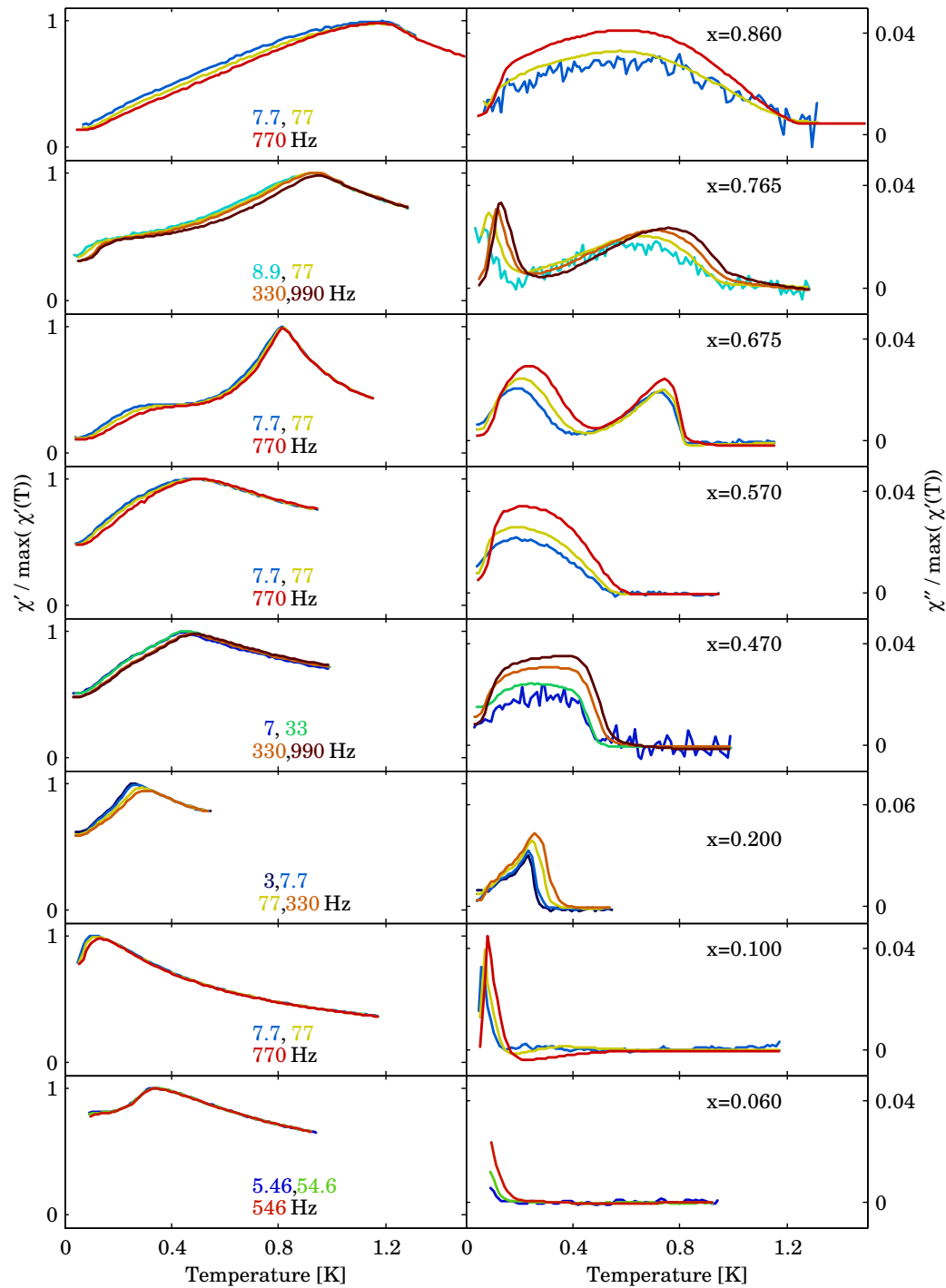


Figure 4.3: Overview of the AC susceptibility data for $x = 0.86, 0.765, 0.675, 0.57, 0.47, 0.2, 0.1$ and 0.06 . Moving from high to low x , the ferromagnetic peak is suppressed by the additional Er content, disappearing completely by $x = 0.57$. Frequency dependent behaviour is seen in all samples, in the form of an embedded spin-glass for $0.6 \lesssim x \lesssim 0.9$ and a more typical spin-glass for $x \lesssim 0.6$. The continual change in the shape of the features in the susceptibility hints at a complex and interesting phase diagram.

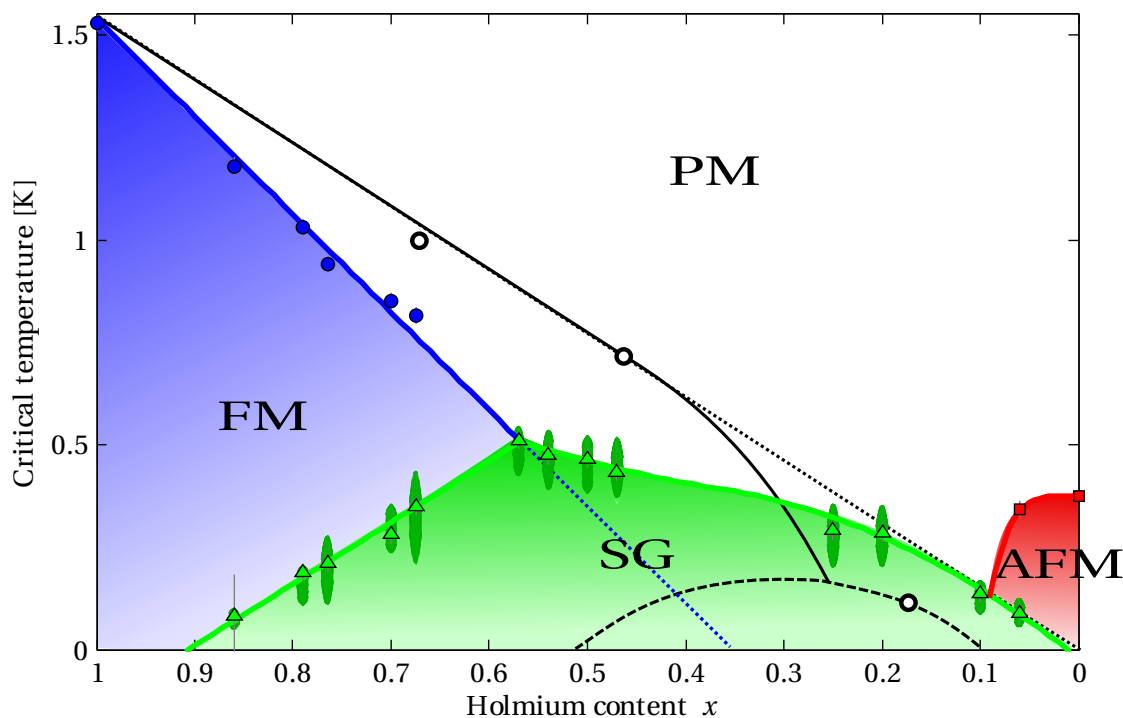


Figure 4.4: Experimental phase diagram of $\text{LiHo}_x\text{Er}_{1-x}\text{F}_4$. Blue circles indicate ferromagnetic order (T_C); red squares show antiferromagnetic order (T_N); green triangles indicate a spin-glass freezing (T_f). The small green ellipses show the range of T_f in the frequency range measured in each sample (typically 1-4 kHz).

assume that this spin-glass is dominated by the ferromagnetic Ho-Ho interactions and will be referred to as a *ferromagnetic spin-glass phase*. Interestingly, in the region around $x = 0.5$, both χ' and χ'' show very broad features below the initial freezing temperature T_f , which is unusual for a typical spin-glass. A reasonable hypothesis is that there are in fact two glassy transitions, a high temperature one corresponding to the freezing of the Ho moments and a low temperature one corresponding to the freezing of Er moments.

Finally, when x drops below 0.3, the shape of the susceptibility curves becomes very consistent with a canonical spin-glass [66]. Given the high concentration of Er spins and the fact that T_f is higher than in $\text{LiHo}_x\text{Y}_{1-x}\text{F}_4$ for a similar x , it is assumed that this spin-glass is primarily due to Er moments and shall therefore be called an *antiferromagnetic spin-glass phase*. At even lower x the spin-glass eventually gives way to the XY antiferromagnet state of LiErF_4 . It is not certain if there is some kind of an embedded/re-entrant spin glass state for $x < 0.1$, although initial data in an $x = 0.06$ sample points towards such a state.

These AC susceptibility results measured on powder samples form the basis on the experimental phase diagram of $\text{LiHo}_x\text{Er}_{1-x}\text{F}_4$, which is shown in Fig. 4.4. The phase diagram is complemented with the results from single crystal AC susceptibility and neutron scattering measurements, adding in a few more points. The ferromagnetic transitions are represented by

blue circles, the antiferromagnetic transitions by red squares and the spin-glass transitions by green triangles. The shaded regions give an idea to the extent in both T and x of each phase. As spin-glass transitions are frequency dependent, the points representing each spin-glass freezing temperature T_f is taken to be the temperature corresponding to the peak in χ' when measured at 1 kHz. Small ellipses underneath each spin glass transition point also show the frequency-dependant range of T_f measured in each sample (typically for frequencies between 1 Hz and 4 kHz). Superimposed on to this phase diagram is that of $\text{LiHo}_x\text{Y}_{1-x}\text{F}_4$ keeping the same x-axis as the fraction of Ho relative to Er / Y, which serves to indicate the much larger extent of the spin-glass region, both in temperature and in composition.

In order to produce the phase diagram, some key assumptions were made. The first is that for $x > 0.5$, a frequency independent peak in χ' with a sudden onset of χ'' corresponds to long range Ising ferromagnetic order, as seen in $\text{LiHo}_x\text{Y}_{1-x}\text{F}_4$. The second assumption is that a frequency independent peak in χ' for small x corresponds to XY antiferromagnetic order, like in LiErF_4 . The final assumption is that a frequency dependent peak in the susceptibility which can clearly be distinguished from either type of long range order is an indication of a spin-glass state. For the time being, no assumption is made about the nature of the spin-glass and is considered to be equivalent for all x .

4.3 Tools for Detailed Investigation

In order to better understand some of the key regions of the phase diagram, additional AC susceptibility measurements are complemented by elastic neutron scattering measurements and mean-field calculations. Elastic neutron scattering measurements were performed on samples of $x = 0.8, 0.5$ and 0.25 in order to determine whether any long-range order is present and characterise the magnetic correlations in the system. Mean-field calculations were also performed and compared to the data obtained from the neutron scattering and additional AC susceptibility measurements. This section details the neutron scattering technique and experiments along with the mean-field calculations.

4.3.1 Neutron Scattering

One of the triumphs of early quantum mechanics was the realisation that particles can behave like waves, with the de Broglie wavelength given by:

$$\lambda = \frac{h}{mv}, \quad (4.6)$$

where v is the velocity of the particle and m its mass. This implies that particles with an appropriate mass and velocity can be scattered via a periodic array of atoms found in a crystal, just like x-rays. Crystallographic diffraction is typically expressed in terms of Bragg's law:

$$n\lambda = 2d \sin\theta, \quad (4.7)$$

where n is the order of diffraction, λ is the wavelength of the particle, d is the spacing between atoms in the crystal, and θ is the scattering angle.

Neutrons with energies between 5 and 25 meV are easily produced via the *moderation* of neutrons produced in nuclear reactors and are very useful probes in condensed matter physics for the following reasons:

- The wavelengths of such neutrons (2–4 Å) is comparable to interatomic distances in solids and liquids, and therefore allows for crystallographic diffraction.
- The energy of these neutrons is similar to the energy scale of many excitations in condensed matter systems. As a neutron interacts with a system it can gain or lose energy via the creation or annihilation of an excitation. Therefore a measurement of the neutron energy can give information on the excitation energy.
- The neutron has a spin $s = 1/2$ and therefore a magnetic dipole moment $\mu_n = -1.913 \mu_N$, where $\mu_N = 5.051 \times 10^{-27} \text{ J T}^{-1}$ is the nuclear magneton. This dipole moment allows neutrons to interact with magnetic moments in a sample, giving information not only on its structure, but also its magnetic structure.
- Neutrons are neutral particles, so interact only via short range nuclear forces, and can penetrate deep into matter. This means that unlike charged particles (e.g. electrons), they measure the bulk properties deep inside the material. They are also insensitive to the total charge of an atom, so, unlike x-rays, can measure very light atoms and more easily distinguish between atoms of very different masses.

Two very good books which introduce neutron scattering are those by Squires [88] and Lovesey [53], with the former slightly more focused on experimental aspects and the latter on the theory.

4.3.1.1 Theory

A neutron scattering experiment essentially consists of illuminating a sample with a beam of neutrons with a known energy and momentum and measuring their final energy and momentum. The fraction of neutrons scattered is related to the *scattering cross-section* of the system, which simply defines that system's ability to scatter neutrons. If there is an initial flux of Φ_0 neutrons, which are scattered into a solid angle $d\Omega$, as a function of their energy E , the *partial differential scattering cross-section* is:

$$\frac{d^2\sigma}{dE'd\Omega} = \frac{\text{no. of neutrons scattered per sec. into } d\Omega, \text{ with energies } [E'; E' + dE']}{\Phi_0 dE' d\Omega}. \quad (4.8)$$

The task at hand in understanding neutron scattering experiments is therefore calculating the various cross-sections resulting from the physical phenomena in condensed matter systems.

In order to do this in a meaningful way, the neutrons and the sample must be treated quantum mechanically. The beam of neutrons is initially in the state $|\mathbf{k}, \sigma\rangle$ and by interacting with the sample gets transformed into the final state $|\mathbf{k}', \sigma'\rangle$. This interaction also transforms the target from an initial state $|i\rangle$ to the final state $|f\rangle$. A perfectly collimated and monochromatic neutron beam can be approximated as a plane wave:

$$|\mathbf{k}, \sigma\rangle = \frac{1}{\sqrt{V}} e^{i\mathbf{k}\cdot\mathbf{r}} |\sigma\rangle. \quad (4.9)$$

Using this approximation, combined with Fermi's Golden rule, allows for the partial differential scattering cross-section for any scattering event to be written as:

$$\frac{d^2\sigma}{dE'd\Omega} = \frac{k'}{k} \left(\frac{m_n}{2\pi\hbar^2} \right)^2 \sum_{if} P_i |\langle \mathbf{k}, \sigma; i | V(\mathbf{Q}) | \mathbf{k}', \sigma'; f \rangle|^2 \delta(\hbar\omega - E_f - E_i), \quad (4.10)$$

where $\frac{k'}{k} \left(\frac{m_n}{2\pi\hbar^2} \right)^2$ is a normalisation term, P_i is the probability of the neutron and sample being in the initial state, $V(\mathbf{Q})$ is the interaction potential between the neutron and sample, E_f and E_i are respectively the final and initial energy of the sample. Two terms in this equation which arise in practically every single neutron experiment are the wave vector transfer \mathbf{Q} and the energy transfer $\hbar\omega$:

$$\text{Wave vector transfer: } \mathbf{Q} = \mathbf{k}' - \mathbf{k}. \quad (4.11)$$

$$\text{Energy transfer: } \hbar\omega = E' - E = \frac{\hbar^2 k'^2}{2M} - \frac{\hbar^2 k^2}{2M}. \quad (4.12)$$

Results from neutron experiments are typically expressed in terms of these two quantities. The three dimensional \mathbf{Q} describes where the scattering originates from in reciprocal space and $\hbar\omega$ the energy transferred to the neutron from the sample. In this way, all neutron scattering data is essentially a 5 dimensional data set representing scattered intensity as a function of (\mathbf{Q}, ω) .

All of the information on the sample comes from the interaction potential, which gives rise to different cross-sections for different physical phenomena and configurations. Neutrons

4.3 Tools for Detailed Investigation

can interact with matter in essentially two ways, either with the nuclei in a material, giving rise to the *nuclear cross-section*, or via the dipole interaction with electrons, giving rise to the *magnetic cross-section* (for a full derivation of the cross-sections, see for example [88]).

The nuclear scattering results from interactions with the nuclei and is normally expressed as the sum of two cross-sections, the *coherent cross-section* and the *incoherent cross-section*. The coherent cross-section is given by:

$$\left(\frac{d^2\sigma}{dE d\Omega} \right)_{coh} = \frac{k'}{k} \frac{1}{2\pi\hbar^2} \sum_{jj'} \overline{b_j b_{j'}} \int \langle e^{i\mathbf{Q}\cdot\mathbf{R}_j(t)} e^{-i\mathbf{Q}\cdot\mathbf{R}_{j'}(0)} \rangle e^{-i\omega t} dt, \quad (4.13)$$

where $\overline{b_j}$ is the average scattering length of the element at position \mathbf{R}_j . This cross-section depends on the correlations between the same nucleus at different times and also the correlations between different nuclei at different times, and can therefore give rise to interference effects.

The incoherent cross-section is given by:

$$\left(\frac{d^2\sigma}{dE d\Omega} \right)_{inc} = \frac{k'}{k} \frac{1}{2\pi\hbar^2} \sum_j (\overline{b_j^2} - \overline{b_j}^2) \int \langle e^{i\mathbf{Q}\cdot\mathbf{R}_j(t)} e^{-i\mathbf{Q}\cdot\mathbf{R}_j(0)} \rangle e^{-i\omega t} dt, \quad (4.14)$$

and only depends on correlations between the same nucleus at different times and therefore cannot give rise to interference effects.

These two cross-sections can be thought of in a more experimental language. The coherent cross-section gives rise to diffraction from the structure, leading to Bragg peaks in the case of a crystalline sample. Incoherent scattering on the other hand scatters neutrons isotropically, and independently of their arrangement within a material, and gives rise to a background signal.

The magnetic cross-section due to interactions between the neutron and electrons in a material is given by:

$$\frac{d^2\sigma}{dE d\Omega} = \frac{k'}{k} (\gamma r_0)^2 \overbrace{\left| \frac{g}{2} f(\mathbf{Q}) \right|^2}^1 \overbrace{e^{-2W(\mathbf{Q})}}^2 \overbrace{\sum_{\alpha\beta} (\delta_{\alpha\beta} - \hat{Q}_\alpha \hat{Q}_\beta)}^3 \times \int dt e^{-i\omega t} \sum_{jj'} e^{i\mathbf{Q}(\mathbf{R}_j - \mathbf{R}_{j'})} \underbrace{\langle S_j^\alpha(0) S_{j'}^\beta(t) \rangle}_4. \quad (4.15)$$

In this equation, there are several important factors:

1. The squared magnetic form factor $\left|\frac{g}{2}f(\mathbf{Q})\right|^2$, which describes the spatial distribution of the electron orbitals that form the moments.
2. The Debye-Waller factor $e^{-2W(\mathbf{Q})}$, which takes into account lattice vibrations that can transfer some of the coherent scattering into incoherent scattering.
3. A polarisation factor $\sum_{\alpha\beta}(\delta_{\alpha\beta} - \hat{\mathbf{Q}}_\alpha\hat{\mathbf{Q}}_\beta)$ due to the dipolar interaction between the neutron and the magnetic moment. This term implies that it is only components of the moment which are perpendicular to the scattering vector which contribute to the cross-section.
4. The position and time dependent spin-spin correlation function $\langle S_l^\alpha(0)S_l^\beta(t) \rangle$.

In practice, it is not possible to create the ideal collimated and monochromatic beams which give rise to the cross-sections stated above. To understand experimental results, it is important to keep in mind that there will be a finite distribution of both the beam divergence and the neutron energy. This results in a measured intensity which is given by the convolution of the scattering cross-section and the experimental resolution, and can be written as:

$$I(\mathbf{Q}, \omega) = \int \frac{d^2\sigma}{dE d\Omega} \Big|_{\kappa', \omega'} R(\mathbf{Q}, \omega; \mathbf{Q}' - \mathbf{Q}, \omega' - \omega) d\mathbf{Q}' d\omega', \quad (4.16)$$

where $R(\mathbf{Q}, \omega; \mathbf{Q}' - \mathbf{Q}, \omega' - \omega)$ expresses the probability that a nominal scattering condition specified by \mathbf{Q} and ω will result in a measurement of a neutron with $\mathbf{Q}' = \mathbf{Q} + \Delta\mathbf{Q}$ and $\omega' = \omega + \Delta\omega$. This leads to the very important observation that in neutron scattering from magnetic materials, the scattered intensity gives information on the spin-spin correlations

4.3.1.2 Instruments

Of the many possible neutron instruments, each specialised for a specific type of measurement, the two which have been used to measure samples of $\text{LiHo}_x\text{Er}_{1-x}\text{F}_4$ will be briefly outlined. The first is E4 at HZB (Berlin, Germany), a thermal neutron diffractometer and the second is RITA-II at PSI (Villigen, Switzerland), a cold neutron triple axis spectrometer.

A diffractometer is one of the simplest neutron scattering instruments in use. The basic idea involves sending a monochromatic and collimated beam of neutrons to the sample. They will interact with the sample and be scattered into a detector, allowing for the \mathbf{Q} dependence of the scattering to be measured. It is important to note that with a diffractometer, the elastic and inelastic neutron scattering processes are measured simultaneously – it is the energy integrated spectrum which is measured.

A simplified schematic representation of E4 is shown in Fig. 4.5. A beam of thermal neutrons with a Maxwellian distribution of wavelengths centred around the moderator temperature are diffracted by a monochromator. This device works on the principle of Bragg scattering,

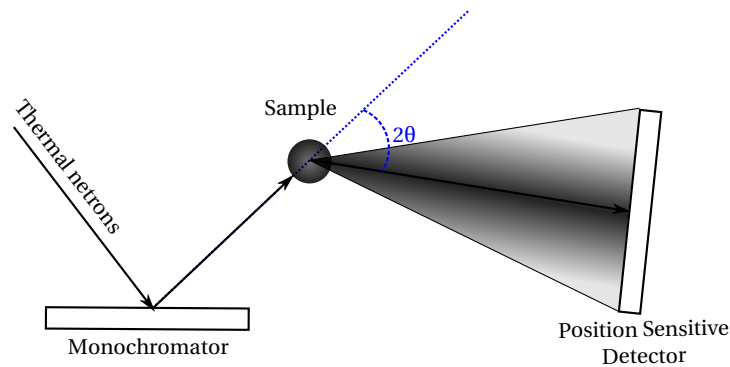


Figure 4.5: Schematic of the E4 diffractometer.

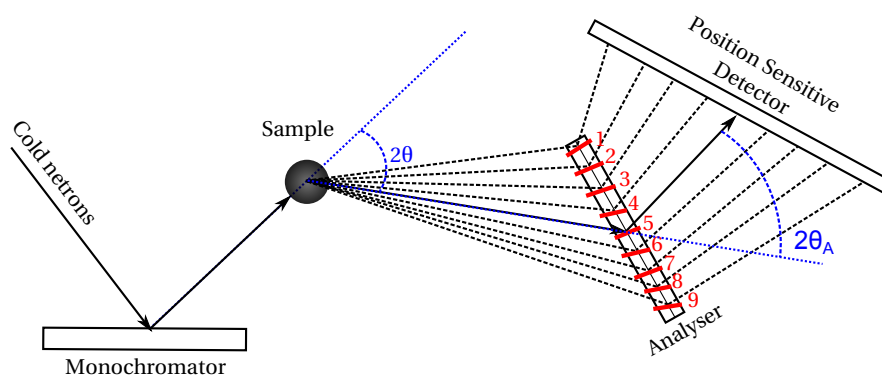


Figure 4.6: Schematic of the RITA-II triple axis spectrometer.

by tuning the angle between the beam and the monochromator, the desired wavelength of neutrons to be scattered to the sample can be selected. These neutrons will then travel to the sample where, if they meet the scattering condition, will be scattered into the detector. In the case of E4, a position sensitive detector is used, which allows for a small region of \mathbf{Q} -space, centred around the \mathbf{Q} corresponding to the scattering angle, to be measured.

A triple axis spectrometer is essentially a diffractometer with an additional analyser between the sample and the detector. The analyser works in the exact same way as a monochromator and can be used to diffract only neutrons with a particular energy into the detector. While these devices are typically used for spectrometry, they also offer benefits when operated as a diffractometer. Specifically, only the inelastic scattering processes which are of an energy lower than the energy resolution will be detected, reducing the intensity of the background. This is particularly useful in systems such as spin-glasses where there is no long range order, so the magnetic scattering is typically *diffuse* (spread out over a large range of \mathbf{Q}) and of relatively weak intensity.

RITA-II is not an ordinary triple axis spectrometer; it has been designed specifically to be more efficient with its use of neutrons. This is achieved by including not just one analyser, but 9 analyser blades which diffract onto separated regions of a position sensitive detector, as can be seen in Fig. 4.6. For the experiments presented in the following sections, the blades are

configured such that they all select the same energy of neutrons, so that up to 9 Q values can be measured simultaneously.

4.3.1.3 Sample Environment

Despite the large scale of neutron scattering sources, the neutron beams produced have very low fluxes, with brightnesses roughly 10^{10} times less than those found in x-ray synchrotron facilities. The net result of this is that experiments are flux limited – the majority of time in most experiments is spent waiting to count enough neutrons to have meaningful statistics. The only way to reduce experiment times is to use large samples, typically on the order of cm^3 . This requirement, coupled with the relatively short amounts of time available for an experiment (on the order of several days) presents a problem for measuring poor thermally conducting LiReF_4 samples at ultra low temperatures.

The solution is to engineer the samples towards good thermal conductivity at the expense of the *mosaicity* (the co-alignment of several pieces of sample). To elaborate on how this is done, the procedure from the starting single crystal to the final sample is explained in detail. Typically, a sample to be measured starts out as a ~ 15 mm diameter and ~ 40 mm long cylinder, which has been grown along a crystallographic axis of choice (to within 2°). The sample is glued onto a goniometer and the alignment verified and improved using a Multiwire laboratories x-ray Laue camera [64]. While remaining glued to the goniometer, the crystal is cut into several wafers (typically 5-8) with dimensions of roughly $40 \times 10 \times 1$ mm. The wafers are cleaned in acetone and gold sputtered, covering all surfaces with a layer of $2\text{--}3 \mu\text{m}$ of gold. This thin layer of gold greatly improves the thermal conductivity between the layers, and between the sample and sample holder.

The sample holder consists of a thin walled copper *coffin* machined out of a single piece of oxygen free high conductivity (OFHC) copper. The wafers are placed into the sample holder one at a time, with a $50 \mu\text{m}$ thick copper foil separating each one. Once all of the wafers have been placed inside the sample holder, the ends of the copper foils are screwed down to the sample holder. With all the wafers inside the sample holder, a copper lid is screwed down tightly, which squeezes all the wafers together, quite possibly cracking them. The entire sample holder is made only from copper, on the one hand to keep the thermal conductivity high and on the other hand reduce the number of *powder lines*¹ observed in the neutron scattering experiment. In order to reduce the background, the top and bottom of the sample holder, which contain a large mass of copper, are covered in a neutron absorbing material such as gadolinium oxide paint or cadmium foil. Photos of selected sample holders used for measurements on $\text{LiHo}_x\text{Er}_{1-x}\text{F}_4$ samples are shown in Fig. 4.7. The beauty of this design ensures that each 1 mm thick wafer is well thermalised to the copper sample holder, decreasing thermalisation times by at least a factor of 10 (compared to using a single crystal).

¹Any non-single crystal material in the neutron beam will create a powder line at a Q value corresponding to the interatomic spacings in that material. Reducing the number of materials in the beam reduces the number of parasitic powder lines, making the data easier to analyse.

4.3 Tools for Detailed Investigation

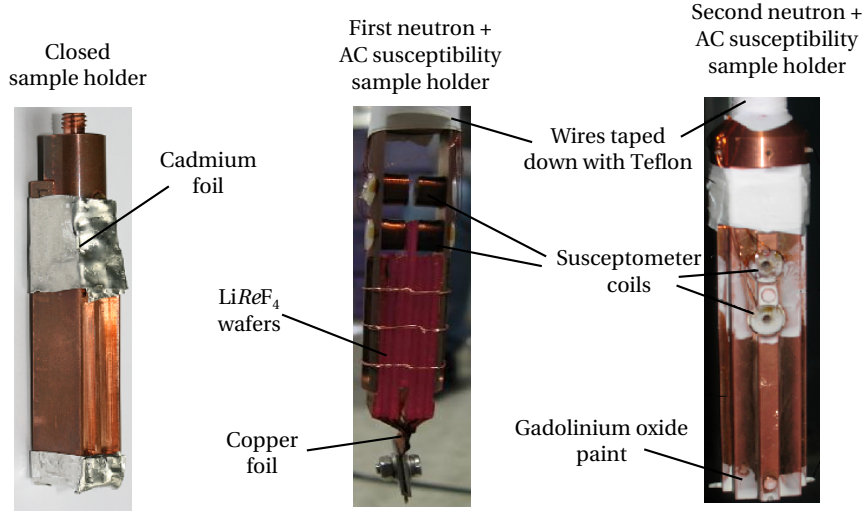


Figure 4.7: Photos of the neutron experiment sample holders. [left] Closed sample holder for the experiment on $x = 0.50$. [centre] Photo illustrating the configuration of the sample and susceptometer coils for *in-situ* AC susceptibility measurements. [right] closed sample holder for experiment on $x = 0.25$ including *in-situ* AC susceptibility.

In the neutron scattering experiment measuring $\text{LiHo}_{0.25}\text{Er}_{0.75}\text{F}_4$, where the system shows typical spin-glass behaviour, the AC susceptibility was measured simultaneously *in-situ*. This was done as spin-glasses typically show path dependent behaviour which makes it difficult to compare measurements taken on different samples in different environments. This was achieved by making the central wafer longer than the others by 1cm and placing a home-made superconducting *split-coil susceptometer* around it. The central photo in Fig. 4.7 shows the cross-section of the sample and coils in the sample holder used for a different experiment. The sample holder in this photo was not rigid enough and the experiment was not successful as a result. For the measurements on $x = 0.25$, the sample holder was made much more rigid as can be seen in the photo on the right in Fig. 4.7.

4.3.2 Mean-Field Calculations

The mean-field (MF) approximation seeks to simplify two-spin interactions by replacing them with a single spin interaction with a *bath* which includes the surrounding spins. In the case of a simple ferromagnet in an external field \mathbf{H} , the Hamiltonian can be written as follows:

$$\mathcal{H} = g\mu_B \sum_i \mathbf{J}_i \cdot \mathbf{H} - \frac{1}{2} \sum_{ij} \mathcal{J}_{ij} \mathbf{J}_i \cdot \mathbf{J}_j. \quad (4.17)$$

The mean-field approximation consists of replacing $\mathbf{J}_i \cdot \mathbf{J}_j$ by:

$$\mathbf{J}_i \cdot \mathbf{J}_j = (\mathbf{J}_i - \langle \mathbf{J}_i \rangle) \cdot (\mathbf{J}_j - \langle \mathbf{J}_j \rangle) + \mathbf{J}_i \cdot \langle \mathbf{J}_j \rangle + \mathbf{J}_j \cdot \langle \mathbf{J}_i \rangle - \langle \mathbf{J}_i \rangle \cdot \langle \mathbf{J}_j \rangle. \quad (4.18)$$

As the MF approximation neglects fluctuations of moments around their mean values, the first term in this equation is neglected.

If an effective field:

$$h_i^{eff} = h + \sum_j \mathcal{J}_{ij} \langle \mathbf{J}_j \rangle, \quad (4.19)$$

where $h = g\mu_B\mathbf{H}$, is introduced then the MF Hamiltonian \mathcal{H}_{MF} can be written :

$$\mathcal{H}_{MF} = - \sum_i \mathbf{J}_i \cdot h_i^{eff} + \frac{1}{2} \sum_i \langle \mathbf{J}_i \rangle \cdot (h_i^{eff} - h). \quad (4.20)$$

Choosing a value for $\langle \mathbf{J}_j \rangle$ allows the effective field to be calculated, and, as long as $\langle \mathbf{J}_i \rangle$ has some arbitrary initial value, \mathcal{H}_{MF} for the i^{th} site can also be calculated. Diagonalising the Hamiltonian gives the corresponding $\langle \mathbf{J}_i \rangle$ for this mean-field for each site, which is used to calculate the new effective field. The Hamiltonian is now a self-consistent equation – the process must simply be repeated until the expectation values of the moments converge. In the case of a ferromagnet, the result is a non-zero magnetization which describes the spontaneous magnetic ordering.

4.3.2.1 Virtual Crystal Mean-Field (VCMF) Calculations

Applying the MF approximation to the LiReF_4 , the Hamiltonian introduced in Eq. 4.1 is replaced with a Hamiltonian for each of the 4 sites i within a unit cell:

$$\mathcal{H}_i^{MF} = \mathbf{J}_i \cdot \mathbf{H}_i + \mathcal{H}_{CF} + A\mathbf{J}_i \cdot \mathbf{I}_i - g\mu_B\mathbf{J}_i \cdot \mathbf{H}. \quad (4.21)$$

The difference between the two Hamiltonians is that in \mathcal{H}_i^{MF} the interactions between magnetic moments have been replaced by the mean-field \mathbf{H}_i :

$$\mathbf{H}_i = \sum_{j(i)} \mathcal{J}_{ex} \langle \mathbf{J}_j \rangle + \sum_j \frac{\mu_0}{4\pi} (g_L\mu_B)^2 \overline{\overline{D}}_{ij}(\mathbf{q}=0) \langle \mathbf{J}_j \rangle, \quad (4.22)$$

where $j(i)$ runs along nearest neighbours (NN) and $\overline{\overline{D}}_{ij}(\mathbf{q}=0)$ is a 3×3 tensor defined as:

$$\overline{\overline{D}}_{ij}(\mathbf{q}=0) = \frac{N}{V} \left(\frac{4\pi}{3} + \mathcal{D}_{ij}^L - \overline{\overline{N}}_{ij} \right), \quad (4.23)$$

where N/V is the normalisation factor, $4\pi/3$ is the Lorentz factor, \mathcal{D}_{ij}^L is the lattice sum of the dipole-dipole interaction and $\overline{\overline{N}}_{ij}$ is the demagnetisation factor. In the routine, \mathcal{D}_{ij}^L is calculated by a direct summation over a sphere with a diameter of 100 unit cells. The Lorentz

4.3 Tools for Detailed Investigation

factor is a correction which takes into account the difference between summing \mathcal{D}_{ij}^L over a finite sized sphere and summing over an infinite sample.

In order to apply this Hamiltonian to $\text{LiHo}_x\text{Er}_{1-x}\text{F}_4$, where there are two different species of ions present, one approach is the so-called *virtual crystal approximation* [23]. In this approximation the magnetic moment operator is written as a sum of the two species of ions:

$$\mathbf{J}_i = x_i \mathbf{J}_i^{\text{Ho}} \oplus (1 - x_i) \mathbf{J}_i^{\text{Er}}. \quad (4.24)$$

This naturally leads to the *virtual crystal mean-field* (VCMF) Hamiltonian:

$$\mathcal{H}_{i,t}^{\text{VCMF}} = \mathbf{J}_i^t (x_i \mathbf{H}_i^{\text{Ho}} + (1 - x_i) \mathbf{H}_i^{\text{Er}}) + \mathcal{H}_{CF}^t + A_t \mathbf{J}_i^t \cdot \mathbf{I}_i^t, \quad (4.25)$$

where t is the index representing the ion type and \mathbf{H}_i^t is the self-consistent mean-field for site i and ion type t .

The algorithm implemented can be summarised as follows:

1. Initialise the mean moments $\langle \mathbf{J}_i \rangle$ within the unit cell (for example random values).
2. The system loops the following sequence until the mean moments $\langle \mathbf{J}_i \rangle$ converge. For the n^{th} step:
 - (a) The mean-field resulting from the mean moment is calculated.
 - (b) The mean-field Hamiltonians $\mathcal{H}_i^{\text{MF}}$ are diagonalized and the mean moments are updated with the result.
 - (c) The change is evaluated $c^n = \sum_i |\langle \mathbf{J}_i \rangle^n - \langle \mathbf{J}_i \rangle^{n-1}|$ and compared to a threshold ϵ :

If $c^n < \epsilon$, break loop
Else, return to 2 for iteration $n + 1$

4.3.2.2 Inhomogeneous Mean-Field (iMF) Calculations

One limitation of the virtual crystal method described above is that the disorder in the system due to the random positions of the different rare-earth ions is neglected. This is particularly important as this disorder is a key ingredient required to form a spin-glass. An improved calculation is the so-called *inhomogeneous mean-field* [23], which has been developed and implemented at LQM by B. Dalla Piazza. In this implementation, a “real” crystal lattice is built up and populated with the correct ratio of Ho:Er. Due to the simplicity of the mean-field approximation this calculation can be carried out on very large lattices, consisting of over a hundred thousand unit cells.

The algorithm can be summarised as follows:

1. A lattice is allocated by randomly populating the sites according to the doping ratio x in $\text{LiHo}_x\text{Er}_{1-x}\text{F}_4$.
2. The mean moments $\langle \mathbf{J}_i \rangle$ are initialised in a random configuration.
3. The following loop is repeated until convergence is reached. For the n^{th} step:
 - (a) For each site i :
 - i. The mean-field Hamiltonian \mathcal{H}^{MF} is calculated according to the site ion type.
 - ii. The Hamiltonian is diagonalised and the mean moment is calculated and updated
 - iii. The change between iterations $c_i^n = |\langle \mathbf{J}_i \rangle^n - \langle \mathbf{J}_i \rangle^{n-1}|$ is calculated.
 - (b) After all sites have been updated, the mean individual change is compared to the threshold ϵ :

If $\frac{1}{N} \sum_i c_i^n < \epsilon$, break loop
 Else, return to 3 for iteration $n + 1$

4.4 Embedded Spin-Glass

Detailed investigations on the embedded spin-glass compounds focussed on three key features of these samples. First, neutron scattering studies were performed in order to characterise the ferromagnetic state and investigate the possibility of a quantum phase transition in a transverse field. Second, neutron scattering and AC susceptibility were used to try to understand spin-glass phase in the system. Finally, a theoretical investigation of the behaviour of T_c as a function of x was performed in order to explain the difference in slope when compared with $\text{LiHo}_x\text{Y}_{1-x}\text{F}_4$.

4.4.1 Ferromagnetic State

Neutron scattering measurements were performed on a single crystal of $\text{LiHo}_{0.79}\text{Er}_{0.21}\text{F}_4$ with dimensions of 5 x 5 x 30 mm cut into four wafers each ~ 1.2 mm thick. The crystal was aligned with the length along the $(1\bar{1}0)$ crystallographic direction with the c-axis perpendicular to the length. The sample was placed in a dilution fridge with a vertical magnet allowing for temperatures down to 50 mK and fields up to 5 T, with the scattering plane perpendicular to the length of the crystal. The incoming neutrons for the measurements had a wavevector of 2.59 \AA^{-1} .

The magnetic long range order has been confirmed by measuring the $(2,2,0)$ and $(1,1,2)$ nuclear Bragg peaks at 1.75 K, 0.05 K in 0 T and 0.05 K in 5 T, as shown in Fig. 4.8. The scans were taken

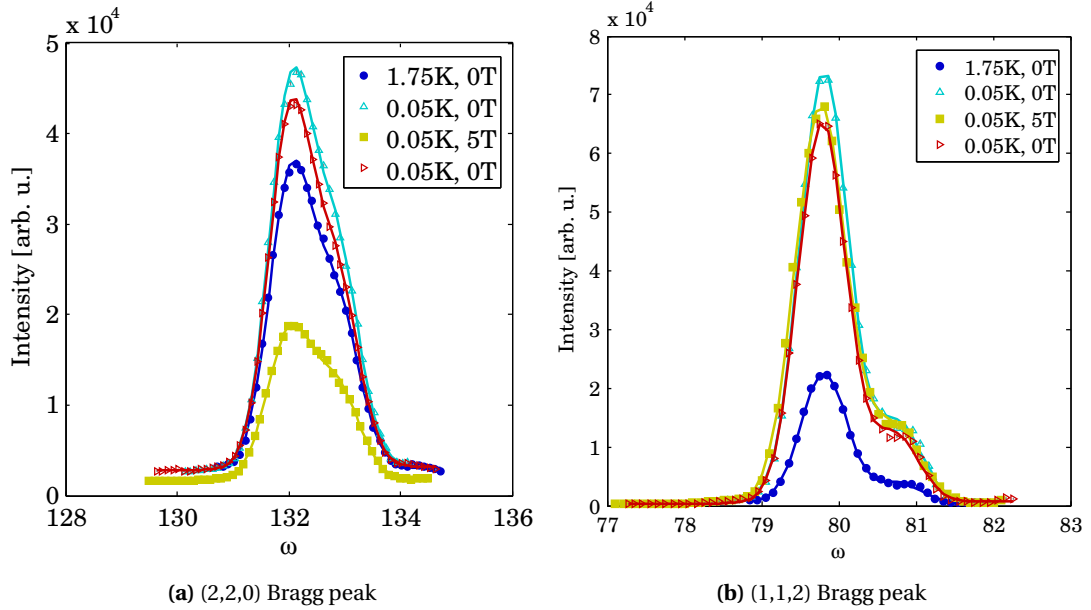


Figure 4.8: ω -scans across the (a) (2,2,0) and (b) (1,1,2) Bragg peaks in several field-temperature configurations in $\text{LiHo}_{0.79}\text{Er}_{0.21}\text{F}_4$.

centred around the aforementioned Bragg peaks, with the intensity measured as a function of ω , the arbitrarily defined sample rotation, which roughly corresponds to a scan transversal to \mathbf{Q} . The intensity of the Bragg peaks (but not their width) increases at low temperature, indicating long range order. The fact that the magnetic scattering is seen at nuclear Bragg peak positions implies the spins have ferromagnetic correlations. In field, the two peaks behave differently, with the (2,2,0) peak intensity decreasing to *below* that at high temperatures and the (1,1,2) remaining constant.

The (2,2,0) Bragg peak was measured as a function of field to understand its strange behaviour, which seemingly implies that the crystal structure is continuously destroyed by the application of a field. Every 0.2 T between 0 and 5 T, the Bragg peak was measured and the resulting fit parameters for the Gaussian peak are shown in Fig. 4.9. The intensity begins to decrease for even small applied fields and does not seem to follow a conventional order parameter curve. When H passes roughly 3 T, the intensity decreases linearly with applied field. The peculiar field dependence does not seem to be related to bad fits of the data, as both the FWHM and the position do not change significantly. Surprisingly, the background measured follows a nearly identical decrease with field as the intensity of the peak.

It is supposed that the most likely reason for such unusual behaviour is that the detector is being adversely affected by the magnetic field. The net result is that the detector efficiency decreases with field. In order to interpret the data measured on the (2,2,0) peak in field, the efficiency of the detector was modelled as a 2nd order polynomial as a function of the applied field. The intensities were then scaled by this polynomial at each field measured giving the

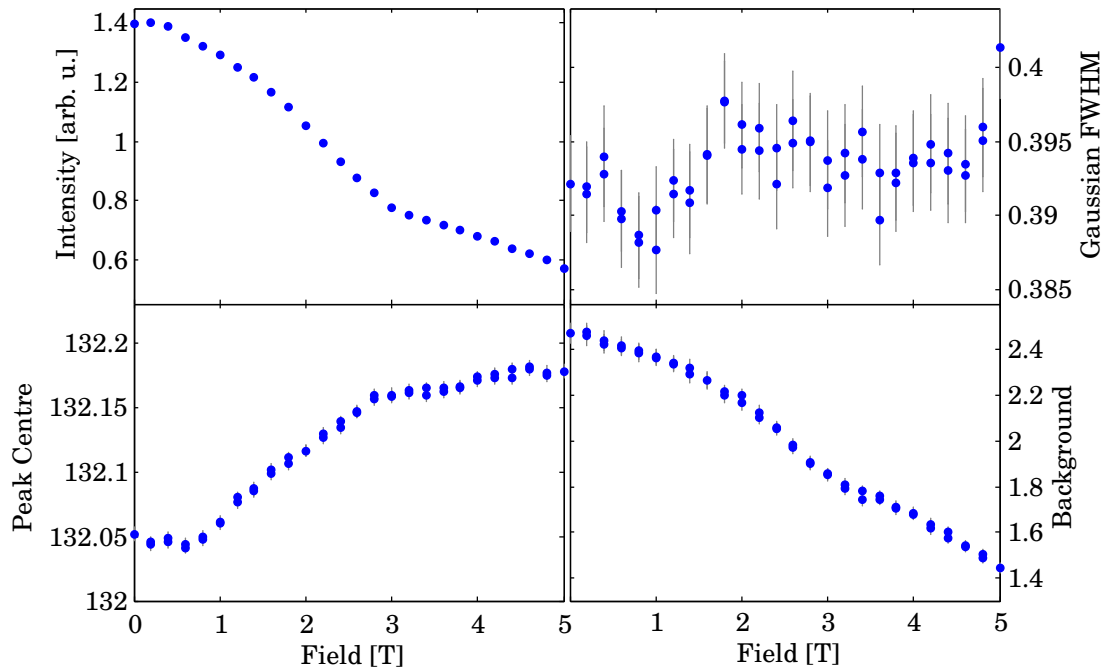


Figure 4.9: H_a field dependence of the (2,2,0) Bragg peak in $\text{LiHo}_{0.79}\text{Er}_{0.21}\text{F}_4$ without any corrections to the data. From the top left window moving clockwise, the panels show the integrated intensity of the peak, the FWHM, the background signal and the peak centre.

true scattered intensity. The raw data (blue circles) is compared with the efficiency corrected data (red triangles) in Fig. 4.10. The result of this scaling is that the background (left side of the figure) becomes much flatter and the intensity of the Bragg peak shows a mean-field-like order parameter. Interestingly, the (1,1,2) Bragg peak, which has also been measured in field does not seem to show this effect. The background signal stays relatively flat, indicating that if there is a change in the efficiency of the detection system it clearly depends on the geometry of the diffractometer.

The field dependence of the (1,1,2) and (2,2,0) Bragg peaks are shown in Fig 4.11. In order to place the behaviour of both peaks on to the same scale, the left axis and corresponding blue points indicates the intensity of the (1,1,2) peak and the right axis the (2,2,0) peak. The intensity of the peaks has been normalised to the nuclear intensity, such that an integrated intensity of 1 corresponds to a purely nuclear peak. The (2,2,0) Bragg peak shows a continuous reduction of the intensity, and thus the magnetisation, which is indicative of a quantum phase transition at $H_C = 3.25$ T. The scans also indicate hysteresis behaviour between ramping the field up from a zero field cooled state (green triangles) and ramping the field back down (red squares), similar to observations in $\text{LiHo}_{0.67}\text{Y}_{0.33}\text{F}_4$ [48]. The data quality is not good enough to determine precisely the value of H_C or begin to infer information about the transition, such as critical exponents.

The (1,1,2) field dependence is somewhat more complicated, but can be explained by the fact

4.4 Embedded Spin-Glass

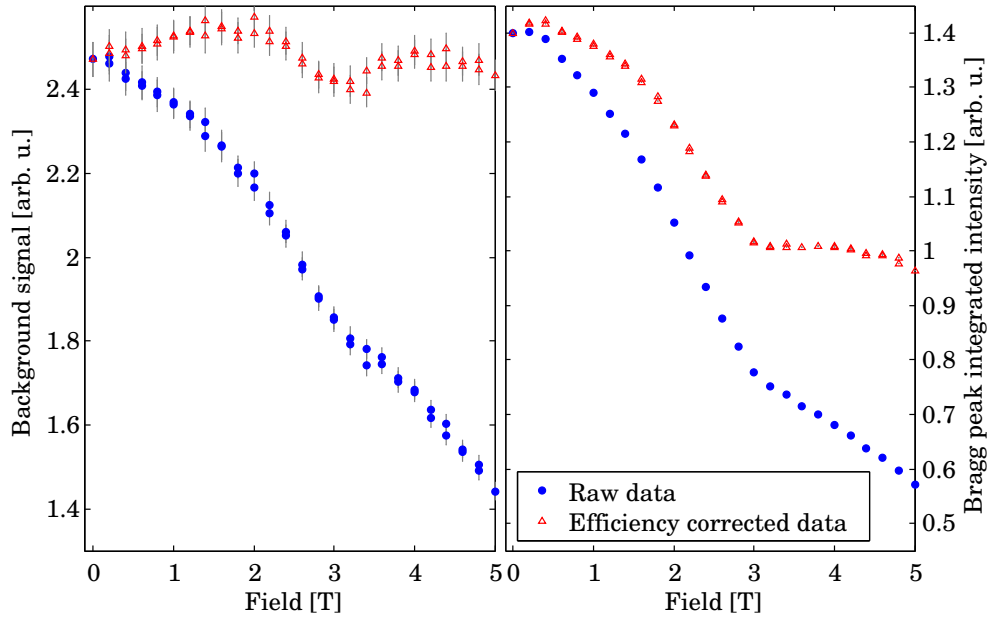


Figure 4.10: H_a field dependent detector efficiency correction for the (2,2,0) Bragg peak at e4. The left panel shows the intensity of the background extracted from fitting the Bragg peak and the right panel the extracted integrated intensity. By assuming the detector efficiency is affected by field, the data become more reasonable (red triangles).

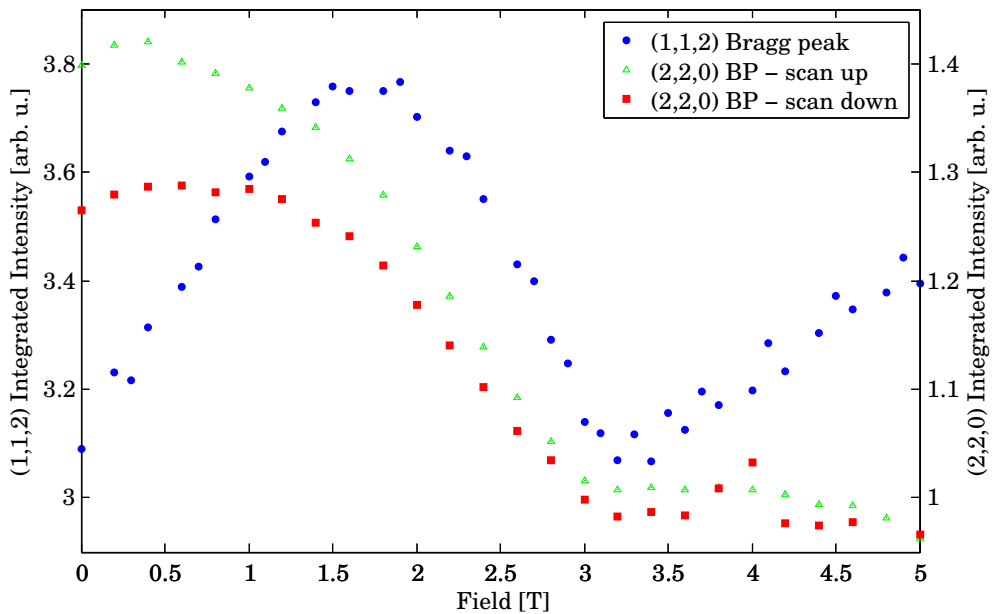


Figure 4.11: H_a field dependence of the (1,1,2) (left axis) and (2,2,0) (right axis) Bragg peaks in $\text{LiHo}_{0.79}\text{Er}_{0.21}\text{F}_4$.

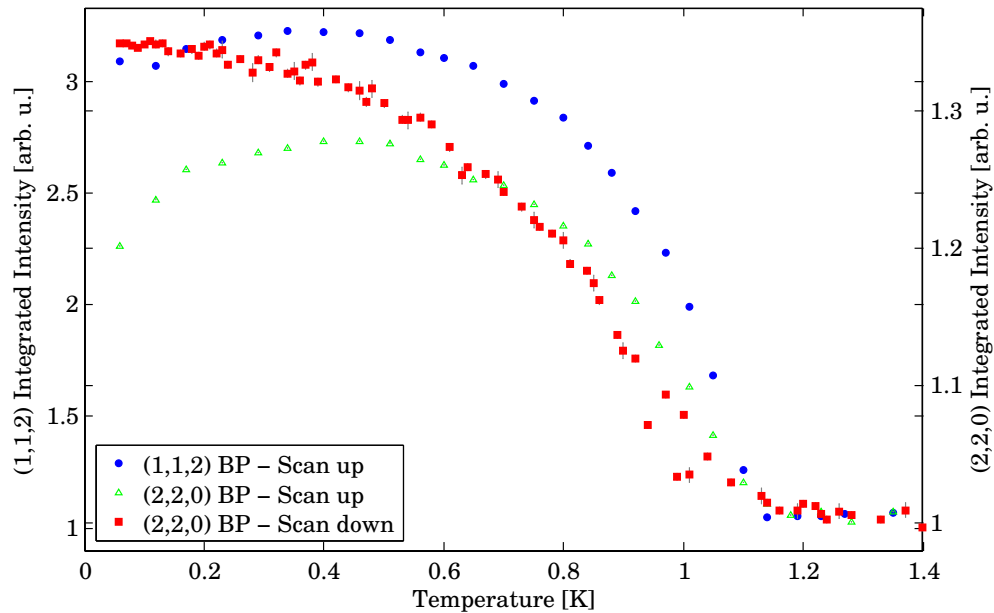


Figure 4.12: Temperature dependence of the (1,1,2) (left axis) and (2,2,0) (right axis) Bragg peaks in $\text{LiHo}_{0.79}\text{Er}_{0.21}\text{F}_4$.

that a component of the magnetic moment lies along the scattering direction. As the neutrons are not sensitive to magnetic moments which are parallel to the scattering direction, the signal starts to grow as the field begins to polarise the spins perpendicular to the scattering plane. As the long range order is destroyed, and the intensity of the (2,2,0) peak begins to decrease rapidly, the intensity of the (1,1,2) peak drops, resulting in a minimum at the H_C found by studying the (2,2,0) peak. As the field increases further, the magnetisation increases as spins are gradually polarised.

The temperature dependence of the two Bragg peaks is shown in Fig. 4.12, following the same convention for representing each Bragg peak as for the field scans. The two scans from low to high temperature, starting from the state achieved by ramping the field up and down again at base temperature, were taken by measuring the Bragg peaks at several temperature points while warming. These two measurements can therefore be considered as pseudo-field-cooled measurements, whereas the scan down in temperature corresponds to a zero-field cooled scan. The scan down in temperature was made by sitting at the (2,2,0) Bragg peak position and measuring the intensity in small time intervals while the fridge cooled naturally from 2 K to base temperature. This scan is therefore almost certainly out of thermal equilibrium, so the high temperature features such as the phase transition temperature and precise order parameter curve are likely to be slightly inaccurate. The low temperature part of the curve is less strongly affected as the intensity becomes relatively temperature independent.

All scans are consistent with a mean-field-like order parameter curve, as is observed in pure LiHoF_4 , although the data quality is not good enough to fit the curve accurately. There is

once again a splitting observed between scans corresponding roughly to zero field cooled and field cooled. Such hysteresis should not be confused with the hysteresis observed in a conventional magnetisation measurement, where the average magnetisation is measured. Removing domains by applying an external field increases magnetisation, leading to hysteresis between zero-field cooled and field cooled scans. Neutron diffraction as carried out here is insensitive to the domains, and the hysteresis implies that the amplitude of the ordered moment (i.e. $\langle J^2 \rangle$) is reduced.

This could either be due to a reduction in the length of the moment, but is more likely due to some of the spins no longer being locked up in the long range order. Given the tendency for spin-glass formation at low temperatures it seems reasonable that these spins which are removed from the long range order and freeze into a spin-glass state via, for example, a *quantum annealing* process [16], where it is the quantum fluctuations that choose the state of the system. The lack of a Lorentzian component in the Bragg peak after being at high field in Fig. 4.8a could simply be due to the lack of resolution of the instrument, with the bulk of the Lorentzian component being lost in the background. It is also possible that unlike in $\text{LiHo}_x\text{Y}_{1-x}\text{F}_4$, where the glassy correlations are ferromagnetic in nature [76, 77], in this compound they may be antiferromagnetic and thus not centred around the (2,2,0) position.

4.4.2 Spin-Glass State

As a spin-glass can be considered as small interacting clusters of spins, which freeze out below T_f , elastic neutron scattering will show diffuse scattering corresponding to the correlation lengths in the clusters at a particular temperature. From the initial AC susceptibility data, it seems likely that the spins involved in the spin-glass are not the same as those in the ferromagnetic state and are thus likely to have antiferromagnetic correlations. This seems to be further confirmed by the drop in Bragg peak intensity in the (2,2,0) Bragg peak when the system is allowed to order in a field and lack of a Lorentzian component in either of the nuclear peak positions. The (1,1,0) position, which due to the crystal structure is a *forbidden reflection*² for nuclear scattering, corresponds to a doubling of the unit cell and thus antiferromagnetic correlations. The same holds true for other positions in reciprocal space which have miller indices that are half of that of a nuclear peak.

The scattering from antiferromagnetic correlations from a spin-glass is typically a rather weak signal, so it is useful to subtract a non-magnetic background in order to resolve the signal. In this case, taking the high-field (5T) signal as a background makes sense, as the system is effectively a polarised paramagnet in a large field, so spins will be polarised along the field direction and there will be no diffuse magnetic scattering. Fig. 4.13 shows the results of scans between (1,1,-4) and (1,1,4) taken at base temperature (50 mK) in 0 T and 5 T. The left panel shows both the scans, one on top of the other, and the right panel shows the resulting magnetic

²The reason why there are so-called forbidden reflections, or systematic absences, is that the unit cell is not the primitive cell, which leads to destructive interference at specific combinations of (h, k, l) , depending on the crystal space group.

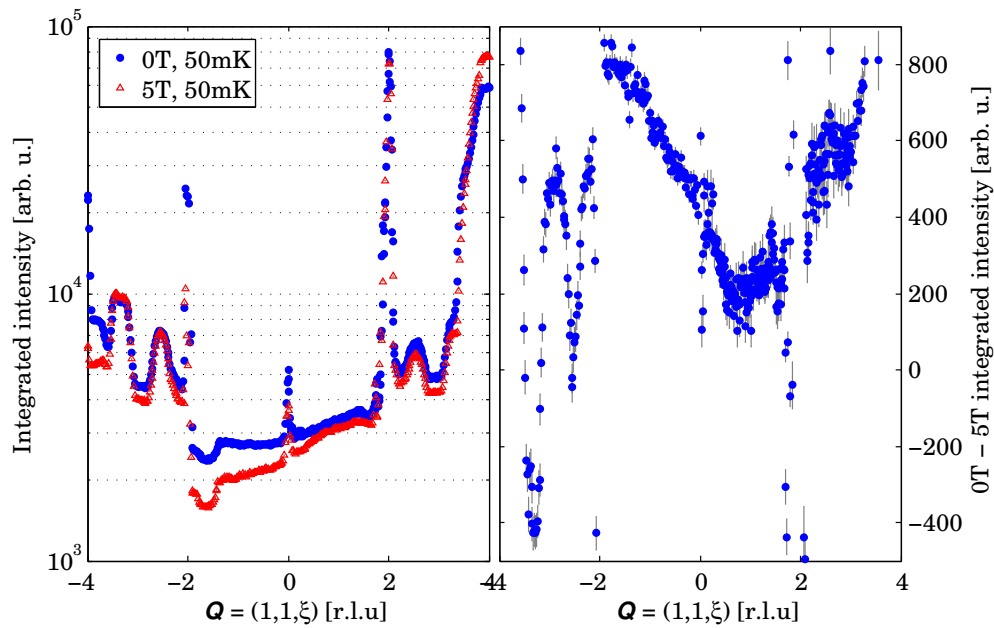


Figure 4.13: [left] Q_l scans centred around $(1,1,0)$ in $\text{LiHo}_{0.79}\text{Er}_{0.21}\text{F}_4$ in 0T and 5 T, searching for short-range correlations. [right] The difference between the signal at 0T and 5T, which is attributed to a change in the detector efficiency that seems to depend both on the field and the configuration of the diffractometer.

signal obtained by subtracting the 5 T scan from the 0 T one. The large signals at $(1,1,-4)$, $(1,1,-2)$, $(1,1,2)$ and $(1,1,4)$ correspond to nuclear Bragg peaks (and ferromagnetic order in low field) and the smaller peak at $(1,1,0)$ is likely due to second order diffraction from the $(2,2,0)$ nuclear peak.

The result initially looks promising – there is indeed a noticeable difference between the scan taken at 0 T and 5 T. Deeper investigation of this difference is however rather inconsistent with what would be expected from a neutron scattering experiment. If there are any short range correlations, they must be symmetric around a certain position in reciprocal space and must also be visible in positions related by symmetry. As an example, consider the large intensity roughly centred at $(1,1,-2)$. If this scattering was due to short range magnetic correlations, then not only should the correlations be symmetric around $(1,1,-2)$, but they should also be seen in the symmetry related $(1,1,2)$ position. One could argue that the peak is in fact symmetric around $(1,1,-2)$, with powder lines at $Q_l < -2$ hiding the magnetic signal, but the feature is clearly not present at the $(1,1,2)$ position. The lack of any symmetric features in the right panel of Fig 4.13 implies that the signal being observed is probably spurious. A reasonable explanation for the signal seen is that it is the angular dependence of the field-dependent detector efficiency observed on the $(2,2,0)$ Bragg peak (Fig 4.10 on page 83). In this case, as Q_l is scanned at 5 T, the detector efficiency changes continuously, leading to the apparent magnetic signal coming from short-range correlations.

To investigate the elusive spin-glass state, detailed powder AC susceptibility measurements

4.4 Embedded Spin-Glass

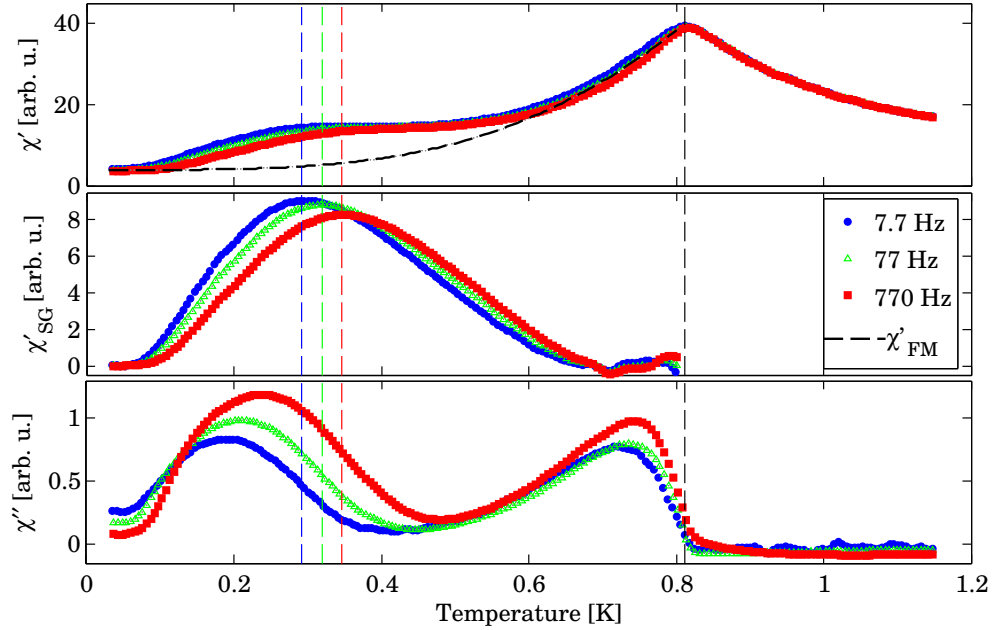


Figure 4.14: Temperature scans taken on $\text{LiHo}_{0.675}\text{Er}_{0.325}\text{F}_4$ at 7.7, 77 and 770 Hz. The peak in χ' at 0.815K is T_C of the ferromagnetic long range order, and the frequency dependence seen at $\sim T = 0.20 - 0.4$ K corresponds to a spin-glass transition. T_f is determined by subtracting a ferromagnetic background signal (dashed line) from the measured curve, leaving the usual peak in the susceptibility (middle panel).

were carried out on a sample of $x = 0.675$. This particular composition was chosen as it shows qualitatively the same behaviour as in $x = 0.79$, but the low temperature peak in χ'' is at a slightly higher temperature, reducing possible problems with thermalisation. This compound is also nicer to study as the peak in χ'' does not move to temperatures below those measurable at the lowest frequencies as is the case for $x = 0.79$.

The $T < 0.5$ K susceptibility of this sample does not seem to have the typical signatures of a spin-glass, which consist of a divergent peak in χ' corresponding to an inflection point in χ'' as can be seen in the top panel and bottom panels of Fig. 4.14. Instead as the peak in χ'' develops, χ' seems to go through a plateau before dropping. One possible interpretation of this is that the susceptibility signal consists of two signals from physically distinct and coexisting features – the ferromagnetic state which forms at $T_C = 0.815$ K and a spin-glass state which develops at $T < 0.5$ K.

The ferromagnetic contribution to χ' is assumed to be well described by an exponential as a function of temperature. In the region 0.65–0.8 K it is also assumed that the spin-glass signal is negligible compared to that of the ferromagnet. The dashed black line in the top panel of Fig. 4.14 shows the fit of the ferromagnetic signal in the 77 Hz data. The middle panel shows the extracted real susceptibility of the spin-glass and the bottom panel shows the imaginary component of the susceptibility. Comparing the second and third panels reveals typical behaviour of a spin-glass in a DC field, as the peak in χ' is clearly rounded. The DC field

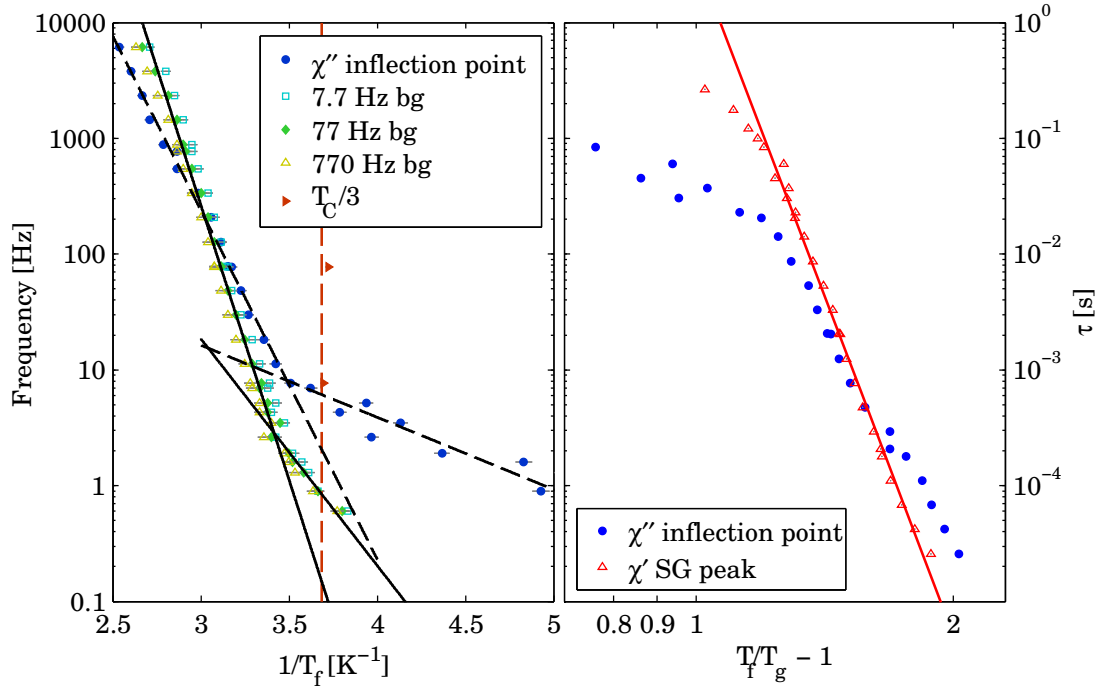


Figure 4.15: Frequency dependence of T_f in $\text{LiHo}_{0.675}\text{Er}_{0.325}\text{F}_4$. The left panel shows the data fit to an Arrhenius law and the right panel to a critical scaling law. In the left panel, the T_f 's found by using backgrounds at 7.7, 77 and 770 Hz are compared and shown to be consistent. The data also compare the relative behaviour of the extracted peak in χ' to the inflection point in χ'' .

here is likely due to the large local fields produced by the long-range ferromagnetic ordering observed in neutron scattering.

From the susceptibility, there are now clearly two features which could be used to identify the spin-glass freezing temperature T_f . The first of these is to take the peak in χ' , which will carry some uncertainty as the peak is very broad, and the second is to take the inflection point in χ'' where the data is noisier. Both of these methods are compared in the left panel of Fig. 4.15, which plots $1/T_f$ as a function of frequency on a log scale. The frequency dependence of the freezing temperature T_f of a spin-glasses can be explained by thermal activation, an Arrhenius law :

$$f = 1/\tau_{\text{char}} = f_0 \exp(-E_a/k_B T). \quad (4.26)$$

The graph shows that there appears to be Arrhenius behaviour at high temperatures, with a possible cross-over to another Arrhenius-like behaviour at lower temperatures. At higher temperatures, the behaviour of the features corresponding to the inflection point in χ'' and the extracted peak in χ' is rather similar, as it should be in a spin-glass. Interestingly at lower temperatures, once the system stops following the initial Arrhenius behaviour, the temperature

4.4 Embedded Spin-Glass

of inflection point in χ'' and the peak in χ' begin to diverge rapidly, with the inflection point moving to lower temperatures than the peak in χ' . This crossover of behaviour happens at very similar temperatures in both features, and has the similar hall-marks as the so-called anti-glass phase in $\text{LiHo}_{0.045}\text{Y}_{0.955}\text{F}_4$ observed by Ghosh *et al.*[31, 32]. Furthermore this graph also compares T_f found using ferromagnetic backgrounds taken at 7.7, 77 and 770 Hz, which give very similar values, indicating that the determination of T_f is independent of the particular background chosen. This implies that the frequency dependent signal from domain wall dynamics in the ferromagnet are not influencing the determination of T_f .

One very popular method used to determine whether a system is a spin-glass or not is to look at the value of the so-called frequency sensitivity \mathcal{K} of T_f [55, 85]:

$$\mathcal{K} = \frac{\Delta T_f}{T_f \Delta \log_{10}(f)}. \quad (4.27)$$

In this method, T_f is normally defined by taking the frequency dependent χ' peak position in temperature scans, as has been done here. ΔT_f is therefore the amount by which T_f has changed by changing the frequency of the measurement by $\Delta \log_{10}(f)$. In this work, the T_f corresponding to measurements at 1 kHz has been used in order to be able to analyse and compare different samples in a similar manner. This gives $\mathcal{K} = 0.027$, which is slightly larger than those seen in a canonical spin-glass, which typically have $\mathcal{K} < 0.01$, but falls into the range of typical insulating spin-glasses with $0.01 < \mathcal{K} < 0.1$. The value is still much smaller than would be expected for a superparamagnet, which typically have $\mathcal{K} > 0.2$.

A different method of treating the frequency dependence of the spin glass supposes a finite temperature phase transition at the glass temperature T_g and therefore critical scaling is expected. The critical scaling of the characteristic time (or equivalently frequency) is normally expressed as [39, 70, 71]:

$$\tau = \tau_0 (T_f/T_g - 1)^{-z\nu} = \tau_0 t^{-z\nu}, \quad (4.28)$$

where z is a dynamical critical exponent and ν is an exponent relating to the spin correlation function. Monte Carlo simulations on a 3D Ising spin-glass and some experimental observations find typical values of $z \sim 7 - 8$.

In order to attempt to fit the data to such a power law, T_g must first be defined in a meaningful way. From the data it is not possible to determine T_g as it certainly occurs at a much lower frequency than that measured. For this reason, T_g was determined by applying a linear fit to $\ln(\tau)$ as a function of $\ln(T_f/T_g - 1)$ for many different values of T_g . The value of T_g which gave the minimum χ^2 of the fit was then chosen to be the correct T_g . Using this approach, T_g was found to be 130 mK, which seems reasonable. The corresponding scaling law plots are shown on the right panel of Fig. 4.15. Once again there is a clear departure from linear behaviour

as the temperature drops below ~ 0.29 K independently of whether the feature in χ' or χ'' is chosen. The imaginary signal seems to shift away from a typical spin-glass behaviour faster than the real signal.

4.4.3 T_C vs. x

It has been experimentally observed that the reduction of T_C as a function of x in $\text{LiHo}_x\text{Er}_{1-x}\text{F}_4$ is more rapid than for $\text{LiHo}_x\text{Y}_{1-x}\text{F}_4$ (cf. Fig. 4.4 on page 69). The following pages detail calculations which have been carried out in an attempt to determine the origin of this increased reduction of T_C .

4.4.3.1 Mean-Field Calculations

The first set of calculations were carried out using the VCMF code introduced in Section 4.3.2.1. The calculations consisted of temperature scans taken between $x = 0$ and $x = 1$ with a total of 101 evenly spaced x values for both Er and Y doped LiHoF_4 . Each scan calculates $\langle J \rangle$ for each temperature calculated, with $\langle J_z \rangle$ showing a mean-field order parameter curve. To extract T_C , each of these curves is fitted with a power law of the form $\langle J_z \rangle \propto H(T_C - T)(T/T_C - 1)^\beta$, where H is a Heaviside step function and $\beta = 0.5$ is the mean-field exponent.

These calculations give a line of T_C vs. x , which is compared to the experimental phase diagram of $\text{LiHo}_x\text{Er}_{1-x}\text{F}_4$ in Fig. 4.16. The solid red line shows the mean-field calculated T_C for $\text{LiHo}_x\text{Y}_{1-x}\text{F}_4$ and the blue solid line that for $\text{LiHo}_x\text{Er}_{1-x}\text{F}_4$. The points are experimentally measured and the dashed lines are guides to the eyes. In the calculations the effect of adding Er into LiHoF_4 is to decrease T_C more slowly than adding Y. Calculations using the iMF code, where a large lattice is populated at random with the correct proportions of Ho and Er (Section 4.3.2.2), give the same result as the VCMF. The effect is not simply due to the disorder in the placement of Er ions.

To better understand what is happening, calculations were carried out in the iMF code using a box of $5 \times 5 \times 5$ unit cells of LiHoF_4 into which a single ion impurity is introduced. In the first case an Y ion is introduced, in the second case an Er ion is introduced and in the third case an Er ion is introduced whose moment is fixed as $\mathbf{J}_x = \mathbf{J}_{Er}^{Max}$ for LiErF_4 . The results of these calculations are shown in Fig. 4.17a, which consists of three unit cells, with the central ion Y, Er and Er fixed in the plane respectively.

This immediately shows why the mean field result gives a higher value of T_C for $\text{LiHo}_x\text{Er}_{1-x}\text{F}_4$ than for $\text{LiHo}_x\text{Y}_{1-x}\text{F}_4$. The non-zero c-axis susceptibility of the Er allows it to be polarised along the Ising axis, increasing $\langle \mathbf{J}_z \rangle$ and thus increasing the ordering temperature. Even when the Er is fixed in the plane, which should enhance the off-diagonal interactions as much as possible, the effect on the nearest neighbours is rather small. In order to understand quantitatively how this affects T_C in each situation, the average z component of the moment $\langle \mathbf{J}_z \rangle$ is calculated and compared to that of pure holmium. For the Y impurity $\langle \mathbf{J}_z \rangle = 5.1$, for the

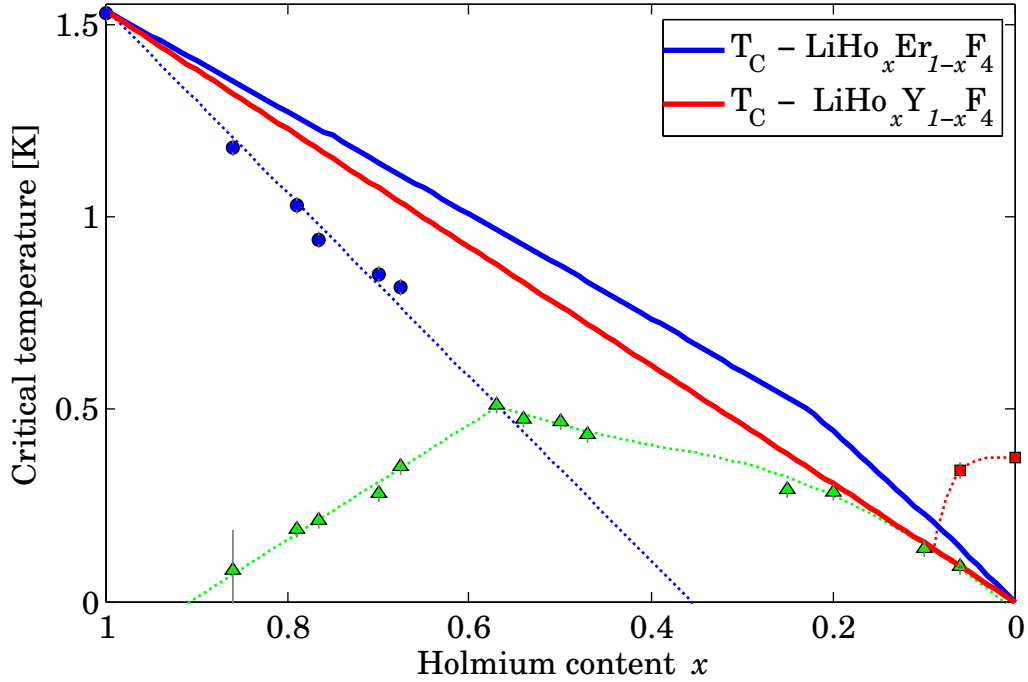


Figure 4.16: Comparison of the mean-field (both VCMF and iMF give identical results when long range order is present) and experimental $T_C - x$ phase diagrams.

free Er ion $\langle J_z \rangle = 5.24$ and for the Er ion fixed in the plane $\langle J_z \rangle = 5.1$ compared to $\langle J_z \rangle = 5.4$ for pure Ho.

In order to try to get a feeling for how the spins are being affected the same results are shown, with the Ising axis and in-plane components of $\langle \mathbf{J} \rangle$ divided by the anisotropic g -factors of Ho, $g_{\parallel} = 13.8$ and $g_{\perp} = 0.74$ [11]. In this way the moments are renormalised such that both components are of similar magnitude, allowing for the small tilting of spins due to the difference in dipole field to be easily seen. The resulting unit cells are shown in Fig. 4.17b.

It is now clearly visible that adding Y increases the frustration of the nearest neighbours, causing neighbours above to tilt inwards and those below outwards. When Er is introduced, it becomes polarised by the mean-field and therefore increases the z component of neighbouring spins slightly. If the Er is fixed in the plane, the situation is effectively the same as with an Y ion. Two neighbours remain unchanged and of the remaining two neighbours, one is polarised more strongly into the plane than with Y but the other less so, giving almost identical values of $\langle \mathbf{J} \rangle$.

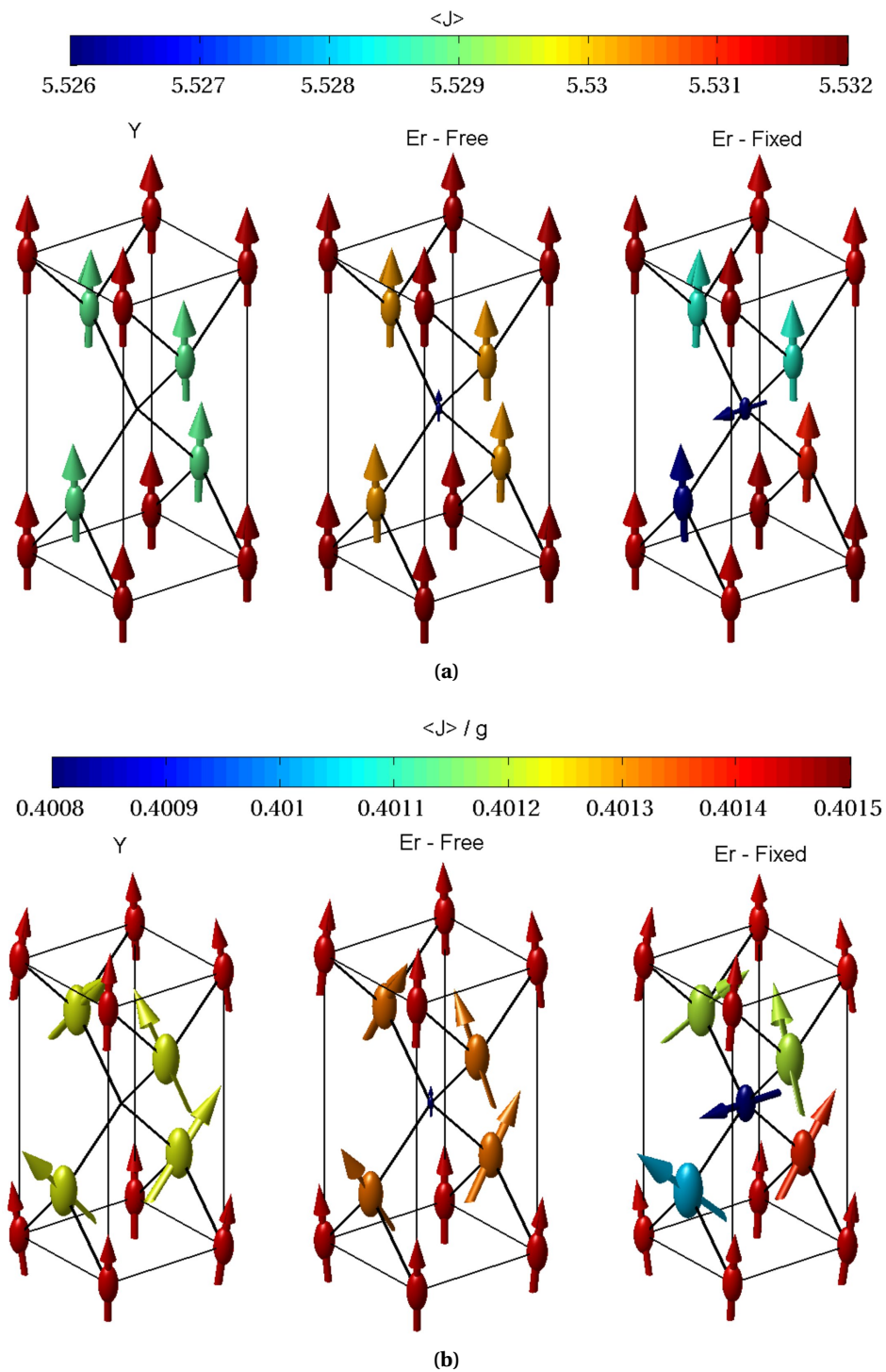


Figure 4.17: (a) Effect of a single impurity on nearest neighbour Ho spins. The left unit cell has an Y impurity, the middle unit cell an Er impurity and the right unit cell an Er impurity whose moment is fixed as $\mathbf{J}_x = \mathbf{J}_{Er}^{Max}$ for LiErF_4 . (b) The same data as in (a), but with the Ising axis and in-plane components of $\langle \mathbf{J} \rangle$ divided by the anisotropic g -factors of Ho, $g_{\parallel} = 13.8$ and $g_{\perp} = 0.74$.

4.4.3.2 Dipole Field Calculations on Near-Neighbour Sites

To fully understand the mean-field calculations, the dipole field at the position of the nearest and next-nearest neighbours has been calculated in three situations. The first situation looks at the dipole field from a Ho ion pointing along the Ising axis, the second for an Er ion in the plane, and finally the effective field created by replacing a Ho ion with an Er ion. To calculate the latter, first the dipole field from a Ho ion is subtracted from the mean-field. The dipole field generated from an Er ion pointing along the a-axis is then calculated and added to the former field. These three situations are shown in Fig. 4.18, going from left to right. In all situations the Ho and Er ions are taken with the maximum moment as determined by mean-field calculations of LiHoF_4 and LiErF_4 respectively. The figures show both the x component of amplitude of the field (pseudo-colour map) and the direction of the field (small green cones). The three unique bonds are shown as J_1 , J_1' and J_2 for the two nearest neighbours and the next nearest neighbour respectively. The dipole field vectors at the end of each of these bonds are summarised in Table. 4.4.

This data clearly shows that although the Er does indeed affect several holmium ions by a relatively large amount in some cases, the net effect is rather small. Due to the symmetry of the dipole interaction and the crystal structure, when the off-diagonal interactions increase in one of the Ho ions, they are effectively decreased in another. Taken with the mean-field calculations on a single impurity, this illustrates that even if the Er ions were to have zero z -axis susceptibility and lie only in the plane, they would probably not contribute to the rapid decrease in T_C , at least while remaining in the mean-field approximation.

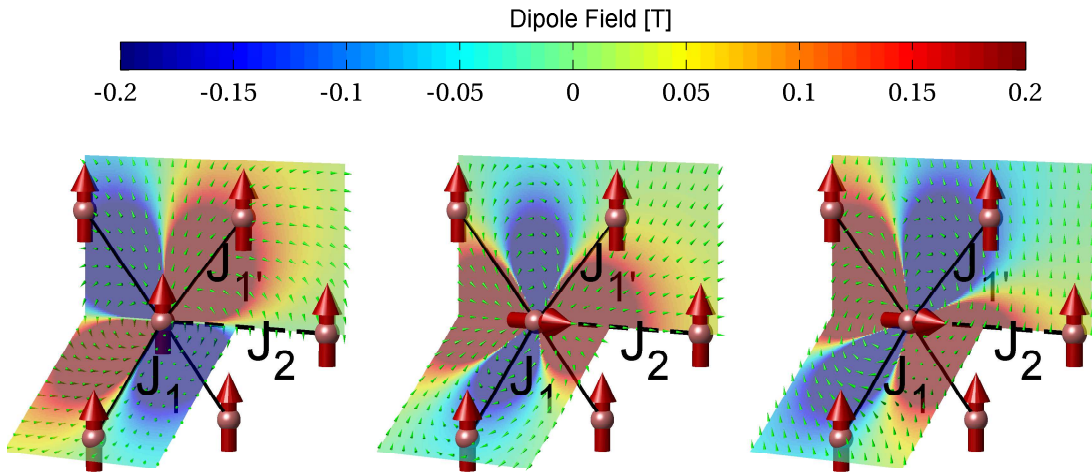


Figure 4.18: Dipole field created by Ho (left), Er (middle) and (right) the effective field generated inside LiHoF_4 by adding the Er ion. This is calculated as the mean-field of LiHoF_4 minus the dipole field generated by the a Ho ion plus that of an Er ion. The colour scale shows the x component of the dipole field and the green cones show its direction.

	Ho ion along z-axis			Er ion along x-axis			MF – Ho + Er		
	J_1	J'_1	J_2	J_1	J'_1	J_2	J_1	J'_1	J_2
Bx	-0.0013	0.1597	0	-0.0684	0.0286	0.0493	-0.067	-0.1311	0.0493
By	0.1657	0	0	-0.0008	0	0	-0.1665	0	0
Bz	0.0613	0.0603	-0.0398	-0.0008	0.0989	0	0.04179	0.05185	0.05198

Table 4.4: Dipole fields generated by Ho and Er ions at neighbouring sites. Units of field are T.

4.4.3.3 Lattice Distortion

Another possibility considered is that the reduction in T_C is due to the lattice becoming distorted by the addition of Er. LiHoF_4 and LiErF_4 have slightly different lattice parameters (unlike in LiHoF_4 and LiYF_4 where lattice parameters are almost identical), with the difference being on the order of 0.5 %. This could conceivably influence both the dipole field and the crystal field parameters in the ions neighbouring an Er ion. From the dipole field calculations already carried out, it is clear that such a small shift in lattice parameters would have a negligible effect on the dipole field strength. Furthermore, as the distortion would likely be symmetric about the Er ion, it is unlikely that any change in the dipole field would have a large net effect. We therefore set out to attempt to calculate if changes in the crystal field, due to distortions in the positions of the fluorine ions in the system, could account for the reduction in T_C .

The resulting crystal field parameters, from symmetric distortions centred around a rare-earth ion were, calculated for lattice distortions up to 1% (for details on the crystal field point charge calculations see Appendix C). The resulting crystal field was then fed into the VCMF code to determine the resulting transition temperature. The results give only a very slight variation from the undistorted crystal field parameter, with variations of $\Delta T_C < 1\%$.

4.4.3.4 Local Quantum Effects

A probable candidate for the rapid decrease of T_C could be a local quantum effect, such as a Ho and Er becoming entangled and forming something similar to a singlet state. This seems probable, as the reduction of T_C is linear with x , implying that it is a single Er site which is causing the reduction. As both holmium and erbium have large spins of 8 and 7.5 respectively, doing direct diagonalisation even on small clusters becomes tricky. One way to overcome this limitation is introduce a reduced Hamiltonian, which effectively replaces the complicated crystal field with a spin half. The literature contains the effective Hamiltonians for both LiHoF_4 [79] and LiErF_4 [49]. One clear limitation of this approach is that it only works when there is a sufficient gap to higher crystal field levels. In this case however, it corresponds to fields higher than 1 T, so should not cause any problems for zero field calculations.

A small cluster consisting of the 8 nearest and next-nearest Ho ions surrounding a central Er ion has been diagonalised in the presence of the LiHoF_4 mean-field. The results of this

4.5 Ferromagnetic Spin-Glass

calculation are identical to those from the mean-field calculation – Er ions get polarised along the c -axis due to the mean-field of the Ho, giving identical expectation values of the Ho and Er moments.

In order to be certain that the limitation in this approach is not due to the effective Hamiltonian, a direct diagonalisation of an Er ion surrounded by its four nearest neighbour Ho ions was carried out by Sergei Isakov at ETHZ (Zurich, Switzerland). As this calculation is very time consuming it was only carried out at zero temperature to see if the Er ion is indeed polarised by the nearby Ho ions. The result from this calculation is identical to that from the reduced Hamiltonian.

4.4.3.5 Other Possibilities

There must be some overlooked effect which is causing the decrease in T_C . Although it can't be said with any real certainty what this effect is, there are two possibilities which seem promising. The first are domain wall pinning effects. If the Er ions play a role in the creation of domain walls and the size and/or mobility of the domain walls affects the stability of the ferromagnetic phase then it seems likely that this could affect T_C . From a manual investigation of the iMF calculations, it certainly seems that domain walls prefer to form at the position of Er spins, but there is no quantitative proof of this as yet. Classical Monte-Carlo calculations using the reduced Hamiltonian are planned in order to test this hypothesis.

The second possible explanation of the reduction in the transition temperature could be due to the Er favouring long range quantum fluctuations in the system, which would reduce the stability of the ordered phase. There is, unfortunately, no way to test this hypothesis, other than ruling out all other possibilities. Hence, despite the efforts in understanding this phenomena, the effect remains a challenge for future theoretical investigation.

4.5 Ferromagnetic Spin-Glass

As x is decreased further, the long range ferromagnetic order is destroyed at $x \sim 0.6$, giving way to a glassy state. While x remains sufficiently large, the characteristic features of the spin-glass appear very broad below the spin-glass freezing transition. The nature of this phase has been investigated by elastic neutron scattering measurements of $\text{LiHo}_{0.50}\text{Er}_{0.50}\text{F}_4$ taken on RITA-II at PSI. A comprehensive AC susceptibility study involving measuring χ_{xx} and χ_{zz} as a function of temperature, frequency and DC field applied along the crystallographic c -axis complements the neutron scattering data.

4.5.1 Neutron Scattering

Elastic neutron scattering was carried out on RITA-II, a cold neutron triple-axis spectrometer at PSI, in order to understand the spin-spin correlations in the system. The experiments

were carried out with the crystallographic $a - c$ plane in the scattering plane and the sample was mounted inside a 5 T vertical magnet (with the field pointing along the a -axis). In order to access as large a range of \mathbf{Q} -space as possible, a relatively high incident energy (for a cold neutron instrument) of 8 meV ($k = 1.96 \text{ \AA}^{-1}$) was used. All available blades of the spectrometer were used in mapping mode, where each blade measures a slightly different point in reciprocal space in order to map regions of \mathbf{Q} -space quickly. The efficiencies of the blades were established by measuring the incoherent scattering from a vanadium sample standard and used to normalise them.

The first area to be studied was around the $(2,0,0)$ nuclear Bragg peak, which would show an increase in intensity if there is long range order and have broad tails if there are short-range ferromagnetic correlations. Fig. 4.19 shows pseudo-colour maps of \mathbf{Q} -space centred

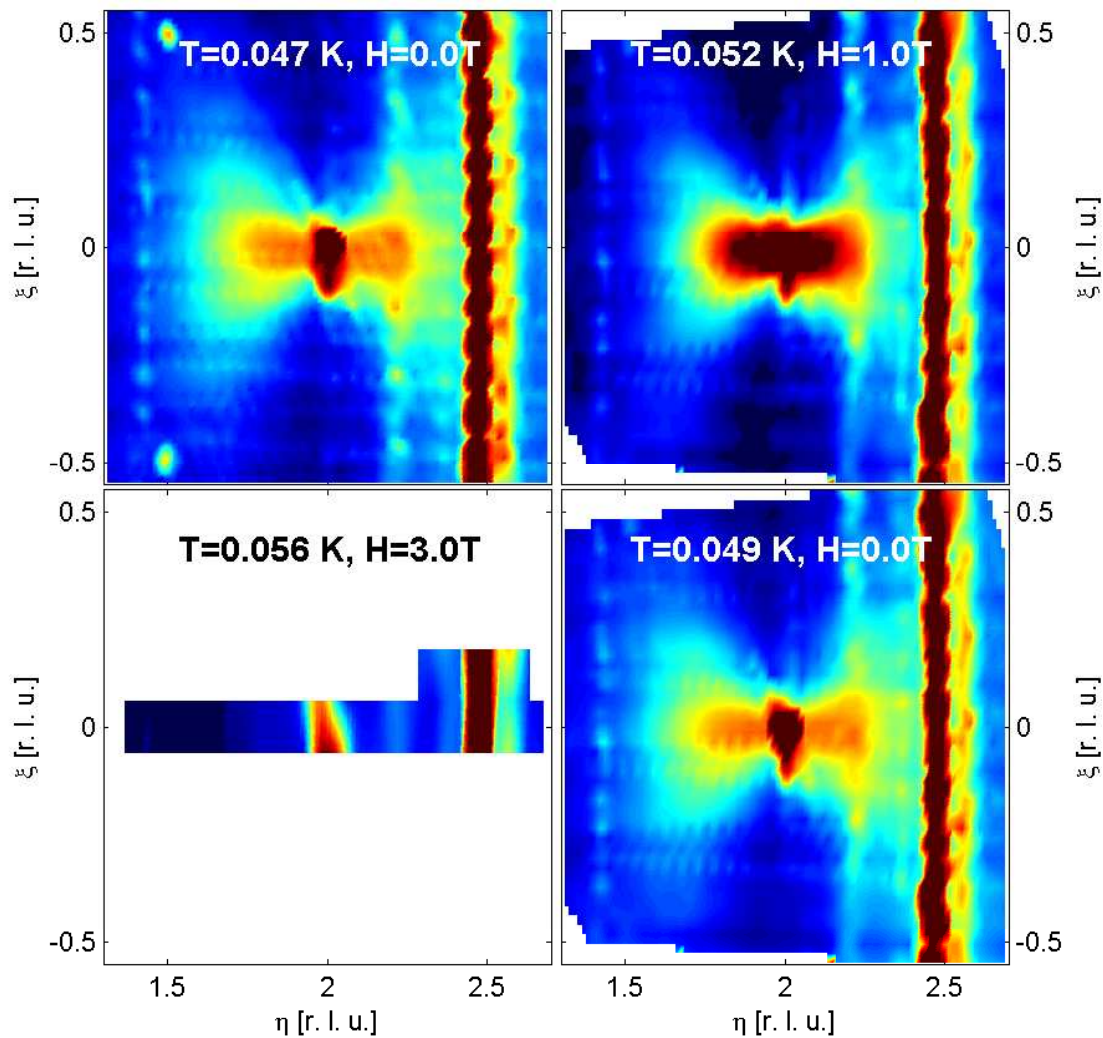


Figure 4.19: $(\eta, 0, \xi)$ scattered intensity pseudo-colour map centred around $(2,0,0)$ in $\text{LiHo}_{0.50}\text{Er}_{0.50}\text{F}_4$ taken at base temperature in zero field and applied field.

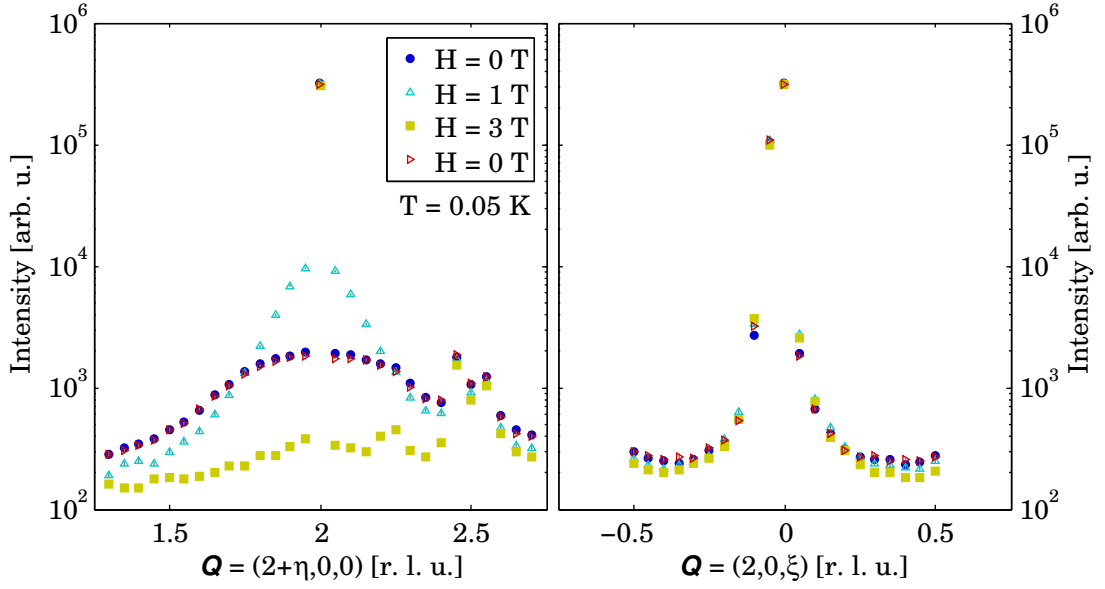


Figure 4.20: [left] Q_h and [right] Q_l scans centred around $\mathbf{Q} = (2, 0, 0)$ in $\text{LiHo}_{0.50}\text{Er}_{0.50}\text{F}_4$ taken at 50 mK and 0, 1, 3 and 0 T.

around $(2, 0, 0)$ at a base temperature of 0.05 K and at fields of 0, 1 and 3 T. At base temperature, there is a very broad component of scattering in the $a - c$ plane, which is centred around the nuclear Bragg peak and destroyed by the application of a 3 T transverse (to the Ising axis) field. This *butterfly* shaped scattering is indicative of needle-like Ising clusters, which have a large correlation length along the c -axis and a much shorter correlation length along the a -axis [77]. Other features in the scans are the presence of second order diffraction from the $(3, 0, 1)$ and $(3, 0, -1)$ Bragg peaks, seen at lattice positions of half these values. At high Q_h there are some aluminium powder lines, which give vertical lines³ of higher intensity scattering.

The magnetic scattering corresponds to a pinch point, where the correlation length along one crystallographic axis is much larger than along the other. This can clearly be seen by comparing scans along the η direction and along the ξ direction starting from $(2, 0, 0)$ as is done in the top two panels of Fig. 4.20. The scans were taken at 50 mK in zero field and the same applied fields of 0, 1 and 3 T. At base temperature, the very broad Lorentzian tail in the $\mathbf{Q} = (2 + \eta, 0, 0)$ scan implies a short correlation length along the a -axis, whereas the lack of any diffuse scattering in the $\mathbf{Q} = (2, 0, \xi)$ scan implies a large correlation length along the c -axis. In an applied field, the Q_h scattering clearly sharpens, corresponding to an increase in correlation length.

This diffuse scattering has been measured as a function of transverse field and temperature. As it is very difficult to resolve the signal from the nuclear scattering at the Bragg peak position, the measurements have been taken with the central blade centred at $\mathbf{Q} = (1.85, 0, 0)$. The other

³The reason why the powder lines are seen as vertical rather than circular, as one would typically expect, is that the value of 2θ remains practically constant between when changing Q_l at these values of Q_h .

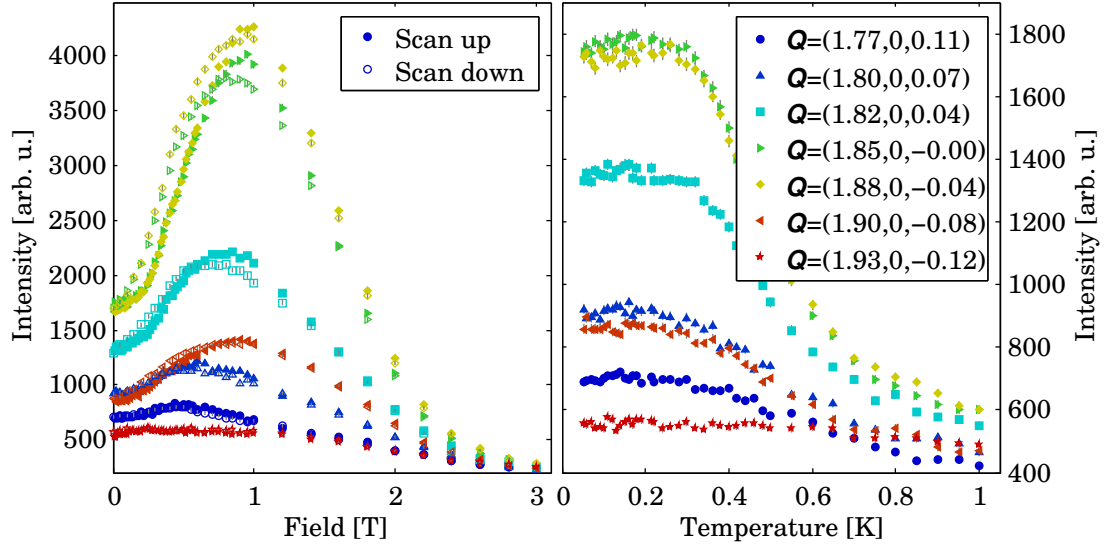


Figure 4.21: [left] H_a field and [right] temperature dependence of ferromagnetic correlations in $\text{LiHo}_{0.50}\text{Er}_{0.50}\text{F}_4$. Measurements were taken with the central blade at $\mathbf{Q} = (1.85, 0, 0)$ to easily resolve the diffuse magnetic scattering from the nuclear scattering. In the field scan, the solid points correspond to the scan from zero field to 3 T and the hollow points the scan back down from 3 T to 0 T.

blades therefore cover a small area of reciprocal space, giving some insights into how the shape of the scattering varies. The results of the field and temperature scans are shown in Fig. 4.21. The field scan shows the scattered intensity close to $\mathbf{Q} = (2, 0, 0)$ increasing and peaking at a field of around 1 T, before decreasing to effectively zero at 3 T. The intensity further away from the Bragg peak begins to decrease almost immediately with the application of a field. This shift of intensity to \mathbf{Q} -values closer to the Bragg peak once again confirms that in a modest transverse field, the spin-spin correlations along the a -axis increase.

Turning to the temperature dependence; the magnetic scattering remains unchanged up until the temperature reaches around 0.35 K, at which point the intensity drops off in a similar manner for all the measured \mathbf{Q} -values. The constant intensity in the temperature range 0.05 – 0.35 K could be an indication that the glass temperature $T_g \sim 0.35$ K has been reached. Below this temperature, the intensity associated with the spin-glass remains constant, and only low frequency relaxation (not observable on neutron time scales) is observed.

Returning to the zero temperature and zero field scattering, the analytical expression for the magnetic cross-section of Ising spins in the quasi-elastic limit is [53]:

$$\frac{d\sigma}{d\Omega} \propto \left[1 - \left(\frac{Q_z}{Q} \right)^2 \right] f^2(\mathbf{Q}) \frac{\chi(\mathbf{Q}, T)}{\chi^0(T)}, \quad (4.29)$$

where z indicates the Ising direction, $f(\mathbf{Q})$ is the magnetic form factor of Ho^{3+} , $\chi(\mathbf{Q}, T)$ is the wave vector and temperature-dependent susceptibility and $\chi^0(T)$ is the single ion suscepti-

4.5 Ferromagnetic Spin-Glass

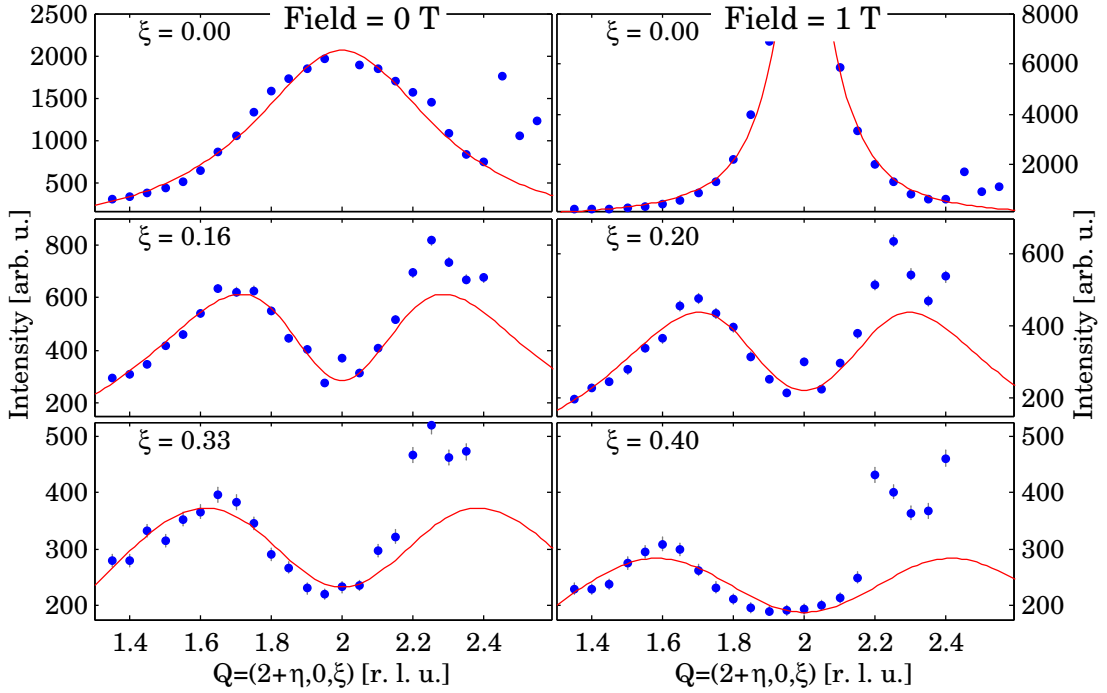


Figure 4.22: Fits of the ferromagnetic correlations using equations 4.29 and 4.30. Data on the left side shows fits in zero field and the right side in a field of 1 T perpendicular to the $a-c$ scattering plane.

bility of the system. If we consider $\mathbf{q} = \mathbf{Q} - \tau^*$, the deviation of \mathbf{Q} from the (2,0,0) reciprocal lattice vector, then the mean-field theory for a uniaxial, dipolar-coupled system gives [1]:

$$\frac{1}{\chi(\mathbf{Q}, T)} \propto 1 + \xi^2 \left[\mathbf{q}^2 + g \left(\frac{q_z}{q} \right)^2 \right], \quad (4.30)$$

where ξ is the in-plane correlation length and g is an anisotropy factor. This behaviour has been observed in the critical scattering of ferromagnetic LiTbF_4 [3], the spin-glass state of $\text{LiHo}_{0.167}\text{Y}_{0.833}\text{F}_4$ [77] and the re-entrant spin-glass state of $\text{LiHo}_{0.46}\text{Y}_{0.54}\text{F}_4$ [48].

\mathbf{Q}_h scans were taken at values of $Q_l = 0, 0.16$ and 0.33 in zero field and $Q_l = 0, 0.2$ and 0.4 in a transverse field of 1T in order to fit the scattering to extract ξ and g . The data along with the fits are shown in Fig. 4.22, where the left side shows the zero field scans and the right side shows scans in 1 T. In zero field a correlation length of $\xi = 16 \pm 1 \text{ \AA}$ and anisotropy factor of $g = 3.3 \pm 0.5 \text{ \AA}^{-2}$ are found. When the transverse field is applied, the in-plane correlation length increases to $\xi = 49 \pm 4 \text{ \AA}$ and the anisotropy factor increases to $g = 32 \pm 5 \text{ \AA}^{-2}$.

One way to think of g is that there exists a correlation length along the Ising axis $\xi_{\parallel} = g^{\frac{1}{2}} \xi^2$, which is defined by the the inverse HWHM of the lobes where their width is maximum. In the work on $\text{LiHo}_{0.167}\text{Y}_{0.833}\text{F}_4$ by Reich et al. [77], the explanation for large g factors is that by diluting the system with Y, the in-plane ferromagnetic correlations must proceed

indirectly via out-of-plane neighbours as the dipolar coupling between in-plane neighbours is antiferromagnetic. This implies that the in-plane correlations will be reduced more rapidly with dilution than those along the Ising axis, increasing g .

By adding in Er ions, the situation becomes more complex, as in zero field the Er ions will tend to sit in the plane and couple antiferromagnetically, therefore reducing the ferromagnetic ξ . However it seems unlikely that the Er ions would sit in a zero field environment. The ferromagnetic correlations of the Ho ions would generate a substantial field (up to the pure Ho mean-field of 1 T) which may therefore polarise Er ions along the c-axis, increasing ξ_{\parallel} . A combination of these two effects leads to very large values of g . Indeed, the determined value of g is much larger than for either the critical scattering of LiTbF_4 [3] or the spin-glass states of $\text{LiHo}_x\text{Y}_{1-x}\text{F}_4$. In the case of $\text{LiHo}_x\text{Y}_{1-x}\text{F}_4$, the value of g was found to be $g = 1.34 \pm 0.33 \text{ \AA}^{-2}$ for $x = 0.46$ [48] and $g = 2 \pm 0.2 \text{ \AA}^{-2}$ for $x = 0.167$ [77].

The large values of g reported here, particularly in the case of the transverse field also have another interpretation. The system is in principle no longer a pure Ising system, as the XY Er ions are at least mediating interactions between the Ho, if they are not directly involved in the ferromagnetic spin clusters. This may imply that Eq. 4.29 and Eq. 4.30 are no longer valid descriptions of the system. This is supported by the observation that if all parameters are allowed to fit simultaneously, both g and ξ evolve as the value of Q_{\parallel} is varied, indicating that the fit is unstable and quite probably not applicable.

The AC susceptibility in this compound shows much broader low temperature features than is typically observed in a spin-glass (see Fig. 4.3 on page 68). These could be caused by a second spin-glass transition occurring below ~ 0.3 K. The spin-glass behaviour seen so far, which is ferromagnetic in nature and corresponds relatively well to the theoretical description of Ising spins, is likely due to the Ho ions. It seems likely that a reasonable proportion of the Er spins would be frozen into these Ising clusters. If there is another species of spin-glass in the system it probably occurs due to the remaining *free* Er spins and would be antiferromagnetic in nature. Several Q vectors corresponding to antiferromagnetic positions were measured, without any evidence of an magnetic scattering, with the possible exception of the region around $Q = (0, 0, 2)$. Fig. 4.23 shows the intensity represented as a pseudo-colour map taken in zero field at 50 mK across a large range of Q , roughly centred around $Q = (0, 0, 2.5)$.

This map of Q -space shows several features, some of which are artefacts of the measurement and one which is possibly due to antiferromagnetic correlations. First; the two circles of high intensity which peak at $Q = (0, 0, 2.5)$ and $Q = (0, 0, 2.9)$ are powder lines from the aluminium cryostat and copper sample holder respectively. Second; the rather broad V shaped low intensity signal which has an apex at around $Q = (0, 0, 2)$ is a *darkish* angle of the magnet, where there is more material in the cryostat which absorbs/scatters neutrons leading to a drop in intensity. Third; the rather broad peaks of increased intensity seen at $Q = (\pm 0.4, 0, 2)$ are believed to be antiferromagnetic scattering. The reason for this is that the $Q = (0, 0, 2)$ is half of the $Q = (0, 0, 4)$ ferromagnetic (nuclear) Bragg peak position, implying a doubling of the

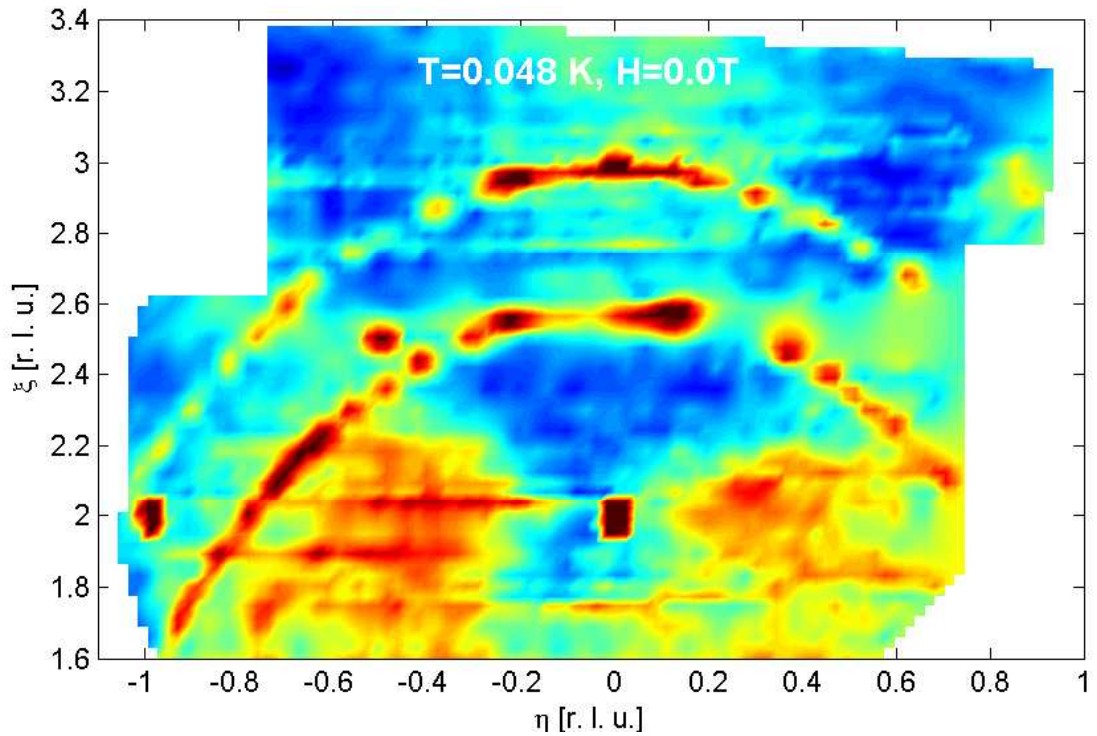


Figure 4.23: $(\eta, 0, \xi)$ scattered intensity pseudo-colour map centred around $(0, 0, 2.5)$ in $\text{LiHo}_{0.50}\text{Er}_{0.50}\text{F}_4$ taken at base temperature in zero field.

real-space separation between correlated spins, as one expects for an antiferromagnet. The decrease in intensity at the $\mathbf{Q} = (0, 0, 2)$ position is surprising and will be discussed later on.

Detailed investigation of this diffuse scattering begins with the Q_h and Q_l dependence of the scattering from $\mathbf{Q} = (0, 0, 2)$, shown in Fig. 4.24. The Q_h dependence in the left panel shows that this scattering is symmetric around the antiferromagnetic Bragg peak position. The correlations are effectively destroyed by a field of 1 T, implying they are not simply due to higher order scattering of ferromagnetic correlations centred around the $(0, 0, 4)$ Bragg peak. In a field of 1 T, the ferromagnetic correlations are higher in intensity and have a larger correlation length, which is clearly not the case here. Surprisingly, the correlations remain at high temperatures, and even increase as Q_h approaches -1. This could be a consequence of the incoherent scattering from the magnetic Ho ions in the paramagnetic state. The Q_l scans shown in the right panel are virtually featureless and consist of a signal which drops off as Q increases, which could be due to the detection of the direct beam decreasing as θ (and Q_l) increases. This scan confirms that there is both a lower background at high fields and a higher background at high temperatures.

Field and temperature scans taken while sitting at the $\mathbf{Q} = (-0.4, 0, 2)$ position, the *peak* in the magnetic scattering, are shown in Fig. 4.25. As the intensity of the scattering is weak, the intensities from the five central blades have been combined to improve statistics. The field scan in the left panel shows typical spin-glass behaviour, where the application of a

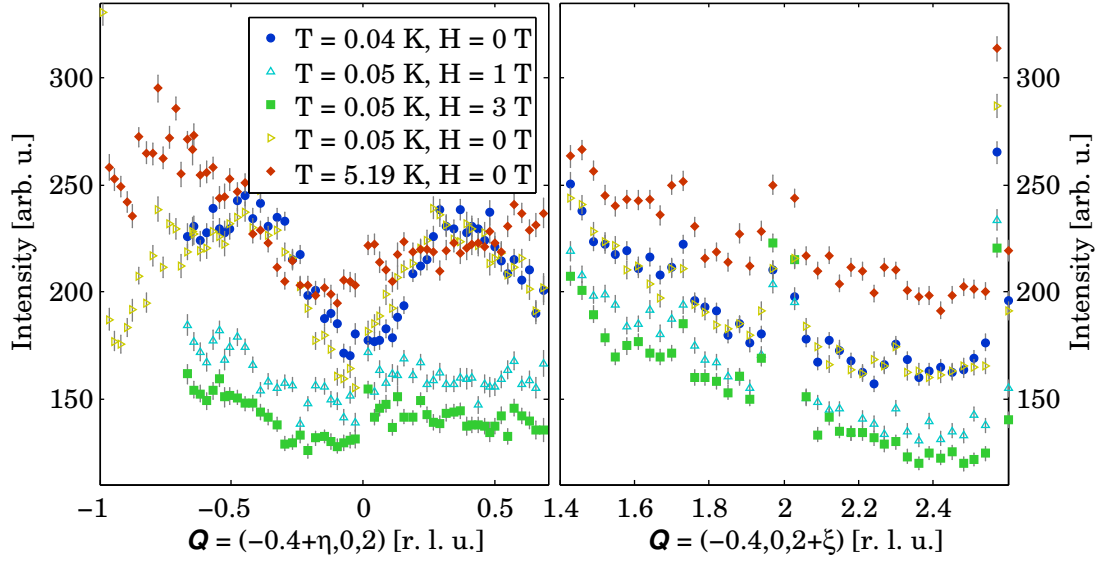


Figure 4.24: Search for antiferromagnetic correlations in $\text{LiHo}_{0.50}\text{Er}_{0.50}\text{F}_4$ consisting of [left] Q_h scans and [right] Q_l scans taken around the $Q = (0, 0, 2)$ position.

field continuously decreases the intensity of the correlations. This scan also demonstrates that there is no path dependence in the scattering. The temperature scans in the right panel confirm that this feature is seemingly independent of temperature, although there is a very slight (just above error bars) drop in intensity above 0.4 K.

The scattering appears to be magnetic in nature, but curiously does not sit at a position either associated with commensurate ferromagnetic or antiferromagnetic correlations. It is unlikely that the scattering is due to some kind of diffuse incommensurate scattering process, although it cannot be ruled out completely. A much more likely scenario is that the diffuse scattering is due to antiferromagnetic correlations with the spins aligned along the c -axis.

To understand why there is no intensity at $Q = (0, 0, 2)$, but only as Q_h moves to non-zero values, we recall that in the general magnetic scattering cross-section for neutrons given in Eq. 4.15 on page 73, there was a term called the polarisation factor:

$$\sum_{\alpha\beta} (\delta_{\alpha\beta} - \hat{Q}_\alpha \hat{Q}_\beta). \quad (4.31)$$

This factor essentially says that due to the dipole interaction between the neutron and the magnetic moment, neutrons will only be scattered if the scattering vector and the alignment of the moment are perpendicular. The result of this polarisation factor is that the scattered intensity will be proportional to the angle φ between the scattering vector and the moment in the following way:

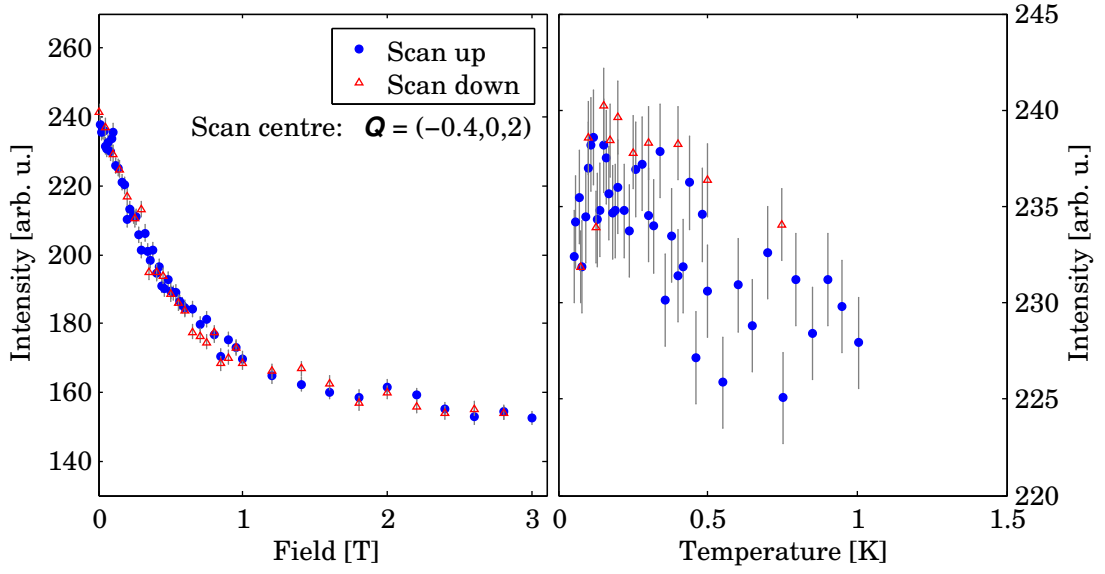


Figure 4.25: [left] H_a field and [right] temperature dependence of the possible antiferromagnetic correlations in $\text{LiHo}_{0.50}\text{Er}_{0.50}\text{F}_4$. Measurements were taken at $\mathbf{Q} = (-0.4, 0, 2)$ as this is where the intensity, thought to come from magnetic scattering, is the strongest.

$$I \propto \sin^2 \varphi. \quad (4.32)$$

It is therefore possible that a peak does exist at the $(0, 0, 2)$ position, but due to the geometry of the spins relative to the scattering wavevector, the intensity drops to zero.

In order to attempt to find the correlation length, the peak is fitted with a Lorentzian line shape multiplied by the angular dependence of the scattering from magnetic moments along the c -axis:

$$I \propto \frac{1}{1 + \mathbf{Q}^2 \xi^2} \sin^2 \varphi, \quad (4.33)$$

where ξ is the correlation length of the spins. Before fitting, the 3 T signal is subtracted from the zero field signal, in order to remove the background as much as possible. The fit is carried out only between $\mathbf{Q}_h = -0.6$ and $\mathbf{Q}_h = 0.6$, as even if the data exists for zero field at lower \mathbf{Q}_h , the background is unknown and is increasing with smaller \mathbf{Q}_h as the detector moves towards the incident neutron beam. The fit to the data is shown in Fig. 4.26 and finds a correlation length of $\xi = 31 \pm 4 \text{ \AA}$, which seems a bit large given the dominant ferromagnetic clusters are only correlated over 16 \AA .

Putting all of this information together, from Fig. 4.19 on page 96 and Fig. 4.21 on page 98, it is clear that there are long, thin Ho clusters, which due to the Ising nature of the Ho^{3+} ions must be oriented along the c -axis. There also appear to be antiferromagnetic correlations, which

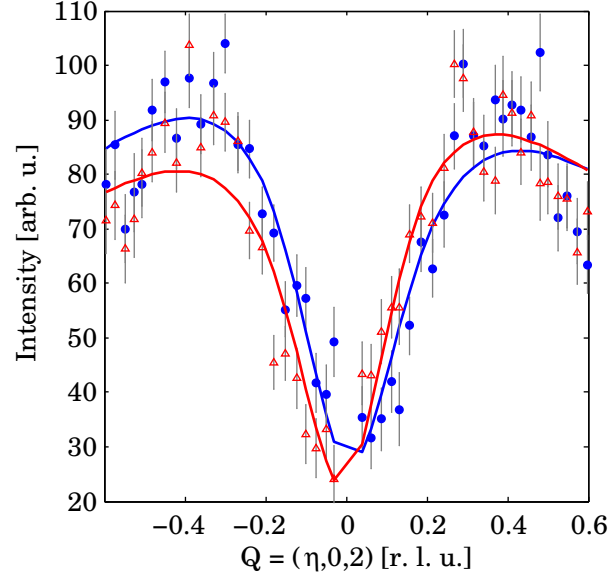


Figure 4.26: Fit of the antiferromagnetic correlations in $\text{LiHo}_{0.50}\text{Er}_{0.50}\text{F}_4$ using the form given in Eq. 4.33 and finding $\xi = 31 \pm 4 \text{ \AA}$.

due to the diminishing intensity at $\mathbf{Q} = (0, 0, 2)$ consist of spins polarised along the c -axis. It therefore seems likely that both Ho and Er spins are polarised along the Ising axis and form the ferromagnetic clusters.

The relative intensity of the scattering from a Ho ion and an Er ion polarised along the c -axis is given by:

$$\frac{I_{Ho}}{I_{Er}} = \frac{\langle J_{Ho}^2 \rangle}{\langle J_{Er}^2 \rangle} \quad (4.34)$$

where $J_z^{Ho} = 5.53$ in the mean-field approximation compared to $J_z^{Er} = 1.75$. This implies that if Ho ions were correlated then the signal would be 10 times more intense than if it were Er ions which were correlated. Given that the amplitude of the Lorentzian component of the antiferromagnetic signal is roughly 10 times less than that of the ferromagnetic signal (the units in all graphs are the same), it seems likely that the antiferromagnetic correlations are due to the Er ions.

4.5.2 Zero Field AC Susceptibility

In order to better understand the origin of the broad susceptibility seen in powder measurements, both χ_{xx} and χ_{zz} were measured in single crystals of $\text{LiHo}_{0.50}\text{Er}_{0.50}\text{F}_4$. The crystals were cut into rectangular cuboids with dimensions of $10 \times 1.2 \times 1.2$ mm with the length being along the a -axis for χ_{xx} and the c -axis for χ_{zz} . Measuring the susceptibility in both directions

4.5 Ferromagnetic Spin-Glass

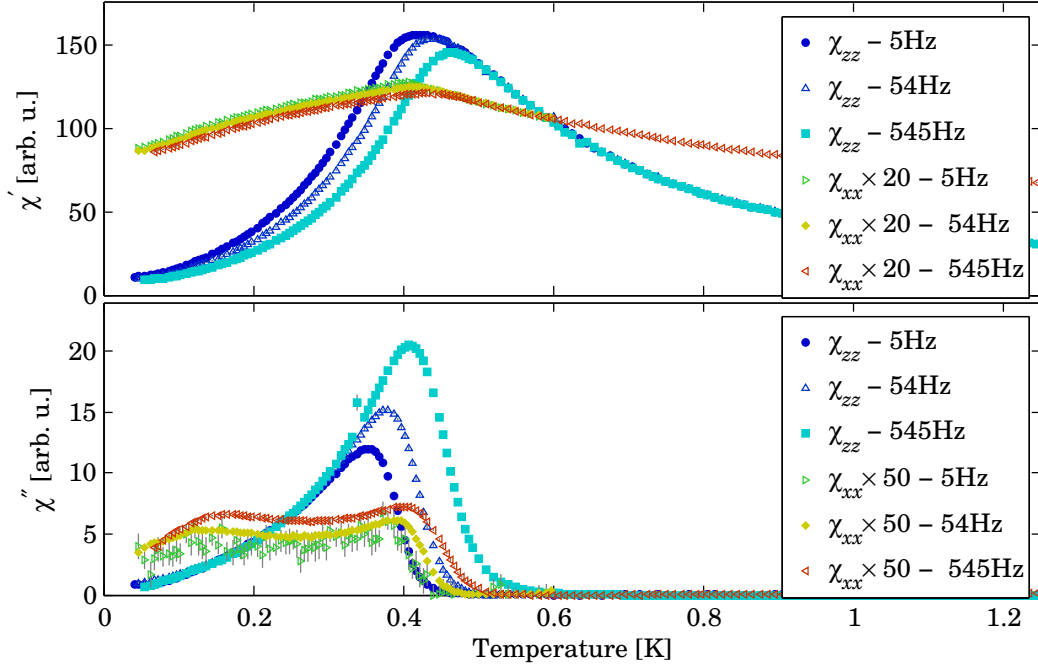


Figure 4.27: Temperature scans on $\text{LiHo}_{0.50}\text{Er}_{0.50}\text{F}_4$ comparing χ_{zz} and χ_{xx} . In order to better compare the two data sets χ_{xx} has been scaled to increase the amplitude of the signal.

allows for a partial separation of Er and Ho moments, as the Ising anisotropy of the Ho ions means that χ_{xx}^{Ho} will effectively be a purely paramagnetic signal. Er on the other hand has a much weaker XY anisotropy, meaning that its signal will be detectable in both χ_{xx} and χ_{zz} , although it is likely that in the latter the signal will be very small compared to that from Ho. Fig. 4.27 shows a comparison of the temperature-dependent susceptibility measured along both directions taken over three decades of frequency.

In χ_{zz} the classical signatures of a spin-glass, consisting of a divergent peak in χ' and a lower temperature peak in χ'' are recovered. In χ_{xx} the real component of the signal remains broad and the imaginary component clearly has two distinct peaks. One of the peaks is at a temperature around 400 mK, and presumably corresponds to the peak in χ''_{zz} , and a low temperature peak at around 150 mK. This data reinforces the conjecture from the neutron scattering data; as the Ho moments freeze out, some of the Er ions get caught up in these ferromagnetic clusters and then at lower temperatures there is an additional freezing of spins.

The frequency dependence of the freezing transition is explored in Fig. 4.28. $T_f(f)$ is taken to be the peak in χ' for a given frequency and is analysed in terms of Arrhenius behaviour in the left panel and as a critical scaling phenomena in the right panel. The inset of the graph shows the frequency dependence of the low temperature peak in χ''_{xx} , which (over the small frequency range where it was possible to extract the peak in the signal) does follow an Arrhenius law.

As the frequency and the temperature are decreased, the freezing temperature begins to

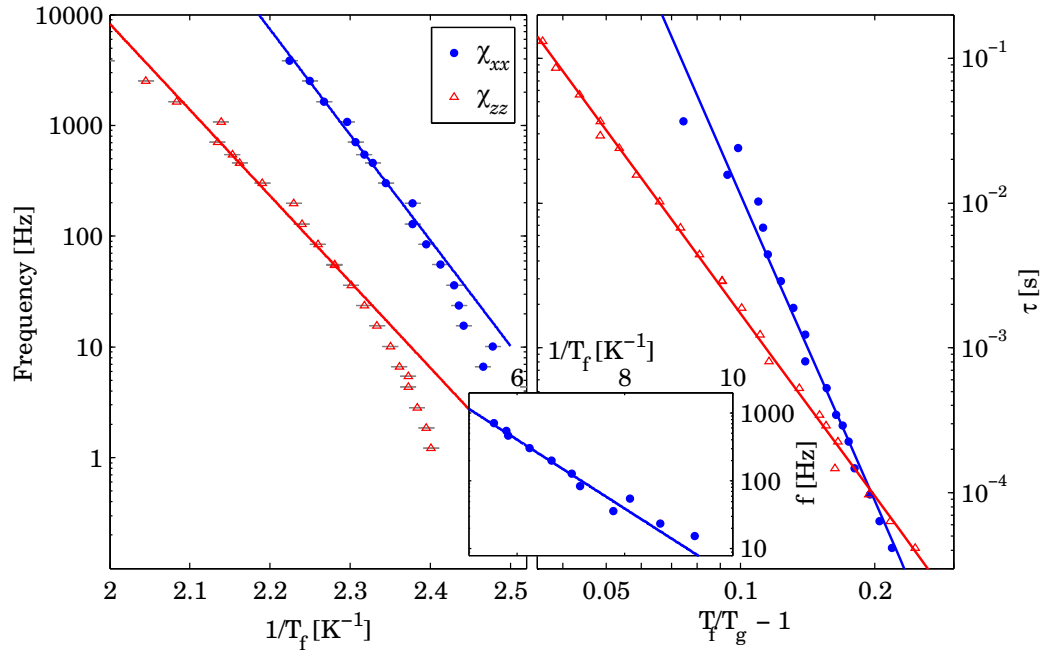


Figure 4.28: Frequency dependence of T_f in $\text{LiHo}_{0.50}\text{Er}_{0.50}\text{F}_4$ expressed in terms of [left] an Arrhenius like behaviour and [right] a dynamic scaling law on the right. The inset shows the frequency dependence of the low temperature peak in χ''_{xx} in the small range of frequencies where the peak was extractable.

deviate from Arrhenius behaviour. Unlike in the embedded spin-glass (shown in Fig. 4.15 on page 88), T_f appears to converge to a zero frequency spin-glass temperature T_g . When plotting as a function of reduced temperature, the power law dependence becomes clear. For χ_{zz} the fit for $T_g = 0.405$ gives $z\nu = 4.1$ and $\tau_0 = 1.5 \times 10^{-9}$ s and for χ_{xx} $T_g = 0.369$, $z\nu = 7.0$ and $\tau_0 = 1.0 \times 10^{-7}$ s. This indicates that even though the freezing seen in χ_{zz} and χ_{xx} is believed to have the same physical origin, there are clearly different dynamics involved.

4.5.3 Susceptibility in a Longitudinal Field

The behaviour of the susceptibility in a DC field was measured by slowly ramping the field while measuring the response from the sample. χ_{xx} was measured with the field along the a -axis and χ_{zz} was measured with the field along the c -axis. A comparison of the two scans taken at 50 mK between 0 and 3 T is shown in Fig. 4.29. The χ_{xx} signal shows typical spin-glass behaviour with the susceptibility dropping off as the field is increased. χ_{zz} on the other hand shows unexpected behaviour for a spin-glass, with a very sharp peak, whose behaviour is near identical in both the real and imaginary channels.

This low field peak in χ_{zz} has been studied in great detail, starting with a hysteresis scan. In ultra low temperature AC susceptibility, hysteresis scans can normally be used to determine whether the ramping of the field is inadvertently heating the sample. AC susceptibility mea-

4.5 Ferromagnetic Spin-Glass

measurements do not measure M directly, only dM/dH (where dH is typically < 1 Oe), which is generally insensitive to the parallel or anti-parallel orientation of domains or clusters in an external field (resulting in magnetisation hysteresis loops). For this reason it is typical that the direction of the scan does not affect the AC susceptibility signal, unless the ramping of the field is heating the sample. This peak is unusual as it does show hysteresis in AC susceptibility, as can be seen in Fig. 4.30, which shows a hysteresis loop at 34 mK starting from a zero-field-cooled (ZFC) state and ramping the field at 1 mT min^{-1} . From top to bottom the panels show χ' , χ'' and the temperature measured on the weak-link thermometer as a function of field.

The large peak in susceptibility is only present when increasing the field from the ZFC state, and not when returning the field to zero. When the field passes to negative values, there is a peak in susceptibility which is both broader and lower in amplitude than the ZFC peak. This peak once again has identical forms of χ' and χ'' , but is at a lower absolute field than the ZFC one. Ramping the field back up to positive values reproduces identical behaviour to the ramp from positive to negative fields (with the peak occurring at a positive field with the same amplitude). Concomitant to the peaks in susceptibility is a magnetocaloric effect which is large enough to heat the weak link thermometer by ~ 7 mK. As the temperature has been controlled on the mixing chamber while simultaneously measured on the weak-link, it is possible to convert the temperature gradient to a heat flow between the sample and the weak-link thermometer. In the ZFC scan, the temperature of the weak-link thermometer perfectly follows the susceptibility. In the peaks produced from the field-polarised state, the magnetocaloric effect is more pronounced and has a second feature at higher field amplitude, which is not clearly visible (but possibly existing) in the susceptibility.

The temperature dependence of the ZFC peak was measured by ramping the field up to 0.1 T from the ZFC state at different temperatures between 30 and 300 mK. On the left side of Fig. 4.31 several selected temperatures are shown to give a general overview of the features present and how they evolve with temperature. At low temperatures, the peak in the susceptibility is sharp and the high field signal is relatively flat. As the temperature is slowly increased, there are several changes in the signal. The peak loses intensity and sharpness, and moves towards lower fields. By the time the temperature is around 0.15 K, the peak is completely suppressed and can no longer be resolved from the background. In order to identify the peak at temperatures above 0.1 K, the scan with increasing field is subtracted from the scan back down, giving a relatively sharp peak at the correct position, allowing for both the position and amplitude of the peak to be accurately extracted.

A second feature, which emerges at higher temperatures is a broad peak that is initially seen at a field just above 40 mT. This peak is first visible around 0.06 K and moves to slightly higher fields, until at 0.1 K its position peaks at 50 mT. The peak then moves towards zero field as the temperature is increased further and disappears completely at around 0.3 K. The amplitude of the peak grows continuously with increasing temperature.

The bottom right panel shows the heating effect on the weak-link thermometer, calculated

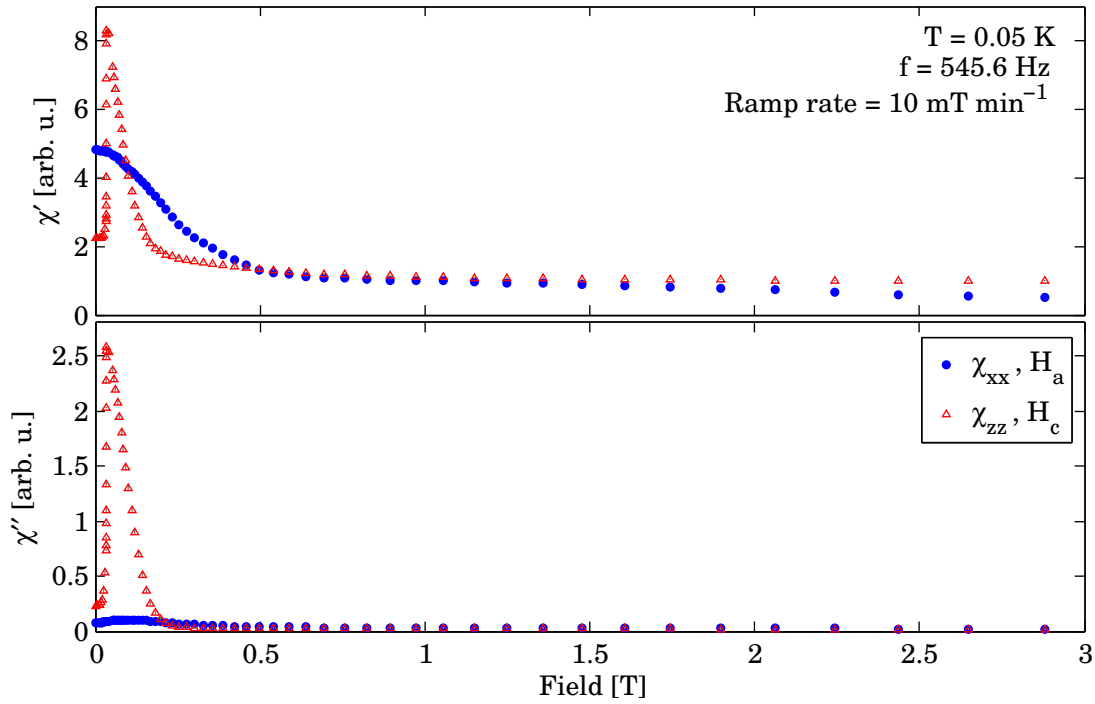


Figure 4.29: H_a and H_c field scans on $\text{LiHo}_{0.50}\text{Er}_{0.50}\text{F}_4$ at $T = 0.05$ K with the field applied along the measurement direction and a ramp rate of 10 mT min^{-1} .

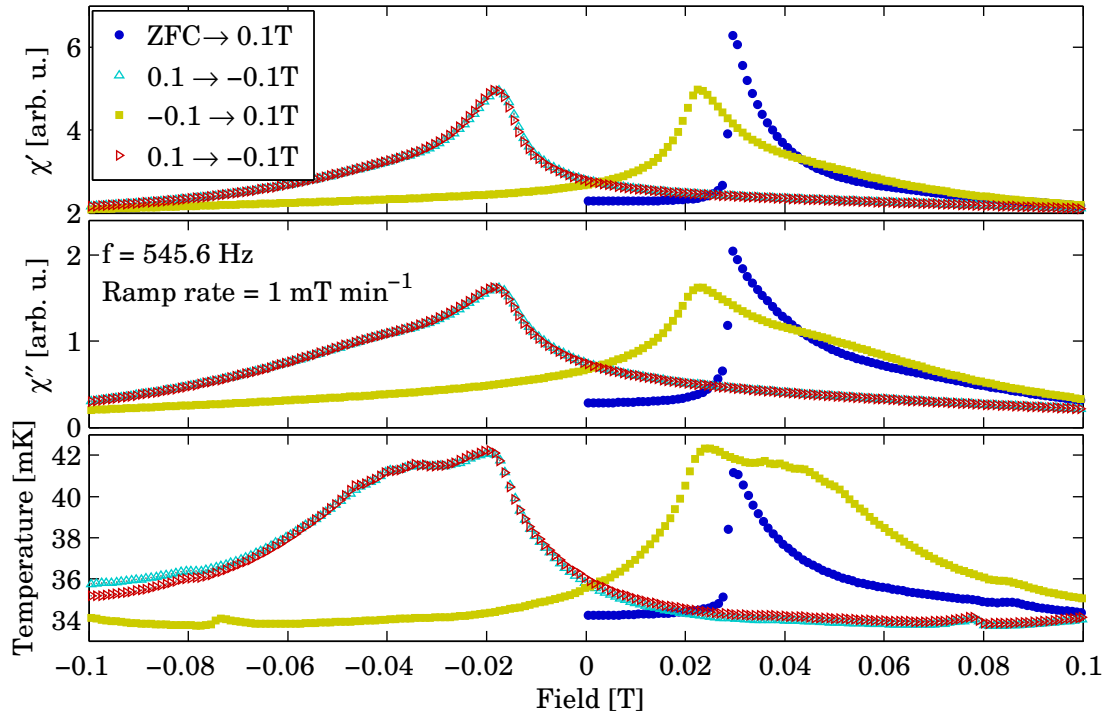


Figure 4.30: Hysteresis in χ_{zz} observed in H_c scans on $\text{LiHo}_{0.50}\text{Er}_{0.50}\text{F}_4$ taken at $T = 34$ mK with a ramp rate of 1 mT min^{-1} . The bottom the panel shows the weak-link temperature.

4.5 Ferromagnetic Spin-Glass

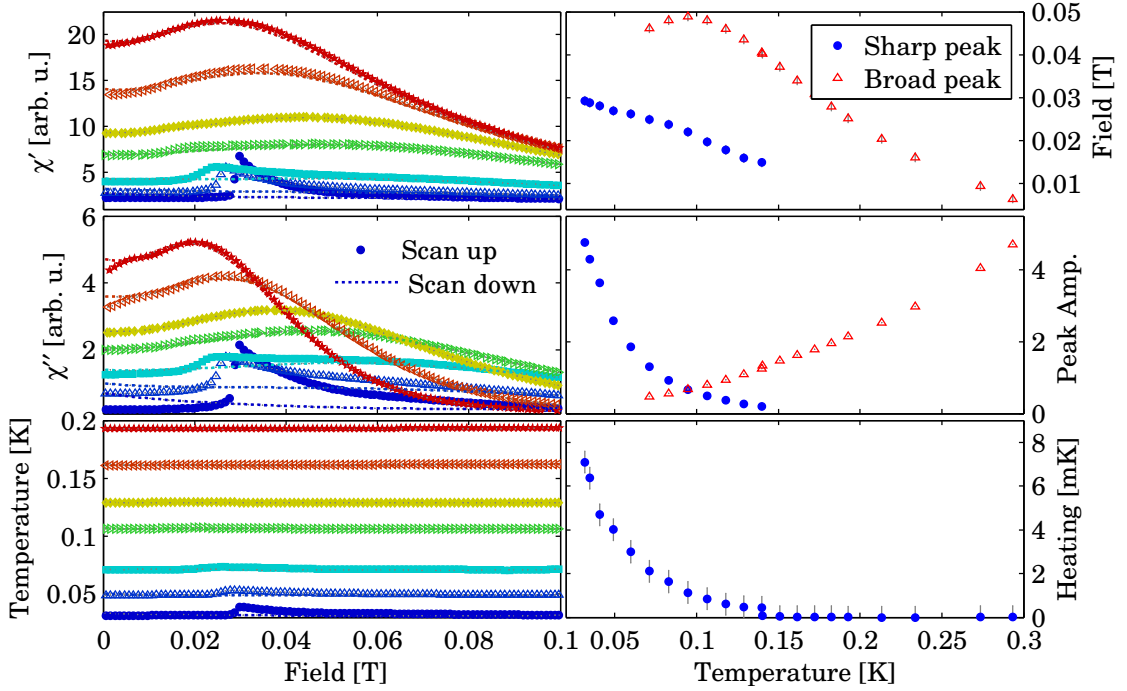


Figure 4.31: [left] H_c field scans of χ_{zz} taken at several selected temperatures in $\text{LiHo}_{0.50}\text{Er}_{0.50}\text{F}_4$. [right] Temperature dependence of the two distinct peaks and the relative heating on the weak-link thermometer due to the magnetocaloric effect.

as the difference in temperature recorded at the start of the scan and at the peak maxima. This graph confirms that the peak in susceptibility and the magnetocaloric effect are due to the same physical process. The peak in temperature always coincides perfectly with the peak position in susceptibility. Furthermore the change in temperature on the weak-link thermometer follows the exact same behaviour as amplitude of the peak in susceptibility.

Temperature scans in a DC field were also carried out by first cooling in zero field then applying a DC field, which is kept fixed while the susceptibility is measured as a function of temperature. The data is shown in Fig. 4.32, which shows χ' (top left) and χ'' (bottom left) for selected fields. On the top right panel, the temperature of the peak of both components of the susceptibility is plotted against the static DC field. The amplitudes of these peaks as a function of applied field is shown in the bottom right panel of the figure.

The application of field the decreases the susceptibility with all features essentially disappearing at a field of 0.15 T. The features shift down to lower temperatures in a roughly exponential manner and, instead of tending towards zero temperature as would be expected for a quantum phase transition, remain at a field independent finite temperature. It is difficult to determine whether the peak eventually shifts to zero temperature as the susceptibility becomes very small and the sample signal is lost in the background.

To complement the measurements of χ_{zz} presented, χ_{xx} has been measured with the DC

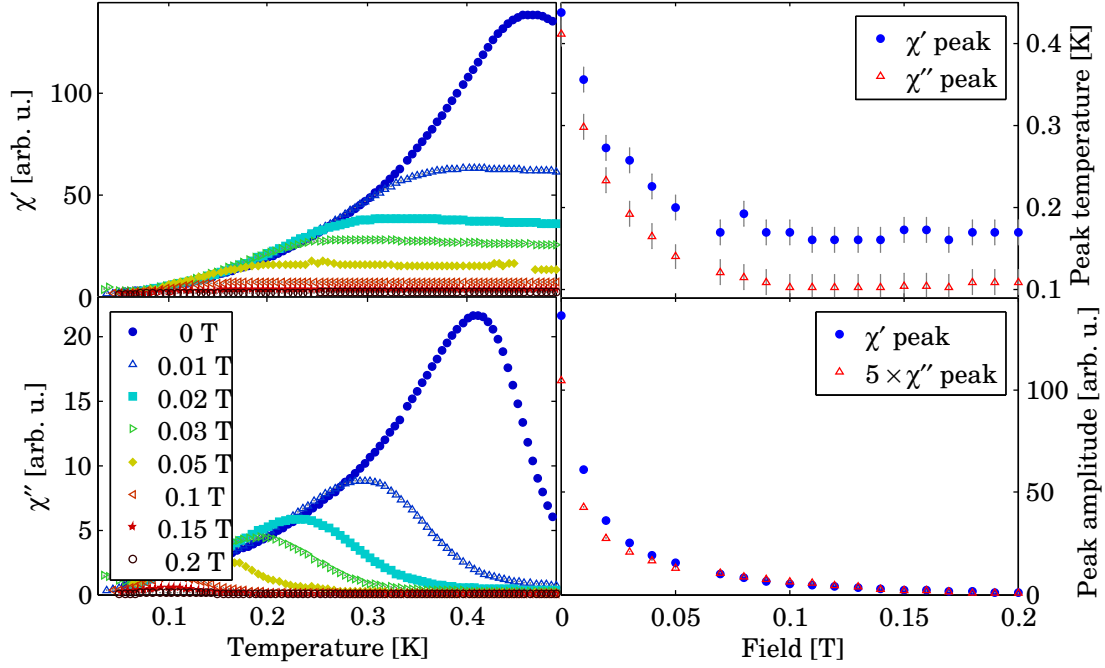


Figure 4.32: Temperature and H_c field dependence of χ_{zz} as seen by temperature scans at constant field in $\text{LiHo}_{0.50}\text{Er}_{0.50}\text{F}_4$.

field oriented along the crystallographic c -axis. The information gained by measuring in this configuration is related only to non Ising spins, therefore measurements are insensitive to Ho ions and only pickup the signal from Er. The first measurement consists of a comparison of χ_{xx} and χ_{zz} field scans, both taken at 34 mK with a field ramp rate of 1 mT per minute. As can be seen in Fig. 4.33, this scan indicates that the large peak is due to the Ho ions, as χ_{xx} remains practically flat and there is definitely no feature at a similar field (even when scaled up by a factor of 20).

The peak in χ_{zz} is most likely due to the needle-like Ising clusters being flipped by the field. By measuring the magneto-caloric effect, which is still present in the scan on χ_{xx} , it becomes clear that the sample is still going through the *transition* and that this is just not visible in the transverse susceptibility. The scan also demonstrates that the magnetocaloric effect is due to the sample responding to the DC field and not that it is being driven by the application of the AC field.

As the field is increased to higher values, a broad peak in χ' is observed at around 0.45 T. The temperature dependence of this peak, and associated features in χ'' have been mapped out by taking field scans while keeping the temperature constant in the range of 0.05–0.6 K. The results of these scans are shown in Fig. 4.34, which show the amplitude of χ' (left) and χ'' (right) as pseudo-colour maps as a function of field and temperature. The plot contains over 50 field scans, which makes this 2D representation a very good way to visualise the data.

4.5 Ferromagnetic Spin-Glass

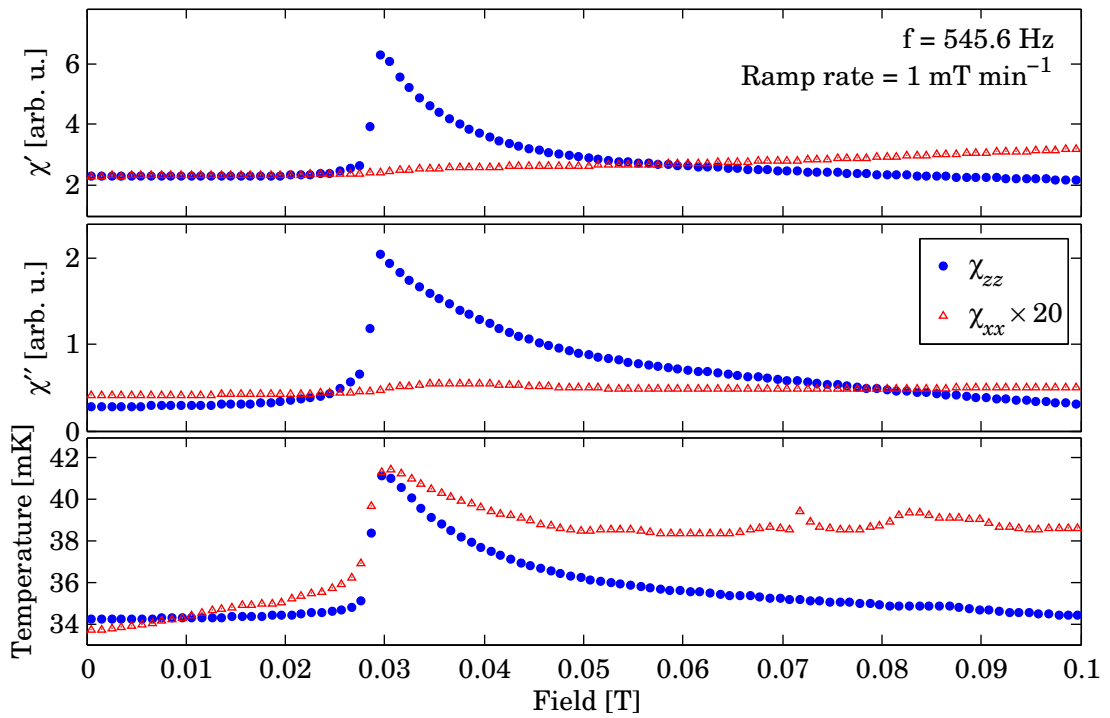


Figure 4.33: Comparison between χ_{xx} and χ_{zz} in H_c field scans in $\text{LiHo}_{0.50}\text{Er}_{0.50}\text{F}_4$.

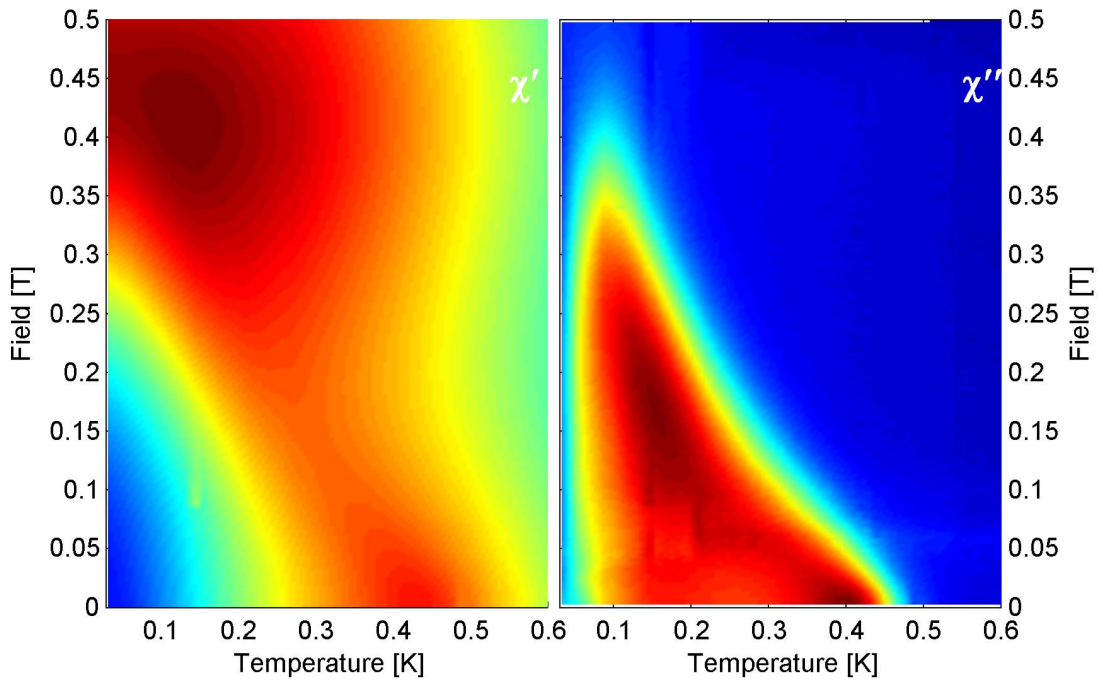


Figure 4.34: Temperature and H_c field dependence of χ_{xx} determined by taking field scans at fixed temperatures in $\text{LiHo}_{0.50}\text{Er}_{0.50}\text{F}_4$.

The scans show that at the lowest temperatures χ' peaks at around 0.45 T and χ'' remains relatively flat. As the temperature is increased, a sharp peak appears in χ'' at a field of 0.3 T and moves to lower fields as the temperature is increased. At the same time, the peak in χ' broadens and becomes a plateau. As the temperature is raised above 400 mK, the spin-glass state is quickly destroyed by any field; the peak in χ'' moves to zero field and χ'' becomes flat.

4.5.4 Field Induced Thermal Runaway

The peak at ~ 0.03 T in χ_{zz} was found to show some rather unusual behaviour as a function of the field ramp rate. The peak in χ grew in amplitude and occurred at higher fields as the ramp rate was increased. Furthermore, an *avalanche*-like effect was also observed: if the field was ramped to just below some critical value and then stopped, the susceptibility would continue to grow and peak as if the field was still ramping. The initial study of this feature used only AC susceptibility and resulted in a compelling story, which subsequent magnetisation measurements, combined with more accurate measurements of the sample temperature, showed to be an inaccurate description of the data. As an example of why it is important to verify results, ideally by using additional experimental techniques, before jumping to conclusions, the original interpretation of the AC susceptibility is given in Appendix D.

The interpretation of this thermal runaway, which occurs when the field is ramped above ~ 0.03 T makes use of simultaneous AC susceptibility, magnetisation and sample temperature measurements, which were made in collaboration with I. Kovacevic of LQM. A photo of the sample, which includes the additional components required to measure magnetisation and

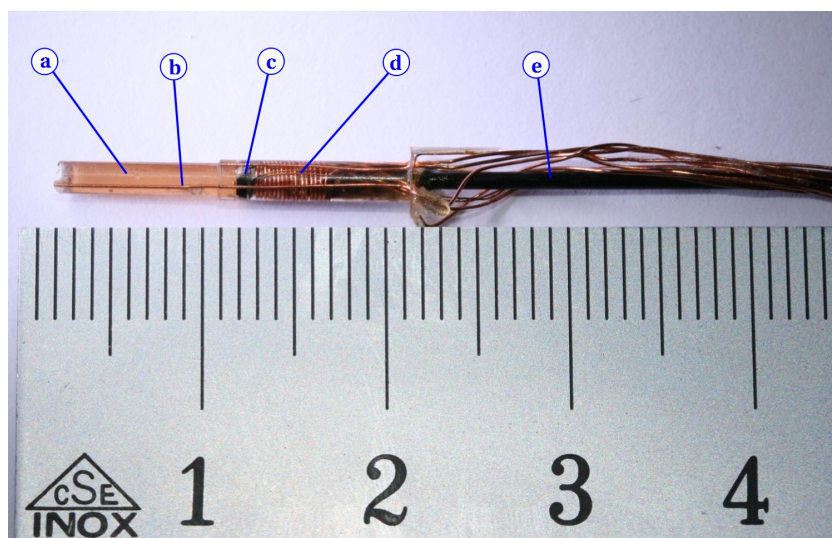


Figure 4.35: Photo of the sample used to measure simultaneous AC susceptibility, magnetisation and magnetocaloric effect. (a) $10 \times 1.2 \times 1.2$ mm sample. (b) $200 \mu\text{m}$ diameter copper wires for thermalisation. (c) Hall probe. (d) Thermometer mounted inside a groove cut out of (e) the carbon fibre support rod. The thermometer is wrapped in its leads to ensure a good thermal contact with the Stycast W19 epoxy resin that encapsulates all components.

4.5 Ferromagnetic Spin-Glass

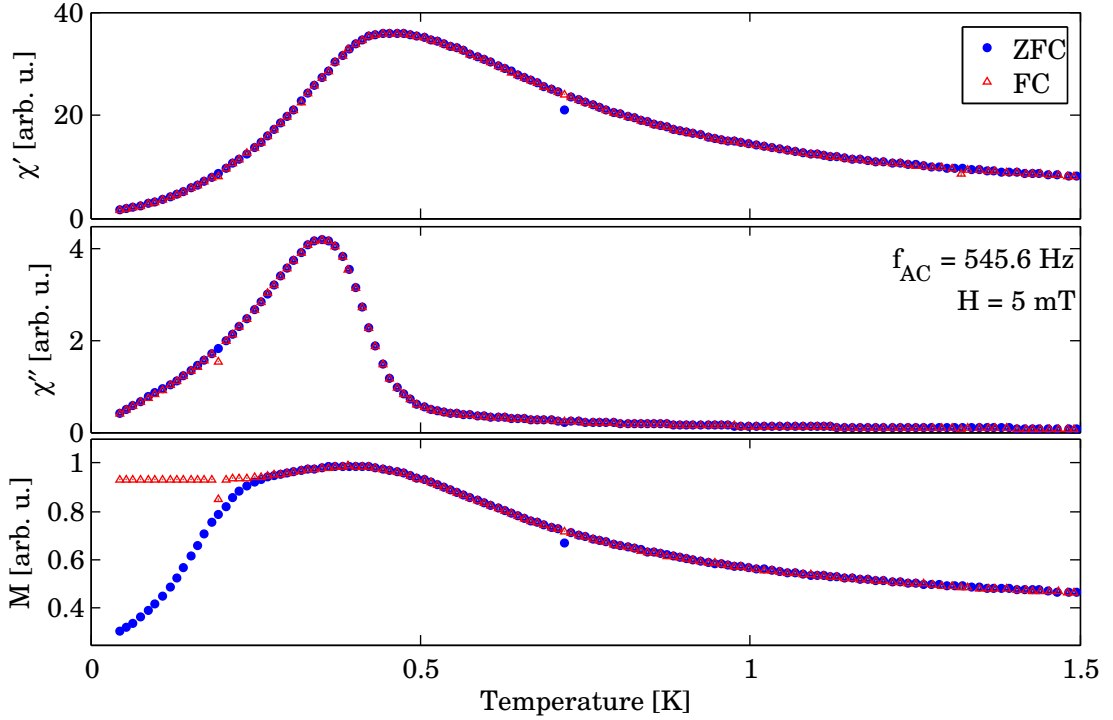


Figure 4.36: Temperature dependent ZFC and FC AC susceptibility and magnetisation measured simultaneously in $\text{LiHo}_{0.50}\text{Er}_{0.50}\text{F}_4$. The magnetisation shows a broad maxima at the same position as the peak in χ'_{zz} and a FC-ZFC splitting at a temperature similar to the second peak in χ''_{xx} (cf. Fig. 4.27 on page 105).

temperature, is shown in Fig. 4.35. The measurement of the magnetisation involves gluing a commercial GaAs Hall effect chip (c) directly on to the top surface of the $1.2 \times 1.2 \times 10$ mm single crystal of $\text{LiHo}_{0.50}\text{Er}_{0.50}\text{F}_4$ (a), as has been done in measurements on $\text{LiHo}_x\text{Y}_{1-x}\text{F}_4$ [84]. The length of the sample is along the crystallographic c-axis, so that when placed into a longitudinal susceptometer, the DC field is along this direction and perpendicular to the surface of the Hall probe. A bare chip RuO_2 thermometer (d), measuring roughly $2 \times 1 \times 0.3$ mm, was placed several mm above the Hall probe, into a groove cut out of a 1.5 mm diameter carbon fibre rod (e), which is used to hold the sample in place inside the AC susceptometer. The thermometer and lower end of the carbon fibre rod are wrapped with the copper leads of the thermometer to ensure a good thermal contact between the thermometer and the Stycast W19 which encapsulates all the components. The susceptibility was measured as usual inside one of the vertical susceptometers and the Hall effect was measured by applying 1 mV ($\sim 1 \mu\text{A}$) at 77 Hz and measuring the resulting Hall voltage using a Signal Recovery 7270 lock-in amplifier.

As a means of checking that the simple magnetometer functioned correctly, the field-cooled (FC) and zero-field-cooled (ZFC) temperature dependence of the sample was measured in a field of 5 mT and is shown in Fig. 4.36. The complex AC susceptibility is plotted in the top two panels and the magnetisation is given in the bottom panel. At $T \sim T_g$ there is a broad bump in the magnetisation, but there is no splitting until a lower temperature, which corresponds to

the low temperature peak in χ''_{xx} (cf. Fig. 4.27 on page 105).

This data is consistent with two physically distinct transitions. At $T_g^{Ho} \sim 0.47$ K there is a freezing to some kind of cluster-glass, where there exist large ferromagnetic clusters which freeze out. This does not necessarily have to result in a visible FC-ZFC splitting, as it is possible that the clusters are very easily aligned by a field. At the lower temperature $T_g^{Er} \sim 0.25$ K the remaining spins freeze into something reminiscent of a conventional spin-glass and therefore there is a FC-ZFC splitting.

Studying the field-dependent magnetisation using this setup requires particular care, as the signal will be a combination of both the magnetisation of the sample and a measure of the external field. In order to determine the magnetisation of the sample, the contribution of the external field must be removed. This has been done by measuring the response from the sample at 6 K and assuming that the magnetisation is much smaller for a given field than at low temperatures. It should be noted that this approach is not perfect as the sample still has a finite magnetisation in field when paramagnetic.

The first scans performed consist of a hysteresis loop taken at 50 mK using a slow ramp rate of 1.6 mT min^{-1} and are shown in Fig. 4.37, which displays χ'_{AC} , χ''_{AC} , T_{sample} and M from top to bottom. The overall shape of the magnetisation hysteresis loop is generally consistent with that of a spin glass; there is an S-shape virgin magnetisation curve and an isothermal remanent magnetisation when the field is ramped from large absolute values back to zero. Curiously, the virgin magnetisation curve does not stay within the hysteresis loop; the magnetisation increases faster once the system has been in the field-polarised state. This is in agreement with both the AC susceptibility and magnetocaloric effect, which clearly show a difference of behaviour between the two states.

The hysteresis loop indicates that the system is certainly not a *pure* spin-glass, where it is very difficult to saturate the magnetisation. Here, it appears that saturation is achieved relatively quickly after rapid rise in magnetisation observed at the same field as the peak in AC susceptibility and sample temperature. It seems likely that this step in magnetisation in the scan after ZFC is due to the alignment of the Ising-like clusters along the field direction. The remaining increase in magnetisation after this event is probably due to the polarisation of any remaining spins which are not involved in the clusters. Once the clusters have been aligned it appears that it is easier to change their orientation than it was when they were frozen in a random configuration, which leads to the steeper slope in the low-field magnetisation.

The really interesting effect observed in the peak in susceptibility is that it depends heavily on ramp rate, even for slow ramp rates of $< 1 \text{ Oe/s}$, as can be seen in Fig. 4.38. The figure shows field scans with ramp rates ranging between 0.2 and 100 mT per minute. The left side of the figure shows the low-field region, up to 0.05 T, corresponding roughly to the peak in χ_{AC} , and the right side shows the high field relaxation of the sample after the peak. The AC susceptibility and magnetocaloric effect increase with increasing ramp rates and are pushed to higher fields. The magnetisation is stretched out, initially unable to keep up with the fast

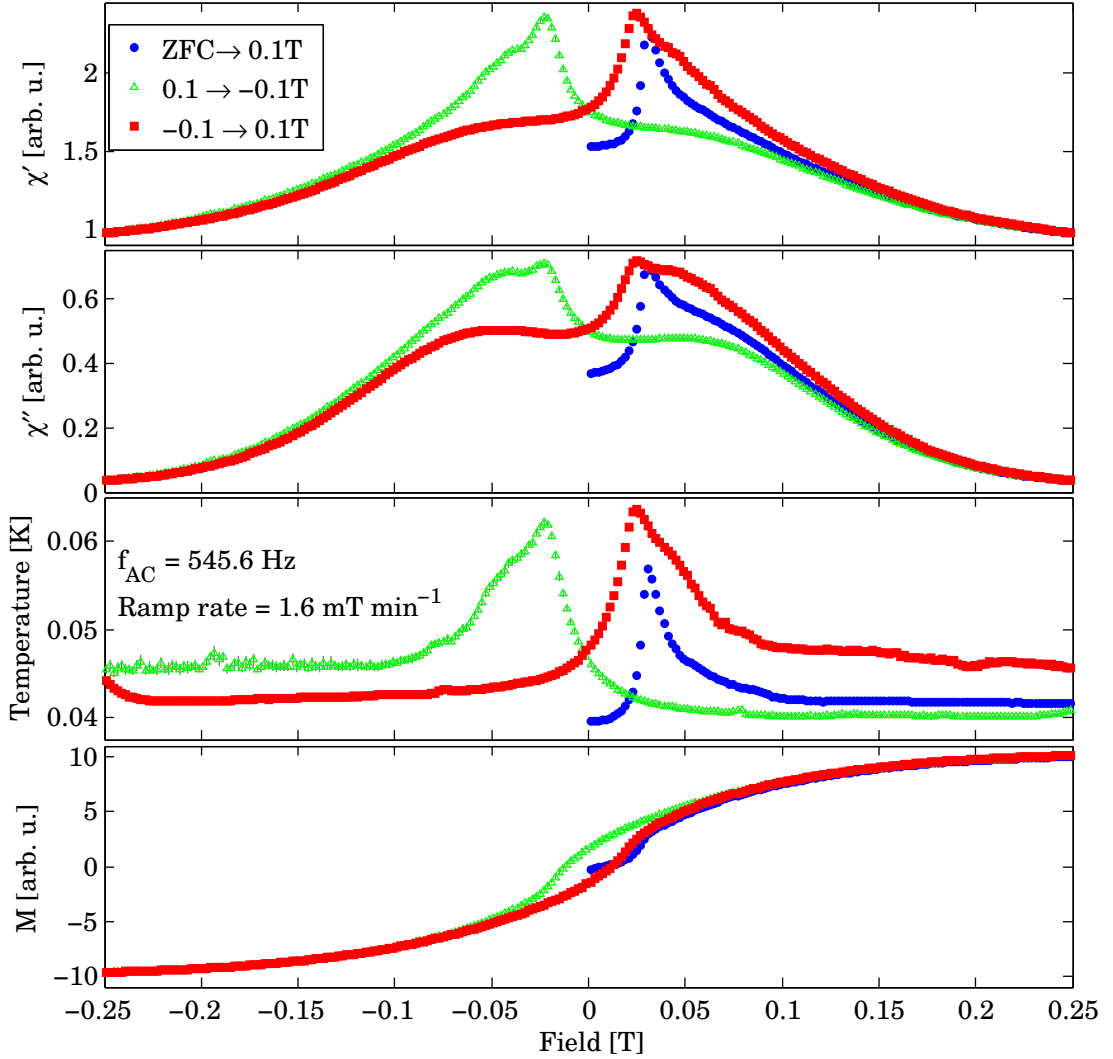


Figure 4.37: Hysteresis scan from a ZFC state in $\text{LiHo}_{0.50}\text{Er}_{0.50}\text{F}_4$, showing the real and imaginary part of χ_{AC} , sample temperature and magnetisation (from top to bottom). The onset of the peaks in χ_{AC} and T_{sample} coincide with a kink in magnetisation, and when the former two peak, a second kink is observed in the magnetisation. The slope of dM/dH is maximum while the susceptibility and temperature increase rapidly, just before the peak.

ramping fields, and then once the temperature begins to rise, suddenly starts increasing. The rate of increase of the magnetisation, dM/dH , in this region increases with the ramp rate.

In these scans, the low field magnetisation appears to decrease for the fastest ramp rates. This is likely not a physical effect and probably due to an imperfect subtraction of background coupled with a quasi-static magnetisation. The magnetisation, magnetocaloric effect and susceptibility features are all triggered by some kind of a critical field $H_c \sim 0.03$ T. It is interesting to note that while there is a very large difference in the high field ($\gtrsim 0.05$ T) susceptibility for different ramp rates, the difference in magnetisation is much smaller. Indeed,

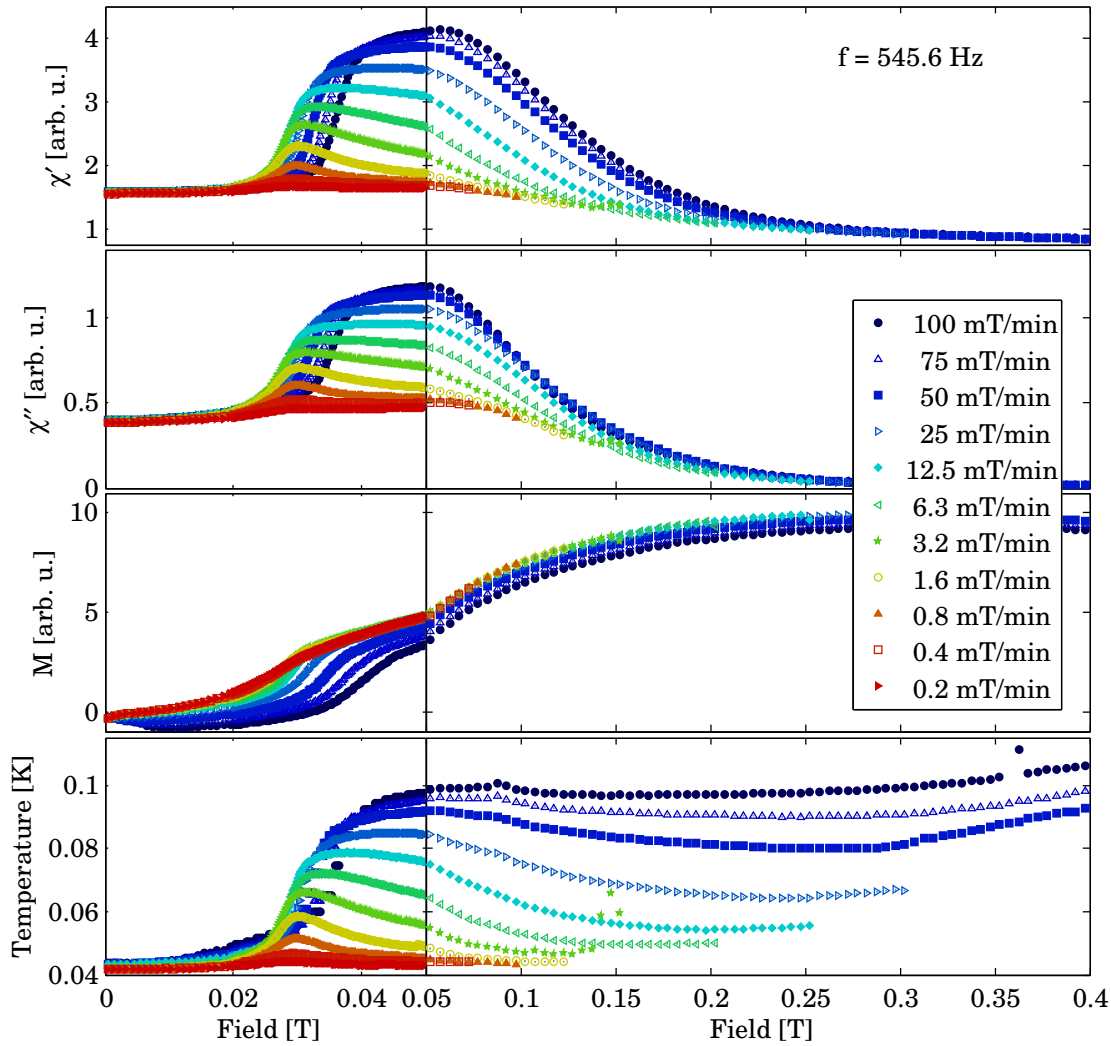


Figure 4.38: H_z field ramp rate dependence of (from top to bottom) AC susceptibility, sample temperature and magnetisation in $\text{LiHo}_{0.50}\text{Er}_{0.50}\text{F}_4$.

it seems as if the field dependence of the magnetisation at these fields is identical, but with a rate dependent constant offset.

The data presented thus far indicate that, after a critical field H_c , a thermal runaway begins. In order to study this thermal runaway process, a somewhat unorthodox scan was attempted. First, the field was ramped up to a value between 0.02 and 0.03 T. Upon reaching this value the field scan was stopped and the susceptibility, temperature and magnetisation were all measured as a function of time over the following hour. These scans are shown in Fig. 4.39, where the black plus signs correspond to the field scan and the coloured points to time scans started once the field indicated in the legend was reached. Once the field ramp is stopped, the temperature, AC susceptibility and magnetisation all continue to increase for around 100 seconds. The AC susceptibility and temperature then peak and relax slowly over more than

4.5 Ferromagnetic Spin-Glass

1000 seconds. The magnetisation does not have any prominent features and appears to be relaxing towards a final value with the slope of the line, dM/dt , decreasing smoothly as time passes.

From all of the scans presented here, it is clear that the temperature of the sample and the AC susceptibility are very closely linked. A reasonable assumption is that the susceptibility is simply reflecting the temperature of the sample, as $\chi(T)$ increases as T increases and the change in T is reflected in the susceptibility. It is therefore possible that the susceptibility is essentially nothing more than a measure of temperature. This would imply that the true field dependent susceptibility remains flat and is negligible compared to the temperature dependent susceptibility. In order to test this conjecture, the temperature of the sample was changed by heating the Hall probe used for magnetisation measurements in zero field. This was achieved by supplying a large voltage through the hall probe and measuring the current passing through it in order to determine the heating power. The AC susceptibility and temperature of the thermometer are measured, both during 200 s long heat pulses and during the cooling of the sample, and are shown in Fig. 4.40.

As the heat is applied, the thermometer immediately jumps up in temperature, due to the better thermal coupling of the heater to the thermometer than the heater to the bulk of the sample. With the current sample configuration, this effect is unavoidable, as the thermal conductivity of the sample is much smaller than that of the Stycast epoxy. Excluding this jump, the susceptibility and the temperature follow identical curves both during the heat pulse and while cooling. For a heat pulse of 198 nW, the form of both the temperature and the susceptibility is very similar to that of a field scan with 1.6 mT per minute ramp rate.

The behaviour of heat pulses in zero-field raises an interesting question: is it possible ramp the field to just below H_C and increase the magnetisation of the sample simply by increasing its energy by heating? The experiment was carried out as follows. First, the field was ramped to $H < H_C$ at 1.6 mT per minute. Second, a heat pulse of 198 nW was applied for the time required to reach the peak in χ_{AC} observed at this ramp rate (~ 200 s). Then the heating was turned off and the relaxation of the sample was measured. During all steps, the AC susceptibility, temperature and magnetisation were all recorded and are shown in Fig. 4.41. The figure also contains a comparison with the data taken previously where no heat pulse was applied, (*cf.* Fig. 4.39).

The results show that in a non-zero field, the heat pulse is capable of increasing the sample temperature by a much larger amount than in zero-field. This could either mean that the specific heat is reduced dramatically in this small field, or that by applying the heat pulse, spins are more easily flipped by the field and release their Zeeman energy. The latter seems quite likely as the magnetisation does end up being higher than when no heat pulse is applied. It is also interesting that after the application of the heat pulse the magnetisation does not relax but remains constant.

There is a strong indication that the low field susceptibility, and possibly the concomitant

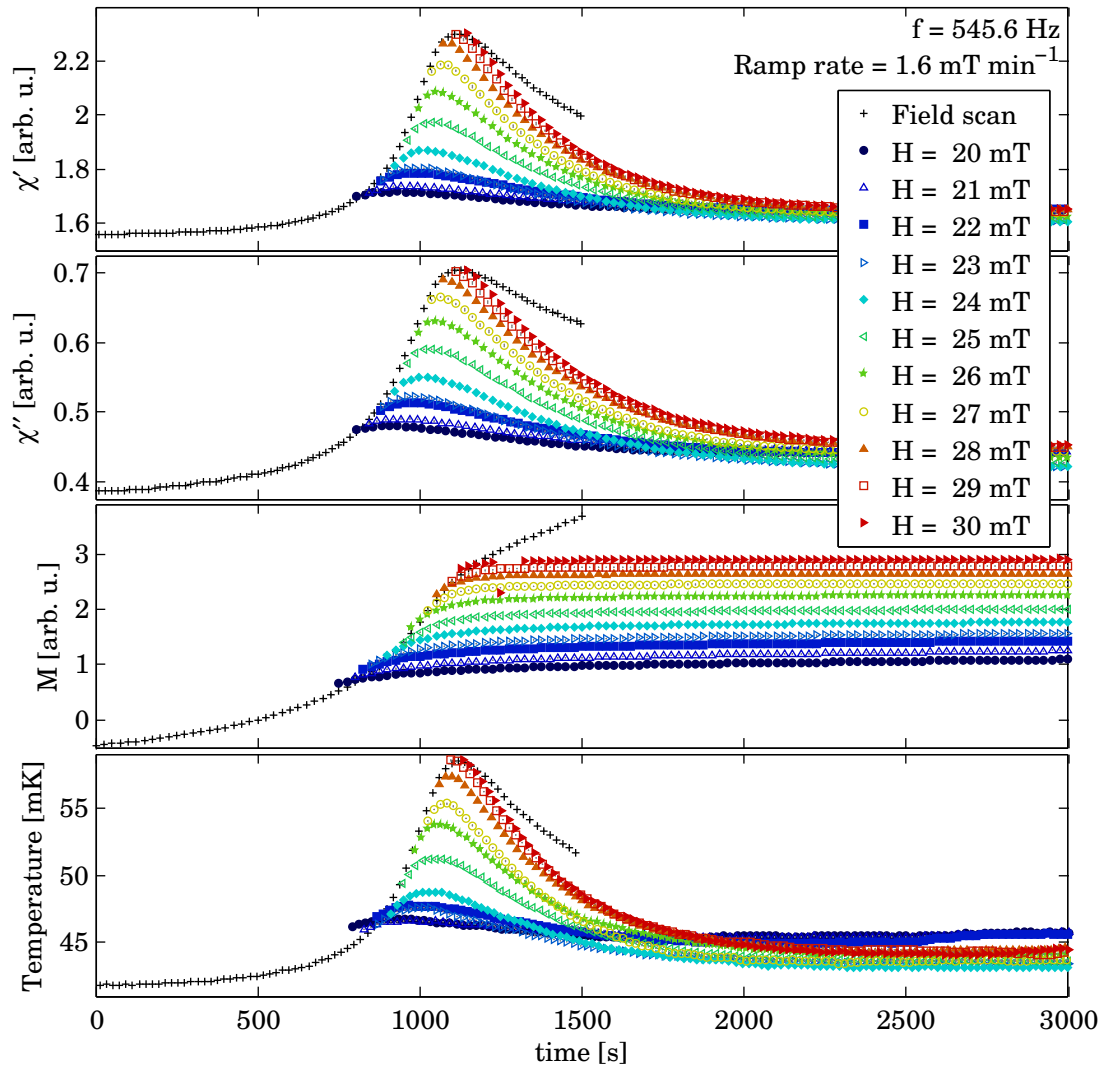


Figure 4.39: H_z field scans with 1.6 mT per minute ramp rate at 50 mK followed by time scans. The field is ramped up to the values in the legend (black pluses) and then the time-dependent response of the sample is measured (coloured points).

4.5 Ferromagnetic Spin-Glass

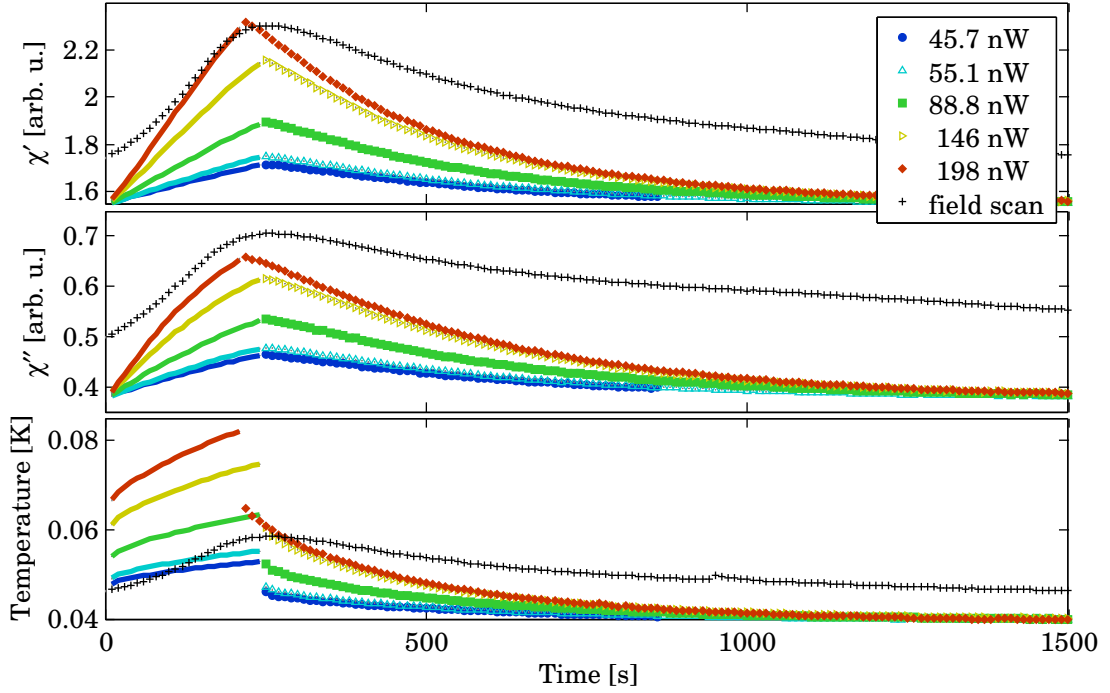


Figure 4.40: Local heating of $\text{LiHo}_{0.50}\text{Er}_{0.50}\text{F}_4$ in zero field at 50 mK followed by time scans showing the relaxation of temperature and susceptibility.

sharp features in magnetisation, are primarily a measure of the sample temperature. The situation is not quite so simple, as the data in Fig. 4.41 does indicate that the susceptibility is at least slightly field dependent. The temperatures from the time relaxation scans with (empty coloured points) and without (solid coloured points) heating cross coincide at 1500 s, whereas the susceptibility coincides around 200 s later. This behaviour makes really understanding what is happening inside the sample rather challenging.

An attempt to model this behaviour begins with the conjecture that the magnetocaloric effect is related to the Zeeman energy released as the Ho spins are flipped to align along the field direction:

$$E = -g\mu_B \mathbf{J}_i \cdot \mathbf{H}, \quad (4.35)$$

where \mathbf{J}_i is the moment of the spin/cluster i which is flipped. If the spins flip spontaneously, it follows that the rate of change of the magnetisation gives the number of spins which are flipping during that time $\sum \mathbf{J}_i \propto dM/dt$ and therefore

$$\dot{W}_z \propto \mathbf{H}(t) \frac{dM}{dt}, \quad (4.36)$$

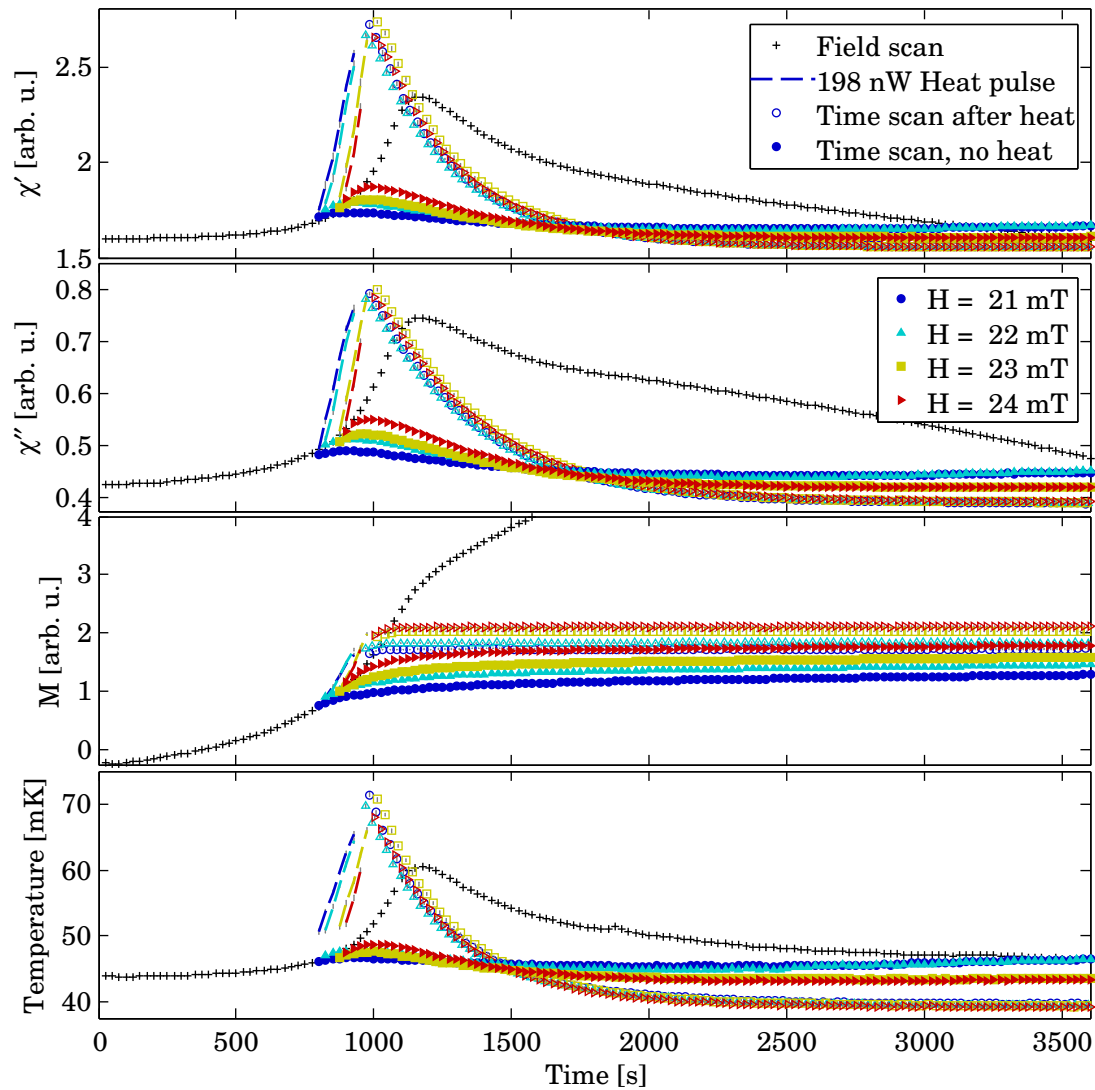


Figure 4.41: Field scan followed by sample heating pulse and subsequent relaxation while measuring AC susceptibility, magnetisation and temperature in $\text{LiHo}_{0.50}\text{Er}_{0.50}\text{F}_4$. The heat pulse was designed to achieve the same peak in susceptibility as the $1.6 \text{ mT} \cdot \text{min}^{-1}$ field scan. The data obtained without the heat pulse is also shown as a comparison to determine the effect of the heat pulse.

4.6 Antiferromagnetic Spin-Glass

allowing for the energy released to be calculated. In order to relate this to the properties being measured, the thermal conductivity of the sample along with its specific heat must be measured. This would allow for a model to be created, where, in principle, all of the quantities are known.

One important question relating to the thermal runaway, is whether it is a microscopic or macroscopic effect. In the case of a macroscopic effect, it would, in principle, be possible to optimise the sample environment to favour thermal conductivity. The net effect would be to keep the sample temperature relatively constant while ramping the field, thus revealing only the field-dependent behaviour. If the thermal runaway is microscopic on the other hand, this would not be possible, as the heat is being generated locally within the sample, and the limiting factor in cooling the sample is the thermal conductivity of the sample.

On the theoretical side, perhaps the key factor in understanding the underlying processes at work is to determine what makes the field of ~ 0.03 T special. There is a large chain of events which is triggered by this particular field and must therefore correspond to some physical change in the system. Given the glassy nature at low temperatures, it is likely that this corresponds to, for example, the field required to flip a single spin, or the smallest cluster present. Understanding this will certainly require additional work to determine what in the system should change at this field. Neutron scattering experiments, in particular small angle neutron scattering (SANS), could also give some insight into this by following the evolution of the ferromagnetic clusters throughout the thermal runaway.

4.6 Antiferromagnetic Spin-Glass

As x drops below 0.3 the AC susceptibility continues to progress towards an archetypal spin-glass signal. The peak in χ' sharpens and a well defined single peak emerges in χ'' . The frequency dependence of the freezing temperature is also very much what is expected for a model spin-glass, as is shown in Fig. 4.42. As has been done for previous samples, the left panel shows the data fit conforming to the expectation of Arrhenius behaviour and the right side to a critical scaling law. For this data set, the susceptibility has been measured while ramping the temperature both up and down, which shows a systematic difference in peak temperature of around 5 mK, likely due to thermalisation effects.

The Arrhenius behaviour give a frequency sensitivity of $\mathcal{K} = 0.068 \pm 0.005$, which has been determined by taking the average between the two scans, both of which fall within the error given for \mathcal{K} . This value is in line with other insulating spin-glasses [66]. For the fits in terms of critical scaling, the zero frequency glass temperature T_g was determined to be 0.205 ± 0.001 K for the scan down in temperature and 0.193 ± 0.001 K for the scan up. The fits give $\tau_0 \simeq 3.7 \times 10^{-7}$ s and $z\nu = 6.3$ for the scans made with decreasing temperature, and $\tau_0 \simeq 5.3 \times 10^{-7}$ s and $z\nu = 8.2$ for those made while ramping the temperature up. The values of the critical exponent are in line with Monte Carlo simulations, which predict $z\nu = 8$ [71] and the τ_0 is in line with other experimental studies of spin-glasses (e.g. Bontemps et al. [14] find

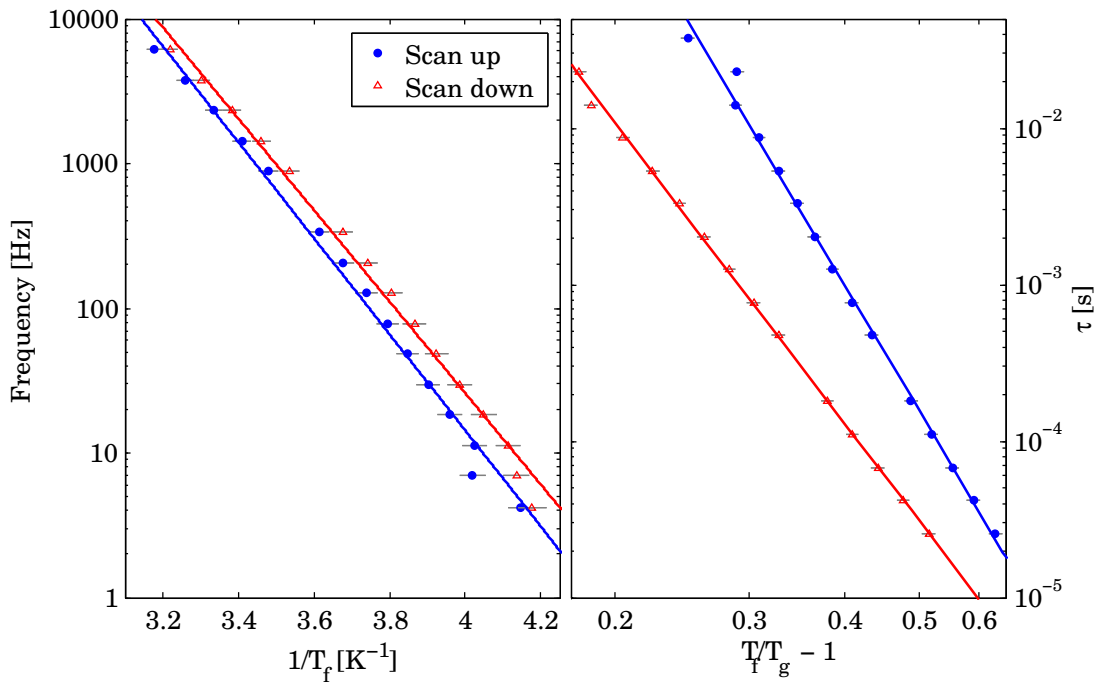


Figure 4.42: Frequency dependence of T_f in $\text{LiHo}_{0.25}\text{Er}_{0.75}\text{F}_4$ expressed in terms of [left] Arrhenius behaviour and [right] critical scaling. The data compares T_f extracted from scans ramping both up and down in temperature, which are offset by 5 mK, probably due to thermalisation issues.

$\tau_0 \approx 2 \times 10^{-7}$ s for $\text{Eu}_{0.4}\text{Sr}_{0.6}\text{S}$.

These results also demonstrate a clear problem with understanding and interpreting spin-glasses. The Arrhenius behaviour and critical scaling are incompatible with each other: if one were able to measure down to sufficiently small frequencies, one of the two would fail. In this case, the reason why they cannot be compatible is that the critical scaling implies a zero frequency transition at a finite temperature, so the freezing temperature must converge to this value at sufficiently small frequencies. The Arrhenius behaviour on the other hand, would show the same logarithmic dependence of T_f down to zero temperature. This raises a fundamental and, according to the literature, very much open question in spin-glasses: which of the two is correct. It is quite common to see Arrhenius behaviour used as a proof of a spin-glass state, even though it gives no information on the properties of the system and even gives completely unphysical energy barriers and characteristic times. Critical scaling on the other hand is well nested in theoretical predictions of spin glasses [71], and while such dynamics are observed in certain systems [72], it is quite common to see $T_f(f)$ considered only in terms of Arrhenius behaviour.

To study the correlations in the spin-glass phase, neutron scattering measurements were carried out on RITA-II at PSI. AC susceptibility was measured simultaneously *in-situ*, which as has been demonstrated in Section. 4.5.4, can be used as local thermometer of the sample.

4.6 Antiferromagnetic Spin-Glass

This gives an independent measurement of the of the sample temperature and not just the temperature of the copper sample holder. The sample was measured with the scattering plane being the $a - c$ plane with a 1 T horizontal magnet, allowing for the field to be aligned anywhere within the scattering plane. For these measurements the field was aligned along the crystallographic a -axis. The measurements were taken in mapping mode, taking advantage of the 9 analyser blades, using an incident neutron energy of 5 meV ($k = 1.55 \text{ \AA}^{-1}$).

To determine the type of correlations present in the spin-glass, three different positions in reciprocal space were measured: $\mathbf{Q} = (2, 0, 0)$, $\mathbf{Q} = (0, 0, 4)$ and $\mathbf{Q} = (1, 0, 0)$. The first two correspond to nuclear Bragg peaks, so are sensitive to ferromagnetic correlations and the final position corresponds to an antiferromagnetic Bragg peak position. Fig. 4.43 compares the scattering from these positions at base temperature, both with and without field, and at 1 K without field. The figure also shows a pseudo-colour map of scattered intensity centred around the $\mathbf{Q} = (1, 0, 0)$ position.

The scans around the nuclear positions (right side) indicate that there are no ferromagnetic correlations in the glassy state; the curves can be fit with Gaussian line-shapes and are independent of the temperature and field. The only slight exception is that in a DC field the intensity of the (0,0,4) Bragg peak increases slightly due to the spins polarising along the field direction. The polarisation of spins is not visible in the scans around the (2,0,0) Bragg peak, as the scattering vector and polarisation direction are parallel.

The $\mathbf{Q} = (1, 0, 0)$ position does have diffuse scattering along the \mathbf{Q}_l direction, corresponding to antiferromagnetic correlations, as can be seen in the top left panel of Fig. 4.43. The peak is fitted with a Lorentzian line shape, which would correspond to correlations which fall off as $e^{-r/\xi}$. The Fourier transform of this exponential decay of correlations gives a Lorentzian distribution, with the HWHM equal to the inverse spin-spin correlation length:

$$I \propto \frac{1}{1 + \mathbf{Q}^2 \xi^2}. \quad (4.37)$$

The increase in intensity seen at $\mathbf{Q} = (1, 0, 2)$ is due to the same magnetic scattering as this is also an antiferromagnetic position. To get a good fit, first the high field data is subtracted from the low field scan in order to remove the non-magnetic background. The curve is then fitted using two coupled Lorentzians with the same width, one centred at $\mathbf{Q} = (1, 0, 0)$ and the other at $\mathbf{Q} = (1, 0, 2)$, giving a correlation length of $\xi = 44 \pm 2 \text{ \AA}$.

The temperature and field dependence of the intensity of the $\mathbf{Q} = (1, 0, 0)$ peak has been measured by sitting at this point in reciprocal space and ramping the field and temperature while measuring the scattered intensity. The left side of Fig. 4.44 shows the temperature dependence and the right side shows the field dependence. The top panels show the scattered intensity, the middle panels χ' and the bottom panels χ'' .

By measuring the temperature-dependent susceptibility in both directions, the relative tem-

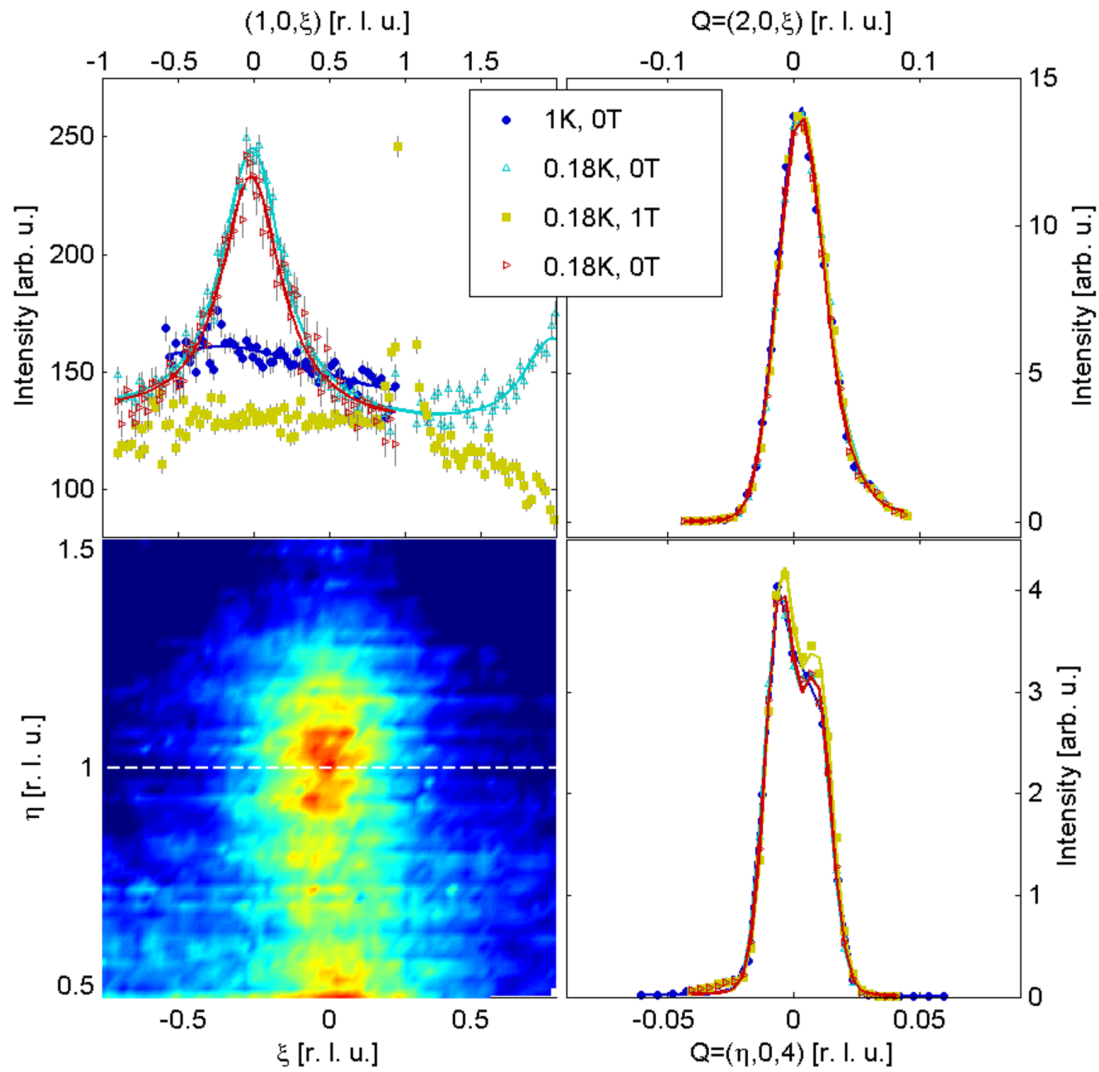


Figure 4.43: Neutron scattering data on $\text{LiHo}_{0.25}\text{Er}_{0.75}\text{F}_4$. [top left] Q_I scans across the $Q = (1,0,0)$ position, showing a broad Lorentzian component, corresponding to antiferromagnetic spin correlations with $\xi = 44 \pm 2 \text{ \AA}$. Scans around the [top right] $(2,0,0)$ and [bottom right] $(0,0,4)$ Bragg peaks indicating an absence of ferromagnetic correlations or order. [bottom left] Pseudo-colour map of scattering intensity within the $a-c$ plane.

4.6 Antiferromagnetic Spin-Glass

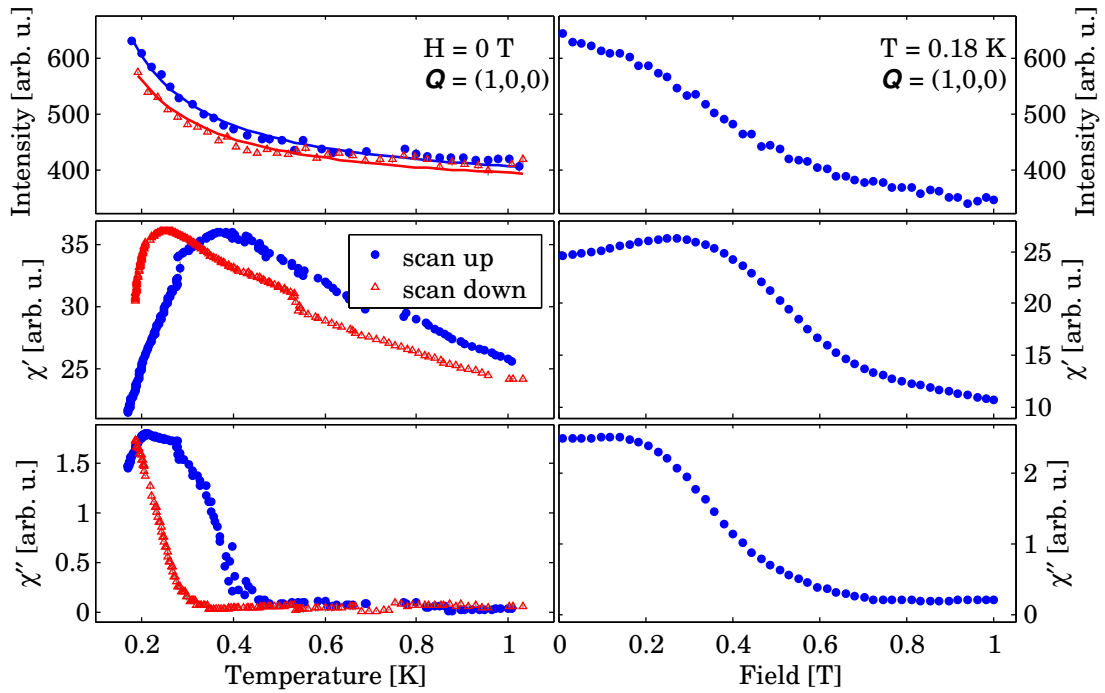


Figure 4.44: [left] Temperature and [right] H_c field dependence of the spin-glass state in $\text{LiHo}_{0.25}\text{Er}_{0.75}\text{F}_4$ determined by simultaneous neutron scattering at $\mathbf{Q} = (1, 0, 0)$ and AC susceptibility. Temperature scans show a continuous decrease in spin-spin correlations which can be described by a power law. The field dependence shows an anomaly at $H_a \sim 0.2$ T in the reduction of spin-spin correlations at the field where χ'' peaks.

perature lag of the sample to the dilution fridge can be seen. There is a difference in the peak position of around 0.1 K, which implies that at these ramping rates, the sample lags the temperature reading by roughly 50 mK. This effect is much less noticeable in the neutron scattering data due to the relatively small temperature dependence of scattered intensity. The scattered intensity decreases monotonically and can be described well by a power law of the form $I = I_0 T^{-1}$. In the field scan, the intensity decreases continuously with an anomaly in the scattered intensity at a field of around 0.2 T, which seems to coincide with the peak in χ'' .

One possible location where a ferromagnetic signal could be seen is from a butterfly-like correlation, as was observed in $\text{LiHo}_{0.50}\text{Er}_{0.50}\text{F}_4$ (*cf.* Section 4.5.1 and in particular Fig. 4.19 on page 96). The top panel in Fig. 4.45 shows the antiferromagnetic correlations at $\mathbf{Q} = (1, 0, 0)$ and extends all the way up to $\mathbf{Q} = (2, 0, 0)$ and down to $\mathbf{Q} = (0.5, 0, 0)$. Scans were not taken at larger \mathbf{Q} , as powder lines from the aluminium cryostat and copper sample enclosure are present and would make the analysis more complicated without bringing much additional information. There appears to be a slight peak in intensity centred around $\mathbf{Q} \sim (1.75, 0, 0)$, which qualitatively seems to have the correct shape for the needle-like Ising clusters seen in $x = 0.50$. Furthermore the intensity increases as $\mathbf{Q} \rightarrow (0, 0, 0)$ which would also correspond to ferromagnetic correlations.

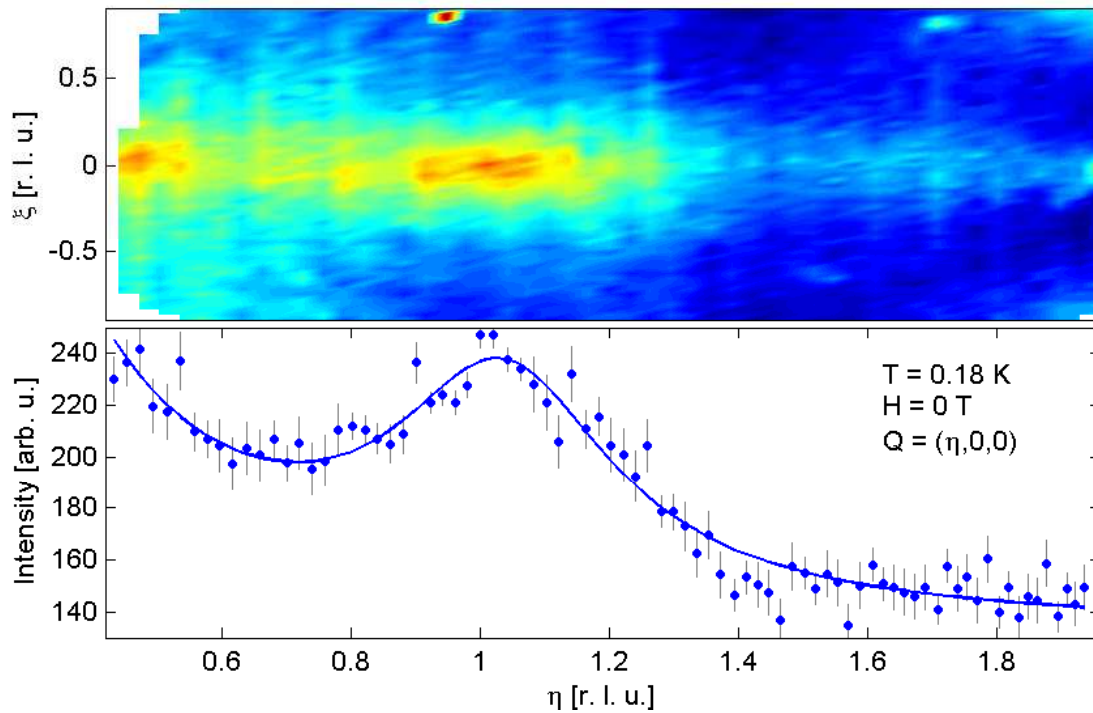


Figure 4.45: Search for ferromagnetic correlations in $\text{LiHo}_{0.25}\text{Er}_{0.75}\text{F}_4$. [top] Pseudo-colour map of scattered intensity between $(0.5, 0, 0)$ and $(2, 0, 0)$ and [bottom] fits to the Q_η line assuming only scattering centred at $Q = (0, 0, 0)$ and $Q = (1, 0, 0)$.

In order to determine whether or not either of these two features is truly due to ferromagnetic correlations, the $Q = (\eta, 0, 0)$ data is fitted with a combination of Lorentzian line-shapes (bottom panel of Fig. 4.45). The best fit consists of two Lorentzians, one centred at $Q = (0, 0, 0)$ and the other at $Q = (1, 0, 0)$, corresponding to ferromagnetic and antiferromagnetic correlations respectively. There is no evidence of short ranged correlations of scans centred around $Q = (2, 0, 0)$ – the apparent peak in the pseudo-color plot seems to be due to a dip in intensity at $Q = (1.4, 0, 0)$. Although the fit does reproduce the data very well, it seems strange that there would be ferromagnetic correlations extending from $Q = (0, 0, 0)$ which are not present at $Q = (2, 0, 0)$. One possible explanation for this is that the instrument is beginning to see the direct neutron beam at small Q resulting in an increased intensity.

The extracted antiferromagnetic correlation length from this data along the a -axis is $\xi = 13 \pm 1 \text{ \AA}$, which combined with the overall shape of the diffuse scattering and the c -axis correlation length of $\xi = 44 \pm 2 \text{ \AA}$, gives ellipsoidal *clusters* of correlated spins. This gives a cluster volume of $V \simeq 2.4 \times 10^3 \text{ \AA}^3$, implying there are around 30 magnetic ions per cluster.

5 Conclusion

5.1 $\text{LiHo}_x\text{Er}_{1-x}\text{F}_4$

The phase diagram of $\text{LiHo}_x\text{Er}_{1-x}\text{F}_4$ shows several distinct phases, all of which have a unique low temperature glassy behaviour. Compounds which corresponded to an embedded spin-glass, a ferromagnetic spin-glass and an antiferromagnetic spin-glass were investigated using a combination of AC susceptibility and elastic neutron scattering. Table 5.1 shows a summary of the phase transitions observed, and in the case of the spin-glasses the associated values obtained from fitting the spin-glass to an Arrhenius law and critical scaling dynamics. All of the compounds seem to show glassy behaviour, and in those where T_f was extractable, the frequency sensitivity \mathcal{K} is within the observed values for insulating spin-glasses. All of the spin-glasses forming in compositions where there is no long-range order can be well fit using a critical scaling approach and in general have a critical exponent similar to the value of $z\nu = 8$ found by Monte Carlo simulations [71]. For the embedded spin-glass phases, the fits are not very good and the values of τ_0 and $z\nu$ vary greatly, which could imply an unconventional spin-glass state.

A graphical representation of the experimental phase diagram is shown in Fig. 5.1. The points are experimental values of the various phase transitions, as determined by AC susceptibility. The phase diagram has been drawn to show 5 distinct phases, ferromagnetic (dark blue), ferromagnetic spin-glass (light blue), antiferromagnetic spin-glass (yellow), antiferromagnetic (AFM) and a fifth phase (green) corresponding to some kind of embedded spin-glass. This latter region has been left with a question mark as it has only been seen through AC susceptibility and did not show up in the neutron scattering experiments.

The embedded spin-glass state shows the ferromagnetic order observed in $\text{LiHo}_x\text{Y}_{1-x}\text{F}_4$, with $T_C(x)$ decreasing faster than for Y doped compounds. Although this was anticipated and was even one of the reasons for adding magnetic Er^{3+} ions in the place of non-magnetic Y^{3+} , it is not explained by mean-field theory. According to mean-field calculations, at high temperatures, the Er ion is polarised by the mean-field originating from the Ho ions, effectively adding a small longitudinal field rather than a transverse one. Investigations involving diago-

Chapter 5. Conclusion

x	T_c [K]	$T_f(1\text{kHz})$ [K]	\mathcal{K}	T_g [K]	$z\nu$	τ_0 [s]
1	1.53	N/A	N/A	N/A	N/A	N/A
0.860	1.20	0.083	0.077	-	-	-
0.790	1.04	0.191	0.044	0.043	12.9	1.3×10^3
0.765	0.95	0.197	0.080	0.174	2.2	1.6×10^{-6}
0.700 ¹	0.85	0.280	0.025	0.156	10	1.3×10^{-5}
0.675	0.815	0.347	0.027	0.228	1.7	1.7
0.570	N/A	0.510	0.024	0.430	9.0	6.2×10^{-11}
0.540	N/A	0.474	0.046	0.396	6.4	4.3×10^{-9}
0.500 ²	N/A	0.471	0.049	0.405	4.1	1.5×10^{-7}
0.500 ¹	N/A	0.437	0.042	0.369	7.0	1.0×10^{-9}
0.470	N/A	0.434	0.054	0.299	6.2	6.4×10^{-9}
0.250	N/A	0.288	0.069	0.199	8.2	3.7×10^{-7}
0.200	N/A	0.286	0.070	0.196	7.5	4.2×10^{-7}
0.100	N/A	0.138	0.080	0.079	8.6	1.3×10^{-5}
0.060	0.342	(0.15)	-	-	-	-
0	0.375	N/A	N/A	N/A	N/A	N/A

¹ Single crystal measurements of χ_{xx} .

² Single crystal measurements of χ_{zz} .

Table 5.1: Summary of transition temperatures and spin-glass parameters in $\text{LiHo}_x\text{Er}_{1-x}\text{F}_4$

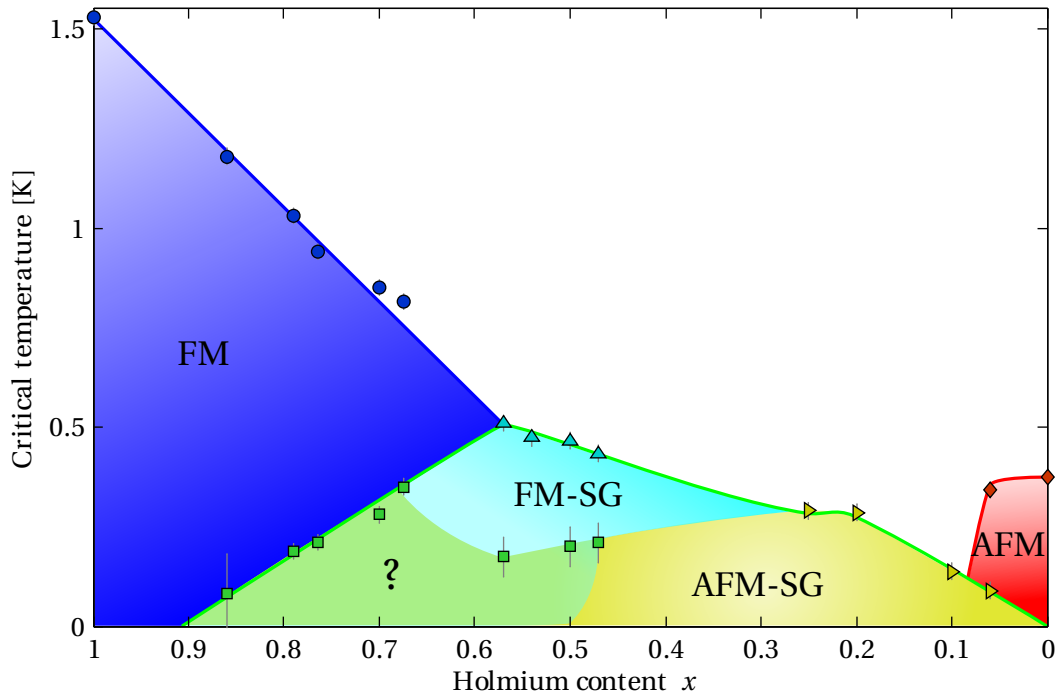


Figure 5.1: Experimental phase diagram of $\text{LiHo}_x\text{Er}_{1-x}\text{F}_4$ indicating 5 possible unique phases.

nalising the spin-half Hamiltonian on a cluster of 9 spins, along with a direct diagonalisation of an Er ion surrounded by its nearest neighbour Ho ions, both in the presence of the LiHoF_4 mean-field, confirm the mean-field result.

The spin-glass state in these compounds appears to be unconventional, as it neither adheres the Arrhenius law nor critical scaling. At high temperatures the data can be fitted by either of the two methods, but as the temperature is decreased below 0.27 K, the slope of the Arrhenius-fit changes and the peak temperature depends much more on frequency. Similar behaviour is observed in the anti-glass phase of $\text{LiHo}_{0.045}\text{Y}_{0.955}\text{F}_4$ studied by Ghosh *et al.* [31, 32]. Neutron scattering experiments failed to see any evidence of this glassy state in the diffuse scattering signal.

At $x = 0.50$ a spin-glass state is observed, which appears to be a combination of a ferromagnetic and an antiferromagnetic spin-glass. Neutron scattering data shows ferromagnetic correlations which have the distinctive “butterfly” shape seen in critical scattering of Ising ferromagnets. This scattering pattern corresponds to large needle-like domains with very large correlation lengths along the Ising axis and a much shorter correlation length in the $a - b$ plane. In this case the correlation length in the plane is $\xi = 16 \pm 1 \text{ \AA}$. There is an indication of antiferromagnetic correlation of spins pointing along the c -axis. As this scattering is seen on the $\mathbf{Q} = (0, 0, 2)$ peak, the scattering drops to zero intensity due to the neutron polarisation factor, but can be fit by the combination a Lorentzian and $\sin^2 \varphi$, where φ is the angle between the spins and the scattering vector.

The frequency dependence of T_f in AC susceptibility shows typical spin-glass behaviour for both χ_{xx} and χ_{zz} measured on single crystals. There is a very large difference in the features seen in these two measurements, which reinforces the argument of two co-existing spin-glass states, as Ising spins do not show up in χ_{xx} . When a DC field is applied parallel to the Ising axis, a very sharp peak is observed at a field of $H_c \sim 0.03 \text{ T}$ and coincides with a rapid increase of the magnetisation. Simultaneous measurements of the AC susceptibility, magnetisation and sample temperature were used to understand this phenomena.

The peak in susceptibility has a large associated magnetocaloric effect and shows a hysteresis effect – even in AC susceptibility. Moreover the peak depends not only on the AC frequency but also the rate at which the DC field is being ramped; the peak increases in intensity and shifts to slightly higher fields as the ramp rate is increased. The magnetisation also shows ramp rate dependence, with the scan initially being stretched out and the sharp increase at H_c becoming more pronounced for higher ramp rates. More interesting still, if the field is ramped up to a value just below the peak field and then stopped, the system still responds as if the field were still being ramped.

As x drops even lower, the ferromagnetic spin-glass disappears and is replaced by one with antiferromagnetic correlations. At the same time, the susceptibility sharpens, revealing a singular peak which is consistent with a single phase spin-glass. The frequency dependence of the freezing in the antiferromagnetic spin-glass compounds is well described by either

an Arrhenius law or critical scaling. Neutron scattering finds antiferromagnetic correlations, which correspond to elliptical clusters of spins, with a c -axis correlation length of $\xi = 44 \pm 2 \text{ \AA}$ and an a -axis one of $\xi = 13 \pm 1 \text{ \AA}$.

5.2 Dilution SQUID

The work on the dilution SQUID project is at a state where all the individual components required to make a magnetometer at ultra low temperatures function correctly. The piezomotor has been shown to be capable of moving the sample at an acceptable rate without perturbing the SQUID sensor. The pickup coils are mounted inside the IVC can in a way which reduces vibrations relative to the superconducting magnet to a sufficiently low level to allow for high sensitivity measurements. The pickup system, including the two-part flux transformer has been shown to be effective at transferring the signal to the SQUID sensor. Finally, the thermal decoupling between the sample and the piezomotor has been demonstrated to be sufficient for operation at temperatures $< 100 \text{ mK}$. This proof-of-concept work is encouraging and indicates that the system should be able to work in the future without any major issues.

6 Outlook

6.1 $\text{LiHo}_x\text{Er}_{1-x}\text{F}_4$

This thesis has focused on giving an overview of the behaviour observed in $\text{LiHo}_x\text{Er}_{1-x}\text{F}_4$. There are therefore quite naturally a large number of possibilities for future experimental and theoretical studies resulting from the work presented here.

Starting with the high- x phases, where re-entrant spin glass phases are observed, there is a clear need for theoretical work to determine the behaviour of dT_C/dx . Perhaps the first step would be to carry out classical Monte Carlo calculations in order to see whether it is domain wall formation/pinning which reduces T_C .

In the spin-glass phases, the most interesting region appears to be the compounds with $x \sim 0.5$, where the spin-glass consists of ferromagnetic clusters. Future research should begin by addressing two phenomena. The first is to complete the understanding of the thermal runaway, which requires the specific heat to be measured. With this information, it is very likely that a very solid description of the jump in magnetisation and resulting magnetocaloric effect can be obtained. The second aspect which would be interesting to investigate is the possible antiferromagnetic correlations seen in neutron scattering. Polarised neutrons would be the ideal probe to determine the magnetic properties, but may not be possible, as the ferromagnetic clusters might depolarise the beam. If an experiment using polarised neutrons is not possible, additional experiments on an instrument which has a detector measuring a large Q space will be sufficient to gain insights into the correlations.

6.2 Dilution SQUID

The dilution SQUID is ready to begin testing, calibration and be used for routine measurements. Calibration is to be done using a paramagnetic salt, with Curie behaviour down to below 20 mK (such as CMN salt) and scaled with data measured in a commercial SQUID magnetometer. This allows for a voltage in a dipole curve to be converted into a magnetic moment

Chapter 6. Outlook

very accurately. The immediate use for the magnetometer is to measure DC magnetisation in $\text{LiHo}_x\text{Er}_{1-x}\text{F}_4$, and as has been done with AC susceptibility, measure other interesting samples which pass through the lab.

For the longer term, there are plans to build a pickup coil which has been optimised for AC susceptibility, allowing for low frequency measurements of AC susceptibility. The modular design allows for the SQUID to be used for even more exotic measurements, such as AC magnetoelectric effect measurements.

A $\text{LiHo}_x\text{Er}_{1-x}\text{F}_4$ Preparation and Quality Control

10 g batches of ${}^7\text{LiF}$ were prepared by dissolving ${}^7\text{LiOH}_x\text{H}_2\text{O}$ (${}^7\text{Li}$, 99.9%+, Cambridge Isotopes Laboratories, Inc.) in 20 ml concentrated aqueous HNO_3 . This solution was evaporated to dryness in a Teflon beaker on a sand bath at 200 °C. The obtained nitrate was dissolved in 15 ml distilled water. The fluoride was precipitated by the addition of 10 ml concentrated aqueous HF acid and evaporated to dryness on a sand bath at 200 °C. An additional 20 ml of HF acid was added and again evaporated to dryness. The dried powder was transferred into a glassy carbon crucible and fluorinated under an Ar/HF mixture at 450 °C for 20 hours. The obtained powder was kept under nitrogen.

10 g batches of ReF_3 ($\text{Re} = \text{Ho, Er}$) were prepared by dissolving $\text{Ho}_2\text{O}_3 / \text{Er}_2\text{O}_3$ in 20 ml concentrated aqueous HNO_3 . Those solutions were evaporated to dryness in a Teflon beaker on a sand bath at 200 °C. The obtained nitrates were dissolved in 15 ml distilled water. The fluorides were precipitated by the addition of 10 ml concentrated aqueous HF acid and evaporated to dryness on a sand bath at 200 °C. An additional 20 ml of HF acid was added and again evaporated to dryness. The dried powders were transferred into glassy carbon crucibles and fluorinated under an Ar/HF mixture at 450 °C for 20 hours. The obtained powders were kept under nitrogen.

Samples of ${}^7\text{LiHo}_x\text{Er}_{1-x}\text{F}_4$ were prepared from mixtures of ${}^7\text{LiF}$, HoF_3 and ErF_3 in a 53:47 (Li:Re) ratio. The salts were mixed and transferred into a glassy carbon Bridgman ampoule. The mixture was melted at 880°C in a Bridgman furnace under inert gas and then cooled to room temperature over the course of 7 days.

The purity of the resulting small single crystals was checked by powder X-ray diffraction. The Ho to Er ratio was checked by EDX measurements which is capable of determining the relative concentrations with an error of 0.5 %. An example EDX spectrum is shown in Fig. A.1. The relative amplitudes of the Ho and Er peaks are used to determine the ratio between the two.

Some ratios of Ho:Er proved difficult to synthesise. In particular, when growing $\text{LiHo}_{0.90}\text{Er}_{0.10}\text{F}_4$, the crystal showed incursions of LiF. This can be seen in Fig. A.2, which shows a scanning

Appendix A. $\text{LiHo}_x\text{Er}_{1-x}\text{F}_4$ Preparation and Quality Control

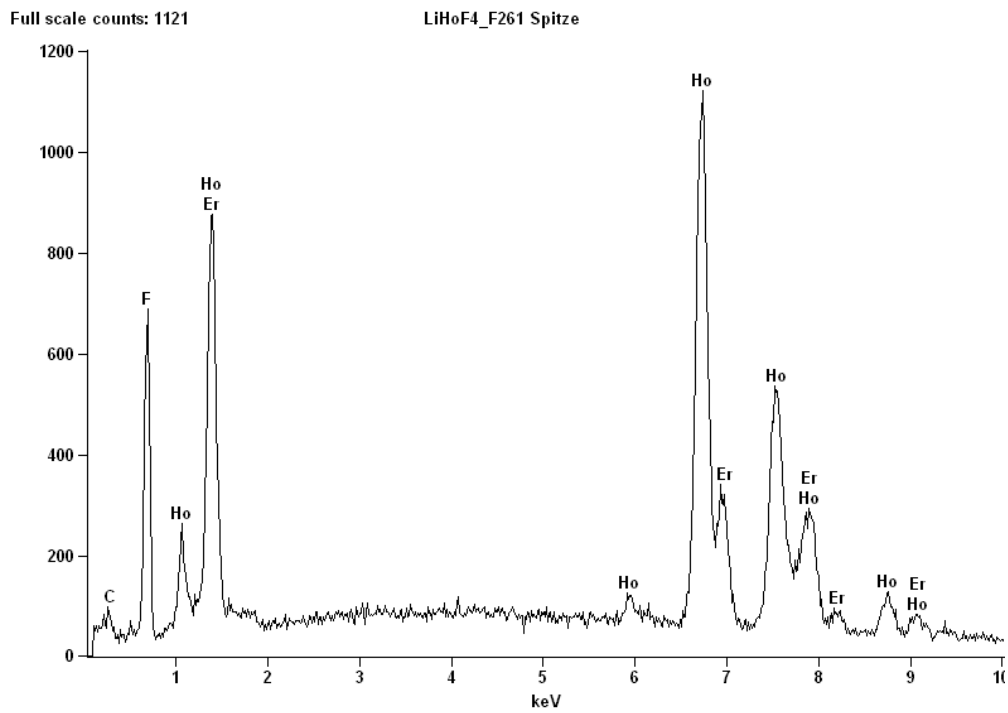


Figure A.1: EDX spectrum of $\text{LiHo}_x\text{Er}_{1-x}\text{F}_4$ used to determine the Ho:Er ratio.

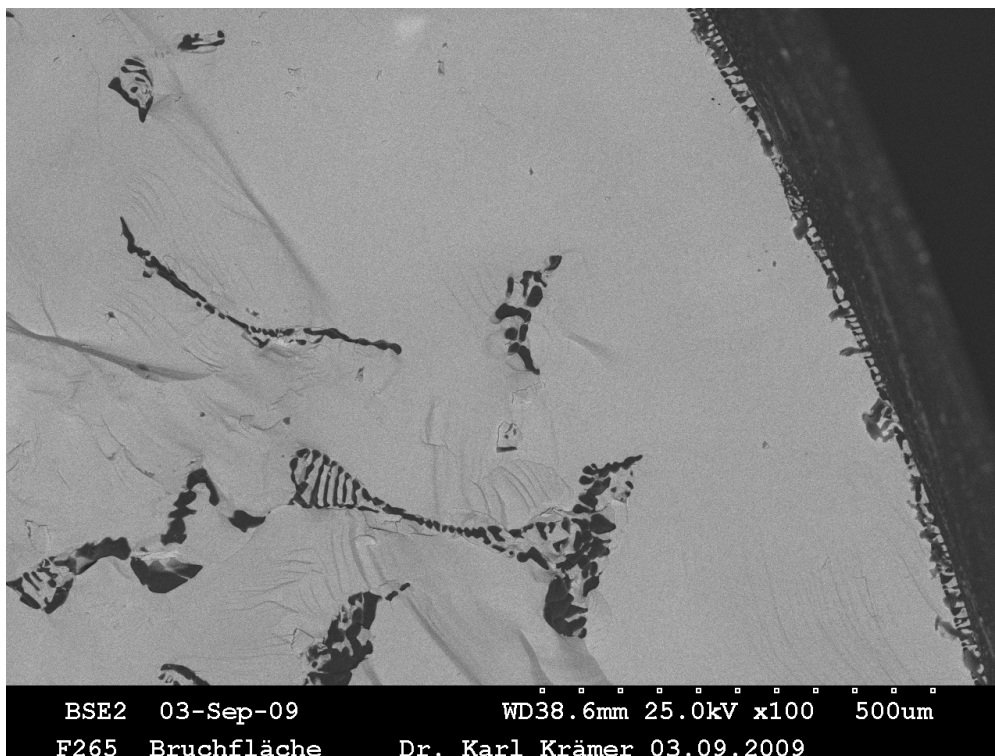


Figure A.2: SEM image of $\text{LiHo}_{0.90}\text{Er}_{0.10}\text{F}_4$ showing LiF inclusions inside the synthesised crystal.

electron microscope (SEM) image of the crystal. The black regions correspond to LiF and the light grey to $\text{LiHo}_x\text{Er}_{1-x}\text{F}_4$. Fortunately, LiF is non-magnetic, so powder AC susceptibility measurements were still possible.

B Determination of T_g in Spin-Glasses

One challenge in analysing AC susceptibility data on spin-glasses is how to model the frequency dependent T_f . Perhaps the most common and straightforward behaviour is that of thermal activation, where the characteristic time τ of the system and the freezing temperature are related via an exponential function:

$$\tau = \tau_0 \exp\left(\frac{E_a}{k_B T}\right) \quad (\text{B.1})$$

Although this simple form can fit the frequency dependence of the spin-glass freezing observed in AC susceptibility, the parameters which one finds are unphysical. Furthermore, in cases where it is possible to measure at very low frequencies (typically \sim mHz) this simple exponential behaviour is no longer obeyed. A more physically justified relationship is that of critical scaling dynamics:

$$\tau = \tau_0 \left(\frac{T_g - T_f}{T_f}\right)^{-z\nu} \quad (\text{B.2})$$

where T_f is the frequency dependent freezing temperature and T_g is a zero-frequency glass temperature. This model of course assumes that there is a true phase transition which occurs at the (non-zero) glass temperature, which can be found in the zero-frequency limit of measurements. The difficulty with this description is that it is not necessarily obvious that there *exists* a T_g , let alone determining its value accurately. In order to calculate T_g we have used the following method.

A large range of possible values of T_g are proposed, and the frequency dependence of T_f is fitted using eq. B.2. For each of these fits the error in the fit χ^2 is calculated and then a plot of χ^2 against T_g is generated, as is shown in fig. .B.1. The minima of each of these curves is then taken as the correct value of T_g .

Appendix B. Determination of T_g in Spin-Glasses

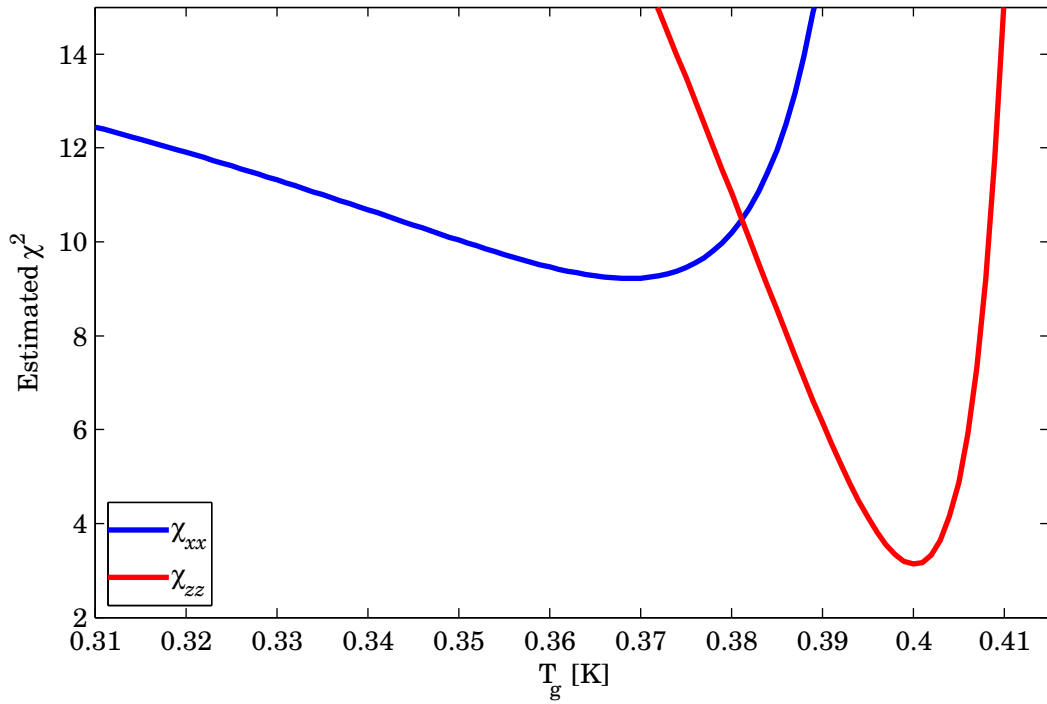


Figure B.1: Determination of T_g in $\text{LiHo}_{0.50}\text{Er}_{0.50}\text{F}_4$. The error in the scaling law fit χ^2 is calculated for various values of T_g . The value of T_g chosen is that which minimises the error in the fit.

C Crystal Field Point Charge Calculation

The *Re* ions in LiReF_4 are surrounded by fluorine ions, which generates a electric potential, the crystal field, at the *Re* site. The crystal-field can be written as [42]:

$$\mathcal{H}_{\text{cf}} = \sum_i \sum_{lm} A_l^m \alpha_l \langle r^l \rangle \left(\frac{2l+1}{4\pi} \right)^{1/2} \tilde{O}_{lm}(\mathbf{J}_i) \quad (\text{C.1})$$

where α_l are the Stevens prefactors, the expectation value $\langle r^l \rangle$ is an average over the $4f$ states and $\tilde{O}_{lm}(\mathbf{J}_i)$ are the Racah operators associated with the spherical harmonics. A_l^m is a special case of the multipole expansion given by:

$$A_l^m = (-1)^m \frac{4\pi}{2l-1} \int \frac{e\rho(\mathbf{R})}{R^{l+1}} Y_{l-m}(\hat{\mathbf{R}}) d\mathbf{R} \quad (\text{C.2})$$

The Racah operators are not typically used, and instead the Stevens operators O_l^m are used, giving the crystal field in terms of the crystal field parameters B_l^m :

$$\mathcal{H}_{\text{cf}} = \sum_i \sum_{lm} B_l^m O_l^m(\mathbf{J}_i) \quad (\text{C.3})$$

Although it is somewhat difficult to accurately calculate this crystal field, a relatively good approximation is to use a point charge model. This corresponds to assuming that the charge distribution $\rho(\mathbf{R})$ is a point charge, and therefore is independent of \mathbf{R} so can be removed from the integral in eq. C.2.

Doing this allows for the crystal field parameters to be written as follows:

$$B_l^m = \mathcal{Y}_l^m \alpha_l \langle r^l \rangle \gamma(l, m) \quad (\text{C.4})$$

Appendix C. Crystal Field Point Charge Calculation

where

$$\gamma(l, m) = \sum_{n=0}^{\infty} \sum_j \frac{4\pi\rho_j(R)}{(2l+1)R_j^{l+1}} T_{lm}(\theta_j, \phi_j) \quad (\text{C.5})$$

with j being the position of the various ions in a unit cell T_{lm} are the tesseral harmonics taking the form below and the sum is being taken over an infinite number of unit cells.

$$\begin{cases} m = 0, & T_{lm}(\theta, \phi) = Y_{lm}(\theta, \phi) \\ m < 0, & \sqrt{1/2}(-1)^m 2Im[Y_{lm}(\theta, \phi)] \\ m > 0, & \sqrt{1/2}(-1)^m 2Re[Y_{lm}(\theta, \phi)] \end{cases} \quad (\text{C.6})$$

The sum is calculated over a finite number of unit cells centred around the *Re* ion. First, a unit cell is populated with the appropriate ions and charges ρ : $Re = 3$, $Li = 1$ $F = -1$. The system is centred around a *Re* ion at $R = 0$ inside this unit cell and there are now j ions within the unit cell. The calculation is carried out on a box of $19 \times 19 \times 19$ unit cells and the sum in $\gamma(l, m)$ is made over those which are within a radius of $8a$ (where a is length the crystallographic a -axis).

D Initial Interpretation of the Thermal Runaway in $\text{LiHo}_{0.50}\text{Er}_{0.50}\text{F}_4$

This Appendix shows the initial data, and subsequent interpretation of the thermal runaway seen in $\text{LiHo}_{0.50}\text{Er}_{0.50}\text{F}_4$ (Section 4.5.4 on page 112). The results presented are the field-dependent AC susceptibility and temperature on the weak-link thermometer (which gives an indication of the sample temperature). Additional measurements, which consisted of simultaneous AC susceptibility, magnetisation and sample temperature, indicated that much the observed behaviour is due to the susceptibility measuring the sample temperature. The initial interpretation is included as an example of why it is important to verify results, ideally by using additional experimental techniques, before jumping to conclusions.

This behaviour is not quite as unexpected as one would think. In spin-glasses there is typically a rather simple relationship between $\chi'(\omega)$ and $\chi''(\omega)$, where imaginary susceptibility can be approximated by the following equation [66]:

$$\chi'' \approx -\frac{\pi}{2} \frac{\partial \chi'}{\partial \ln \omega} \quad (\text{D.1})$$

where $\omega = 2\pi f$. From the data it is possible to see this kind of behaviour indirectly, by looking at the frequency dependence of the susceptibility at a constant field. In χ' at essentially all fields, the signal decreases logarithmically with frequency, as each of the scans is simply offset by the same constant from the last and the frequencies are equally spaced on a logarithmic scale. This would correspond to a straight line if $\chi'(\omega)$ were plotted against $\ln \omega$, and the derivative of this signal would therefore be a constant. We see that indeed the frequency dependence of $\chi'(\omega)$ is relatively constant, with all the scans falling on top of each other. The small fluctuations in the imaginary signal could be attributed to the changes in temperature between scans, which is on the order of 2 milliKelvin.

It was noticed that the peak amplitude appeared to depend on the *rate* at which the DC field was swept. In order to explore this possibility, field scans were carried out at rates between 0.1 mT min^{-1} up to 100 mT min^{-1} . The results are shown in Fig. D.2, with the left panels zoomed in around the region of the peak in susceptibility and the right panels showing the

Appendix D. Initial Interpretation of the Thermal Runaway in $\text{LiHo}_{0.50}\text{Er}_{0.50}\text{F}_4$

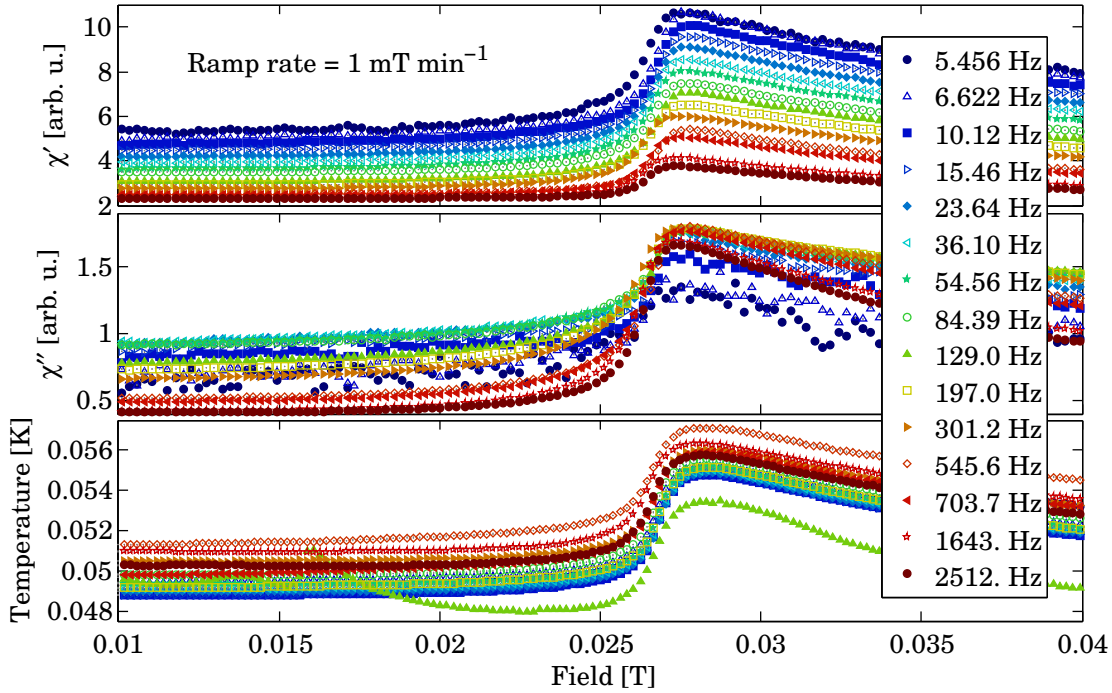


Figure D.1: Frequency dependence of χ_{zz} in H_c scans on $\text{LiHo}_{0.50}\text{Er}_{0.50}\text{F}_4$ Frequency dependence of χ_{zz} in H_c scans on $\text{LiHo}_{0.50}\text{Er}_{0.50}\text{F}_4$ at $T = 0.05$ K taken in the range of 5.456–2512 Hz with a ramp rate of 1 mT min^{-1} .

entire range measured. What is seen is that the peak effectively grows and gets more stretched out as the ramp rate increases, particularly on the high field side of the peak. At the same time the magnetocaloric effect associated with the peak increases with the ramp rate.

A summary of the rate (left side) and frequency (right side) dependences is shown in Fig D.3. The peak field decreases slightly as the ramp rate is increased from slowest ramping before rapidly increasing to higher fields. During this process, the peak amplitude increases as the logarithm of the ramp rate. Turning to the frequency dependence, the peak amplitude decreases as the logarithm of the AC excitation frequency. The amplitude of the peak in χ'' initially increases with frequency then levels off and stays relatively constant for all frequencies above around 20 Hz.

The relaxation of the transition across the peak was studied by ramping the field up to a set value, then stopping the field and measuring the susceptibility as a function of time. The system was put into the ZFC state before each scan and the field was ramped up with a rate of 1 mT per minute. This was done for fields for 20 mT to 30 mT in 1 mT steps, which corresponds to fields both below and above the peak position. The results are shown in Fig. D.4, where the black points correspond to the various field scans and the coloured points show the relaxation of the system after the field scan.

As the field gets closer to some critical field, the relaxation observed steadily grows. A small

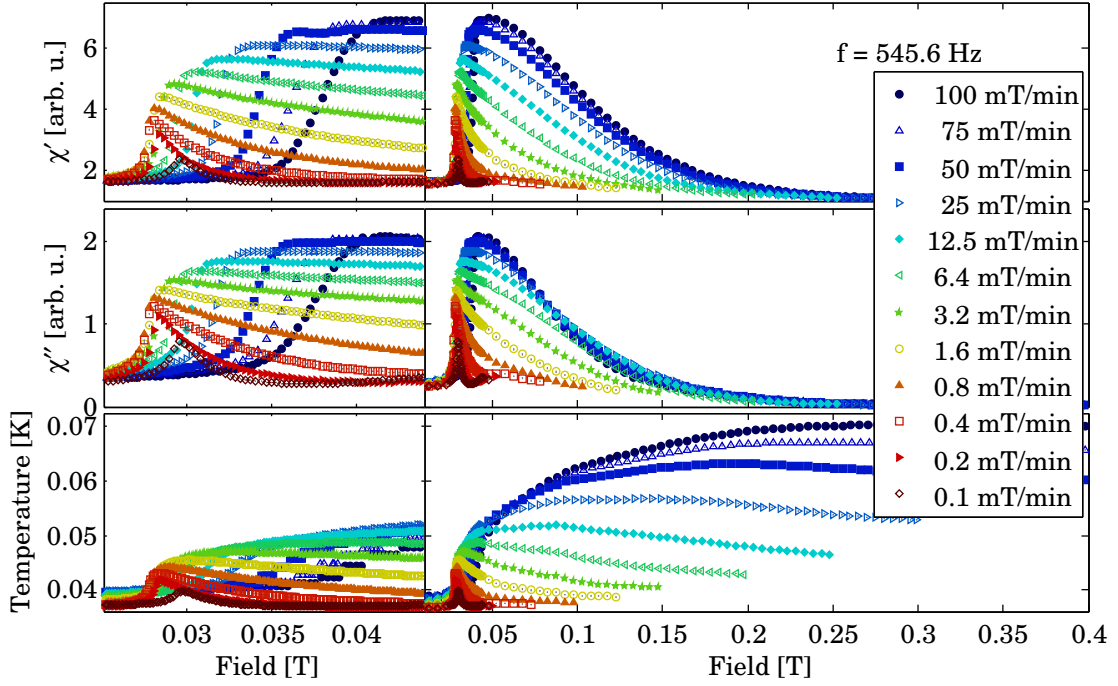


Figure D.2: Rate dependence of χ_{zz} in H_c scans on $\text{LiHo}_{0.50}\text{Er}_{0.50}\text{F}_4$ at $T = 0.04$ K.

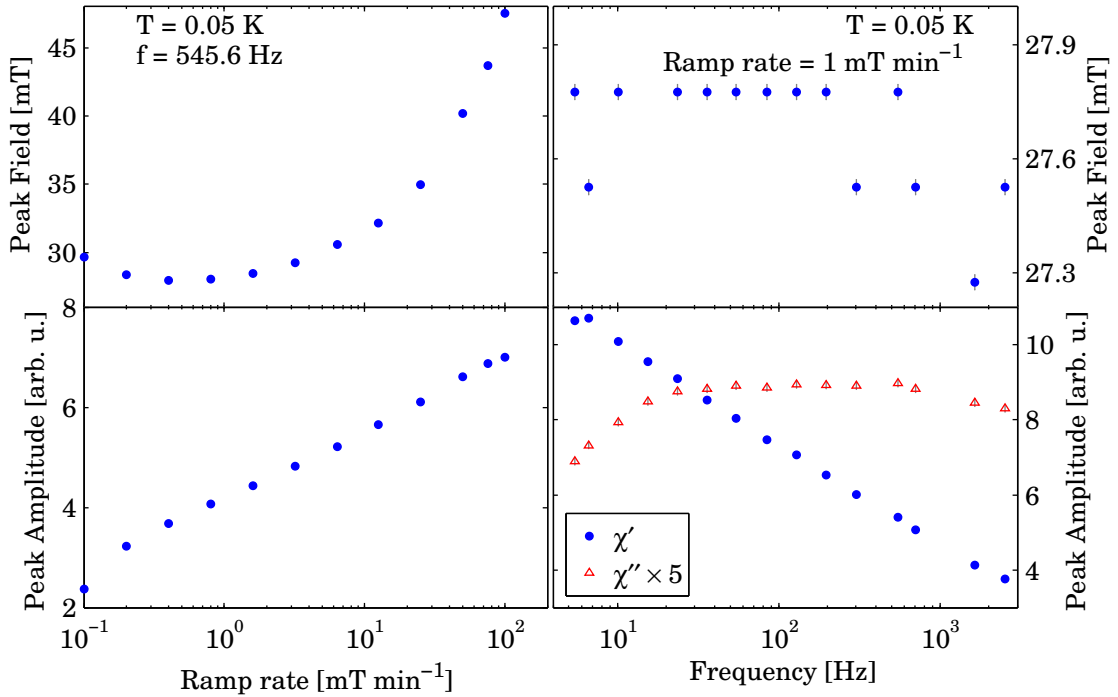


Figure D.3: Rate and frequency dependence of χ_{zz} peak in H_c field scans.

Appendix D. Initial Interpretation of the Thermal Runaway in $\text{LiHo}_{0.50}\text{Er}_{0.50}\text{F}_4$

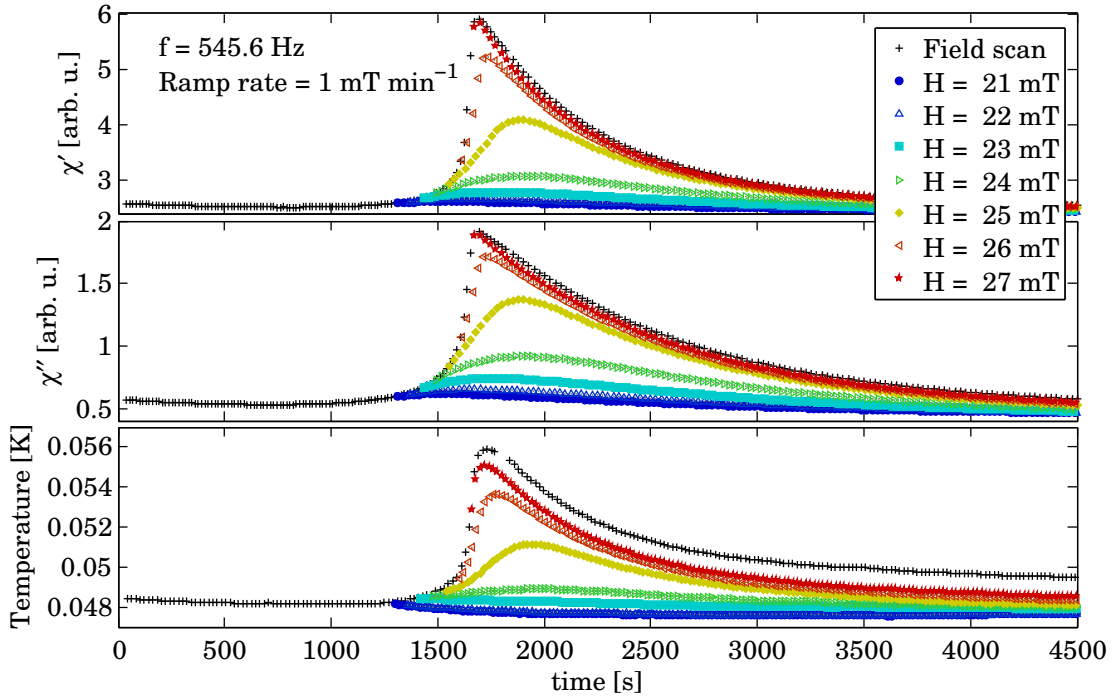


Figure D.4: H_c field scans to below peak field followed by time scans at $T = 0.048$ K measuring χ_{zz} on $\text{LiHo}_{0.50}\text{Er}_{0.50}\text{F}_4$. The field is initially ramped up with a rate of 1 mT min^{-1} and once stopped the relaxation of the sample is measured as a function of time for each field value.

bump is seen at low fields, which as the field is increased grows steadily in amplitude and sharpening. Once the field has reached the critical field, it seemingly has no effect on the system; the curve from the pure relaxation and that from a field scan overlap perfectly. Once again the peak in the susceptibility and the magnetocaloric effect coincide perfectly.

The non-reversible spin avalanche is presumably a transition from a true spin-glass state into a ferromagnetic state which is masked by the glassiness of the system in zero field. In such a transition it seems likely that the relaxation rate of the system will depend not on an external factor but on the dynamics of a spin-glass. In order to see whether this is the case, the ramp rate dependence of the susceptibility is plotted in Fig. D.5 as a function of time, with $t = 0$ being fixed to the peak in χ' . The data has also been normalised to make comparisons easier. It is clear that there is indeed a unique relaxation time over a very large range of ramp rates. The exception to this is that as the ramp rate passes a critical rate, the relaxation occurs more rapidly. This seems logical as the field gets to very large values, so it will be easier to destroy the glassy phase and polarise the spins.

Turning to the magnetocaloric effect, the temperature being measured on the weak link can be expressed as a flux of energy flowing from the sample into the weak link. Assuming that the thermal link between the thermometer and the sample is of high quality it is possible to make

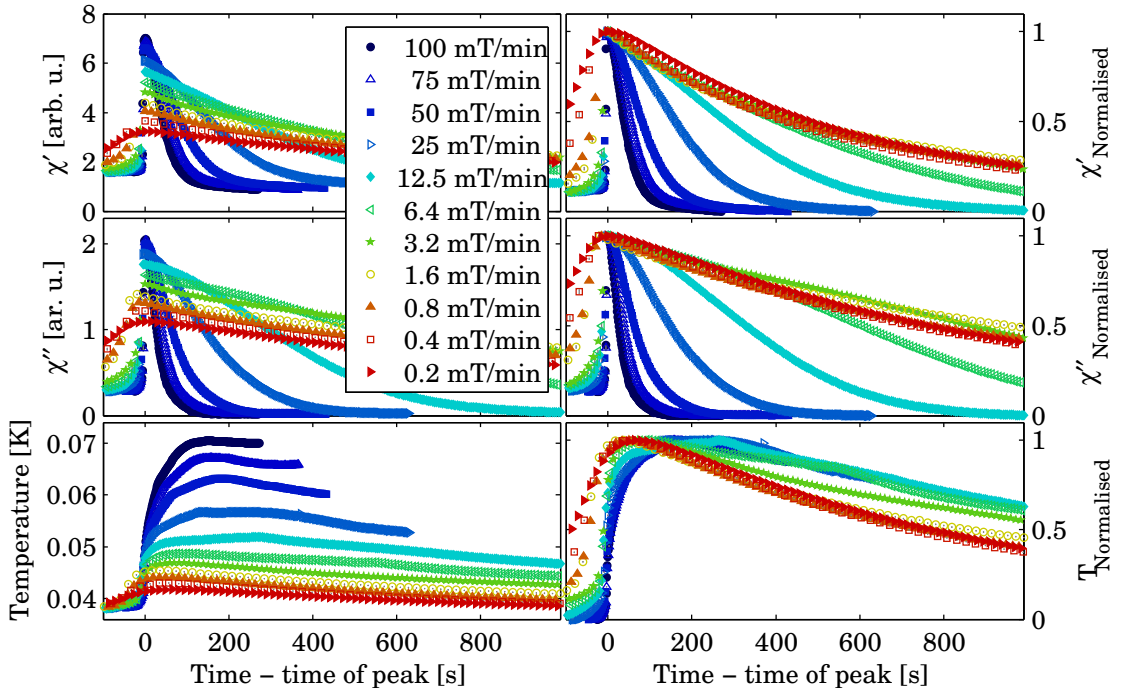


Figure D.5: Rate dependence of χ_{zz} in H_c scans on $\text{LiHo}_{0.50}\text{Er}_{0.50}\text{F}_4$ at $T = 0.04$ K, with the data shown in units of time since the peak in χ .

a simple model of the thermal gradient ΔT between the mixing chamber and the weak link:

$$\frac{dQ}{dt} = \kappa \Delta T \quad (\text{D.2})$$

where κ is the total thermal conductivity of the weak link at temperature T and dQ/dt is the heat flux. Importantly, this implies that the temperature measured on the weak link is directly proportional to the energy released by the sample. The weak link consists of two copper blocks connected with a 5 cm thin walled stainless steel tube, which is effectively a thermal insulator at sub-Kelvin temperatures. The thermal conductivity is achieved by using a copper foil which has a cross-section of $10 \times 0.1 \text{ mm}^2$. The thermal conductivity of copper at such temperatures can vary rather dramatically depending on the purity and crystalline structure, but a typical value is $\kappa \sim 0.5 \text{ W (cm K)}^{-1}$ [73].

The fact that this heat flux is rate dependent can be naturally explained if it is related to the Zeeman energy released by flipping the spin clusters observed by neutron scattering:

$$E = -g\mu_B \mathbf{J}_i \cdot \mathbf{H} \quad (\text{D.3})$$

Where in this case \mathbf{J}_i is the moment of cluster i . In the case of a system where many spins begin to flip spontaneously, as is the case in the avalanche, it follows that the rate of change of

**Appendix D. Initial Interpretation of the Thermal Runaway in
LiHo_{0.50}Er_{0.50}F₄**

the magnetisation gives the number of spins which are flipping during that time $\sum \mathbf{J}_i \propto dM/dt$ and therefore

$$\dot{W}_z \propto \mathbf{H}(t) \frac{dM}{dt} \quad (\text{D.4})$$

where \dot{W}_z is the rate at which the Zeeman energy is released from the system. Indeed similar behaviour has been observed in the spin ice compound Dy₂Ti₂O₇ [87].

Bibliography

- [1] A. Aharony. Critical behavior of magnets with dipolar interactions. v. uniaxial magnets in d dimensions. *Physical Review B*, 8(7):3363–3370, October 1973. doi: 10.1103/PhysRevB.8.3363. URL <http://link.aps.org/doi/10.1103/PhysRevB.8.3363>.
- [2] A. Aharony. New singularities in the critical behavior of random ising models at marginal dimensionalities. *Phys. Rev. B*, 13(5):2092–2098, Mar 1976. doi: 10.1103/PhysRevB.13.2092.
- [3] J. Als-Nielsen. Experimental test of renormalization group theory on the uniaxial, dipolar coupled ferromagnet LiTbF_4 . *Physical Review Letters*, 37(17):1161–1164, October 1976. doi: 10.1103/PhysRevLett.37.1161. URL <http://link.aps.org/doi/10.1103/PhysRevLett.37.1161>.
- [4] C. Ancona-Torres, D. M. Silevitch, G. Aeppli, and T. F. Rosenbaum. Quantum and classical glass transitions in $\text{LiHo}_x\text{Y}_{1-x}\text{F}_4$. *Phys. Rev. Lett.*, 101(5):057201, Jul 2008. doi: 10.1103/PhysRevLett.101.057201.
- [5] Attocube Systems AG. Performance test of the anpz30/lt at 35 mk and 15 tesla. Technical report, http://attocube.de/nanoPOSITIONING/download/ACS_AppNote_P07_35mK_15T%20v1%201.pdf, 2007.
- [6] Attocube Systems AG. Working principle of attocube’s positioners. http://attocube.de/nanoPOSITIONING/working_principal.html, accessed 02, 2012.
- [7] J. E. Battison, A. Kasten, M. J. M. Leask, J. B. Lowry, and B. M. Wanklyn. Ferromagnetism in lithium holmium fluoride- LiHoF_4 . ii. optical and spectroscopic measurements. *Journal of Physics C: Solid State Physics*, 8(23):4089–4095, 1975. URL <http://stacks.iop.org/0022-3719/8/4089>.
- [8] P. Beauvillain, J-P. Renard, and P-E. Hansen. Low-temperature magnetic susceptibility of LiErF_4 : evidence of antiferromagnetic ordering at 0.38k. *J.Phys.C: Solid State Phys*, 10: 709–712, 1977.
- [9] P. Beauvillain, J-P. Renard, and J. Magarino. Determination of crystal field parameters of LiR_2F_4 ($R = \text{Tb, Ho, Er}$) by high temperature susceptibility measurements. *Journal of Magnetism and Magnetic Materials*, 15-18:31–32, 1980.

Bibliography

- [10] K. Binder and A. P. Young. Spin-glasses - experimental facts, theoretical concepts, and open questions. *Rev. Mod. Phys.*, 58(4):801–976, OCT 1986.
- [11] D. Bitko and T. F. Rosenbaum. Quantum behavior for a model magnet. *Phys. Rev. Lett.*, 77:940–943, 1996.
- [12] S. J. Blundell. Spin-polarized muons in condensed matter physics. *arXiv:cond-mat/0207699*, July 2002. doi: 10.1080/001075199181521. URL <http://arxiv.org/abs/cond-mat/0207699>. *Contemporary Physics* 40, 175 (1999).
- [13] J. C. Bonner and M. E. Fisher. Linear magnetic chains with anisotropic coupling. *Physical Review*, 135(3A):A640–A658, 1964. doi: 10.1103/PhysRev.135.A640. URL <http://link.aps.org/doi/10.1103/PhysRev.135.A640>.
- [14] N. Bontemps, J. Rajchenbach, R. V. Chamberlin, and R. Orbach. Dynamic scaling in the $\text{Eu}_{0.4}\text{Sr}_{0.6}\text{S}$ spin-glass. *Physical Review B*, 30(11):6514–6520, December 1984. doi: 10.1103/PhysRevB.30.6514. URL <http://link.aps.org/doi/10.1103/PhysRevB.30.6514>.
- [15] W. A. Bosch, O. W. B. Benningshof, R. Jochemsen, and O. Usenko. Srd1000, a 13-point reference device for precision thermometry below 8 k. Technical report, <http://hdleiden.home.xs4all.nl/srd1000/>, 2012.
- [16] J. Brooke, D. Bitko, T. F. Rosenbaum, and G. Aeppli. Quantum annealing of a disordered magnet. *Science*, 284:779, 1999.
- [17] V. Cannella and J. A. Mydosh. Magnetic ordering in Gold-Iron alloys. *Physical Review B*, 6(11):4220–4237, December 1972. doi: 10.1103/PhysRevB.6.4220. URL <http://link.aps.org/doi/10.1103/PhysRevB.6.4220>.
- [18] P. B. Chakraborty, P. Henelius, H. Kønberg, A. W. Sandvik, and S. M. Girvin. Theory of the magnetic phase diagram of LiHoF_4 . *Physical Review B*, 70(14):144411, October 2004. doi: 10.1103/PhysRevB.70.144411. URL <http://link.aps.org/doi/10.1103/PhysRevB.70.144411>.
- [19] R. V. Chamberlin, M. Hardiman, and R. Orbach. Reversibility and time dependence of the magnetization in Ag:Mn and Cu:Mn spin glasses. *Journal of Applied Physics*, 52(3):1771–1772, March 1981. ISSN 00218979. doi: doi:10.1063/1.329709. URL http://jap.aip.org/resource/1/japiau/v52/i3/p1771_s1.
- [20] J. H. Claassen. Coupling considerations for SQUID devices. *Journal of Applied Physics*, 46(5):2268–2275, May 1975. ISSN 00218979. doi: doi:10.1063/1.321821. URL http://jap.aip.org/resource/1/japiau/v46/i5/p2268_s1.
- [21] John Clarke and Alex I. Braginski. *The SQUID Handbook*. WILEY-VCH Verlag GmbH & Co. KGaA, Weinheim, 2004.
- [22] J. R. Clem. Ac losses in type ii superconductors. *Physica C*, 153–155:50, 1988.

- [23] B. Dalla Piazza. Mean-field calculations on the diluted dipolar magnet $\text{LiHo}_{1-x}\text{Y}_x\text{F}_4$. Master's thesis, LQM - EPFL, 2009.
- [24] M. A. de Vries, A. C. Mclaughlin, and J.-W. G. Bos. Valence bond glass on an fcc lattice in the double perovskite Ba_2YMoO_6 . *Physical Review Letters*, 104(17):177202, April 2010. doi: 10.1103/PhysRevLett.104.177202. URL <http://link.aps.org/doi/10.1103/PhysRevLett.104.177202>.
- [25] M. A. de Vries, J. O. Piatek, H. M. Rønnow, J. S. Lord, and J.-W. G. Bos. Kinetic constraints of a quantum spin liquid in a rocksalt-ordered double perovskite. *Nature*, In preparation.
- [26] F. J. Di Salvo, J. A. Wilson, B. G. Bagley, and J. V. Waszczak. Effects of doping on charge-density waves in layer compounds. *Physical Review B*, 12(6):2220–2235, 1975. doi: 10.1103/PhysRevB.12.2220. URL <http://link.aps.org/doi/10.1103/PhysRevB.12.2220>.
- [27] J. Eisenstein. Superconducting elements. *Reviews of Modern Physics*, 26(3):277–291, July 1954. doi: 10.1103/RevModPhys.26.277. URL <http://link.aps.org/doi/10.1103/RevModPhys.26.277>.
- [28] T. Fennell, J. O. Piatek, R. A. Stephenson, G. J. Nilsen, and H. M. Rønnow. Spangolite: an $s = 1/2$ maple leaf lattice antiferromagnet? *Journal of Physics: Condensed Matter*, 23(16):164201, April 2011. ISSN 0953-8984, 1361-648X. doi: 10.1088/0953-8984/23/16/164201. URL <http://iopscience.iop.org/0953-8984/23/16/164201>.
- [29] K. H. Fischer and J. A. Hertz. *Spin Glasses*. Cambridge University Press, 1991.
- [30] C. Frondel. Crystallography of spangolite. *Am. Mineral.*, 34:181, 1949.
- [31] S. Ghosh, R. Parthasarathy, T. F. Rosenbaum, and G. Aeppli. Coherent Spin Oscillations in a Disordered Magnet. *Science*, 296(5576):2195–2198, 2002. doi: 10.1126/science.1070731. URL <http://www.sciencemag.org/cgi/content/abstract/296/5576/2195>.
- [32] S. Ghosh, T. M. Rosenbaum, G. Aeppli, and S. N. Coppersmith. Entangled quantum state of magnetic dipoles. *Nature*, 425:48, 2003.
- [33] M. J. P. Gingras and P. Henelius. Collective phenomena in the $\text{LiHo}_x\text{Y}_{1-x}\text{F}_4$ quantum ising magnet: Recent progress and open questions. *Journal of Physics: Conference Series*, 320:012001, September 2011. ISSN 1742-6596. doi: 10.1088/1742-6596/320/1/012001. URL <http://iopscience.iop.org/1742-6596/320/1/012001>.
- [34] Fedor Gömöry. Low frequency magnetic measurements on high-Tc superconducting materials. *Thermochimica Acta*, 174(0):299–320, January 1991. ISSN 0040-6031. doi: 10.1016/0040-6031(91)80167-H. URL <http://www.sciencedirect.com/science/article/pii/004060319180167H>.
- [35] R.G. Goodrich, D. Hall, E. Palm, and T. Murphy. Magnetoresistance below 1 k and temperature cycling of ruthenium oxide-bismuth ruthenate cryogenic thermometers.

Bibliography

- Cryogenics*, 38(2):221–225, February 1998. ISSN 0011-2275. doi: 10.1016/S0011-2275(97)00100-8. URL <http://www.sciencedirect.com/science/article/pii/S0011227597001008>.
- [36] P. E. Hansen, T. Johansson, and R. Nevald. Magnetic properties of lithium rare-earth fluorides: Ferromagnetism in LiErF_4 and LiHoF_4 and crystal-field parameters at the rare-earth and li sites. *Phys. Rev. B*, 12(11):5315–5324, Dec 1975. doi: 10.1103/PhysRevB.12.5315.
- [37] M. Hase, I. Terasaki, and K. Uchinokura. Observation of the spin-Peierls transition in linear Cu^{2+} (spin-1/2) chains in an inorganic compound CuGeO_3 . *Physical Review Letters*, 70(23):3651–3654, June 1993. doi: 10.1103/PhysRevLett.70.3651. URL <http://link.aps.org/doi/10.1103/PhysRevLett.70.3651>.
- [38] F. C. Hawthorne, M. Kimata, and R. K. Eby. The crystal structure of spangolite, a complex copper sulfate sheet mineral. *American Mineralogist*, 78:649, 1993.
- [39] P. C. Hohenberg and B. I. Halperin. Theory of dynamic critical phenomena. *Reviews of Modern Physics*, 49(3):435–479, July 1977. doi: 10.1103/RevModPhys.49.435. URL <http://link.aps.org/doi/10.1103/RevModPhys.49.435>.
- [40] D. Hüser, L. E. Wenger, A. J. van Duynveldt, and J. A. Mydosh. Dynamical behavior of the susceptibility around the freezing temperature in (Eu,Sr)S. *Physical Review B*, 27(5):3100–3103, March 1983. doi: 10.1103/PhysRevB.27.3100. URL <http://link.aps.org/doi/10.1103/PhysRevB.27.3100>.
- [41] M. T. Hutchings. *Solid State Physics*, volume 2. Academic Press, New York, 1964.
- [42] J. Jensen and A. R. Mackintosh. *Rare Earth Magnetism*. Clarendon Press, Oxford, 1991.
- [43] D. C. Johnston. The puzzle of high temperature superconductivity in layered iron pnictides and chalcogenides. *arXiv:1005.4392*, May 2010. doi: 10.1080/00018732.2010.513480. URL <http://arxiv.org/abs/1005.4392>. *Advances in Physics* 59, 803-1061 (2010).
- [44] K. Jonason, E. Vincent, J. Hammann, J. P. Bouchaud, and P. Nordblad. Memory and chaos effects in spin glasses. *Physical Review Letters*, 81(15):3243–3246, October 1998. doi: 10.1103/PhysRevLett.81.3243. URL <http://link.aps.org/doi/10.1103/PhysRevLett.81.3243>.
- [45] P. E. Jönsson, R. Mathieu, W. Wernsdorfer, A. M. Tkachuk, and B. Barbara. Absence of conventional spin-glass transition in the ising dipolar system $\text{LiHo}_x\text{Y}_{1-x}\text{F}_4$. *Phys. Rev. Lett.*, 98(25):256403, Jun 2007. doi: 10.1103/PhysRevLett.98.256403.
- [46] T. Jonsson, K. Jonason, P. Jönsson, and P. Nordblad. Nonequilibrium dynamics in a three-dimensional spin glass. *Physical Review B*, 59(13):8770–8777, April 1999. doi: 10.1103/PhysRevB.59.8770. URL <http://link.aps.org/doi/10.1103/PhysRevB.59.8770>.
- [47] D. Kasinathan, K. Koepernik, O. Janson, G. J. Nilsen, J. O. Piatek, and H. Rosner. Electronic structure of $\text{KTi}(\text{SO}_4)_2 \cdot \text{H}_2\text{O}$ - a $S=1/2$ frustrated chain antiferromagnet. *In preparation*, 2012.

- [48] C. Kraemer. *Quantum Phase Transitions in a Magnetic Model System*. PhD thesis, ETH Zürich, 2009.
- [49] C. Kraemer, N. Nikseresht, J. O. Piatek, N. Tsyrlin, B. Dalla Piazza, K. Kiefer, B. Klemke, T. F. Rosenbaum, G. Aeppli, C. Gannarelli, K. Prokes, A. Podlesnyak, T. Strässle, L. Keller, O. Zaharko, K. W. Krämer, and H. M. Rønnow. Dipolar antiferromagnetism and quantum criticality in LiErF_4 . *Science*, 336(6087):1416–1419, June 2012. ISSN 0036-8075, 1095-9203. doi: 10.1126/science.1221878. URL <http://www.sciencemag.org/content/336/6087/1416>.
- [50] Laurent P. Lévy. Critical dynamics of metallic spin glasses. *Physical Review B*, 38(7):4963–4973, 1988. doi: 10.1103/PhysRevB.38.4963. URL <http://link.aps.org/doi/10.1103/PhysRevB.38.4963>.
- [51] F. London. *Superfluids*. Wiley, New York, 1950.
- [52] H. London. *Proceedings of the International Conference on Low-Temperature Physics*. Oxford University Press, 1951.
- [53] S. Lovesey. *Theory of neutron scattering from condensed matter*. Claren, 1984.
- [54] L. Lundgren, P. Svedlindh, P. Nordblad, and O. Beckman. Dynamics of the Relaxation-Time spectrum in a CuMn Spin-Glass. *Physical Review Letters*, 51(10):911–914, 1983. doi: 10.1103/PhysRevLett.51.911. URL <http://link.aps.org/doi/10.1103/PhysRevLett.51.911>.
- [55] R. Mahendiran, Y. Bréard, M. Hervieu, B. Raveau, and P. Schiffer. Giant frequency dependence of dynamic freezing in nanocrystalline ferromagnetic $\text{LaCo}_{0.5}\text{Mn}_{0.5}\text{O}_3$. *Phys. Rev. B*, 68(10):104402, Sep 2003. doi: 10.1103/PhysRevB.68.104402.
- [56] H. Maletta and W. Felsch. Insulating spin-glass system $\text{Eu}_x\text{Sr}_{1-x}\text{S}$. *Physical Review B*, 20(3):1245–1260, 1979. doi: 10.1103/PhysRevB.20.1245. URL <http://link.aps.org/doi/10.1103/PhysRevB.20.1245>.
- [57] H. Maletta, W. Felsch, and J.L. Tholence. Spin glass behaviour in the non-metallic system $(\text{EuSr})\text{S}$. *Journal of Magnetism and Magnetic Materials*, 9(1–3):41–43, 1978. ISSN 0304-8853. doi: 10.1016/0304-8853(78)90017-3. URL <http://www.sciencedirect.com/science/article/pii/0304885378900173>.
- [58] J. Mallinson. Magnetometer coils and reciprocity. *Journal of Applied Physics*, 37(6):2514–2515, May 1966. ISSN 00218979. doi: doi:10.1063/1.1708848. URL http://jap.aip.org/resource/1/japiau/v37/i6/p2514_s1.
- [59] E. Maxwell and M. Strongin. Filamentary structure in superconductors. *Phys. Rev. Lett.*, 10:212, 1963.
- [60] G. Mennenga, L. J. Jongh, and W. J. Huiskamp. A comparative study of the magnetic ordering specific heats of four $S = 1/2$ dipolar magnets: LiRF_4 ($R=\text{Er, Dy, Ho, Tb}$). *Journal of Magnetism and Magnetic Materials*, 44:48–58, 1984.

Bibliography

- [61] S. K. Misra and J. Felsteiner. Low-temperature ordered states of lithium rare-earth tetrafluorides (LiRF_4). *Phys. Rev. B*, 15(9):4309–4312, May 1977.
- [62] A. Morello, W. G. J. Angenent, G. Frossati, and L. J. de Jongh. Automated and versatile SQUID magnetometer for the measurement of materials properties at millikelvin temperatures. *Review of Scientific Instruments*, 76(2):023902–023902–7, January 2005. ISSN 00346748. doi: doi:10.1063/1.1841831. URL http://rsi.aip.org/resource/1/rsinak/v76/i2/p023902_s1?isAuthorized=no.
- [63] M. Mück. *Manual for the dc SQUID electronics type ez SQUID SQECC-100k*. ezSQUID.
- [64] Multiwire Laboratories, Ltd. <http://www.multiwire.com/products.html>.
- [65] H. Mutka, L. Zuppiroli, P. Molinié, and J. C. Bourgoin. Charge-density waves and localization in electron-irradiated 1T-TaS₂. *Physical Review B*, 23(10):5030–5037, May 1981. doi: 10.1103/PhysRevB.23.5030. URL <http://link.aps.org/doi/10.1103/PhysRevB.23.5030>.
- [66] J. A. Mydosh. *Spin Glasses: An Experimental Introduction*. Taylor & Francis, 1993.
- [67] S. Nagata, P. H. Keesom, and H. R. Harrison. Low-dc-field susceptibility of CuMn spin glass. *Physical Review B*, 19(3):1633–1638, February 1979. doi: 10.1103/PhysRevB.19.1633. URL <http://link.aps.org/doi/10.1103/PhysRevB.19.1633>.
- [68] G. J. Nilsen, H. M. Rønnow, A. M. Läuchli, F. P. A. Fabbiani, J. Sanchez-Benitez, K. V. Kamenev, and A. Harrison. A new realisation of the $s = 1/2$ frustrated chain antiferromagnet. *Chem. Mater.*, 20(1):8–10, 2007. ISSN 0897-4756. doi: 10.1021/cm7023263. URL <http://dx.doi.org/10.1021/cm7023263>.
- [69] H. Nishimori. *Statistical physics of spin glasses and information processing – an introduction*. Clarendon Press, Oxford, 2001.
- [70] A. T. Ogielski. Dynamics of three-dimensional ising spin glasses in thermal equilibrium. *Phys. Rev. B*, 32(11):7384–7398, Dec 1985. doi: 10.1103/PhysRevB.32.7384.
- [71] A. T. Ogielski and I. Morgenstern. Critical behavior of three-dimensional ising spin-glass model. *Phys. Rev. Lett.*, 54(9):928–931, Mar 1985. doi: 10.1103/PhysRevLett.54.928.
- [72] C. C. Paulsen, S. J. Williamson, and H. Maletta. Evidence for a phase transition in the spin glass $\text{Eu}_{0.4}\text{Sr}_{0.6}\text{S}$ from dynamic susceptibility measurements. *Physical Review Letters*, 59(1):128–131, July 1987. doi: 10.1103/PhysRevLett.59.128. URL <http://link.aps.org/doi/10.1103/PhysRevLett.59.128>.
- [73] E. Pobell. *Matter and Methods at Low Temperatures*. Springer, third edition, 2007.
- [74] J. A. Quilliam, C. G. A. Mugford, A. Gomez, S. W. Kycia, and J. B. Kycia. Specific heat of the dilute ising magnet $\text{LiHo}_x\text{Y}_{1-x}\text{F}_4$. *Phys. Rev. Lett.*, 98(3):037203, 2007. doi: 10.1103/PhysRevLett.98.037203. URL <http://link.aps.org/abstract/PRL/v98/e037203>.

- [75] J. A. Quilliam, S. Meng, C. G. A. Mugford, and J. B. Kycia. Evidence of Spin Glass Dynamics in Dilute $\text{LiHo}_x\text{Y}_{1-x}\text{F}_4$. *Phys. Rev. Lett.*, 101(18):187204, OCT 31 2008.
- [76] D. H. Reich, T. F. Rosenbaum, G. Aeppli, and H. J. Guggenheim. Ferromagnetism, glassiness, and metastability in a dilute dipolar-coupled magnet. *Phys. Rev. B*, 34(7):4956–4958, Oct 1986. doi: 10.1103/PhysRevB.34.4956.
- [77] D. H. Reich, B. Ellman, J. Yang, T. F. Rosenbaum, G. Aeppli, and D. P. Belanger. Dipolar magnets and glasses: Neutron-scattering, dynamical, and calorimetric studies of randomly distributed ising spins. *Phys. Rev. B*, 42(7):4631–4644, Sep 1990. doi: 10.1103/PhysRevB.42.4631.
- [78] H. M. Rønnow, R. Parthasarathy, J. Jensen, G. Aeppli, T. F. Rosenbaum, and D. F. McMorrow. Quantum Phase Transition of a Magnet in a Spin Bath. *Science*, 308(5720):389–392, 2005. doi: 10.1126/science.1108317. URL <http://www.sciencemag.org/cgi/content/abstract/308/5720/389>.
- [79] H. M. Rønnow, J. Jensen, R. Parthasarathy, G. Aeppli, T. F. Rosenbaum, D. F. McMorrow, and C. Kraemer. Magnetic excitations near the quantum phase transition in the ising ferromagnet LiHoF_4 . *Phys. Rev. B*, 75(5):054426, 2007. doi: 10.1103/PhysRevB.75.054426. URL <http://link.aps.org/abstract/PRB/v75/e054426>.
- [80] M.C. Runyan and W.C. Jones. Thermal conductivity of thermally-isolating polymeric and composite structural support materials between 0.3 and 4 k. *Cryogenics*, 48(9–10):448–454, October 2008. ISSN 0011-2275. doi: 10.1016/j.cryogenics.2008.06.002. URL <http://www.sciencedirect.com/science/article/pii/S0011227508000933>.
- [81] M. Schechter. $\text{LiHo}_x\text{Y}_{1-x}\text{F}_4$ as a random-field ising ferromagnet. *Physical Review B*, 77(2):020401, January 2008. doi: 10.1103/PhysRevB.77.020401. URL <http://link.aps.org/doi/10.1103/PhysRevB.77.020401>.
- [82] M. Schechter and P. C. E. Stamp. Derivation of the low-T phase diagram of $\text{LiHo}_x\text{Y}_{1-x}\text{F}_4$: a dipolar quantum ising magnet. *Physical Review B*, 78(5):054438, 2008. doi: 10.1103/PhysRevB.78.054438. URL <http://link.aps.org/doi/10.1103/PhysRevB.78.054438>.
- [83] D. Schmalfuß, P. Tomczak, J. Schulenburg, and J. Richter. The spin-1/2 heisenberg antiferromagnet on a 1/7-depleted triangular lattice: Ground-state properties. *Physical Review B*, 65(22):224405, May 2002. doi: 10.1103/PhysRevB.65.224405. URL <http://link.aps.org/doi/10.1103/PhysRevB.65.224405>.
- [84] D. M. Silevitch, G. Aeppli, and T. F. Rosenbaum. Switchable hardening of a ferromagnet at fixed temperature. *Proceedings of the National Academy of Sciences*, 107(7):2797–2800, February 2010. ISSN 0027-8424, 1091-6490. doi: 10.1073/pnas.0910575107. URL <http://www.pnas.org/content/107/7/2797>.

Bibliography

- [85] Manoj K. Singh, W. Prellier, M. P. Singh, Ram S. Katiyar, and J. F. Scott. Spin-glass transition in single-crystal BiFeO₃. *Phys. Rev. B*, 77(14):144403, Apr 2008. doi: 10.1103/PhysRevB.77.144403.
- [86] B. Sipos, A. F. Kusmartseva, A. Akrap, H. Berger, L. Forró, and E. Tutis. From mott state to superconductivity in 1T-TaS₂. *Nature Materials*, 7(12):960–965, November 2008. ISSN 1476-1122. doi: 10.1038/nmat2318. URL <http://www.nature.com/nmat/journal/v7/n12/full/nmat2318.html>.
- [87] D. Slobinsky, C. Castelnovo, R. A. Borzi, A. S. Gibbs, A. P. Mackenzie, R. Moessner, and S. A. Grigera. Unconventional magnetization processes and thermal runaway in Spin-Ice Dy₂Ti₂O₇. *Physical Review Letters*, 105(26):267205, December 2010. doi: 10.1103/PhysRevLett.105.267205. URL <http://link.aps.org/doi/10.1103/PhysRevLett.105.267205>.
- [88] G. L. Squires. *Introduction to the theory of thermal neutron scattering*. Dover Publications, 1997.
- [89] S. M. A. Tabei, M. J. P. Gingras, Y.-J. Kao, and T. Yavorskii. Perturbative quantum monte carlo study of LiHoF₄ in a transverse magnetic field. *Physical Review B*, 78(18):184408, November 2008. doi: 10.1103/PhysRevB.78.184408. URL <http://link.aps.org/doi/10.1103/PhysRevB.78.184408>.
- [90] M. Tarzia and G. Biroli. The valence bond glass phase. *EPL (Europhysics Letters)*, 82(6):67008, June 2008. ISSN 0295-5075, 1286-4854. doi: 10.1209/0295-5075/82/67008. URL <http://iopscience.iop.org/0295-5075/82/67008>.
- [91] Y. J. Uemura, T. Yamazaki, D. R. Harshman, M. Senba, and E. J. Ansaldo. Muon-spin relaxation in AuFe and CuMn spin glasses. *Physical Review B*, 31(1):546–563, January 1985. doi: 10.1103/PhysRevB.31.546. URL <http://link.aps.org/doi/10.1103/PhysRevB.31.546>.
- [92] G. K. White and P. J. Meeson. *Experimental Techniques in Low-Temperature Physics*. Oxford Science Publications, 2002.
- [93] C. R. Wiebe, J. E. Greedan, P. P. Kyriakou, G. M. Luke, J. S. Gardner, A. Fukaya, I. M. Gat-Malureanu, P. L. Russo, A. T. Savici, and Y. J. Uemura. Frustration-driven spin freezing in the s=1/2 fcc perovskite Sr₂MgReO₆. *Physical Review B*, 68(13):134410, October 2003. doi: 10.1103/PhysRevB.68.134410. URL <http://link.aps.org/doi/10.1103/PhysRevB.68.134410>.
- [94] J. A. Wilson, F. J. Di Salvo, and S. Mahajan. Charge-density waves and superlattices in the metallic layered transition metal dichalcogenides. *Advances in Physics*, 24(2):117–201, 1975. ISSN 0001-8732. doi: 10.1080/00018737500101391. URL <http://www.tandfonline.com/doi/abs/10.1080/00018737500101391>.
- [95] P. Xu, J. O. Piatek, P.-H. Lin, B. Sipos, H. Berger, L. Forró, H. M. Rønnow, and M. Grioni. Superconducting phase in the layered dichalcogenide 1T-TaS₂ upon inhibition of the

Bibliography

- metal-insulator transition. *Physical Review B*, 81(17):172503, May 2010. doi: 10.1103/PhysRevB.81.172503. URL <http://link.aps.org/doi/10.1103/PhysRevB.81.172503>.
- [96] M. I. Youssif, A. A. Bahgat, and I. A. Ali. Ac magnetic susceptibility technique for the characterization of high temperature superconductors. *Egypt. J. Sol.*, 23:2, 2000.
- [97] B. Zhang and Z. Zhu. Design of an inchworm-type linear piezomotor. *Proceedings of SPIE*, 2190(1):528–539, May 1994. ISSN 0277786X. doi: doi:10.1117/12.175214. URL http://spiedigitallibrary.org/proceedings/resource/2/psisdg/2190/1/528_1.
- [98] F. Zwick, H. Berger, I. Vobornik, G. Margaritondo, L. Forró, C. Beeli, M. Onellion, G. Panaccione, A. Taleb-Ibrahimi, and M. Grioni. Spectral consequences of broken phase coherence in 1T- TaS₂. *Physical Review Letters*, 81(5):1058–1061, 1998. doi: 10.1103/PhysRevLett.81.1058. URL <http://link.aps.org/doi/10.1103/PhysRevLett.81.1058>.

Julian Piatek

Avenue de Sévery 4
CH-1004 Lausanne
Switzerland
☎ +41 (0)78 719 63 82
✉ julian.piatek@gmail.com

27 years old
British, Australian
Single
Swiss B Permit



Innovation drives excellence

Objective

R&D oriented business role in a market leading company

Experience

03/2007–present **Laboratory for Quantum Magnetism (LQM)**, *Swiss Institute of Technology (EPFL)*, Lausanne, Switzerland.

PhD Thesis, Master Thesis, Part-time research internship

- Design, development, implementation & testing of a – unique in the world – magnetisation measurement system
- Planning and management of research projects
- Laboratory infrastructure development and consumables administration
- Teaching assistant for General Physics course for engineers
- Supervisor of several internship students

10/2006–03/2007 **Laboratory of Physics of Living Matter (LPMV)**, *EPFL*, Lausanne, Switzerland.

Part-time research internship in Collaboration with Berna Biotech

- Atomic force microscopy (AFM) research on a potential influenza vaccine

10/2005–09/2006 **Plasma Physics Research Center (CRPP)**, *EPFL*, Lausanne, Switzerland.

Part-time research internship

- Plasma diagnostics using extreme ultra-violet (EUV) spectroscopic techniques

09/2002–06/2003 **Disking International**, Petersfield, United Kingdom.

Retail Unit Manager

- Management of shop, sales, stock and local advertising
- Computer diagnostics, repair and technical support

09/2001–06/2003 **Fareham College**, Fareham, United Kingdom.

IT Facilitator - evenings adult education classes

Education

2009 – 2012 **Ph.D. Physics**, Laboratory for Quantum Magnetism.
Swiss Institute of Technology (EPFL), Lausanne, Switzerland

2007 – 2009 **M.Sc Physics**, Diplômé Ingénieur Physicien.
Swiss Institute of Technology (EPFL), Lausanne, Switzerland

2003 – 2007 **Physics**, with *Erasmus University Exchange – EPFL, Lausanne, Switzerland.*
Imperial College of Science, Technology and Medicine, London, United Kingdom

2000 – 2002 **A-levels**, *Maths, Further Maths, Physics, Chemistry, French.*
Alton College, Alton, United Kingdom

Languages

English Mother tongue
French Fluent
Spanish Intermediate
German Basic

Skills and Interests

Skills I am a highly motivated and autonomous person who enjoys challenges, technology management and have excellent analytical and problem solving skills. I am also a flexible team player with good communication skills.

Interests I have a great interest in discussing with friends and family the emergent technology daily news. My favourite hobbies include activities such as scuba diving and snowboarding with friends and family and playing the bass guitar.

Publications

- J. O. Piatek, B. Dalla Piazza, N. Nikseresht, I. Živkovic, K. W. Krämer, N. B. Christensen, and H. M. Rønnow. Phase diagram with enhanced spin glass region of a mixed Ising/ XY alloyed model magnet $\text{LiHo}_x\text{Er}_{1-x}\text{F}_4$. *In Preparation*.
- J. O. Piatek, I. Živkovic, and H. M. Rønnow. Piezomotor driven dilution fridge SQUID magnetometer. *In Preparation*.
- T. Fennell, J. O. Piatek, R. A. Stephenson, G. J. Nilsen, and H. M. Rønnow. Spangolite: an $s = 1/2$ maple leaf lattice antiferromagnet? *Journal of Physics: Condensed Matter*, 23(16):164201, April 2011.
- P. Xu, J. O. Piatek, P.-H. Lin, B. Sipos, H. Berger, L. Forró, H. M. Rønnow, and M. Grioni. Superconducting phase in the layered dichalcogenide 1T-TaS_2 upon inhibition of the metal-insulator transition. *Physical Review B*, 81(17):172503, May 2010.
- M. A. de Vries, J. R. Stewart, P. P. Deen, J. O. Piatek, G. J. Nilsen, H. M. Rønnow, and A. Harrison. Scale-free antiferromagnetic fluctuations in the $s = 1/2$ kagome antiferromagnet herbertsmithite. *Physical Review Letters*, 103(23):237201, December 2009.

References available upon request